



UiT The Arctic University of Norway

Faculty of Health Sciences

Department of Medical Biology

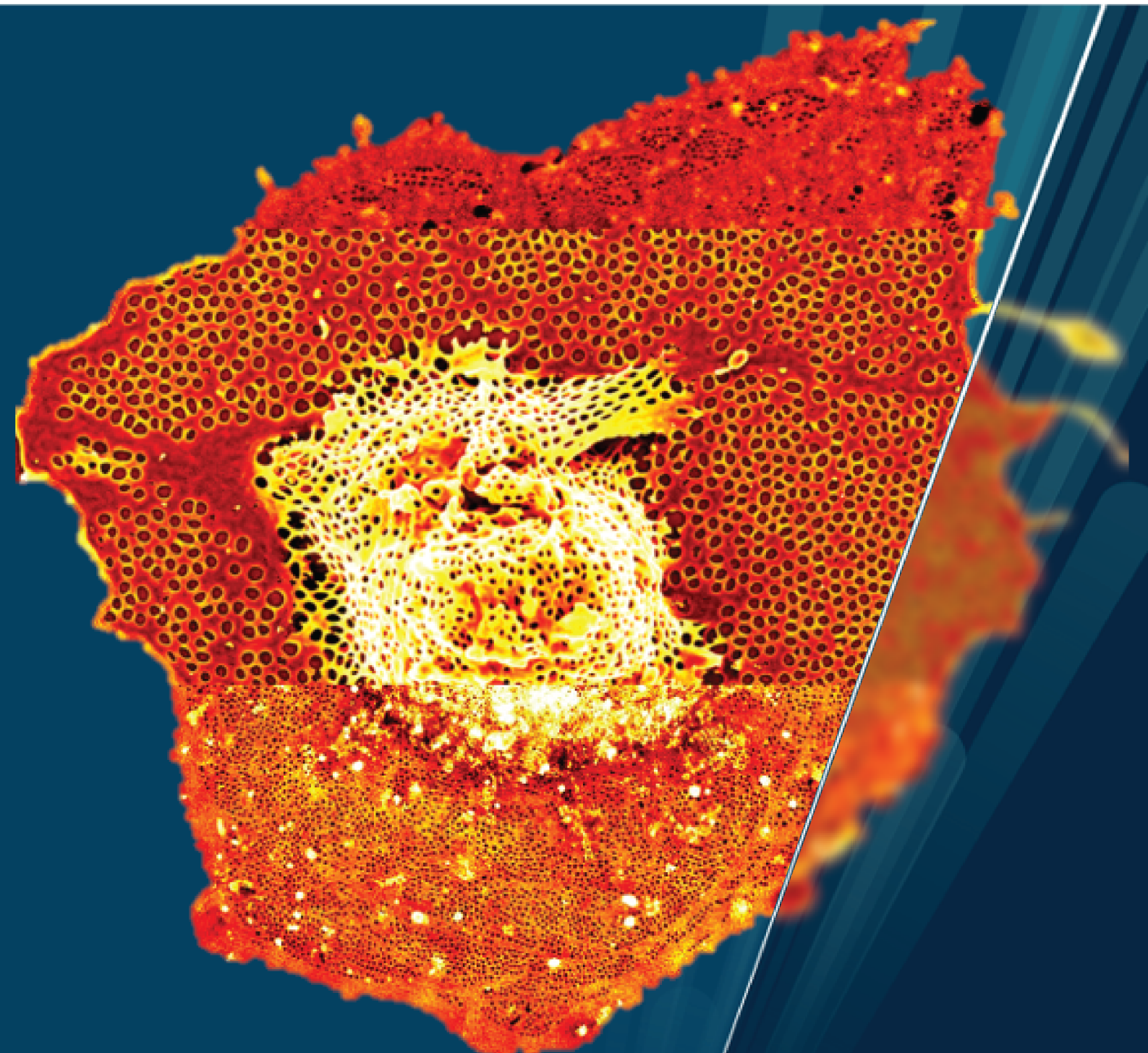
Unraveling nanoscale alterations in liver cell fenestrations

— *Morphological studies via optical super-resolution microscopy approaches*

Hong Mao

A dissertation for the degree of Philosophiae Doctor

November 2020



Unraveling nanoscale alterations in liver cell fenestrations

Morphological studies via optical super-resolution microscopy approaches

Hóng Máo

A dissertation for the degree of Philosophiae Doctor



Vascular Biology Research Group

Department of Medical Biology

Faculty of Health Sciences

UiT–The Arctic University of Norway

November 2020

Table of Contents

LIST OF PAPERS.....	VII
ABBREVIATIONS.....	IX
SUMMARY	XII
INTRODCUTION.....	1
1 The Liver.....	1
1.1 Hepatic Triad.....	1
1.2 Liver Sinusoids.....	2
2 Liver Sinusoidal Endothelial Cells (LSECs).....	2
2.1 Scavenger Function of LSECs	4
2.1.1 Scavenger Receptors (SRs).....	4
2.1.2 FcγRIIb2.....	7
2.1.3 Functional Biomarker for LSECs.....	8
2.2 Dynamic Changes of Fenestrae.....	8
2.3 Atherosclerosis.....	9
2.3.1 Nitric Oxide & Reactive Oxygen Species (NO & ROS)	10
2.3.2 Oxidized Low-Density Lipoprotein (oxLDL).....	11
2.4 Platelets	13
2.5 Drugs and Liver (fenestrae)	14
2.5.1 Caffeine and Its Metabolites	14
2.5.2 Sildenafil	17
2.6 Other Factors and Fenestrae.....	18
2.6.1 Species.....	18
2.6.2 Age & Intralobular location	19
2.6.3 Specimen Processing & Methods of Visualization.....	20
3 Super-Resolution Microscopy.....	22
3.1 Single-Molecule Localization Microscopy	23
3.1.1 <i>d</i> STORM.....	24
3.2 SIM.....	29
4 Long-Term Preservation of LSECs.....	30
AIMS OF THE STUDY.....	32

SUMMARY OF PAPERS	33
GENERAL DISCUSSION.....	37
Methodological considerations	37
Rat and Mouse Models.....	37
Primary Cell Culture	37
Treatments & LSECs	39
Microscopy.....	40
Challenges in Our Study	41
Fenestrae Size vs. Microscopy.....	41
Treatments vs. Fenestrae	42
Long-Term Preservation Challenge	44
CONCLUSION	45
REFERENCES.....	46
PAPERS I-IV	73

ACKNOWLEDGEMENTS

The project was funded by the Tromsø Research Foundation/Trond Mohn, the University of Tromsø-The Arctic University of Norway, the Research Council of Norway FRIMED (grant no. 262538); and Marie Skłodowska-Curie Grant Agreement (No. 766181, project: DeLIVER). The practical work presented in this thesis was carried out at the Vascular Biology Research group and the Optical Nanoscopy Research group, University of Tromsø; the Biogerontology group, ANZAC Research Institute, University of Sydney, and the Microbial Imaging facility, the ithree Institute, University of Technology Sydney. All the support is gratefully acknowledged.

This thesis was accomplished under the supervisions of Prof. Peter McCourt, Prof. Karen Sørensen, Cristina Øie and Balpreet Singh Ahluwalia. I hereby express my sincere gratefulness to my dear supervisors, for their guidance in the fields of liver sinusoidal endothelial cells, super-resolution microscopies and scientific English:

Peter, as my main supervisor, sincerely thank you for offering me this ‘arctic expedition’ research position via an oversea call and picking me up from the airport the first day I landed here and Sydney; for providing me all the opportunities, including exploring research facilities in other institutes locally & internationally and training me as a more independent researcher in the lab; for sharing your experience and being patient to the ‘demanding’ me when I encountered difficulties; for your precious time spared and spent on correcting my grammar errors and among all the various synonyms throughout the thesis writing; for showing me the land “Down Under”, special thanks to Prof. Gunbjørg Svineng for her tasty homemade meatballs, and offering me to meet the McCourt clan for Christmas. All in all, so grateful for all these, which made me who I am today.

Karen, as my co-supervisor, many thanks for your expertise, advice, leading me to the north and the SEM work in the lab, particularly for your sweet smile all the time, no matter the situation they were. And for always with encouraging and approved feedback, enlightened and motivated me further up, especially in ‘dark’ times; also for careful checking my thesis writing with patient and inspiring suggestions, and prompt reply for all my questions while with your busy schedules. It was very delightful to have you as my supervisor leading me along the scientific journey, your persistently hard-working and rigorous attitude towards science are always my pursuing in science.

Cristina and Balpreet, both as my co-supervisors, very grateful for demonstrating and providing me the platform with super-resolution microscopy. Especially for Cristina, thank you for showing me the lab works such as perfusion, and cell culture... and imaging with Viola Mönkemöller and Deanna Wolfson (⇐ thanks to you two as well!); and for being my daily ‘opponent’ in science, training me regularly towards a more matured scientist; Also, for your advice on thesis writing, not limiting and expanding my perspectives on viewing science. Special thanks to Deanna for allowing me independent

work in the OMX lab, also sharing her tips and advice in science, for inspiring the caffeine test idea during the bionano meeting in my first year.

Special thanks to Ruomei Li and Ana Oteiza, for both showing me the LDL world in the lab and helped me out with manuscript correction with detailed suggestions and advice. Additionally, thanks to Ana as a careful and considerate officemate, for tidying my desk before I arrived back from AU...

Particularly, Ruomei, words are certainly not enough to express my gratitude to you (probably I may try to express these more efficiently in Chinese), you have been my savior in tough times and through: not only when I first came to Tromsø for guiding me the city (town?) and thereafter, and also for being there and answering my endless questions when my project stuck with obstacles. You always came with unique perspectives, those insightful suggestions kept me thinking and guided me towards a new direction in science. Also, thanks for being the thesis images quality control, encouraging me with tips on preparation of thesis and presentations in this nearly accomplished period... Overall, all the help means a lot to me. I am really lucky and blessed to have you as my scientific 'advisor' during my journey. You deserve a big heartfelt thank you from me for all your support!

Many thanks to Robin Dikemann and Prof. Thomas Husser, for guiding and providing me the *d*STORM platform with expertise, and all the efforts in aiding with the analysis of image data to make our life easier. Furthermore, Robin, thank you for introducing our group with machine learning technique with a user-friendly workflow, also for assisting the method paper in Heidelberg, great teamwork. Additionally, I am grateful to have you together, exploring the big wild zoo city, especially survived Concord 75, altogether with Sebastian and Kevin, blue mountain trekking...

Thank Prof. David Le Couteur and Prof. Victoria Cogger for one-year hosting me for lab work at ANZAC Research Institute, Sydney. It was a good experience for me to broaden my horizon about the research activities on the other side of the world. Thanks to Glen P. Lockwood and Sophie Kang for preparing the cells. Also, thanks to Nicholas Hunt for further investigating research work with home-built *d*STORM after my leave. Thanks to Gabrielle and Helena for their kindness during my stay. Also, thanks to Prof. Cynthia Whitechurch for allowing me as a superuser weekly visits to their SIM facility at UTS for 3 months.

Also thanks to Kenneth Bowitz Larsen, Tom-Ivar Eliertsen, Randi Olsen and Augusta Hlin Aspar Sundbø for aiding in confocal, super-resolution microscopies and SEM.

I also would like to express my thanks and gratitude to our group members for the nice social environment: Prof. Bård Smedsrød, for sharing his humor in daily work life and inviting us to the summer parties in his home. All the ladies: Annett K. Larsen, Jaione Simón-Santamaría and Gianina Dumitriu, always with a warm smile when greeting.

Specifically, Annett, for giving me the warm hug with a safe trip wish to China for last Christmas in the dark time. Jaione, for lending me your comfy sofa chair the first year when I was with less furniture in the apartment. Gianina, for sharing life experiences with travel tips and plants. Speaking of plants, thanks to Javier Sánchez Romano for taking care of the plants (especially the >3 yo ‘giant’ avocado treelet) in the office during stuck in China (as well as former officemate Jan Ole Olsen, thanks to you), also for sharing the thesis preparation advice. And Ingelin Kyrrestad, for warm greetings from the Arctic to China during my second stuck for pandemic, and telling her interesting project results. Sabin Bhandari, for sharing and discussions we had, and offering the help for grammar check for my thesis during your busy finalizing period. Kjell for all the jokes and tricks, especially the ‘painful’ broken finger. Gahl and Kjetil, for beer brewery experience. Finally, the McKids (Larissa, Karolina and Christopher), for sharing the office in the past years, comfy sofa after tired writing days and for accompanying the Hurtigruten trip to Bergen ... Eike, for sharing all the ‘in/appropriate’ jokes (too long to be specified here).

Thanks to all my friends, for all your support and concern, make it possible for me to overcome those frustrating periods in my study and life. In Tromsø, thanks to Ali, Tina and Kirs for tripping to Senja, Kirs’ hometown and Lofoten. Special thanks to Yu-Fen Chang for being a good listener and your hand-writing card with great humor as always. Also, to our common friend Bolor, thank you for hosting me in Stavanger, also our hiking trips (conquered two famous rocks there), being a patient listener... Also thanks to: Ting in Bergen, Xianwen and Zhibo (the No. 3) in Ås with their individual family members as well as the No. 1 in Denmark, for having me in their homes when I visited there, visiting me in Tromsø as well, concerning my progressing, etc.

For those in China, I do appreciate the time we spent together in the past years, though short, still like a family gathering every time we met again (great fun/food); Thanks to No. 2 for guiding her hometown and the trip in southern China. Chu-qing, as the youngest ‘brother’ among our family, thank you for the hiking and patience in those hard times; also for the invitation to ever experience as a best man from ‘the No. 5’s wedding’, for all the entertaining oversea conversations.... Looking forward to meeting you again!

To those who helped/supported, or even just accompanied with your kindness along the journey, I thank your appearance with minor or trivial favors from you, which might mean a lot for me, thank you again! Hope we all manage to survive this pandemic health crisis and become the ‘superhuman’ as Friedrich Nietzsche referred to.

Last but not least, lots of love and gratefulness to my parents, sister and her family in China, for your always being there, made me through all the frustrating and difficulties. Your support means the whole world to me. Thank you, all of you!

Tromsø, Nov. 2020

Hong Mao

高岸为谷，深谷为陵

—《诗经·小雅·十月之交》

Non semper ea sunt quae videntur.

Phaedrus

"Things are not always what they seem; the first appearance deceives many. The intelligence of a few perceives what has been carefully hidden."

Roman poet — Phaedrus

LIST OF PAPERS

Paper I

Hong Mao, Robin Diekmann, Hai Po H. Liang, Victoria C. Cogger, David G. Le Couteur, Glen P. Lockwood, Nicholas J. Hunt, Mark Schüttpelz, Thomas R. Huser, Vivien M. Chen and Peter A.G. McCourt

Cost-efficient nanoscopy reveals nanoscale architecture of liver cells and platelets

Nanophotonics, 2019; **8**: 1299–1313, eISSN 2192-8614, DOI: 10.1515/nanoph-2019-0066

Paper II

Hong Mao, Karolina Szafrńska, Deanna L. Wolfson, Balpreet Singh Ahluwalia, Cynthia B. Whitechurch, Glen P. Lockwood, Robin Diekmann, David Le Couteur, Victoria C. Cogger, Peter A.G. McCourt

Effect of caffeine, theobromine and other xanthines on liver sinusoidal endothelial cell ultrastructure

Manuscript

Paper III

Hong Mao, Larissa D. Kruse, Ruomei Li, Ana Oteiza, Victoria C. Cogger, David Le Couteur, Balpreet Singh Ahluwalia, Karen K. Sørensen, Cristina Øie, Peter A. G. McCourt

Impact of oxidized low-density protein on liver sinusoidal endothelial cells ultrastructure

Manuscript

Paper IV

Viola Mönkemöller, Hong Mao, Wolfgang Hübner, Gianina Dumitriu, Peter Heimann, Gahl Levy, Thomas Huser, Barbara Kaltschmidt, Christian Kaltschmidt & Cristina Øie

Primary rat LSECs preserve their characteristic phenotype after cryopreservation

Sci Rep, 2018 **8**:14657, DOI:10.1038/s41598-018-32103-z

ABBREVIATIONS

A2MR	α_2 -macroglobulin receptor
AcLDL	Acetylated low-density lipoprotein
AFM	Atomic force microscopy
BFP	Back focal plane
BME	β -mercaptoethanol
cAMP	Cyclic adenosine monophosphate
CD	Cluster of differentiation
cGMP	Cyclic guanosine monophosphate
CLEVER-1	Common lymphatic endothelial and vascular endothelial receptor-1
CNS	Central nervous system
CVD	Cardiovascular disease
dSTORM	direct stochastic optical reconstruction microscopy
DMSO	Dimethyl sulfoxide
DMEM	Dulbecco's modified Eagle's medium
ED	Erectile dysfunction
EM	Electron microscopy
EM-CCD	Electron-multiplying charge-coupled device
epi	epifluorescence
eNOS	Endothelial NOS
FBS	Fetal bovine serum
Fc γ R	Fc gamma-receptor
FEEL-1	<u>F</u> asci <u>l</u> in, <u>E</u> pidermal growth factor (EGF)-like, laminin-type <u>E</u> GF-like, <u>l</u> ink domain-containing scavenger receptor-1
FITC	Fluorescein isothiocyanate
fPALM	Fluorescence photoactivation localization microscopy
FSA	Formaldehyde treated serum albumin
FWHM	Full-width-at-half-maximum
GC	Guanylate cyclase

GFP	Green fluorescent protein
HARE	Hyaluronan receptor for endocytosis
HDL	High-density lipoprotein
HILO	Highly inclined and laminated optical sheet
HNE	4-hydroxynonenal
IDL	Intermediate-density lipoprotein
IgG	Immunoglobulin G
iNOS	Inducible nitric oxide synthase
KC	Kupffer cell
LDL	Low-density lipoprotein
LPS	Lipopolysaccharide
LRP	Low-density lipoprotein receptor-related protein
LSEC	Liver sinusoidal endothelial cell
MDA	Malondialdehyde
MEA	β -mercaptoethylamine
MR	Mannose receptor
MSR	Macrophage scavenger receptor
NAD	Nicotinamide adenine dinucleotide
NADPH	Nicotinamide adenine dinucleotide phosphate
NAFLD	Non-alcoholic fatty liver disease
NK	Natural killer cell
NMN	Nicotinamide mononucleotide
nNOS	Neuronal nitric oxide synthase
NO	Nitric oxide
NPC	Nonparenchymal cell
oxLDL	Oxidized low-density lipoprotein
PALM	Photoactivated localization microscopy
PC	Parenchymal cell
PDE	Phosphodiesterase

PH	Partial hepatectomy
PSF	Point spread function
PUFA	Polyunsaturated fatty acid
QE	Quantum efficiency
RAP	Receptor-associated protein
RNS	Reactive nitrogen species
ROS	Reactive oxygen species
S1P	Sphingosine 1-phosphate
SC	Stellate cell
sCMOS	Scientific complementary metal-oxide semiconductor
SEM	Scanning electron microscopy
SIL	Sildenafil
SIM	Structured illumination microscope
SMLM	Single-molecule localization microscopy
SPARC	Secreted protein acidic and rich in cysteine
SR	Scavenger receptor
STED	Stimulated emission depletion
TEM	Transmission electron microscopy
TIRF	Total internal reflection fluorescence
tPA	Tissue plasminogen activator
ULDL	Ultra low-density lipoproteins
VLDL	Very low-density lipoproteins

SUMMARY

The endothelium makes up the innermost cell layer of blood vessels. It consists of a thin layer of simple squamous cells, forming an interface between circulating blood and the surrounding tissue. Endothelial cells of different vascular beds are specialized according to tissue-specific functions. For this project emphasis was placed upon high-resolution methods enabling the study of liver sinusoidal endothelial cells (LSECs) below the diffraction limit of visible light (~200 nm). LSECs have unusual morphology with as much of 20% of their surface covered with cellular fenestrations - holes through the cells of 50-300 nm diameter. These allow bi-directional flow of plasma from the sinusoids to the surrounding hepatocytes, while retaining blood cells in the sinusoidal lumen. Little is known about the function of fenestrations, their regulation, and their role in the transfer of metabolites, viruses, lipoproteins and pharmaceuticals to other cells of the liver.

There are two major challenges with the study of LSEC fenestrations; i) the majority have diameters smaller than the diffraction limit of visible light and; ii) they disappear rapidly in cultured LSEC, and there are no cell line alternatives that express fenestrations. To address the first challenge, the project used classical super resolution imaging technologies such as scanning electron microscopy, and two novel super-resolution optical microscopy modalities: *d*STORM (direct stochastic optical reconstruction microscopy) and SIM (structured illumination microscopy) to study the *in vitro* effects of xanthines, sildenafil and oxidized LDL on LSEC fenestrations. One of the xanthines, theobromine, and sildenafil increased both the frequency and diameter of fenestrations in cultured LSEC. While oxidized LDL caused major disruptions in LSEC fenestration morphology. Finally, to address the second challenge, namely the rapid loss of fenestrations in LSEC, a cryopreservation method for freshly isolated LSEC was developed such that they can be used at researchers' convenience, rather than directly after isolation from live

INTRODCUTION

1 The Liver

The liver is the largest (2-3% of average body weight) organ in the body. It is highly vascularized and at rest, it receives up to 25% of total cardiac output every minute - arterial and portal blood mix within the hepatic sinusoids before draining into the systemic circulation (37). The circulation system connects the liver via two large blood vessels: the hepatic artery and portal vein. The hepatic artery carries oxygen-rich blood from the aorta, while the portal vein carries nutrient-rich blood from the entire gastrointestinal tract, the spleen and pancreas. Blood vessels in the liver subdivide into small capillaries known as liver sinusoids, that lead to a “hepatic lobule”.

1.1 Hepatic Triad

The lobules of the liver are small and approximately hexagonal divisions of the liver, defined at the microscopic/histological scale. A hepatic lobule is a building unit of the liver tissue, consisting of a portal triad, with hepatocytes as the parenchymal cells (PCs) arranged in linear cords between a capillary network, and a central vein (Fig.1). Liver sinusoids (capillaries) are lined in between the hepatocyte sheets, and blood from the hepatic portal vein and hepatic artery enters through the portal triads, and then drains to the central vein (Fig. 2) (258). In the liver lobule, as the metabolic zonation of liver tissue (Fig. 1), hepatic cells differ structurally and functionally from one zone to another (203, 385). Regions up to 100 μm in diameter around the portal triads were considered as part of the periportal zone, and regions up to 100 μm in diameter around the central veins were regarded as the centrilobular/perivenous/pericentral zone (349, 441).

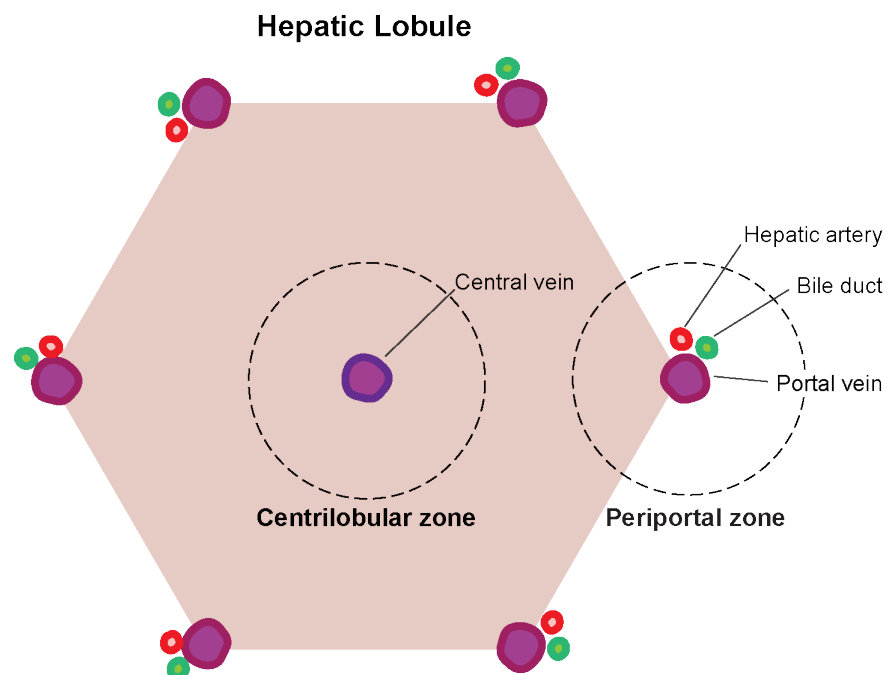


Fig. 1 Hepatic lobule and zonation

1.2 Liver Sinusoids

The liver sinusoids (~5-10 μm in diameter) are the home of nonparenchymal cells (NPCs) (Fig. 2) (250, 452, 463). ~70% of liver sinusoidal endothelial cells (LSECs, highly perforated endothelial cells) as endothelial cells line the wall of the sinusoids with 20% of Kupffer cells (KCs, liver resident macrophages) located mostly on the luminal side of the LSECs (Fig. 2) (458-460). The LSECs separate the blood from the perisinusoidal space (i.e. space of Disse) and nearby sheets of hepatocytes. Located in the space of Disse are the other NPCs: approximately 10% of stellate cells (SCs, pericytes of the sinusoids) and <1% of natural killer cells (NK, also called pit cells or liver associated lymphocytes) (209, 391, 448, 464). The microvilli of hepatocytes project into this space and considerably increase the surface of the hepatocytes (282). The number of sinusoidal NPCs accounts for 30-35% of the total number of liver cells by counting nuclei, however, they comprise only around 6% of the total liver volume (36). Together with NPCs, sinusoids function as a physical and selective barrier between the blood and the hepatocytes.

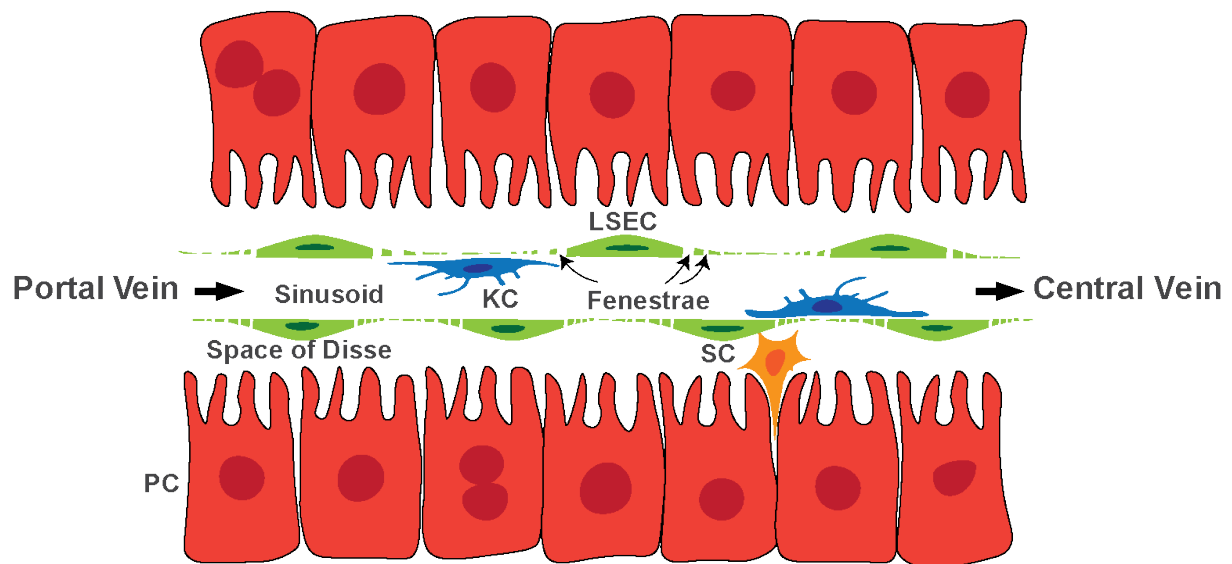


Fig. 2 Schematic view of the microanatomy of the liver sinusoids and its main cell types

2 Liver Sinusoidal Endothelial Cells (LSECs)

Morphologically, individual LSEC is flat cells (0.3 μm at the periphery, <5 μm at the center) (109, 387, 457, 460) with a smooth surface (no cytoplasmic projections such as filopodia or lamellipodia or microvilli) (332). LSEC possesses a great number of unique characteristics (54, 462). The most prominent characteristic of LSECs is that they are perforated with a large number of non-diaphragmed pores with diameters of 50-300 nm (183), called fenestrations or fenestrae (Latin for “window”; singular, fenestra-is any small opening or pore used as a term in biological sciences), it accounts for 5-20% of the

surface of the LSEC. Fenestra diameter ranges depending on species, age, intralobular location, as well as methods of visualization (54, 224, 317, 462, 463). Fenestrae are either scattered alone across the endothelial surface or clustered into groups of tens to hundreds. Multiple fenestrae grouped in clusters form 'sieve plates' (460, 462). They function as a dynamic biofilter, which allows the bidirectional transport (according to the size) of substrates between the blood and the hepatocytes. LSECs are responsible for the efficient clearance of macromolecules and small particles from blood, e.g. metabolites, pharmaceutical drugs, oxidized lipoproteins, and small viruses via direct scavenging or filtration of the plasma through (135, 383, 394, 395), i.e. only particles smaller than the fenestrae can reach the hepatocytes or leave the space of Disse.

Taking lipoproteins as an example, Fraser et al. showed that fenestrae allow chylomicron remnants (diameter: 30-80 nm) produced from dietary fat to enter the space of Disse for further metabolism by hepatocytes, while obstructing the passage of larger chylomicrons, triglyceride-rich lipoproteins (diameter: 200-1000 nm) (120, 126). Likewise, very low-density lipoproteins (VLDL, up to 90 nm in diameter) secreted from hepatocytes into the space of Disse, are able to pass through the endothelial filter to the bloodstream. These suggest the filtering function of the liver sieve (fenestrae) is of great importance in the metabolism of triglyceride-rich lipoproteins (126, 172, 223).

Endocytosis is a process whereby cells bring extracellular material and plasma membrane into the cell interior, i.e. a coat protein (commonly clathrin) on the cytoplasmic side of the plasma membrane, polymerizes a coat that draws the membrane with it into a vesicle. Frequently, the endocytosis occurs when a ligand (e.g. a nutrient molecule with a carrier protein or an attacking virus with endocytic fate) binds to an extracellular receptor molecule, leading to the formation of a clathrin-assembled/coated vesicle. In more detail, the ligand can vary from a broad range of exogenous sources such as bacteria, yeast, viruses; or modified endogenous sources (oxidized lipoprotein, advanced glycation end-products). Blood borne waste substances are taken by hepatic KCs and LSECs, which complementarily constitute the largest scavenger cell system in mammals, i.e. particles above 200 nm in diameter are phagocytosed KCs; materials roughly <200 nm, are endocytosed via clathrin-mediated (nonphagocytic) clearance in LSECs (377).

Compared to other endothelial cells, the high endocytic capacity is a key functional feature of LSECs. LSECs present with numerous endocytic vesicles, and show efficient clathrin-mediated endocytosis through particular endocytosis receptors, making them the most effective scavengers (specialized clearance) to clear blood-borne waste macromolecules and nanoparticles in the body (394). Together with the presence of fenestrae and absence of basal lamina, LSECs are unique and distinctive from any other type of endothelial cell in the body.

2.1 Scavenger Function of LSECs

LSECs lining in the sinusoids, assist in clearing macromolecular waste in the mixed blood from both hepatic portal vein (nutrient-rich) and hepatic artery (oxygen-rich) and regulate hepatic vascularity (332, 395). The role as a scavenger cell for LSEC is a relatively novel finding, it was not until the discovery of LSECs as the major site for clearance of blood-borne hyaluronan (a connective tissue polysaccharide), thereafter the physiological significance of LSECs as scavenger cells was established (390, 392). Other physiological and pathophysiological macromolecules were then found to be cleared by the LSEC (391). Today, LSEC is considered to play a vital role in the clearance of blood-borne waste (macromolecules and nanoparticles). A variety of substances are scavenged by LSECs including extracellular matrix proteins and polysaccharides (391, 394), oxidized lipo-/proteins (233, 388, 409, 430), oligonucleotides (261), virus (adenovirus) (135) and virus-like particles (BK- & JC-polyomavirus-like) (324, 383). Compared to KC or hepatocytes, in LSECs, clathrin protein is more highly expressed, and almost twice the number of clathrin-coated pits are packed in the plasma membrane (208). Thus, clathrin-mediated endocytosis is predominant in LSECs (155). Furthermore, to fulfill their scavenger role in clearing wastes, LSECs are well equipped with specific receptors for endocytosis.

2.1.1 Scavenger Receptors (SRs)

Scavenger receptors (SRs) are cell surface receptors (protein receptor) that bind to the aforementioned ligands and promote the removal of the target (non-/altered-self). In 2017, the latest definition of the various groups of mammalian SR was categorized into 11 different classes (SR-A to SR-L, except for SR-C that is currently only found in *Drosophila*/fruit fly (215), based on their structure and function (342). Initially, systematic attempts subdivided SR into ‘classes’ (A, B...) based on their sequences, and each class was subdivided further into ‘types’ based on additional variations in the sequences caused by alternative splicing (gene expression that results in a single gene coding for multiple proteins) (215). Accordingly, LSECs are reported to express SR class A, B, E, H and L, i.e. SR-A1/1.1, SR-B1/1.1&B2, SR-E1&E3, SR-H1&H2 and SR-L (93, 186, 332, 340, 394). The SRs and FcγRIIb2 constitute the main waste-clearing receptors on LSEC (394).

SR-A1/1.1

SR-A1, also known as macrophage scavenger receptor 1 (MSR1), designated CD204 (cluster of differentiation 204). SR-A1.1 was known as SR-AII, is featured with a shortened C terminal tail, a splice variant form of SR-A1(357). To avoid confusion with the current SR-AII, no receptor is designated as SR-A2 after the 2017 scavenger receptor nomenclature (342). SR-A1/1.1 are both reported to be present on LSECs (186).

SR-A1/1.1 recognizes diverse macromolecules such as modified LDL such as acetylated LDL (acLDL) and oxidized LDL (oxLDL), but not native LDL (212, 217, 357, 408). Apart from that, this receptor binds to beta amyloid (main peptides found in the brains of people with Alzheimer's disease) (129), and surface molecules of gram-positive/negative bacteria such as lipopolysaccharide (LPS) (91, 152).

SR-A expression is predominantly expressed in macrophages, monocytes, mast cells and dendritic cells in mice and humans (190). Besides these, they are also present on vascular smooth muscle cells and endothelial tissues (32, 186). Interestingly, the expression in LSECs is weak under normal conditions, however, enhanced expression was reported after malondialdehyde (MDA)-acetaldehyde serum albumin intravenous administration (93). Furthermore, a rat study demonstrated the expression of SR-A on LSECs (301), wherein the expression of SR-A was responsible for carrying out the uptake of acLDL in the liver, and the authors further theorized about the role of the receptor in preventing the accumulation of cholesterol under normal condition. Moreover, studies have shown that in atherosclerotic lesions with an accumulation of oxLDL (an SR-A ligand), the expression of SR-A was elevated, further suggesting that it has a role in atherogenesis (173, 270). However, in the late 90s, studies reported negligible effect on liver uptake and degradation of serum acLDL (238, 430), suggesting that SR-A receptor may be of minor importance for plasma clearance of these ligands (154).

SR-B1/1.1&B2

SR-B1 (also known as SR-BI) and SR-B1.1 (known as SR-BII) are two splice variants, with identical cDNA sequences apart from the region encoding the C-terminal cytoplasmic domain, which is different (454). Both are highly expressed in the liver, adrenal glands, duodenum, ovaries and testis ((3, 354). The expression of SR-B1 in LSECs was demonstrated by Malerod, *et al.* (254) and Ganesan, *et al.* (134). The crucial involvement of upregulated SR-B1 in non-alcoholic fatty liver disease (NAFLD) pathogenesis was suggested in the livers from mice fed with high-fat diets when compared to control mice (345). SR-B1 binds to high-density lipoprotein (HDL), oxLDL, apoptotic cells, unmodified LDL and VLDL (3, 214, 438). Additionally, SR-B1 was shown to have a protective effect on atherosclerosis development (57, 76).

SR-B2 (CD36) is the prototype class B type SR (13). It is one of the most widely investigated SRs, expressed on adipocytes, capillary endothelial cells, heart and skeletal muscles and platelets (2, 111, 145, 413, 414), as well as on LSECs in the liver. However, the expression of SR-B2 in LSEC vary among species, e.g. very low expression in male Sprag Dawley rat LSECs (233)(Bhandari et al. BMC accepted), highly expressed in human LSEC (406). SR-B2 is involved in the metabolism of lipoprotein such as oxLDL in cardiovascular disease (112, 198). Akin to SR-B1, SR-B2 also binds to HDL, LDL, VLDL, apoptotic cells, and collagen (62, 366, 414).

SR-E1&E3

SR-E1 (LOX-1, lectin-type oxidized LDL receptor) is the class E SR with C-type lectin-like domains and is expressed on vascular endothelial cells, platelets, smooth muscle cells, adipocytes, and macrophages (70, 367, 480). It was considered as the major endothelial SR for oxLDL (binding, uptake and degradation). Apart from that, SR-E1 also recognizes apoptotic cells and gram-positive/negative bacteria (455, 482). SR-E1 in LSECs is expressed in low levels under normal conditions; while during various pathophysiological events (i.e. cardiovascular disease and cancer), the expression is increased (17, 319). Furthermore, a rat study demonstrated the SR-E1 expression in LSECs was upregulated by aldehyde-modified proteins (93).

SR-E3 (MR/mannose receptor, CD206) is a member of the SR-E group and belongs to the C-type lectin family. Traditionally, the receptor is associated with macrophages (263, 397). Nevertheless, SR-E3 is also expressed in other cell types, including sinusoidal endothelial cells of the liver (LSECs), spleen and lymph node (237, 252, 259, 265); glomerular mesangial cells of kidney (236). Studies from mice, rats, pigs and humans, showed that LSECs highly express SR-E3 (96, 97, 237, 252, 255, 259). And the receptor is considered as an important LSEC endocytosis receptor (394), which also mediates uptake of a wide range of endogenous glycoproteins and microbial glycans, and is further proposed to play a role in immunity and glycoprotein homeostasis (225, 391, 397). The broad ligand specificity of SR-E3 is due to the following reasons: as a pattern recognition receptor, the amino-terminal extracellular region of SR-E3 has three distinct domains binding to its specific ligands: i.e. (outer) the cysteine-rich (amino-terminal) domain binds specific sulfated sugars (116); the fibronectin type-II repeat domain binds to collagen (264, 305); the eight adjoining carbohydrate recognition domains (also called C-type lectin-like domains) bind to glycoproteins and glycolipids, which have terminal D-mannose, L-fucose, and/or *N*-acetyl-D-glucosamine residues (106, 421). Apart from these specific binding ligands, SR-E3 also binds to numerous endogenous ligands, such as a lysosomal enzyme (96, 396), and tissue plasminogen activator (tPA, a protein involved in the breakdown of blood clots) (387). Furthermore, soluble ligands for this receptor have been shown to distribute rapidly and predominantly to LSECs [reviewed in Smedsrod (386), Sorensen, *et al.* (394), Sorensen, *et al.* (395)]. SR-E3 expressed on LSECs clear denatured collagen (255), which may prevent the onset of pseudo-capillarization or fibrosis (6). The receptor also benefits LSECs in maintaining high lysosomal degradation capacity, such as for the degradation of formaldehyde treated serum albumin (FSA) (96).

SR-H1&H2

The current known members in SR class H are: SR-H1 (stabilin-1/FEEL-1: fascilin, Epidermal growth factor (EGF)-like, laminin-type EGF-like, link domain-containing scavenger receptor-1 or CLEVER-1: common lymphatic endothelial and vascular

endothelial receptor-1) and SR-H2 (stabilin-2/FEEL-2 HARE: hyaluronan receptor for endocytosis). Primarily, SR-H1 is expressed in two cell types: alternatively-activated macrophages in mammals (340) and sinusoidal endothelial cells of bone marrow, spleen, lymph nodes and liver (141, 259). In contrast, SR-H2 is not detected in macrophages, but otherwise demonstrates the same cell and tissue expression as SR-H1 (110, 340). Both have similar size and structure (41% homology), are considered as the primary SRs of LSECs, involved in the binding, uptake and degradation of various ligands (e.g. hyaluronan and AGEs: advanced glycation end-products) (232, 281), as well as mediating the uptake and degradation of oxLDL and FSA in LSEC (233). An SR-H1&2 double-knockout mice study demonstrated mild liver fibrosis and severe kidney pathology, indicating SR-Hs are pivotal for the removal of compounds toxic to the kidney (370).

Though two receptors have mostly similar ligand profile, SR-H1 has no affinity for hyaluronan (340, 344), but binds SPARC (secreted protein acidic and rich in cysteine, known as osteonectin or basement-membrane protein 40, involved in development and tissue remodeling); in contrast, SR-H-2 binds hyaluronan but not SPARC (221, 394). Furthermore, they have different intracellular distribution patterns. In mature LSECs, SR-H2 is expressed throughout the cell including the cell surface, while SR-H1 has primarily intracellular distribution (394). Interestingly, SR-H2 is expressed in all liver vascular endothelia during embryonic development, becoming only expressed on liver sinusoids at embryonic day 19.5 in mice (481).

SR-L

SR-L1 (also known as LRP-1: low-density lipoprotein receptor-related protein 1, or A2MR: α_2 -macroglobulin receptor; or CD91) is a cell surface receptor belonging to the family of low-density lipoprotein receptors, which serves as the principal clearance receptor for plasma cholesterol (166, 342). It is expressed in the liver, lung, brain, intestine, and muscles, i.e. hepatocytes, neurons, activated astrocytes, and fibroblasts (166, 456). It interacts/mediates endocytosis of abundant ligands, such as ApoE (proteins involved in lipoprotein metabolism) (188), a receptor-associated protein (RAP) (343), tPA (363), in addition to viruses, trypsin-activated α_2 -macroglobulin, cytokines, growth factors and others (167). The expression of SR-L1 on LSEC was reported with immunofluorescence in rats (322). SR-L1 reported in that study is associated with partial hepatic clearance of RAP (5%) and trypsin-activated α_2 -macroglobulin (10%). The occurrence of SR-L1 in LSEC may indicate the involvement of LSECs in the liver lipid homeostasis and lipid filter functions (395).

2.1.2 Fc γ RIIb2

Apart from SRs, there are other endocytosis receptors in LSECs such as Fc γ RIIb2 (Fc gamma-receptor Iib2/CD32b), The Fc receptors are proteins found on the surface of

certain cells (e.g. B lymphocytes, natural killer cells, macrophages, human platelets and mast cells), which contributes to protect the immune system. The name is derived from the specific binding Fc (fragment crystallizable) region for an antibody part. A Latin letter is placed after the 'Fc' part of the name to identify the antibody binding type. The most common class of antibody is immunoglobulin G (IgG), accordingly, the receptor is called Fc-gamma receptors (FcγRs).

Hepatic FcγRs mediate clearance of circulating IgG complexes. This was previously considered to be mediated via KCs only (117). Later, the LSEC FcγRIIb2 was found to contribute to the removal of small soluble immune complexes (159, 201, 243, 384). In mice, the liver accounts for 72% of the expression of FcγRIIb2 in the body, and 90% of this is on LSECs (133). FcγRIIb2 is demonstrated to be the only FcγR in rat LSECs (297). Therefore, the unique expression of FcγRIIb2 in rat and human LSEC can be used as a biomarker to distinguish LSECs from other liver cell types (257).

2.1.3 Functional Biomarker for LSECs

As fenestration is the gold standard for ultrastructural LSEC-specific identity, the functional biomarker for this cell is the specific and effective uptake/clearance of soluble macromolecules via LSEC signature receptors (394). For instance, FSA is one of the most studied markers in LSECs (84, 469). After intravenous administration of FSA, the ligand distributes nearly exclusively in LSECs where it is internalized via SR-H1/2-mediated endocytosis (35, 97, 233). In mouse liver, tail vein injections of fluorescein isothiocyanate labeled FSA (FITC-FSA, ~2.5 μg/g body weight), resulted in abundant uptake in LSECs (while negative in other liver vasculature) (383). AcLDL has been used as a functional marker to identify LSECs in many studies. However, this ligand is recognized by most SRs and endocytosed by endothelial cells in many other vascular beds (84).

Additionally, all macromolecule ligands for LSEC endocytosis receptors can be considered as functional markers (395). Of note, use of the same compound intravenously or in *in vitro* culture, can vary in dose and exposure time to identify cells (low dose and short exposure times are advised for *in vitro* experiments). Furthermore, labeling strategies by either using a fluorescent tag or a radioactive tracer, allows for visualization and tracking of the internalized ligand and/or quantification of the uptake and degradation (e.g. FITC) (395, 435).

2.2 Dynamic Changes of Fenestrae

Fenestrations are dynamic with respect to size and number. They alter in response to pharmacological agents (11, 241, 427) and during certain disease states such as fibrosis,

there is a significant decrease in fenestration number (84, 183). Thus, the structural integrity of fenestrae is considered to be vital for liver homeostasis, i.e. maintenance of a regular exchange of fluids, solutes, particles and metabolites between the hepatocytes and sinusoidal blood. The alteration of fenestrae can have an adverse influence on hepatocytes and liver function (462). However, the exact mechanism by which hepatotoxins induce defenestration remains to be elucidated.

The structure of fenestrae is supported by the LSEC actin and microtubule cytoskeleton. Its diameter is speculated to be mediated by a Ca^{2+} -calmodulin actomyosin complex (52, 54, 318). In the past decades, a number of studies have shown that these dynamic structures play a role in various physiological and pathological situations, such as lipoprotein metabolism (126), hypoxia (130), bacterial endotoxic induction (87), cirrhosis (295), fibrosis (122) and liver cancer (440). Also, whole mount electron microscopic studies investigating the mechanism of response to hormones and cytoskeletal altering drugs, showed alteration of calcium concentrations within LSECs also changed the fenestrae diameter (318). In addition, the number of fenestrae changes by drugs interfering with the cytoskeleton (401). Recently, Mönkemöller, *et al.* (293) demonstrated the association between the cytoskeleton and the plasma membrane, supporting the formation of fenestrations, using 3D structured illumination microscopy (3D-SIM) and single-molecule localization microscopy.

2.3 Atherosclerosis

Atherosclerosis is a progressive, chronic inflammatory disease. It is characterized by gradual thickening of the arterial wall to form an atherosclerotic plaque (fatty deposit), which leads to severe narrowing or closure of blood flow, impeding the supply to different organs. Ultimately, the progress may cause ischemic heart disease, strokes and peripheral vascular disease, collectively known as cardiovascular disease (CVD) (211, 346). Atherosclerosis contributes to the major mortality and morbidity of CVD in western countries. The hallmark of early atherosclerosis is the lipid-laden cell (mainly macrophages, also called foam cells) accumulation in the sub-endothelial area of the arterial wall (245, 375). These foam cells in the atherosclerotic plaques stimulate inflammatory responses, and vulnerable plaques may become unstable with a thin fibrous cap, which may (abruptly) rupture, leading to thrombosis formation or blood clots, often triggering a heart attack or stroke (140, 234, 245, 246).

Atherogenic lipoproteins such as excessive low-density lipoproteins (LDLs) in blood plasma are transported from the vascular space into the arterial wall, mainly via transcytosis (382). LDLs retained in the extracellular matrix of subendothelial space, are further modified by oxidation or enzymatic activity and aggregation. The process also enhances the recruitment and migration of monocytes into the subendothelial space (358).

Furthermore, the modified LDLs increase the phagocytosis by monocytes-derived macrophages in the atherosclerotic lesions (359). Uncontrolled uptake of such lipoproteins by macrophages leads to the formation of foam cells (346). Elevated levels of LDL in the circulation are directly associated with the development of atherosclerosis (107, 108, 267, 268). Studies have suggested the important role of oxidative modification of LDL in the development of these progressions, as non-modified LDL incubated with macrophages do not appear to elicit abnormal cholesterol accumulation (143, 402, 403).

LSECs play a role in controlling the level of lipoproteins in circulation, defenestrated LSECs impair hepatic uptake of lipoproteins, leading to hyperlipoproteinemia (lipid disorder) (124). Similarly, the defenestration of LSECs is associated with the progression of NAFLD. Therefore, the dysfunction of LSECs in the early stages of NAFLD might indicate the severity of subsequent progression of NAFLD (291, 378).

2.3.1 Nitric Oxide & Reactive Oxygen Species (NO & ROS)

Endothelial cells secrete vasoactive chemicals involving vasodilators such as nitric oxide (NO), which is a vital mediator in regulation of the smooth muscle tone and blood pressure, platelet activation and vascular cell signaling (150). For example, NO binds to soluble guanylate cyclase (GC, a NO-sensitive GC), inducing the formation of intracellular cyclic guanosine monophosphate (cGMP) from guanosine triphosphate (GTP), and increased levels of cGMP leading to smooth muscle relaxation (vasodilation). Additionally, the NO-cGMP pathway also plays an important role in mediating blood pressure (38).

Moreover, NO is also an important mediator in liver physiology and pathophysiology. For instance, though the low flow rates are lower in liver sinusoids compared to other capillary beds, LSECs respond to elevated shear stress, producing vasodilatory mediators, such as NO that play a key role in regulating hepatic vascular blood pressure to maximize time for fluid and solute exchange to happen (269, 339).

In mammals, three isoforms of nitric oxide synthases (NOSs) generate NO: neuronal NOS (nNOS), inducible NOS (iNOS) and endothelial NOS (eNOS) (210). The oxidation of L-arginine is catalyzed by NOS and produces NO and citrulline (189). In liver biology, the role of nNOS is little known. And nNOS and iNOS are predominantly found in the cytosol; whereas eNOS binds to the membrane on the cell. This is found mainly expressed in LSEC as well as other endothelial cells (e.g. cells in the hepatic artery, portal vein, central vein) (239). eNOS-derived NO sustains liver homeostasis and prevents pathological conditions in the liver, whereas iNOS-derived NO acts as a pro-inflammatory mediator, which is detrimental (194). In pathological conditions, iNOS generates a large amount of NO that is the main source of reactive nitrogen species (RNS). NO reacts with reactive oxygen species (ROS) to form RNS. ROS/RNS oxidatively

damage biomolecules (e.g. lipids, proteins, and nucleic acids), rendering them dysfunctional and in the process causing cell damage and stress, mainly in hepatocytes, as well as KCs and endothelial cells (7).

Oxidative stress is a term frequently used to indicate a condition where cells are exposed to excessive levels of chemical-derived/molecular oxygen (213). A feature of oxidative stress is increased levels of ROS, which has been reported pre-/clinically in many cardiovascular diseases, such as diabetes, hypertension and atherosclerosis (63, 341, 381, 426, 439). ROS are involved in the initiation and progression of the atherosclerotic plaque and are generated by various cellular processes (56).

2.3.2 Oxidized Low-Density Lipoprotein (oxLDL)

LDL (density: 1.019-1.063 g/mL, commonly known by the misnomer as "bad cholesterol", referring to its involvement in both heart/vascular disease in general) is one of the five major groups of lipoproteins, namely chylomicrons/ultra low-density lipoproteins (ULDL), very low-density lipoprotein (VLDL), intermediate-density lipoprotein (IDL), low-density lipoprotein (LDL) and high-density lipoprotein (HDL) based on the overall density naming convention. LDL is the main carrier for the delivery of fat molecules (lipids, including cholesterol) in blood circulation via LDL receptor mediated endocytosis to peripheral tissues (60). It can experience oxidation in the arterial wall (during atherosclerosis) or in the plasma circulation (15, 180, 193, 331).

Structurally, LDL is a spherical particle (~21-27.5 nm in diameter and ~3 million Dalton in mass) and contains a single apolipoprotein B-100 molecule (ApoB-100), which acts as a ligand for LDL receptors, along with 80-100 additional ancillary proteins) (64, 348). The hydrophobic core of the LDL particle consists of polyunsaturated fatty acid (PUFA, i.e. linoleate) and thousands of esterified/ unesterified (free) cholesterol molecules, as well as a triglyceride. This core is surrounded by a hydrophilic shell (monolayer) of phospholipids and unesterified (free) cholesterol, the ApoB-100 is embedded in the monolayer (103). LDL also carries lipophilic antioxidants such as α -tocopherol (a type of vitamin E) and β -carotenoid (provitamin A) (169).

LDL can be oxidized by the major cells in the arterial wall such as endothelial cells, macrophages and smooth muscle cells, as well as the cell enzyme systems: 15-lipoxygenase, myeloperoxidase and NADPH-nicotinamide adenine dinucleotide phosphate), or copper/iron in a cell-free system (200, 483). However, the oxLDL from a cell-free system is not distinguishable from that of a cellular system in physicochemical and biological comparison (103, 404, 405). Both the protein and lipid of LDL are modified during the oxidative modification. Subsequently, the affinity of LDL for the LDL receptor is reduced. Eventually, the molecule is turned into a ligand for SRs, which is no longer recognized by the LDL receptor (217, 328, 405, 480).

The oxidation initiates with the peroxidation of PUFA in LDL, its decomposition generates reactive aldehydes such as MDA (a marker for oxidative stress), 4-hydroxynonenal (HNE) and hexanal/hexanaldehyde. They can cross-link and react with free amino groups of ApoB-100, gradually leading to an increased net negative surface charge of the molecule and structural changes (200, 405, 465, 483). LDL particles become aggregated as oxidation progresses (67, 233). The composition of LDL particles impacts the level of oxidation in LDL, e.g. the amount of antioxidant/peroxide and free amino groups of ApoB-100. Thus, oxidation of LDL can result in a wide variety of heterogeneous LDL, which might be modified from various defined conditions or even prepared via isolation from biological sources (103, 104). Moreover, the level of oxidation in LDL particles influences the biological properties of oxLDL, i.e. the affinity to macrophages affects the pathogenic properties of oxLDL. The variable effects of oxLDL reported in the literature might thus partly be attributed to the heterogeneity of LDL preparations from different laboratories (176, 204, 217).

The oxidation of LDL can occur and be present in the plasma of healthy individuals (15, 94, 180, 181, 193). Circulating oxLDL may exist in different forms, broadly categorized into three classes based on their modification levels:

- 1) minimally modified LDL, a modified form of LDL that is prepared via long term storage of LDL. This type of LDL is chemically different from the unmodified form recognized by the LDL receptor but not by most of the known SRs (28, 230).
- 2) mildly oxLDL, a moderate oxidized form of LDL that is prepared with less extensive oxidation (1.5-4 h incubation with copper ion).
- 3) heavily oxLDL, a long-term extensively oxidized form of LDL (≥ 12 h incubation with copper ion), that induces a change in surface charge, i.e. increased net negative charge/electrophoretic mobility, making it into a ligand recognized by SRs (217, 230, 328, 405).

Minimally modified LDL and mildly oxLDL are reported to comprise the main types of circulating oxLDL (4, 67, 179, 180). Heavily oxidized LDL is rarely found in the circulation of healthy individuals but is predominantly detected in atherosclerotic lesions (331, 479). The reason why blood borne heavily oxLDL is normally undetectable might be due to the presence of antioxidants in plasma (28, 416, 465), and its efficient uptake by KC (resident liver macrophages) and LSECs (231, 238, 429). This is in contrast to the slow blood clearance of mildly oxLDL, which is cleared from the circulation by uptake in LSECs (233).

Mildly oxLDL has been suggested to be the precursor of heavily oxLDL in the intima (innermost layer of an artery), it has pathogenic properties itself and is a physiological pro-atherogenic molecule in the body (199, 453). However, the much slower uptake of intravenously injected mildly oxLDL than heavily oxLDL (327), as well as its longer

retention in circulation, may be sufficient to allow it to enter and accumulate in the arterial intima (4). Therefore, oxLDL plays a key role in the development of atherosclerosis, and is also associated with the aging process, development of Alzheimer's disease and diabetes (27, 59, 140, 205, 242, 375, 403, 404, 465).

2.4 Platelets

Platelets (thrombocytes from Greek, meaning 'clot cell') are cellular components of blood derived from megakaryocytes of the bone marrow that enter the circulation(249). Platelets were first studied for their role in hemostasis (stopping bleeding) and thrombosis (blood clotting). Circulating unactivated platelets are lens-shaped structures (maximum 2-3 μm in diameter) (196, 289, 334), while activated platelets cover their surface with cell membrane projections. They primarily play a central role in hemostasis and liver homeostasis. In addition, platelets also transport molecules associated with numerous physiological processes, e.g. wound healing, immune responses, cell activation and proliferation (10, 278, 314, 315, 338, 376, 445, 471). In 1996, platelets were first shown to be beneficial for hepatocyte proliferation in rats undergoing partial liver resection (partial hepatectomy: PH) (425). Liver regeneration in 70% PH rats was enhanced with the administration of platelets via the portal vein, which was considered to be a promising novel therapy for patients with PH by platelet-rich plasma transfusion (271).

Following liver injury or PH, LSECs play a key role in this complex process for liver regeneration. The major changes in shear stress (frictional force of vessel lumen when fluid 'slide' across the luminal surface) caused by resection are sensed by LSECs, which proliferate and coordinate the interactive regeneration of different cell types (sinusoidal progenitor cells, platelets and inflammatory cells.) (339). The platelets involved in this process, which are trapped within the liver, interact with liver cells by initially adhering to LSECs (170). Subsequently, activated platelets release granules or vesicles containing chemotactic agents to attract more platelets to the site, but also contain molecules that protect hepatic tissue and stimulate liver regeneration (288). For instance, the co-culture of platelets and LSECs triggers platelets to secrete sphingosine 1-phosphate (S1P, lysosphingolipid, a bioactive lipid mediator), which induces LSEC proliferation and prevents apoptosis (207, 312). Moreover, platelets activate/enhance LSECs to secrete growth factors (e.g. interleukin-6 and vascular endothelial growth factor), which are required for tissue regeneration (207, 288, 313). Finally, LSECs and hepatocytes can internalize platelets (288, 339). Studies showed platelets accumulated in the liver sinusoidal space, and large numbers of platelets were observed in the space of Disse and inside some hepatocytes (99, 304, 321). A transmission electron microscopy (TEM) photograph of a protruding platelet into Disse's space through a pore in LSEC was presented by Murata, *et al.* (300).

Of note, the repair response to liver injury can result in regeneration or fibrosis depending on whether the injury is acute or chronic. In acute liver injury, platelets predominantly contribute to regeneration, whereas in chronic liver damage, platelets participate in fibrogenesis and can actively block regeneration. Therefore, the role of platelets is pleiotropic, and can be beneficial or deleterious to liver function in these processes depending on the condition (68).

2.5 Drugs and Liver (fenestrae)

2.5.1 Caffeine and Its Metabolites

Caffeine (1,3,7-trimethylxanthine) is a xanthine alkaloid, and the related methylxanthines: theobromine (3,7-dimethylxanthine) and theophylline (1,3-dimethylxanthine), are widely distributed in plants all over the world. Coffee (*Coffea arabica*), kola nuts (*Cola acuminata*), tea (*Thea sinensis*) and chocolate (*Cocoa bean*) are the primary sources of these compounds. The earliest recorded utilization of caffeine-containing beverages was tea, which is a popular drink regarded as prolonging life in the Tang Dynasty of China (618-907 AD) (136).

Apart from its natural occurrence in some drinks or foods, nowadays caffeine is applied as a food additive, and as a drug or as part of pharmaceutical preparations. It has become the most universally consumed psychoactive or central nervous system (CNS) stimulant in the world (81). The nervous system is sensitive to caffeine, as caffeine mainly mediates its effect through adenosine receptors. Adenosine is a compound interacting with G-protein-coupled adenosine receptors, which have broad physiological importance. Stimulation of the receptors can initiate discrepant effects, such as bronchospasm, inhibition of neutrophil degranulation, smooth muscle contraction, vasodilatation and regulation of heart rate (151, 175, 442). Since caffeine has a similar molecular structure to adenosine (both have a comparable double bond ring structure), it has the potential to occupy adenosine receptor sites (118), which prevents adenosine stimulation of the receptors by acting as an adenosine receptor antagonist. Caffeine consumption thus results in inhibitory effects to the CNS, including pharmacological effects such as mild CNS stimulation and wakefulness, the capability to sustain intellectual activity, and decreased reaction times, which are similar to the effects of other methylxanthines (92, 337).

In humans, ingested caffeine is rapidly absorbed from the gastrointestinal tract into the bloodstream and metabolized in the liver (99%) to three primary dimethylxanthines, with paraxanthine (1,7-dimethylxanthine) as the major metabolite (approximately 80%), theobromine (roughly 11%) and theophylline (around 5%) (40, 227, 368). In nature, paraxanthine is only found as a metabolite of caffeine, and is not (yet) discovered in plants. It is a different case for the other two metabolites of caffeine in animals and some

species of bacteria, which are found in plants. The absence of food containing paraxanthine has limited the interest in its metabolic fate. Similarly, paraxanthine is also a psychoactive CNS stimulant (277, 400). In *in vitro* studies of hepatocyte toxicity, paraxanthine was reported to be less harmful than caffeine and the least harmful of the caffeine-derived metabolites (146).

Theophylline was first extracted from tea leaves and chemically identified around 1888. Its first clinical use appeared in 1902 (290). In 1922, it was reported as an asthma treatment (373). Akin to caffeine, theophylline is also a potent inhibitor of adenosine receptors in the human brain (398, 399). Its ability to compete with adenosine receptor ligand binding is more potent (44), especially in its respiratory stimulating effects (347). Additionally, theophylline (50 μM) was shown to accelerate human granulocyte apoptosis via an adenosine-receptor-mediated effect (476, 477), as adenosine can delay the apoptosis of granulocytes (449). In contrast to caffeine, theophylline is significantly more active in cardiac stimulation, coronary dilation and smooth muscle relaxation, as well as with greater toxic effects on the cardiovascular system, and similarly for the gastrointestinal system (24, 95, 407). Moreover, theophylline has a greater potential to cause CNS seizures than caffeine (398).

Theobromine is the primary xanthine alkaloid found in cocoa bean and chocolate (380). In particular, theobromine has contributed to one of the most innocuous and pleasant habits: chocolate consumption. It was first identified in 1841, the name derives from the name of the cocoa plant, “the food of Gods” (*Theobroma*). Its effect in the human nervous system is similar to, but lesser than caffeine. The main pharmacological effects of theobromine include diuresis, vasodilatation, myocardial stimulation and smooth muscle relaxation, while the adverse effects include nausea and anorexia (353). It is a more potent cardiac stimulant than caffeine and was used previously as a dilator of coronary arteries in humans, at a dose of 300-600 mg/day (411). Another report found that daily dosing of 979 mg theobromine with cocoa for 3 weeks lowered systolic blood pressure and increased heart rate (434). Compared to the effect of caffeine or theophylline, the action of theobromine on the CNS is weak or virtually absent (82).

In humans, apart from the aforementioned metabolites of caffeine, more than 25 metabolites have been identified overall after caffeine administration, which reveals the rather complex metabolism of caffeine (65). Additionally, the pharmacokinetics of these metabolites differ substantially in humans. Comparative pharmacokinetics of caffeine and its derived methylxanthines was reported in 1986 (226) - the total plasma clearance rate of caffeine and paraxanthine were similar in magnitude (2.07 ± 0.96 and 2.20 ± 0.91 mL /min/kg, respectively), which are greater than those of theobromine and theophylline (1.20 ± 0.40 and 0.93 ± 0.22 mL /min/kg, respectively). Additionally, when the interindividual variability for the rate was considered, while theophylline gave the least variable (1.6-fold range), caffeine (3.2-fold), paraxanthine (2.7-fold) and theobromine (2.6-fold) had wider variability. Furthermore, the half-lives of caffeine (4.1 ± 1.3 h) and

paraxanthine and (3.1 ± 0.8 h) were shorter than those of theobromine (7.2 ± 1.6 h) and theophylline (6.2 ± 1.4 h). Another study in healthy individuals showed that the elimination half-life of caffeine may range from 1.5 to 9.5 hours (about 5 hours in mean; estimated as total plasma clearance rate of 0.078 L/h/kg) (45, 61). The wide range of half-life of caffeine is due to variations in individual physiological/environmental features (e.g. pregnancy, obesity, smoking), which affects its metabolism.

Despite the long history of use of caffeine, concerns have been raised regarding the continued use of high levels of caffeine for long-term health. It is generally considered to be safe in moderate amounts (≤ 400 mg/day) in healthy adults (81, 307). This dose recommendation was based primarily on published human data reviewed by Nawrot, *et al.* (307) in a comprehensive literature search on the aspect of general toxicity, cardiovascular effects, effects on bone status and calcium balance, behavioral effects, carcinogenic and genotoxic potential, and effects on reproductivity (pre-/postnatal development). From very early times, adverse effects of a very large dosage of caffeine have been noted (especially in people not used to the substance), such as nervousness, anxiety, insomnia, irregular heartbeats, excess stomach acid and heartburn (90). If consumed with adequate quantities, it can cause significant toxicity (plasma concentration >40 mg/L) and even be fatal (10 g/person) (21, 128, 202, 216, 307).

To evaluate the effect of caffeine, the metabolism of caffeine should be taken into consideration, as the overall impact on homeostasis is the sum of caffeine, and its metabolites: paraxanthine, theobromine and theophylline. Hitherto, most of the researches have focused on skeletal muscle regarding the topic of caffeine, and carbohydrate homeostasis. However, the liver plays a potentially important role in the regulation of the circulating levels of caffeine and blood glucose concentrations. Additionally, the liver is exposed to a far higher concentration of caffeine than any other tissue of the body. A primary hepatic metabolic action of caffeine is known to cause a net glucose uptake (284, 336). Moreover, caffeine is proposed to protect against fibrosis and effects from ethanol in the liver (85, 89). In 2006, the protective effect of caffeine against liver fibrosis was investigated by Chan, *et al.* (66). Thereafter, in an *in vitro* culture study of human and rodent hepatic stellate cells, the anti-fibrotic effects of caffeine have been evaluated indicating the attenuated progression of liver fibrosis by inhibiting adhesion and activation of hepatic stellate cells (379). Morphological evidence for anti-fibrotic activity of caffeine was shown by Hsu, *et al.* (184), where therapeutic caffeine treatment decreased portal resistance and pressure in thioacetamide-induced cirrhotic rats.

Biologically, the effects of caffeine have been studied for some time (119, 128). Apart from the effect of caffeine in the antagonism of adenosine receptors in CNS, it also functions in the inhibition of phosphodiesterases (PDEs). Caffeine acts as a nonselective competitive inhibitor of PDEs (428). Thus, it can modulate intracellular levels of cyclic adenosine monophosphate (cAMP) - the induction of cAMP strongly inhibits oxidative bursts in neutrophils and suppresses inflammation (309). Additionally, in a study of rats

injected with D-galactosamine and/or lipopolysaccharide (LPS), caffeine decreased liver damage, which implicates the anti-inflammatory effect of administrated caffeine (5, 158).

2.5.2 Sildenafil

Sildenafil (Viagra [sildenafil citrate]) is a vasoactive agent for the treatment of male erectile dysfunction (ED), and has been in use since 1998. Akin to caffeine, a known PDE inhibitor, sildenafil is a potent and selective inhibitor of cGMP-specific PDE type 5 inhibitor, due to its similar molecular structure to that of cGMP (23). Sildenafil causes the cGMP levels to increase via inactivating PDEs that metabolize cGMP. As forementioned, cGMP is an intracellular mediator of the NO pathway, and can cause an increase in NO synthesis - NO can lead to relaxation of the vascular smooth muscle structure (vasodilation), increases in blood flow, inhibition of platelet aggregation and microcirculation (415).

Sildenafil was introduced due to serendipitous discovery of its induction of penile erections while it was originally being tested for treatment of hypertension (high blood pressure) and angina pectoris (a symptom of ischemic heart disease) in the 1980s. However, its induction of marked penile erections redirected its market for ED, rather than for angina (41, 422). It thus became an often-cited example of drug repositioning (14). Additionally, a satisfactory investigation was conducted with the intravenous formulation of sildenafil for more emergent treatment of pulmonary artery hypertension (475).

Orally administered sildenafil has a terminal half-life of between 3-6 hours and is rapidly absorbed with a maximum plasma concentration achieved within an hour. It is rapidly and almost exclusively metabolized by the liver (298, 450). Therapeutic dosages of sildenafil range from 10 to 100 mg/day and are well tolerated in the dosage range studied, with no clinically appreciable effects on blood pressure or heart rate (142, 195). Liver toxicity relevant to sildenafil has been considered very rare, but other specific adverse events were noted, including headaches, flushing, dyspepsia, visual/hearing loss, hypotension, cardiovascular risk (144, 191, 272).

In the last decade, some cases of sildenafil-associated hepatotoxicity have been reported. In humans, few studies were investigated on hepatotoxicity with sildenafil consumption under medical supervision, resulting in an enlarged liver, severe cholestasis in the sinusoids, and cellular alterations (large appearances of eosinophilic granulocytes and necroinflammation) in the portal area (100, 144, 466). In 2011, a histological rat liver study on the effects of sildenafil citrate demonstrated dilation of the central vein, lysed red blood cells and a cytostructural distortion of the organ (105). Moreover, long-term exposure to sildenafil overdoses produced significant biochemical and structural

alterations in liver tissues (i.e. hepatocyte nuclear alterations, necrosis, inflammatory cells infiltration and hepatic vessels congestion), which might affect the function of the organ.

Despite the abovementioned reported potential (and highly variable) hepatotoxicity, there are studies showing beneficial applications of sildenafil. Research in 2012 (in rats) showed sildenafil at low doses accelerates hepatic regeneration after partial hepatectomy, which might suggest it adequately induces liver regeneration (474). And another study demonstrated that sildenafil may suggest a new perspective to protect against DNA damage observed in atherosclerosis (356).

2.6 Other Factors and Fenestrae

Studies have demonstrated that the diameter and number of fenestrae vary not only from species to species, but also between individuals of species, as well as within a single individual under diverse physiological and pharmacological statuses (54). Additionally, some other aspects also affect the structure of fenestrae, including age, intralobular regions and methods of visualization.

2.6.1 Species

With the detailed description of LSEC-fenestrae by Wisse in 1970 (460), there followed an abundance of early studies of LSEC-fenestrae in various species. Although most of these were conducted on mice and rats, other animals were studied including fish (283), birds (125, 127), and many mammals (125, 183, 253, 320, 417, 419, 468). Notably, all LSECs in different species carry the same ultrastructural fenestrae characteristics, namely fenestrae clustered as sieve plates. Most fish studies reported only the existence of fenestrae (114, 131, 174, 283, 362, 418, 420), albeit a research article on goldfish described organized sieve plates with fenestrae (50-200 nm) (311). Moreover, the diameter and number of fenestrae varies from species to species, also between individuals of a species, even within a single individual under different physiological and pharmacological situations, but similar fenestrae were observed for both sexes of a species (253, 283).

The fenestra diameter of the abovementioned species ranges from 50 nm to 300 nm, which is also reported in a human study (183), and the smallest average size of fenestrae was from rabbit and sheep studies (125, 468). The same human study (183) appeared with big variations in porosity (the percentage of total membrane surface that is perforated by fenestrae, with total cell surface being 100%) and frequency (total number of fenestrae per area), as well as in the rat and mouse studies (123, 125, 401). The variations in fenestration patterns between different species were proposed to be related to dietary

cholesterol (54). By comparing rats with rabbits and chickens (both are lower in porosity), the fenestrae tended to be smaller and fewer in the latter two species, respectively. This resulted in a prolongation of cholesterol-rich chylomicron remnants in circulation, in which are considered to be atherogenic. That might explain studies demonstrating the vulnerability of rabbits and chickens to dietary cholesterol, and the development of atherosclerosis (71, 127, 467). Moreover, within the same species (rat), individual variations can be clearly noted with average diameters from 60 nm to 245 nm, porosity from 2.4% to 17.6% and frequency (3.4-20.0 / μm^2) (19, 73, 197, 296, 316, 447, 451, 462). In those studies, many other factors also contribute to these variations, such as intralobular region, age and preparations of specimens, which will be discussed in the next sections.

2.6.2 Age & Intralobular location

An interesting finding from Vidal-Vanaclocha, *et al.* (441) showed clustered and free fenestrae distributed differently in centrilobular and periportal regions, with free fenestrae prevailing in the periportal zone (around 60% of total pores), and clustered fenestrae prevailing in the centrilobular region (roughly 75% of the total number of pores). Moreover, in most of the studies, a zonal gradient is observed with larger fenestrae at greater frequencies and higher porosity in the centrilobular sinusoids (19, 183, 441, 462); allowing more exchange of oxygen in the centrilobular region ascribed to the partial drop of oxygen tension across the lobule in the periportal zone (262). However, there are studies showing larger fenestrae in the periportal region (251, 462, 469); with lower porosity that is at odds with the former studies. These controversial findings might indicate further investigation is needed to confirm the pattern of zonal difference for LSECs.

During intrauterine life, the fetal liver serves as a hematopoietic organ in mammals, this function declines in late fetal life, and then the liver becomes an exocrine gland of the digestive system (79, 286, 470). This dramatic transformation in liver function between embryos and adults is considered to cause transformative alterations of the sinusoidal endothelium in the fetal and adult livers. Few studies have been performed to show the difference between the sinusoids of the fetal and postnatal liver (19, 303). Bankston, *et al.* (18) found that fetal liver sinusoids possess fenestrae with diaphragms permeable to carbon before 17-days gestation, functioning as a sieve for carbon to reach the extravascular space. In 1977, Naito and Wisse observed, using TEM, LSECs on the 15-20th day of gestation in rat fetuses, and the continuity of endothelial lining was found to be only interrupted by the passage of blood cells (303). In addition, the zonal variations in fenestration patterns were reported to exist already in the fetal period of rats. The differences in fenestrae size between liver zones were larger in fetal sinusoids (measured at 18 and 21st days of gestation) than in the sinusoids of new-born (1 and 5-day old)

animals, with the geometric diameter of fenestrae being smaller in the sinusoidal periportal zone than in the centrilobular region (19). In the same study, average adult liver fenestrae tended to be smaller than both fetal and new-born fenestrae. Thus, the LSECs with fenestrae appear and function also in the fetal liver, though with different zonal distribution, size, and morphology compared to adult liver fenestrae.

Furthermore, Le Couteur, *et al.* (222) reported marked ultrastructural changes in the sinusoidal endothelium of old rats (24-27 months) compared with young rats (4-7 months) in SEM, where the porosity dropped almost 60% from 4.1% (young) to 2.5% (old) in old rat, as well as the loss of fenestrae in both periportal and centrilobular regions. Congruent defenestration patterns (loss of fenestrae) were also observed in other old mice (451), baboon (75) and human studies (285). In rats, the loss of fenestrations leads to blockade of lipoprotein (with an average diameter of around 50 nm) passage into the space of Disse (171), which might contribute to hyperlipidemia and atherosclerosis associated with old age (484).

2.6.3 Specimen Processing & Methods of Visualization

To better understand the structure of fenestrae and sieve plates, different methodologies can be used, each involving multiple stages of specimen processing prior to visualization. Processing considerations include pressure or direction of perfusion (anterograde or retrograde to inherent blood flow), and whether the specimens are tissue or cellular (*in vitro*, *in vivo*, *in situ*). Methods of visualization involving respective preparations for the methodologies also have limitations themselves.

In the first place, specimen conditions such as *in vitro* cell culture, *in vivo/in situ* tissue specimens can result in variations in LSEC morphology. By comparison, *in vivo/in situ* samples are more representative of the inner environmental situation for the cells. However, the geometric surroundings complicate the analysis of LSECs under various conditions, so *in vitro* studies simplify the factors to limited/controlled conditions to better understand the function of the LSECs in the liver. Therefore, both approaches have their respective merits, but both definitely give comparable parameters for LSECs. Cultured LSECs retain their fenestra-forming capacity totally (401). An early study in mice (*in vitro* and *in situ*) demonstrated the parameters of LSECs fenestrae (size, porosity and frequency) in both situations, with larger fenestrae size, lower porosity and frequency from cultured *in vitro* LSECs. Although the study did not focus on the comparison of both conditions, the results revealed the distinctions of both conditions (401). In most *in situ* rat studies, the average size of LSEC fenestrae ranges from 60 to 121 nm, porosity from 2.4% to 17.6%, and frequency (5.74-20.0/ μm^2), together with the zonal and young/old variations (19, 73, 125, 127, 197, 222, 317, 441, 447, 451, 462, 463). Nevertheless, *in vitro* studies give a larger average fenestrae size (118-215 nm), with smaller range

variations in porosity (2.8-8.2%) and frequency (3.4-3.9) (47, 51, 469). Therefore, the culture conditions definitely induce the parameter changes in LSEC fenestrae, as the geometric analysis comes to more flattened dimensions, which increase the accuracy of the measurements. On the other hand, this changes the pattern for LSECs from their inner *in situ* environment.

Fenestrae and sieve plates are delicate structures that can contract, break, dilate or coalesce during specimen processing. Thus, to preserve their integrity, careful processing is required. However, in order to examine the walls of the sinusoids, the removal of blood is a necessity. Compared with a large series of human needle biopsies fixed by immersion, resulting in blood cells and precipitates on a sinusoidal surface (311), perfusion fixation provides good preservation of ultrastructural details in the rat liver (303), as well as removing blood cells and precipitates. Of note, the pressure and direction of perfusion can impact fenestration size (447). Endothelial fenestrae are very vulnerable to different pressures of liver perfusion (121, 130). Low pressure (12 cm water pressure, physiological portal pressure) is recommended, to avoid pressure-induced perfusion artifacts and damage to LSEC, typically demonstrated as large gaps within the cell membrane (461). Additionally, a low flow rate (3 mL/min) assures the pressures have no influence on fenestration size (447). Apart from that, the direction (anterograde and retrograde) of perfusion (i.e. two opposite flow senses: porta-cava; cava-porta, respectively) are proposed to manifest variations on fenestrae parameters (441). In both periportal and centrilobular zones, the average values of fenestrae size, frequency and porosity are all larger in retrograde perfused specimens. Thus, via the portal vein in whole liver perfusion of fixative/buffer is the preferred method for liver perfusion. Fixation of specimens for electron microscopy requires quick performance to prevent ultrastructural changes, occurring as the outcome of rapid autolytic processes from the liver itself (74).

The diameter of fenestrations is below the resolution limit of conventional light microscopy (about 200 nm). In the past decades, observation of fenestrae was limited to electron microscopy on liver tissue or cultured LSECs. Transmission and scanning electron microscopy (TEM&SEM) were widely used to visualize fenestrae to study LSECs. For liver tissue, TEM preparation requires embedding in a resin, then slicing to less than 100 nm sections on an ultramicrotome. The methodology was applied to observe the continuity of LSEC surface, and the passage of substances through fenestrae (303), as well as measuring the size of fenestrae and porosity of LSECs (283, 462, 463). In contrast, SEM has been more frequently used to study fenestration size, porosity and frequency as it allows the observation of a large surface area of LSECs and measurements of numerous fenestrae within the field of view.

Notably, the geometric analysis of LSEC fenestrations is highly related to the method of visualization. For example, in one study, the average diameter of rat LSEC fenestra was reported to be 147.2 and 174.6 nm (centrilobular and periportal regions, respectively)

from TEM assessment, and 104.8 and 110.7 nm (same respective region as above) by SEM measurement (462). In both cases (TEM&SEM), SEM results are generally smaller than TEM measurements (283, 463). The preparative differences might explain this, as SEM preparative procedures may induce 15-30% shrinkage of the tissue due to critical point drying (462). Moreover, the results reported from SEM-based studies for LSEC parameters (size, number and porosity) give wide variations in the literature (74).

Given the above limitations of classical SEM and TEM preparation (extensive sample preparative requirements), new technologies have been introduced in the field of studying parameters of LSEC fenestrae, such as cryo-TEM (46), atomic force microscopy (AFM) (48, 50, 53), three-dimensional structured illumination microscopy (3D-SIM) (72) and direct stochastic optical reconstruction microscopy (*d*STORM) (294), all of which possess the advantage of the preparation of wet cell specimens (thus avoiding cell shrinkage). Moreover, AFM and SIM allow the achievement of live cell imaging of LSEC fenestrae dynamics in real time.

3 Super-Resolution Microscopy

Optical resolution describes the capability of an imaging system to resolve detail in the object being imaged. However, the wave-like property of light limits the obtainable resolution (1), i.e. using traditional light microscopes, cellular structure and objects that are spaced by less than the diffraction (i.e. spreading out of the light wave) limit of about 200 nm apart cannot be discerned by conventional light microscopes. A large amount of fundamental biology of the cell occurs at the subcellular scale in the size range of tens to a few hundred nm, which is beyond the reach of conventional light microscopy. Conventionally, the wavelength of visible light ranges from 400 to 700 nm, for one microscope with a high numerical aperture (NA) objective (NA=1.4), the resolution limit is about 200 nm laterally (x and y directions) and about 500 nm along the optic axis (in the z direction) (153).

Using electrons instead of photons was an early approach to attain detailed biological information. As the de Broglie wavelength (matter wavelength) of an electron is much shorter than visible light, electron microscopy (EM) has a much higher resolution than optical microscopes (229). Though achieving atomic resolution (about 0.05 nm) (102), EM has many practical issues that constrain its utility for biological studies. The main issue is that electrons carry an electric charge, and while traveling, they interact with the medium. Since electrons interact with molecules in the air, samples have to be viewed in a vacuum (or low pressure), which is incompatible with living cells or tissue. The interaction of electrons with the sample prohibits their deep penetration into the sample. Therefore, fixation, dehydration, and ultra-thin sectioning are required to prepare a sample for EM, and these procedures may result in artifacts, such as shrinkage of the

specimen and alteration of tissue structure (78). Additionally, the low pressure and ultra-thin sectioning requirements further make EM incompatible with live-cell imaging. Therefore, methods that combine both the non-destructive nature of optical microscopy and the nanoscale resolution of EM are highly desired for biological research. Over the last decades, several super-resolution microscopy (also known as nanoscopy) modalities have been devised that allow diffraction “unlimited” optical microscopy. Notably, the 2014 Nobel Prize in Chemistry was jointly awarded to three laureates: Stefan Hell, Eric Betzig and William Moerner for their contribution in the development of super-resolved fluorescence microscopy (365). The utilization of super-resolution microscopy allows the aforementioned resolution limit to be reduced to around 100 nm for SIM, and 20 nm for single-molecule localization microscopy (SMLM). Theoretically, some of these novel fluorescence microscopies (e.g. non-linear SIM) are capable of unlimited resolution (148).

3.1 Single-Molecule Localization Microscopy

Since the end of the 20th century, with the progression of single-molecule spectroscopy, photoswitches are widely applied in super-resolution fluorescence microscopy. The technique combines photoswitches displaying long-lasting dark states with precise single-molecule localization, and is termed localization microscopy (31, 168, 361). During the last years, the technique underwent various advancements (164, 185, 333, 431, 444) and has found its place among established fluorescence super-resolution microscopies such as SIM and stimulated emission depletion (STED) (147, 165).

Early in 1995, Betzig proposed the general principle of isolating and localizing single fluorescent molecules in a crowded environment, as one of the foundations of far-field optical super-resolution microscopy (30). Thereafter, three research groups independently developed similar optical super-resolution methods with ~20 nm lateral sub-diffraction resolution. Specifically, Betzig and collaborators termed theirs as ‘photoactivated localization microscopy’ (PALM) (31). Hess and colleagues (University of Maine) called it ‘fluorescence photoactivation localization microscopy’ (fPALM) (168). Zhuang and collaborators (Harvard University) developed STORM: stochastic optical reconstruction microscopy (361). In common, they all used effective means to determine if a single molecule is being probed. The position of the molecule can be localized precisely via fitting a model to its point-spread-function (PSF, a spread-out point source/object mathematically describing the detected intensity distribution in a two/three-dimensional function) of the optical microscope, whereas the precision is mainly confirmed by the number of collected photons and the signal-to-noise ratio (371, 423, 478). During the imaging process, the majority of photoswitches are nonfluorescent, small fractions are stochastically activated and precisely localized over time. The density of activated fluorophores must be low enough to allow single-molecule localization,

which is preferably no overlapping central parts of their PSFs. Subsequently, by reconstructing from all localizations, i.e. the imaging of single-molecules obtained within a series of data (hundreds to thousands of images), to form a super-resolved image.

The theory behind the technique is based on an Impressionist painting technique called “Pointillism”, in which small, distinct dots of color are applied in patterns to form an image. Likewise, the SMLM uses photoactivatable/photoswitchable fluorescent proteins or fluorophores as those dots. The exact position of individual molecules can be plotted, and a single super-resolved image (~20 nm) generated from the fusion of position information from thousands of individual images. Photoswitches are molecules that can be switched between two distinct states by external approaches. The molecules are switched between a fluorescent bright (‘on’) and dark (‘off’) state (i.e. ‘blinking’) upon illumination with light of different wavelengths.

In localization microscopy, photoswitches are used to label a structure of interest (cellular proteins). Of note, fPALM uses fluorescent proteins such as photoactivatable/photobleachable proteins (green fluorescent protein, GFP), while PALM uses photoswitchable proteins (e.g. green fluorescent protein Dronpa) (8). Additionally, the first fluorophores applied for STORM were coupled carbocyanine fluorophores with photoswitching properties (361). Thereafter, the requirement of coupling these organic fluorophores was replaced via the introduction of special buffer systems that serve a similar purpose. The latter method is thus called direct STORM (*d*STORM), which is one of the easiest and most used STORM method (437).

3.1.1 *d*STORM

With the aid of a suitable buffer system, *d*STORM utilizes the photoswitching properties of commercially available fluorophores to achieve the localization by irradiating the sample with either one or two wavelengths of light (160, 161, 432). The state of non-fluorescent(‘off’) is triggered by the same wavelength, which also excites the molecule’s fluorescence (‘on’) for localization. The fluorescent (‘on’) state can be reversibly recovered by the use of laser light at lower wavelength regions, such as 405 nm or 488 nm. During the transition of a blinking, highly reactive oxygen is formed as a side product, which causes photodamage to the sample as well as fluorophore photobleaching (433). Controlling the oxygen content in the buffer medium with an enzymatic oxygen scavenging system, as well as adding thiolated molecules to the buffer medium allows almost seamless adjustment of the rates when photoswitching occurs (350). Therefore, enzymatic oxygen removal is frequently used in imaging buffer systems containing enzymes such as glucose oxidase or reducing agents: β -mercaptoethylamine (MEA) (160), β -mercaptoethanol (BME) (235), or ascorbic acid (443), resulting in more stable fluorescence emission (433). Notably, cyanine derivative dyes such as Cy2, Cy3, Cy5

and particularly Alexa Fluor 647 work optimally in oxygen-free environments, but rhodamine dyes like Alexa Fluor 488/555/568 and Atto 488 do not blink favorably under similar conditions, instead, demanding residual fractions of oxygen or another oxidizing agent (302). Thus, careful selection of the buffer system and dyes under suitable power level and conditions (e.g. concentration and pH) to induce the desired photo blinking, and control or prolong the blinking states is needed for SMLM. Furthermore, especially engineered optimizations such as fluorophores exhibiting high fluorescence quantum yield, high photostability, and minimal intrinsic “blinking” have been established to improve the efficiency of photoswitching for single-molecule detection. All of these have dramatically improved significant high localization statistics of reversibility for photoswitching.

Since *d*STORM enables 5 times greater spatial resolution than 3D-SIM for typical biological samples, it is an outstanding option for attaining more structural detail. The relative thinness of LSECs allows the application of TIRF/HILO (highly inclined and laminated optical sheet) imaging techniques (with lower background results, see Fig. 3), which is typically used in SMLM (323). A deeper insight of structural details of fenestrations in LSECs in an aqueous environment was obtained by Mönkemöller, *et al.* (294) via *d*STORM. The results from SIM and *d*STORM measurements from that article demonstrated similar results (average diameter: 129 ± 33 nm for 3D-SIM and 120 ± 38 nm for *d*STORM), while the fenestration diameters below 50 nm were measured in *d*STORM analysis.

Generally, to visualize tiny holes in biological samples (‘negative imaging’) is much more demanding compared to a fluorescently labeled cytoskeleton (‘positive imaging’). Therefore, super-resolved imaging of LSECs is a challenging task since multiple experimental parameters have to be considered, such as low background, the density of the fluorophores, localization precision and post-processing. The data thus has to be interpreted with care (98), as both primary data acquisition and post-processing are prone to artifacts. Avoiding nonspecific binding of the fluorophores to coverslip surfaces is helpful to have a significantly lower background. The labeling density of fluorophores is also an important parameter to be considered, it was suggested that the mean density of the fluorophores has to be twice as high as the desired resolution, i.e. 10^4 and 10^6 molecules/ μm^2 for resolution of 20 nm in 2D and 3D, respectively (323). However, the increasing density of labeling also gives rise to the increased probability of non-specific signals, which results in an inaccuracy of fluorophore positions. To separate fluorescence signal, *d*STORM applies a Gaussian function to an emitted fluorophore, connected fluorophores data can then be processed via fitting multiple Gaussian functions, which is possible, though time-consuming with software packages (177, 329). For quantitative data analysis, such as measuring the diameter of fenestrations in LSECs, localization precision is crucial. Ideally, each fluorescing molecule would be switched on/off and counted only once. It is possible to overcount the true signal, especially when the background is high and the fluorophore is dim. Re-emitted fluorophore signals needing

to be counted multiple times by a localization algorithm have to be corrected. Post-processing of the data thus has effective impacts on the quality of super-resolved images. Apart from the aforementioned overcounting correction, the total number of localizations is lowered by filtering out values of detected photos below a certain threshold, which can lead to low quality of the reconstructed super-resolved image. However, longer acquisition times generating more processable raw data can somewhat compensate for this. Typically, *d*STORM requires a collection of 10,000-50,000 frames to achieve a high spatial resolution.

Cost-efficiency

Among popular super-resolution imaging concepts, SMLM stands out for its simplicity of technique, implementation and impressive spatial resolution. It has quickly been commercialized and manufactured with products from such as Zeiss, Nikon, Applied Precision, and Leica (132). Nevertheless, current commercial devices are expensive (>\$200K), which limits its widespread utilization as a routine microscopy system like a traditional fluorescence microscope (248). Principally, SMLM is a simple wide-field fluorescence microscope-based technique. After the launch of commercial high-end SMLM systems, researchers start searching the substitutions for all high-end components in a cost-effective manner.

Firstly, the laser is always one of the most expensive components. Due to the SMLM system application of wide-field illumination, the imaging quality of SMLM is not sensitive to the minor degradation on stability (laser output). In contrast, a uniform spatial distribution of high-power illumination intensity is the most important factor. The industry-grade high-power laser diodes (a semiconductor device), costing a few hundred dollars, can provide satisfactory illumination intensity. Therefore, the high-end scientific-grade laser is not necessary for SMLM. Secondly, the camera for image recording is another factor that can be considered to reduce costs. The critical parameters of cameras that determine the reconstructed image resolution are quantum efficiency (QE) and read noise. Early applications of cameras on SMLM systems were mainly electron-multiplying charge-coupled device (EM-CCD) camera (~90% QE), which is about \$35K with excess noise (unwanted signal). However, a camera using complementary metal-oxide semiconductor (CMOS, ~70% QE) with significantly higher readout rates in comparison to EM-CCD cameras (308), significantly enhanced the sensitivity and decreased the noise with lower cost (247, 306). The scientific CMOS (sCMOS) camera is half the price of an EM-CCD, and has been widely adopted in SMLM systems (220). An even cheaper industry-grade CMOS camera (~\$400 cost, ~71%) has demonstrated capabilities for super-resolved imaging. (247). In addition, the objective lens is the key component in the SMLM setup. It directly determines the collected photon number, which is related to image resolution. A high-NA objective lens is usually expensive (NA >1.4, ~\$7K). Previous studies demonstrated that a low-cost objective lens (NA=1.3, oil immersion, ~\$700) with dramatically (50%) decreased collection efficiency, and produced

compromised resolution. Therefore, among the aforementioned key factors (laser, camera, and objective) for cost-efficient SMLM devices, the quality of the objective lens has the most pronounced impact on the resolution of reconstructed super-resolved images (248).

As mentioned above, the quality of the objective lens is the most profound factor in the resolution of super-resolved images. In addition, the illumination scheme is another relevant parameter that can influence the image quality (Fig. 3). In general, high-intensity illumination is preferred to eventually guarantee sufficient fluorescent photons gathered. Many optical arrangements are possible to illuminate photons, such as 'epi'-illumination (a single lens functions as both the condenser and objective), which is the most frequently used mode of illumination; highly inclined and laminated optical sheet (HILO) illumination and total internal reflection fluorescence (TIRF) illumination. In wide-field, epi-illumination, the laser beam is focused at the back focal plane (BFP) of the objective lens, creating an illumination of the sample by a collimated beam, the entire volume of the sample above and below the focus is illuminated. The imaging depth is therefore not limited. However, the signal to background ratio is impaired, and photobleaching in the whole volume needs to be considered. When the objective lens supports sufficiently high angles of illumination: the HILO illumination mode can be achieved by moving the focus of the laser beam towards the edge of objective lens to illuminate only part of the sample, which reduces the background; Further tilting the angle of laser beam, enables the TIRF illumination, which is a broadly used method with sub-diffraction limit illumination volume to avoid background. TIRF microscopy is a near-field approach that has the exciting laser beam incident beyond the critical angle (smallest angle of incidence that yields total reflection) from the glass side of the interface (formed via the coverslip and aqueous sample), such that all the light will be reflected back toward the objective at the glass side. The electric field of the reflected beam still extends into the sample, exciting all fluorophores within 100-200 nm above the aqueous side of the interface, and this is the "evanescent field", which decays exponentially away from the interface. The penetration depth depends on incidence angle, excitation light wavelength and refractive indexes of the interface (42) Background fluorescence, therefore, is largely eliminated as no fluorophores higher up in the sample (outside of the focal plane) are excited, engendering a very good signal to background ratio (437).

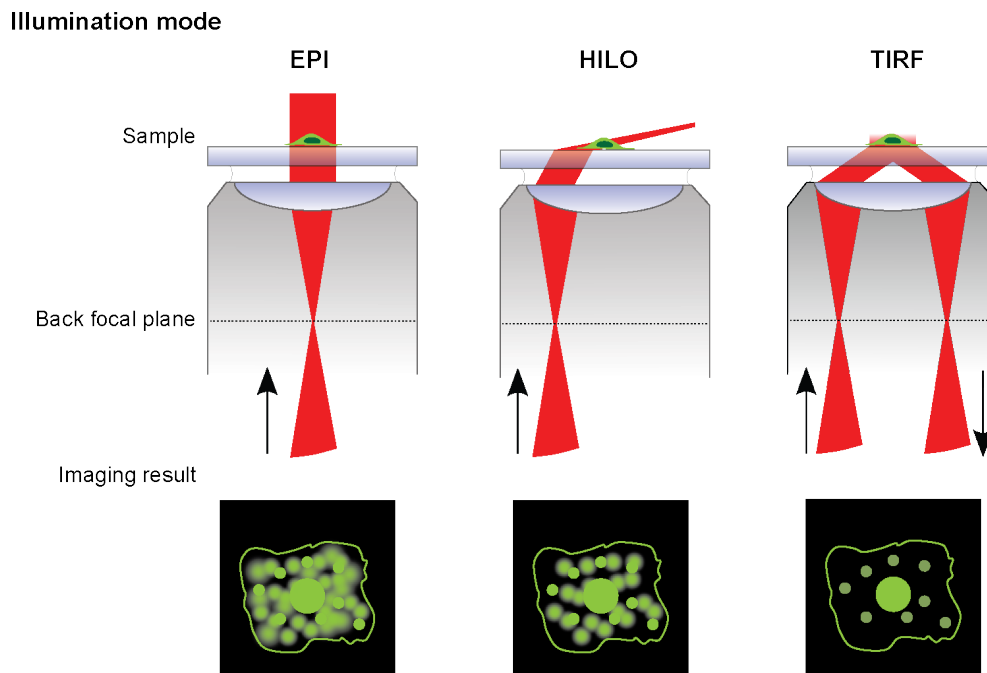


Fig. 3 Illumination schemes. EPI: in widefield epi-illumination, a collimated beam illuminates the entire depth of the sample is used, resulting in a high background fluorescence; HILO: highly inclined and laminated optical sheet illumination mode, beam exit the objective at an angle, resulting gradually decreasing penetration depth with less background; TIRF: total internal reflection fluorescence illumination mode, further shallowing the angle of incidence on the coverslip, reaching critical angle creates a shallow illumination field (evanescent field) of the sample, the intensity of the evanescent wave decays exponentially away from the coverslip. This results in improved contrast for the region of the sample close to the glass coverslip.

Moreover, one study has reported performing dSTORM on standard fluorescence microscopes with super-resolution capabilities at a very low cost (178). Thus, the cost was dramatically reduced by omitting the microscope body and substituting the most expensive parts with cost-effective alternatives, e.g. exchanging the EM-CCD camera for a standard charge-coupled device (CCD) camera (30-40% QE); swapping the scientific-grade laser with industry-grade lasers; substituting ultra-stable laser table for a breadboard. Other less expensive and essential components remained to ensure localization precision in the range of 40-60 nm (full width at half maximum: FWHM, a general estimate for the resolution that at least achieved). Thus, the purchase cost had been reduced by almost one order of magnitude compared to commercially available super-resolution microscopes. Alternatively, an industry-grade CMOS camera in standard setups can further contribute a considerable cost reduction without marked compromising of the image quality (86, 247). Furthermore, the cumbersome and expensive procedure of conventional SEM has motivated researchers to perform dSTORM to view fenestrations at a low cost. Thereby, a cost-efficient SMLM setup, imaging of LSECs and platelets has achieved a resolution of 50 nm for fenestration, and with the investigation of drugs and toxins on cellular morphology was applied (256).

3.2 SIM

Structured Illumination Microscopy (SIM) is a super-resolution fluorescence microscopy technique that provides both increased resolution and excellent optical sectioning. Several commercial super-resolution SIM systems are accessible to users at academic imaging facilities, including the DeltaVision OMX (GE/Applied Precision), ELYRA (Zeiss) and N-SIM (Nikon). These systems allow fluorescently labeled fixed or living biological specimens imaged with visible light, mounted on a microscope slide (with coverslip or glass-bottomed dish) as traditional, widefield, light microscopes. Compared to other super-resolution techniques, SIM only requires a linear, incoherent response to the intensity of the excitation light; and in terms of light effects, SIM is mild for imaged specimens. Linear (standard) SIM gives a two-fold improvement of the optical diffraction limit, which results in ~ 100 nm lateral and ~ 300 nm axial resolution, and with TIRF, even finer details can be resolved. Using nonlinear SIM, it is possible to obtain (theoretically) unlimited resolution; practically, signal-to-noise ratio (SNR) of the data defines the attainable resolution (148, 163). Nonlinear SIM data with ~ 50 nm resolution has been reported in biological imaging (351).

Two-dimensional (2D) SIM was shown in 1999 by Heintzmann, *et al.* (162), as well as in 2000 by (147). Thereafter, the technique further developed to three dimensions (3D) in 2008 by (149). In typical SIM imaging, the fluorescence excitation light is controlled to form a periodic pattern of fine stripes, which illuminate the specimen. During imaging, the pattern of stripes (of known frequency) mixes with the structure of specimen (with unknown frequency) to produce a sinusoidal pattern of Moiré fringes. Thereby the difference-frequency mixing with illumination pattern shifts them into the resolvable frequency band. Reconstruction algorithms compute this super-resolved information and with a double spatial resolution image. Essentially, all modern fluorophores are compatible with SIM, and several fluorophores labeled to samples can be imaged simultaneously due to much lower illumination intensity for SIM than that for STED; and fewer raw images and less time are needed to generate a super-resolved image compared to localization methods. Therefore, SIM is a good option for live-cell imaging among all these super-resolved methods mentioned. However, the 3D data set of SIM is sensitive to aberrations, particularly to spherical aberrations. Microscope calibration and refractive index matching to minimize image artifacts is a demanding aspect of this technology.

It was first shown by Cogger, *et al.* (72) that it is possible to investigate LSECs on super-resolved SIM. The experiment was performed on isolated rat LSECs to demonstrate fenestrations and their distribution in sieve plates. To visualize the cell membrane, the components were labeled with a CellMask dye following cellular fixation. The dye gives fairly uniform staining of the plasma membrane, which shows the morphology of rat LSEC fenestrations with an average diameter measured as 123 nm. Furthermore, the interaction between the actin cytoskeleton and fenestration distribution was investigated (72, 293). Thin actin filaments surround fenestrations, and thick bundles of tubulin form

rings around the sieve plates. 3D-SIM was further applied to assess the localization of lipid raft labeled with stain Bodipy FLC5 ganglioside GM1 in rat LSECs. Rafts are preferentially distributed in the perinuclear regions of LSECs rather than the sieve plate regions. These observations suggest the postulation of non-raft and actin filament-diminished regions forming fenestrations (410).

4 Long-Term Preservation of LSECs

Cryopreservation is a prevailing topic of high importance for biological materials such as cells, tissues and organs. It has been used both in many research fields and clinical areas. It is a process by cooling to very low temperatures (typically -80 °C in dry ice or -196 °C using liquid nitrogen) to preserve structurally intact biological materials (335). It enables standardization of experimental work overtime, also secures lifesaving banks of cells and tissue ready for surgical transplantation and transfusion at the time of need. It is widely accepted as a preferred technique for achieving long-term storage. Nowadays, various samples are stored in such an approach, including blood, stem cells, tissues, oocytes, sperm and environmental specimens (9, 228).

Optimal cryopreservation permits the storage of samples by maintaining viability and functionality (139). In the past, processes of freezing and thawing have been studied extensively. Suboptimal conditions lead to cell damage. Two basic damage mechanisms are the mechanical damage caused by the formation of intracellular ice crystals (33, 412), and the osmotic damage ascribed to high intracellular salt concentrations following water loss after crystallization. Intracellular freezing is lethal, Mazur, *et al.* (276) discussed the rate of cooling that decides the rate of water converted to ice, and described the optimal freezing rate for successful cryopreservation. Based on that, the freezing and thawing processes are now mostly standardized and controlled, such as the utilization of freezing container (with a desired cooling rate of 1 °C/min, such as Nalgene, Mr. Frosty or Planer). The storage temperature should be below the glass transition temperature of -130 °C, to avoid biochemical reactions and recrystallization processes (274, 287). For a wide range of cell types, not surprisingly, the cooling rate has a strong influence on the post-thaw recovery (275); and a recent study suggests the warming rates are not critical for slowly cooled samples (16).

In addition, traditional cryopreservation is applied by coating the material to be frozen with a class of molecules, termed as cryoprotectants, which avoid additional damage caused by the formation of ice crystals during freezing (364). Cryoprotectants simply increase the total concentration of all solutes in the system, thus, reduce the amount of ice formed at any given temperature; the molecules require the capability to penetrate the cells and have low toxicity. In 1959, dimethyl sulfoxide (DMSO) was introduced as a cryoprotectant (244). It is extensively used in the research laboratories, as it provides

good cellular viability as long as cryoprotectant can be quickly removed in the post-thaw period (260). Concentrations of DMSO <2% (v/v) are seldom effective as cryoprotectants, whereas concentrations higher than 12% (v/v) are often toxic. Within this range, the most effective concentration varies from species to strains (83). Additionally, whole serum (fetal bovine serum or newborn calf serum) is an alternative freeze medium (vehicle solution), it gives greater pH control and protection against freeze damage due to increased levels of albumins (83).

Cryopreservation protocols routinely used for established cell lines and primary cultures are quite similar. For example, cryopreservation and storage of embryo-derived stem cell lines are well established (355): generally with the employment of a conventional cryoprotectant solution (10% (v/v) dimethyl sulfoxide (DMSO) in cell medium (e.g. Dulbecco's modified Eagle's medium, DMEM) supplemented with 10–90% (v/v) fetal bovine serum, FBS); slowly cooling in cryovials (at or around 1°C/min), and rapid thawing by swirling the samples within a 37°C water bath to complete the process. Reports from human embryonic stem cell lines achieved high levels of survival rates (>80%) following cryopreservation by applying a DMSO-FBS-DMEM cryoprotectant solution with a cooling rate of 0.5-1 °C/min (77, 473). For the cryopreservation of platelets, 5-10% DMSO with a slow cooling method has become the most widely used (83, 369). Notably, a washing procedure is preferred after cryoprotectant -loaded cells thawed prior to the application, as there are concerns of an osmotically induced lysis for the cells.

Currently, new methods are being investigated due to the inherent toxicity of cryoprotectants (364). One recent T-cell study shows the post-thaw recovery is lower than that of other when cryopreserved in a DMSO solution (25). Nonetheless, cryopreservation studies with regards to LSECs are lacking, with the exception of one study, which achieved LSECs that retained functional and morphological characteristics upon thawing and culturing (292).

AIMS OF THE STUDY

The overall aim of this thesis was to study the morphological alterations of fenestrations in liver sinusoidal endothelial cells, following challenges with oxidized LDL and xanthenes, dynamically visualized via optical super-resolution microscopy. Additionally, develop a cost-efficient microscope and cryopreservation approach to aid our flexibility in extending the investigation of these structural phenomena.

Specifically, the main hypotheses were:

- Optical super-resolution microscopy approaches are useful tools to study the dimensions and dynamics of LSEC fenestrations;
- Cost-efficient microscopes allow super-resolved optical imaging on LSECs;
- LSEC fenestrations are dynamic structures that interact with/are affected by exogenous agents such as oxLDL and xanthenes;
- Cryopreservation approaches retain the fenestrated morphology and function for LSECs.

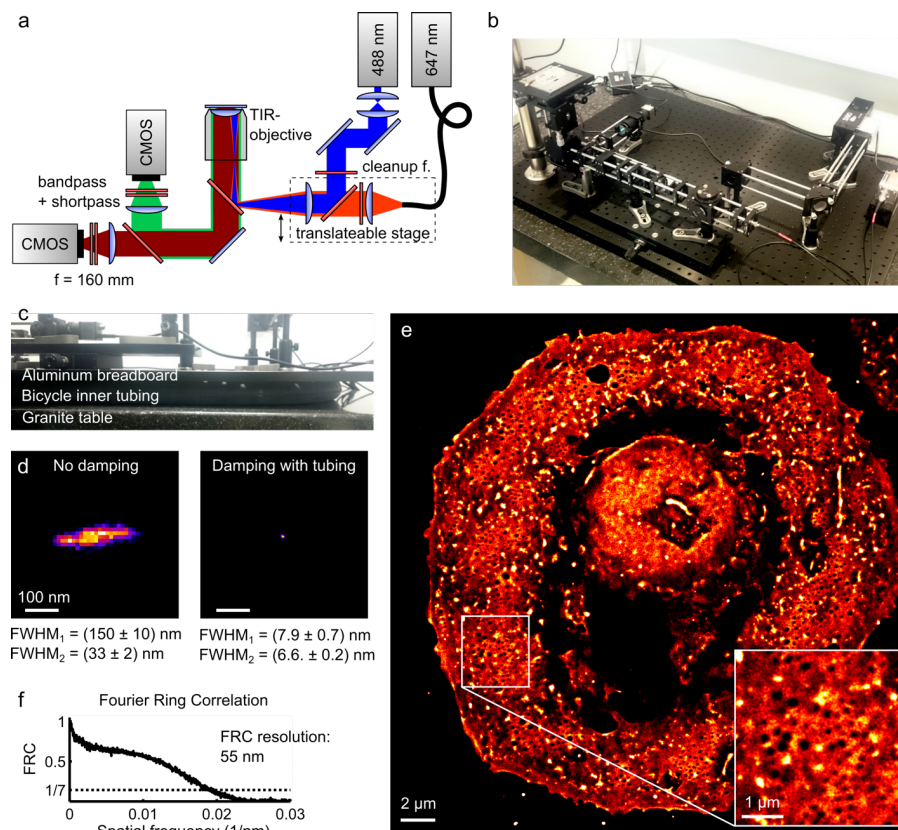
SUMMARY OF PAPERS

Paper I: Cost-efficient nanoscopy reveals nanoscale architecture of liver cells and platelets

Objectives: Single-molecule localization microscopy (SMLM) provides a powerful toolkit to specifically resolve intracellular structures at the nanometer scale, even approaching resolution classically reserved for electron microscopy (EM). Although instruments for SMLM are technically simple to implement, researchers tend to stick to commercial microscopes for SMLM implementations.

Methods Here we demonstrated the construction and use of a “custom-built” multi-color channel SMLM system to study liver sinusoidal endothelial cells (LSECs) and platelets, which costs significantly less than a commercial system. The microscope allows the introduction of highly affordable and low-maintenance SMLM hardware and methods to laboratories that, for example, lack access to core facilities housing high-end commercial microscopes for SMLM and EM.

Results: Using our custom-built microscope and freely available software from image acquisition to analysis, we imaged LSECs and platelets with a lateral resolution down to about 50 nm. Furthermore, we applied this microscope to examine the effect of drugs and toxins on cellular morphology.



Acknowledgment to Robin Diekmann.

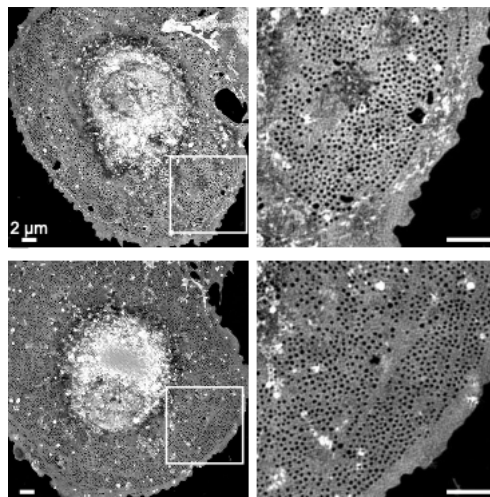
Paper II: Effect of caffeine, theobromine and other xanthines on liver sinusoidal endothelial cell ultrastructure

Objectives: Xanthines such as caffeine and theobromine are among the most consumed psychoactive stimulants in the world, either as natural components of coffee, tea and chocolate, or as food additives. Caffeine has been reported to have anti-fibrotic effects in the liver. The present study aimed to assess if xanthines are of any benefit for liver sinusoidal endothelial cells (LSECs).

Methods: Cultured primary rat LSECs were challenged with xanthines at concentrations that can be obtained by upper normal consumption of xanthine containing beverages and food stuff (*in vivo* “physiological” concentrations), and at *in vivo* toxic concentrations. The cell cultures were examined with scanning electron microscopy and structured illumination microscopy. LSEC viability was monitored with endocytosis assays.

Results: With the exception of toxic concentrations of theobromine, all xanthine challenges had no negative effects on LSEC ultrastructure as judged by LSEC fenestration status, and function as judged by endocytosis studies. In most xanthine challenges, the fenestration diameter was reduced, while there was a simultaneous tendency to increased fenestration frequency. Theobromine at physiological concentrations and theophylline at toxic concentrations induced significantly increased LSEC porosity, which is a function of both fenestration frequency and diameter.

Conclusion: Plasma concentrations of theobromine that are obtained from normal intake ranges (such as consuming 40-80 g of dark chocolate or 110 g of regular milk chocolate) can increase the porosity of LSEC. This increased porosity in LSEC may improve liver function by improving the bi-directional exchange of substrates between the plasma and the hepatocytes that surround LSEC. Given that LSEC porosity is reduced during ageing, theobromine may therefore contribute to the positive effects of chocolate as a useful adjunct to improving liver health in the elderly.



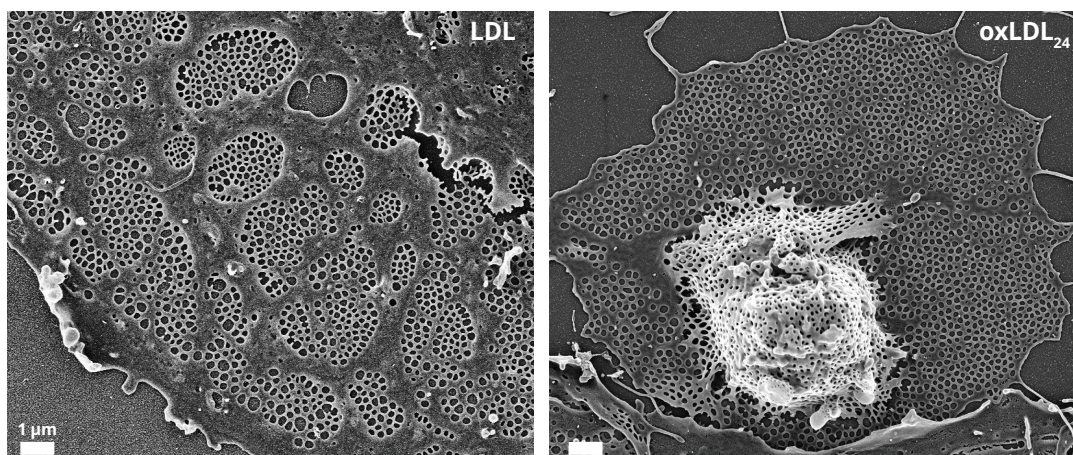
Paper III: Impact of oxidized low-density protein on liver sinusoidal endothelial cells ultrastructure

Objectives: Atherogenesis is associated with elevated levels of proinflammatory oxidized LDL (oxLDL) in the circulation. *In vivo*, oxLDL causes endothelial swelling in the liver, and disrupts the ultrastructure of liver sinusoidal endothelial cells (LSECs). The present study aimed to map the kinetics of this disruption *in vitro* using super-resolution microscopy.

Methods: Freshly isolated and cultured rat LSECs were challenged with oxLDL at various physiological concentrations and at varying levels of oxidation (oxidized for 3h oxLDL₃; 24h oxLDL₂₄). The cell cultures were examined with scanning electron microscopy and in real-time with structured illumination microscopy. LSECs viability was monitored with endocytosis and lactate dehydrogenase (LDH) detection assay.

Results: oxLDL challenge disrupted LSEC ultrastructure – increasing oxLDL concentrations and oxidation levels increased the level of disruption which manifested as loss of sieve plates, fusion of fenestrations within sieve plates, and gap formation in LSECs. Importantly, these effects were not uniform across all LSEC. LSEC maintained the ability to endocytose ligands irrespective of the type/concentration of oxLDL. However, increasing oxidation levels and concentrations of oxLDL inhibited LSEC mediated degradation of the endocytosed ligands. LDH release was only slightly increased after oxLDL challenge, irrespective of the type/concentration of oxLDL.

Conclusion: oxLDL disrupts LSEC morphology *in vitro*, manifesting as loss of sieve plates, fusion of fenestrations and large gap formation. However, LSEC remains viable and maintain scavenging functionality during oxLDL challenge, suggesting these cells are functionally robust in the presence of this cytotoxic compound.



Paper IV: Primary rat LSECs preserve their characteristic phenotype after cryopreservation

Objectives: Liver disease is a leading cause of morbidity and mortality worldwide. Recently, the liver nonparenchymal cells have gained increasing attention for their potential role in the development of liver disease. Liver sinusoidal endothelial cells (LSECs), a specialized type of endothelial cells that have unique morphology and function, play a fundamental role in maintaining liver homeostasis. Current protocols for LSEC isolation and cultivation rely on freshly isolated cells which can only be maintained differentiated in culture for a very short time. The present study aimed to improve the flexibility of studying LSEC by developing a cryopreservation protocol such that LSEC can be isolated in bulk from rat livers and stored for later use, at researchers' convenience instead of the same day of isolation.

Methods: Freshly isolated rat LSECs were cryopreserved using a freezing medium containing 70% culture medium RPMI 1640, 20% fetal bovine serum and 10% dimethyl sulfoxide. Cell cultures were examined with scanning electron microscopy and structured illumination microscopy to determine effects on morphology compared to non-cryopreserved controls. Cryopreserved LSEC receptor expression and functional viability were monitored with immunohistochemistry and endocytosis assays, respectively.

Results: Here reported a protocol to cryopreserve rat LSECs that, upon thawing, maintain full LSEC-signature features: fenestrations, scavenger receptor expression and endocytic function on par with freshly isolated cells. We have confirmed these features by a combination of biochemical and functional techniques, and super-resolution microscopy.

Conclusion: Cryopreservation of LSECs has no detrimental effects on their morphology or function, and thus allows for greater flexibility and convenience for the study of this cell type. Our findings offer a means to standardize research using LSECs, opening the prospects for designing pharmacological strategies for various liver diseases, and considering LSECs as a therapeutic target.

GENERAL DISCUSSION

Methodological considerations

Rat and Mouse Models

Laboratory rats and mice are bred and kept for scientific research; rats are less commonly used for research than mice. Mice are the most broadly used experimental mammals, they had important contributions in most areas of biomedical research (115). They are ideal for the study of aging, as they have a relatively short lifespan and share 99% of their genes with humans (39). C57Bl6 mice are among the most common mice reported in the scientific literature (58). Furthermore, they are the most susceptible strain to develop diet-induced atherosclerosis among inbred strains examined (330, 372). Therefore, they are important animal models for research in aging and diet-related atherosclerosis.

Rats, on the other hand, rapidly became the most frequently used species in behavioral studies such as learning (22). They are becoming heavily used in biomedical research due to their fertility, size and tractability (calmness and ease of handling) (436). Sprague Dawley rats are outbred multipurpose breed albino rats, which are also extensively used in medical and nutritional research (88, 182, 240).

The metabolic differences between albino and pigmented animals have been noted in drug metabolism tests. This is explained by drug binding to melanin, for example, chloroquine is an antimalarial agent showing distinct affinity to melanin (279, 325). The eye has the highest concentration of chloroquine due to binding by melanin (280), and chloroquine accumulates in the uveal tract of pigmented animals, but not albino animals (206, 266). Therefore, when testing drugs in albino rats, one should consider whether the binding to melanin is an issue for the study. Our study is focusing on liver endothelial cells for caffeine test, and choosing Sprague Dawley albino rats raises no such concern.

In our studies, we have used both rat and mouse models. However, the yield of LSECs from rats is 5-10 times higher than that from mice. Thus, rats LSEC production always enough to cover the needs for all the ongoing LSEC experiments in our lab, and the leftover cells have the possibility to be cryopreserved for future uses. Furthermore, the handling of rats is easier than mice due to their size and tractability. Nevertheless, for studies such as aging, rats' housing and feeding costs take a greater proportion than mice in research budgets. Therefore, when it comes to choosing the ideal experimental animal, there are always multiple concerns regarding the purpose of the studies.

Primary Cell Culture

Primary cell culture refers to a culture from the time of isolation until its first cell subculture. As opposed to the culture of immortalized cell lines, *in vitro* (Latin for "in the

glass”) primary cell cultures are generally considered more representative of *in vivo* (Latin for "within the living") tissues than cell lines (138). Additionally, for LSEC, there is no cell line to date that expresses all the specialized receptors nor maintains morphological features of LSEC (332).

Though the primary cell culture was not widely spread until the 2000s (424), this culture approach still presents its advantage over cell lines, such as more realistic functional responses, especially for drug testing responses (80). Therefore, it is suitable for oxLDL and drug challenges in our LSEC studies (Papers II and III). Moreover, density gradient separation in Percoll and selective substrate adherence were applied to obtain purified primary LSECs (389). And with the same protocol, the purity was reported >95% from previous studies from our groups (233, 292).

Cell Viability and Endocytic Ability

After purification of the LSECs, *in vitro* LSEC studies are recommended to be performed in the same day (within 24h) since the endocytic ability decreases sharply thereafter and ceases around day 4 (49); together with this, the disappearance of fenestrae occurs over the same period (55). Therefore, our studies took place within the same day of isolation and purification of LSECs, because of these morphological and endocytic concerns. In addition, Paper IV provided an alternative approach to cryopreserve primary LSECs for long-term utilization, which showed retention of functional and morphological characteristics of LSECs upon thawing and culturing.

Furthermore, lactate dehydrogenase (LDH) is a stable cytoplasmic enzyme in all cells. Once the plasma membrane is damaged, LDH is rapidly released into the culture supernatant. The LDH cytotoxicity detection assay kit (assay including controls, are performed in triplicate) is a simple and precise colorimetric method to measure LDH activity, i.e. the amount of dye (formazan) proportionally produced to the number of lysed (dead/plasma membrane-damaged) cells in 30 minutes. The maximum LDH activity is determined by lysing the cells with 1% Triton X-100 (1%, Triton X-100 does not interfere with LDH activity). Cell-free supernatant is also collected to incubate with the reaction mixture from the kit. Therefore, the LDH assay was applied to determine the viability of LSECs after treatment with oxLDL due to morphological changes caused by this agent, such as large gaps forming in the cytoplasmic domain. Moreover, the endocytosis test also reflects LSEC viability. The labeling with a radioactive tracer bound to the internalizing ligand (FSA) is a quantitative measurement of endo-lysosomal traffic, and has been used frequently in our research group to monitor the function of LSECs (232, 377, 394, 395).

Treatments & LSECs

oxLDL

oxLDLs are modification products derived from native non-pathological biomolecules and are pro-inflammatory molecules associated with the pathophysiology of diseases such as atherosclerosis and the aging process, development of Alzheimer's disease and diabetes (27, 59, 140, 205, 242, 375, 403, 404, 465). Additionally, the modification of the molecules makes them susceptible to the anti-atherogenic defense mechanism namely SR-mediated uptake in endocytically active cells. Endothelial cells are such endocytically active cells, the uptake (via SRs) of chemically modified LDL has been a common way to distinguish them from smooth muscle cells and pericytes (137, 446). LSECs contain well-developed endocytosis machinery and have high expression of endocytosis receptors (discussed in sections 2.1).

On the other hand, as discussed in section 2, the fenestrae size of LSECs have great importance in filtering lipoproteins, obstructing the passage of chylomicrons and triglyceride-rich lipoproteins (the largest of the circulating lipoprotein particles (>200 nm in diameter), and has a great effect on the metabolism of triglyceride-rich lipoproteins (126, 171, 223).

OxLDL doses were selected based on previous work by Oteiza, *et al.* (327). The direct exposure of LSECs to a high dose of oxLDL((80 µg/mL) (69), is to resemble the oxLDL concentration (10-60 µg/mL) reported in plasma of cardiovascular disease (CVD) patients (180).

Agarose Gel (REM)

Due to there being no standard protocol to prepare or compare the oxLDL, the oxidation level of oxLDLs varies in the literature. However, relative agarose gel electrophoresis mobility (REM) (310) of oxLDLs is a validation approach to verify the level of oxidation, as the increasing net negative charge is proportional to oxidation levels.

Xanthines

Doses for xanthines in Paper II were determined based on the physiological plasma concentration after consuming such compounds. Caffeine plasma concentrations are usually between 2-10 µg/mL (approximately 10-50 µM, rarely exceeding 50-60 µM during normal human consumption in adults (128), with toxic effects are occurring at plasma caffeine concentrations more than 40 µg/mL (216). Therefore, our high dose (150 µg/mL) of caffeine is a toxic concentration in plasma. Paraxanthine is the major metabolite (approximately 80%) of caffeine in humans, and in rats, caffeine is metabolized to roughly similar amounts for paraxanthine, theophylline and theobromine (12, 29, 326). And caffeine and paraxanthine are equally potent in rats (326). 370 mg

theobromine from 82g chocolate (40-80g of dark chocolate or 110g of regular milk chocolate) was rapidly absorbed in humans and produces a plasma concentration of 8.05 $\mu\text{g/mL}$ after 2h (273, 299, 352). Therefore, we selected 8 $\mu\text{g/mL}$ as a physiological concentration for all three compounds (caffeine, paraxanthine, theobromine) in our rat LSEC study. For theophylline to achieve adequate control of adult asthma, the required plasma concentration is 8-20 $\mu\text{g/mL}$ in humans (20, 34, 360). We chose 20 $\mu\text{g/mL}$ as a physiological concentration for theophylline in our study. High doses (150 $\mu\text{g/mL}$) was chosen as a toxic level for our study for all compounds.

Microscopy

As mentioned in Section 3, using photons to attain detailed biological information, the resolution limit is about 200 nm laterally (x and y directions) (153). However, using electrons instead of visible light gives a much higher resolution (in electron microscopy) than in optical microscopes (229). Therefore, the quality of images is well within the range for the purpose of statistical analysis. Nevertheless, the interaction of electrons with molecules in the air and in the samples limits its utility for biological studies and prohibits their deep penetration into the sample. Moreover, the preparation (fixation, dehydration and ultra-thin sectioning) of EM may cause artifacts (shrinkage/alteration) on specimen structure (78), not to mention the possibility of live-cell imaging.

With the development of super-resolution microscopy, the resolution limit of photons has been overcome. SIM and SMLM (dSTORM) are promising methods that allow the visualization of liver nanopore (fenestrae). Additionally, the possibility of live cell and multicolor imaging further extended its application in biological research. By combining two or more super-resolution techniques on the same sample, new dimensions of information appear and offset the drawback of each technique. Therefore, in both Paper II and Paper III, we combine both SEM and SIM to add new dimensions of information for our LSEC studies, SEM mainly for high-resolved morphological demonstration and statistical analysis, and SIM for morphological validation from the SEM results, as well as wet/live cell tracking the alteration of effect following substance challenges.

SEM, SIM and dSTORM Analysis

In Paper II, the effect of treatments was analyzed with SEM images. The design of experiment was followed as a previous study (296), morphometric measurements were conducted on coded pictures to control the observer bias, as well as the imaging was blinded for each treatment. Fenestrae were denoted as open pores with diameters between 50-300nm (54, 183), those larger (>300 nm) were considered as gaps. Fiji software was used to identify and measure the area of all fenestrae (circularity 0.6-1.0) and gaps (circularity 0.1-1) as mentioned in Paper I, for Paper II. As the previous study (447), the

fenestrae diameters were distributed into a gaussian pattern with 10-nm steps between 50-300 nm. The range was further sub-populated into ‘S’, ‘M’ and ‘L’ regions to numerically compare the relative increase of each region to the control group (Paper II). SIM images in Paper II were mainly for validation purposes for the SEM results, the fenestration detection was conducted with pixel classification workflow in the freely available machine learning image processing software Ilastik (26, 393) described in Paper I (applied in *d*STORM analysis as well). The automatically segmented fenestrations were then exported to Fiji, the identification (standard) is the same as SEM analysis in Fiji mentioned above. Of note, due to the resolution limit of SIM being around 100 nm, the real data of diameter analyzed from SIM images was in the same magnitude. However, the resolution from *d*STORM images presents a better resolution in Paper I compared to that from SIM images.

***d*STORM**

SMLM (e.g. *d*STORM) stands out among all the super-resolution microscopy modalities for its simplicity of technique, implementation and 5 times greater spatial resolution compared with SIM for typical biological samples. In a 2014 study of both SIM and *d*STORM measurements of fenestrae size demonstrating similar results for fenestration diameters, notably, fenestration sizes below 50 nm were only measured in *d*STORM analysis (294). In contrast to SEM, *d*STORM allows the cost reduction and avoids unnecessary cumbersome procedures in sample preparation. In Paper I, cost efficiency can be further enhanced by building a home-built set-up with 10% of the cost of a high-end commercial system, allowing 50 nm-cellular morphological visualization of fenestrae interactions with drugs and toxins. However, the limitation of *d*STORM is that to achieve a high-resolved image, the technique requires long acquisition times for a collection of 10,000-50,000 frames during imaging.

Challenges in Our Study

In our study of LSEC fenestrations, there are the following major challenges:

Fenestrae Size vs. Microscopy

As mentioned in Section 2, the average size of fenestrations (50-300 nm) is, however, partially below the conventional optical resolution limit (i.e. ~200 nm) and there are no specific cell surface markers for fenestrations. Therefore, the visualization of fenestrations has been limited to EM and AFM in the past decades until the development of super-resolution optical microscopy techniques.

More and more studies have investigated LSEC fenestrae via super-resolution optical microscopy. SIM, SMLM and STED are promising methods that ensure liver nanopore

visualization. Furthermore, their application to live cells and multicolor imaging is a major advantage of these methods, though the strategy of each technique is adopted differently. SIM exerts the phase modulation of visible light obtained via a moving grid with high-frequency pitch to potentially detect structures with a size of 100 nm. SMLM detects particular fluorophores that are separately emitted in time and space, thus distinguish one from the other even when they are very close (20 nm). STED utilizes reduced spot size of the detection light beam, such that only very close fluorophores are revealed. Primarily, nanoscopes are used by physicists and biophysicists; with their merits in resolution and live cell capabilities, nanoscopes are expected to be included in most biological laboratories soon (101, 323, 472).

Thus, in Paper I, we demonstrated a simple and cost-effective *d*STORM microscope using off-the-shelf components. The total cost of the microscope was 10% of a commercial high-end platform. With freely available software from image acquisition to analysis, we resolved LSEC fenestrations from mice and rat LSECs with a lateral resolution down to about 50 nm. Mouse and rat LSEC fenestrations are highly similar in morphology and organization, and are likewise difficult structures to visualize, as it is the absence of staining that visualizes fenestrations. Background staining and other sources of noise therefore require extra attention in our case. That said, the industrial CMOS cameras used in this study provided sufficient wide-field fluorescence image data, easily detected single blinking fluorescent molecules, and the read noise of about 6.4 electrons per pixel was not an issue in our study. Additionally, the performance of this particular CMOS camera was extensively evaluated in a previous study (86). Intracellular structures were easily visualized at super-resolution with our microscope. Moreover, the LSEC actin cytoskeleton was also easy to visualize, and the resolution of our microscope enabled us to see structures resembling fenestrations, which are encircled by a ring of actin (293).

Furthermore, we also investigated the primary cultures of platelets. Features that particularly captured our interest were super-fine filaments, some thinner than 100 nm, emanating from their plasma membranes. These filaments were membrane structures with an actin skeleton and would be sufficiently long and thin to pass through LSEC fenestrae and, for example, interact with the underlying hepatocytes in the *in vivo* context, which has been observed in previous TEM study (300). Given that platelets have a role in the resolution of fibrosis (218, 219), this super-resolution microscope will be a useful tool to study the platelet: LSEC “synapse” in future studies.

Additionally, combining two or more super-resolution techniques on the same sample, adds new dimensions of information to emphasize the advantages of each technique, at the same time offset individual drawbacks. Such a multimodal approach is known as correlative super-resolution microscopy, and this offers new opportunities in this burgeoning field (113, 157).

Treatments vs. Fenestrae

As mentioned in Section 2.2, fenestrations are dynamic with respect to size and number; their alterations respond to pharmacological agents (11, 241, 427) and are associated with disease states such as fibrosis (183). The alteration of fenestrae can have an adverse influence on hepatocytes and liver function (462).

All three fenestrae-resolvable microscopies (SEM, SIM and *d*STORM) have been utilized in our study, to visualize the *in vitro* effects of exogenous agents such as xanthines, sildenafil and oxLDL regarding alterations of LSEC fenestrations.

Caffeine has been reported to have anti-fibrotic/-inflammatory effects in the liver (5, 66, 158, 184, 379). One of the xanthines, theobromine (also as a metabolite of caffeine, Paper II) and sildenafil [Paper II and Hunt, *et al.* (187)] increased both the frequency and diameter of fenestrations in cultured LSEC. In most xanthine challenges, the fenestration diameter was reduced, while there was a simultaneous tendency to increased fenestration frequency. Theophylline at toxic concentrations induced significantly increased LSEC porosity, which is a function of both fenestration frequency and diameter.

OxLDL is a major atherogenic substance (15, 479), mainly removed by cells lining in the liver sinusoids (238, 429). In our study (Paper III), we tested the effect of both mildly oxLDL₃ and heavily oxLDL₂₄. Previous studies have shown that heavily oxLDL was taken up both by Kupffer cells and LSECs (429), and mildly oxLDL was only recognized by LSECs (233). This indicates that LSECs play an important role in eliminating plasma oxLDLs, which demonstrates the importance of the liver cell clearance system in the prevention of cardiovascular disease (180, 192, 386).

In Paper III, oxLDL challenge caused major disruptions in LSEC fenestration ultrastructure – increasing oxLDL concentration and oxidation levels aggravated the level of disruption that manifested as loss of sieve plates, fusion of fenestrations within sieve plates, and gap formation in LSECs. Importantly, these effects were not uniform across all LSEC. Similar to the previous *in vivo* finding (327), which showed similar negative effects (reduced fenestration), our *in vitro* investigation on rat LSECs with relevant concentrations appeared with more profound alterations on fenestrations: smaller fenestrations are disappearing or become smaller in our study. Moreover, the loss of sieve plates demonstrated on our SEM results, was apparent in previous that *in vivo* finding (327), though was not discussed by those authors.

Furthermore, the potential for live imaging on SIM was a leading advantage (43, 374). Our real-time live imaging visualized the progression of changes in LSEC during the challenge with oxLDLs (80 µg/mL) within 30 minutes (20 time-points). Mildly oxidized oxLDL₃ in our *in vitro* findings elicited a slower response than heavily oxidized oxLDL₂₄ on LSECs with regard to alterations in morphology. However, after sufficient time oxLDL₃ will elicit similar structural changes as the heavily oxLDL₂₄ does in the early

stages. Thus, we speculate mildly oxLDL with a longer circulatory life may act “like” heavily oxLDL for pathogenic properties as a physiological proatherogenic molecule (28, 453).

Additionally, LSEC maintained the ability to endocytose ligands irrespective of the type/concentration of oxLDL. However, increasing oxidation levels and concentrations of oxLDL inhibited LSEC mediated degradation of the endocytosed ligands. This would suggest that the early endocytic machinery continues to function as (essentially) normal, but subsequent steps in the endo-lysosomal pathway are inhibited by oxLDL. This might be at the level of intracellular transport from endosomes to lysosomes, such that oxLDL-mediated disruptions to LSEC morphology may disrupt intracellular transport routes. Another possibility is that heavily oxidized oxLDL, with all its chemical modifications, causes lysosomal “indigestion” and renders the lysosome less able to degrade other substrates (such as FSA) as well (156). LDH release was only slightly increased after oxLDL challenge, irrespective of the type/concentration of oxLDL, which indicates that the cell membranes are still largely intact and functional even after 2 hours of oxLDL challenge (80 µg/mL).

Long-Term Preservation Challenge

Finally, the challenge of the rapid loss of fenestrations and scavenging function in LSEC was solved by a cryopreservation approach for freshly isolated LSEC. It was previously reported that the endocytic ability decreases sharply thereafter and ceases around day 4 (49); the disappearance of fenestrae occurs in the same period (55). For the sake of having functional fenestrae in our *in vitro* study, we normally experiment within the same day after isolation the cells to avoid the loss of fenestrae progression.

Cryopreservation is a prevailing topic of high importance for biological materials such as cells, tissues and organs. It enables the standardization of experimental work. It is widely accepted as a preferred technique for achieving long-term storage (9, 228). Prior to our Paper IV study, cryopreservation studies with regards to LSECs were non-existent, we achieved LSECs that retained functional and morphological characteristics upon thawing and culturing. By developing such that, LSECs can be used at researchers’ convenience, rather than directly after isolation from livers.

CONCLUSION

New microscopy methods have been developed to look at very small filter holes (fenestrations) in liver cells. These holes are crucial for good health, and our new methods are helping us to find ways to keep these fenestrations during aging and liver disease. These methods have helped to show that theobromine (from chocolate) and sildenafil (a.k.a Viagra) appear to be beneficial for LSEC fenestrations in *in vitro* experiments. These findings are still to be confirmed *in vivo* in animal models. We also showed that oxidized LDL has very negative *in vitro* effects on LSEC fenestrations and morphology.

Specifically, the main conclusions were:

Paper I demonstrated the effectiveness of a custom-built SMLM microscope to perform super-resolution imaging of primary cells for only a fraction of the cost of a commercial microscope for SMLM. We believe that our work will contribute to the strong current movement of democratizing the access to super-resolution microscopy, making super-resolution available to a wide range of laboratories as a routine lab microscope.

Paper II shown *in vitro* xanthine treatments with caffeine, theobromine, theophylline and paraxanthine elicit changes in fenestration size, porosity and frequency in rat LSECs. Caffeine in high doses may have an inhibitory impact on the uptake of soluble macromolecules, and increase smaller-sized fenestrations in LSECs. Theobromine in physiological dose increases fenestration frequency and porosity in rat LSECs. These findings remain to be confirmed *in vivo*. However, if theobromine elicits similar effects in animal studies, it might prove to be a useful (and simple) intervention - via chocolate - to improve LSEC porosity in elderly people.

Paper III demonstrated oxLDL disrupts LSEC morphology *in vitro*, manifesting as loss of sieve plates, fusion of fenestrations and large gap formation. However, LSEC remains viable and maintain scavenging functionality during oxLDL challenge, suggesting these cells are functionally robust in the presence of this cytotoxic compound.

Paper IV reported a protocol to cryopreserve rat LSECs that, upon thawing, maintain full LSEC-signature features: fenestrations, scavenger receptor expression and endocytic function on par with freshly isolated cells. We have confirmed these features by a combination of biochemical and functional techniques, and super-resolution microscopy. Our findings offer a means to standardize research using LSECs, opening the prospects for designing pharmacological strategies for various liver diseases, and considering LSECs as a therapeutic target.

REFERENCES

1. Abbe E. Beiträge zur Theorie des Mikroskops und der mikroskopischen Wahrnehmung. *Archiv f mikrosk Anatomie*. 1873;9(1):413-68.
2. Abumrad NA, el-Maghrabi MR, Amri EZ, Lopez E, Grimaldi PA. Cloning of a rat adipocyte membrane protein implicated in binding or transport of long-chain fatty acids that is induced during preadipocyte differentiation. Homology with human CD36. *J Biol Chem*. 1993;268(24):17665-8.
3. Acton S, Rigotti A, Landschulz KT, Xu S, Hobbs HH, Krieger M. Identification of scavenger receptor SR-BI as a high density lipoprotein receptor. *Science*. 1996;271(5248):518-20.
4. Ahotupa M, Asankari TJ. Baseline diene conjugation in LDL lipids: an indicator of circulating oxidized LDL. *Free Radic Biol Med*. 1999;27(11-12):1141-50.
5. Akashi I, Kagami K, Hirano T, Oka K. Protective effects of coffee-derived compounds on lipopolysaccharide/D-galactosamine induced acute liver injury in rats. *J Pharm Pharmacol*. 2009;61(4):473-8.
6. Ala-Kokko L, Pihlajaniemi T, Myers JC, Kivirikko KI, Savolainen ER. Gene expression of type I, III and IV collagens in hepatic fibrosis induced by dimethylnitrosamine in the rat. *Biochem J*. 1987;244(1):75-9.
7. Alban FTE, Gyamfi D, van Golen RF, Heger M. Chapter 8 - Reactive oxygen and nitrogen species and liver ischemia-reperfusion injury: an overview. In: Patel VB, Rajendram R, Preedy VR, editors. *The Liver*. Boston: Academic Press; 2018. p. 79-96.
8. Ando R, Mizuno H, Miyawaki A. Regulated fast nucleocytoplasmic shuttling observed by reversible protein highlighting. *Science*. 2004;306(5700):1370-3.
9. Angel S, von Briesen H, Oh YJ, Baller MK, Zimmermann H, Germann A. Toward Optimal Cryopreservation and Storage for Achievement of High Cell Recovery and Maintenance of Cell Viability and T Cell Functionality. *Biopreserv Biobank*. 2016;14(6):539-47.
10. Anitua E, Andia I, Ardanza B, Nurden P, Nurden AT. Autologous platelets as a source of proteins for healing and tissue regeneration. *Thromb Haemost*. 2004;91(1):4-15.
11. Arias IM. The biology of hepatic endothelial cell fenestrae. *Prog Liver Dis*. 1990;9:11-26.
12. Arnaud MJ. Comparative metabolic disposition of [1-Me14C]caffeine in rats, mice, and Chinese hamsters. *Drug Metab Dispos*. 1985;13(4):471-8.
13. Asch AS, Barnwell J, Silverstein RL, Nachman RL. Isolation of the thrombospondin membrane receptor. *J Clin Invest*. 1987;79(4):1054-61.
14. Ashburn TT, Thor KB. Drug repositioning: identifying and developing new uses for existing drugs. *Nat Rev Drug Discov*. 2004;3(8):673-83.
15. Avogaro P, Bon GB, Cazzolato G. Presence of a modified low density lipoprotein in humans. *Arteriosclerosis*. 1988;8(1):79-87.
16. Baboo J, Kilbride P, Delahaye M, Milne S, Fonseca F, Blanco M, et al. The Impact of Varying Cooling and Thawing Rates on the Quality of Cryopreserved Human Peripheral Blood T Cells. *Sci Rep*. 2019;9(1):3417.
17. Balzan S, Lubrano V. LOX-1 receptor: A potential link in atherosclerosis and cancer. *Life Sci*. 2018;198:79-86.
18. Bankston PW, Pino RM. The development of the sinusoids of fetal rat liver: morphology of endothelial cells, Kupffer cells, and the transmural migration of blood cells into the sinusoids. *Am J Anat*. 1980;159(1):1-15.

19. Barbera-Guillem E, Arrue JM, Ballesteros J, Vidal-Vanaclocha F. Structural changes in endothelial cells of developing rat liver in the transition from fetal to postnatal life. *J Ultrastruct Mol Struct Res.* 1986;97(1-3):197-206.
20. Barnes PJ. Theophylline for COPD. *Thorax.* 2006;61(9):742-4.
21. Baselt RC. Pathology-epitomes of progress: therapeutic drug monitoring. *West J Med.* 1982;136(5):420-1.
22. Beach FA. The snark was a boojum. *American Psychologist.* 1950;5(4):115.
23. Bender AT, Beavo JA. Cyclic nucleotide phosphodiesterases: molecular regulation to clinical use. *Pharmacol Rev.* 2006;58(3):488-520.
24. Benowitz NL, Osterloh J, Goldschlager N, Kaysen G, Pond S, Forhan S. Massive catecholamine release from caffeine poisoning. *JAMA.* 1982;248(9):1097-8.
25. Berens C, Heine A, Muller J, Held SA, Mayer K, Brossart P, et al. Variable resistance to freezing and thawing of CD34-positive stem cells and lymphocyte subpopulations in leukapheresis products. *Cytotherapy.* 2016;18(10):1325-31.
26. Berg S, Kutra D, Kroeger T, Straehle CN, Kausler BX, Haubold C, et al. ilastik: interactive machine learning for (bio)image analysis. *Nat Methods.* 2019;16(12):1226-32.
27. Berliner JA, Heinecke JW. The role of oxidized lipoproteins in atherogenesis. *Free Radic Biol Med.* 1996;20(5):707-27.
28. Berliner JA, Territo MC, Sevanian A, Ramin S, Kim JA, Bamshad B, et al. Minimally modified low density lipoprotein stimulates monocyte endothelial interactions. *J Clin Invest.* 1990;85(4):1260-6.
29. Berthou F, Ratanasavanh D, Alix D, Carlhant D, Riche C, Guillouzo A. Caffeine and theophylline metabolism in newborn and adult human hepatocytes; comparison with adult rat hepatocytes. *Biochem Pharmacol.* 1988;37(19):3691-700.
30. Betzig E. Proposed method for molecular optical imaging. *Opt Lett.* 1995;20(3):237-9.
31. Betzig E, Patterson GH, Sougrat R, Lindwasser OW, Olenych S, Bonifacino JS, et al. Imaging intracellular fluorescent proteins at nanometer resolution. *Science.* 2006;313(5793):1642-5.
32. Bickel PE, Freeman MW. Rabbit aortic smooth muscle cells express inducible macrophage scavenger receptor messenger RNA that is absent from endothelial cells. *J Clin Invest.* 1992;90(4):1450-7.
33. Bischof JC, Rubinsky B. Large ice crystals in the nucleus of rapidly frozen liver cells. *Cryobiology.* 1993;30(6):597-603.
34. Blanchard J, Harvey S, Morgan WJ. Variability of the serum protein binding of theophylline in patients with asthma and cystic fibrosis. *Br J Clin Pharmacol.* 1992;33(6):653-6.
35. Blomhoff R, Eskild W, Berg T. Endocytosis of formaldehyde-treated serum albumin via scavenger pathway in liver endothelial cells. *Biochem J.* 1984;218(1):81-6.
36. Blouin A, Bolender RP, Weibel ER. Distribution of organelles and membranes between hepatocytes and nonhepatocytes in the rat liver parenchyma. A stereological study. *J Cell Biol.* 1977;72(2):441-55.
37. Blumgart LHB, J. *Surgery of the liver, biliary tract, and pancreas.* 3rd ed. Philadelphia: Saunders Elsevier; 2007. p. 3-30.
38. Boerrigter G, Lapp H, Burnett JC. Modulation of cGMP in heart failure: a new therapeutic paradigm. *Handb Exp Pharmacol.* 2009(191):485-506.
39. Boguski MS. Comparative genomics: the mouse that roared. *Nature.* 2002;420(6915):515-6.

40. Bonati M, Latini R, Galletti F, Young JF, Tognoni G, Garattini S. Caffeine disposition after oral doses. *Clin Pharmacol Ther.* 1982;32(1):98-106.
41. Boolell M, Allen MJ, Ballard SA, Gepi-Attee S, Muirhead GJ, Naylor AM, et al. Sildenafil: an orally active type 5 cyclic GMP-specific phosphodiesterase inhibitor for the treatment of penile erectile dysfunction. *Int J Impot Res.* 1996;8(2):47-52.
42. Born M, Wolf E, Bhatia A. XIV. Principles of optics: Pergamon; 1975.
43. Bottomley AL, Turnbull L, Whitchurch CB, Harry EJ. Immobilization Techniques of Bacteria for Live Super-resolution Imaging Using Structured Illumination Microscopy. *Methods Mol Biol.* 2017;1535:197-209.
44. Boulenger JP, Patel J, Marangos PJ. Effects of caffeine and theophylline on adenosine and benzodiazepine receptors in human brain. *Neurosci Lett.* 1982;30(2):161-6.
45. Brachtel D, Richter E. Absolute bioavailability of caffeine from a tablet formulation. *J Hepatol.* 1992;16(3):385.
46. Braet F, Bomans PH, Wisse E, Frederik PM. The observation of intact hepatic endothelial cells by cryo-electron microscopy. *J Microsc.* 2003;212(Pt 2):175-85.
47. Braet F, De Zanger R, Baekeland M, Crabbe E, Van Der Smissen P, Wisse E. Structure and dynamics of the fenestrae-associated cytoskeleton of rat liver sinusoidal endothelial cells. *Hepatology.* 1995;21(1):180-9.
48. Braet F, De Zanger R, Kalle W, Raap A, Tanke H, Wisse E. Comparative scanning, transmission and atomic force microscopy of the microtubular cytoskeleton in fenestrated liver endothelial cells. *Scanning Microsc Suppl.* 1996;10:225-35; discussion 35-6.
49. Braet F, De Zanger R, Sasaoki T, Baekeland M, Janssens P, Smedsrod B, et al. Assessment of a method of isolation, purification, and cultivation of rat liver sinusoidal endothelial cells. *Lab Invest.* 1994;70(6):944-52.
50. Braet F, Kalle WH, De Zanger RB, De Grooth BG, Raap AK, Tanke HJ, et al. Comparative atomic force and scanning electron microscopy: an investigation on fenestrated endothelial cells in vitro. *J Microsc.* 1996;181(Pt 1):10-7.
51. Braet F, Spector I, De Zanger R, Wisse E. A novel structure involved in the formation of liver endothelial cell fenestrae revealed by using the actin inhibitor misakinolide. *Proc Natl Acad Sci U S A.* 1998;95(23):13635-40.
52. Braet F, Spector I, Shochet N, Crews P, Higa T, Menu E, et al. The new anti-actin agent dihydrohalichondramide reveals fenestrae-forming centers in hepatic endothelial cells. *BMC Cell Biol.* 2002;3:7.
53. Braet F, Wisse E. AFM imaging of fenestrated liver sinusoidal endothelial cells. *Micron.* 2012;43(12):1252-8.
54. Braet F, Wisse E. Structural and functional aspects of liver sinusoidal endothelial cell fenestrae: a review. *Comp Hepatol.* 2002;1(1):1.
55. Braet F, Wisse E, Probst I. The long-term culture of pig liver sinusoidal endothelial cells: the Holy Grail found. *Eur J Cell Biol.* 2005;84(9):745-8.
56. Brandes RP, Schroder K. Differential vascular functions of Nox family NADPH oxidases. *Curr Opin Lipidol.* 2008;19(5):513-8.
57. Braun A, Trigatti BL, Post MJ, Sato K, Simons M, Edelberg JM, et al. Loss of SR-BI expression leads to the early onset of occlusive atherosclerotic coronary artery disease, spontaneous myocardial infarctions, severe cardiac dysfunction, and premature death in apolipoprotein E-deficient mice. *Circ Res.* 2002;90(3):270-6.
58. Brayton C, Treuting P, Ward J. Pathobiology of aging mice and GEM: background strains and experimental design. *Veterinary pathology.* 2012;49(1):85-105.

59. Brinkley TE, Nicklas BJ, Kanaya AM, Satterfield S, Lakatta EG, Simonsick EM, et al. Plasma oxidized low-density lipoprotein levels and arterial stiffness in older adults: the health, aging, and body composition study. *Hypertension*. 2009;53(5):846-52.
60. Brown MS, Goldstein JL. Receptor-mediated endocytosis: insights from the lipoprotein receptor system. *Proc Natl Acad Sci U S A*. 1979;76(7):3330-7.
61. Busto U, Bendayan R, Sellers EM. Clinical pharmacokinetics of non-opiate abused drugs. *Clin Pharmacokinet*. 1989;16(1):1-26.
62. Calvo D, Gomez-Coronado D, Suarez Y, Lasuncion MA, Vega MA. Human CD36 is a high affinity receptor for the native lipoproteins HDL, LDL, and VLDL. *J Lipid Res*. 1998;39(4):777-88.
63. Campagnaro BP, Tonini CL, Nogueira BV, Casarini DE, Vasquez EC, Meyrelles SS. DNA damage and augmented oxidative stress in bone marrow mononuclear cells from Angiotensin-dependent hypertensive mice. *Int J Hypertens*. 2013;2013:305202.
64. Campos H, Blijlevens E, McNamara JR, Ordovas JM, Posner BM, Wilson PW, et al. LDL particle size distribution. Results from the Framingham Offspring Study. *Arterioscler Thromb*. 1992;12(12):1410-9.
65. Carrillo JA, Benitez J. Clinically significant pharmacokinetic interactions between dietary caffeine and medications. *Clin Pharmacokinet*. 2000;39(2):127-53.
66. Chan ES, Montesinos MC, Fernandez P, Desai A, Delano DL, Yee H, et al. Adenosine A(2A) receptors play a role in the pathogenesis of hepatic cirrhosis. *Br J Pharmacol*. 2006;148(8):1144-55.
67. Chang YH, Abdalla DS, Sevanian A. Characterization of cholesterol oxidation products formed by oxidative modification of low density lipoprotein. *Free Radic Biol Med*. 1997;23(2):202-14.
68. Chauhan A, Adams DH, Watson SP, Lalor PF. Platelets: No longer bystanders in liver disease. *Hepatology*. 2016;64(5):1774-84.
69. Chen C, Khismatullin DB. Oxidized low-density lipoprotein contributes to atherogenesis via co-activation of macrophages and mast cells. *Plos One*. 2015;10(3):e0123088.
70. Chui PC, Guan HP, Lehrke M, Lazar MA. PPARgamma regulates adipocyte cholesterol metabolism via oxidized LDL receptor 1. *J Clin Invest*. 2005;115(8):2244-56.
71. Clark SA, Angus HB, Cook HB, George PM, Oxner RB, Fraser R. Defenestration of hepatic sinusoids as a cause of hyperlipoproteinaemia in alcoholics. *Lancet*. 1988;2(8622):1225-7.
72. Cogger VC, McNerney GP, Nyunt T, DeLeve LD, McCourt P, Smedsrod B, et al. Three-dimensional structured illumination microscopy of liver sinusoidal endothelial cell fenestrations. *J Struct Biol*. 2010;171(3):382-8.
73. Cogger VC, Muller M, Fraser R, McLean AJ, Khan J, Le Couteur DG. The effects of oxidative stress on the liver sieve. *J Hepatol*. 2004;41(3):370-6.
74. Cogger VC, O'Reilly JN, Warren A, Le Couteur DG. A standardized method for the analysis of liver sinusoidal endothelial cells and their fenestrations by scanning electron microscopy. *J Vis Exp*. 2015(98):e52698.
75. Cogger VC, Warren A, Fraser R, Ngu M, McLean AJ, Le Couteur DG. Hepatic sinusoidal pseudocapillarization with aging in the non-human primate. *Exp Gerontol*. 2003;38(10):1101-7.
76. Covey SD, Krieger M, Wang W, Penman M, Trigatti BL. Scavenger receptor class B type I-mediated protection against atherosclerosis in LDL receptor-negative mice involves its expression in bone marrow-derived cells. *Arterioscler Thromb Vasc Biol*. 2003;23(9):1589-94.

77. Cowan CA, Klimanskaya I, McMahon J, Atienza J, Witmyer J, Zucker JP, et al. Derivation of embryonic stem-cell lines from human blastocysts. *N Engl J Med.* 2004;350(13):1353-6.
78. Crang RFEK, K. L. Artifacts in Biological Electron Microscopy Science. 1988;242(4876):309.
79. Crawford JM, Burt AD. Anatomy, pathophysiology and basic mechanisms of disease. *MacSween's Pathology of the Liver: Elsevier;* 2012. p. 1-77.
80. Cree IA, Glaysher S, Harvey AL. Efficacy of anti-cancer agents in cell lines versus human primary tumour tissue. *Curr Opin Pharmacol.* 2010;10(4):375-9.
81. Curatolo PW, Robertson D. The health consequences of caffeine. *Ann Intern Med.* 1983;98(5 Pt 1):641-53.
82. Czok G. Concerning the question of the biological effectiveness of methylxanthines in cocoa products. *Zeitschrift für Ernährungswissenschaft.* 1974;13(4):165-71.
83. Day J, Stacey G. Cryopreservation and freeze-drying protocols 2007.
84. DeLeve LD. Liver sinusoidal endothelial cells in hepatic fibrosis. *Hepatology.* 2015;61(5):1740-6.
85. dePaula, Farah A. Caffeine Consumption through Coffee: Content in the Beverage, Metabolism, Health Benefits and Risks. *Beverages.* 2019;5:37.
86. Diekmann R, Till K, Muller M, Simonis M, Schuttpelz M, Huser T. Characterization of an industry-grade CMOS camera well suited for single molecule localization microscopy - high performance super-resolution at low cost. *Sci Rep.* 2017;7(1):14425.
87. Dobbs BR, Rogers GW, Xing HY, Fraser R. Endotoxin-induced defenestration of the hepatic sinusoidal endothelium: a factor in the pathogenesis of cirrhosis? *Liver.* 1994;14(5):230-3.
88. Drachman RH, Root RK, Wood Jr WB. Studies on the effect of experimental nonketotic diabetes mellitus on antibacterial defense: I. Demonstration of a defect in phagocytosis. *The Journal of Experimental Medicine.* 1966;124(2):227-40.
89. Dranoff JA. Coffee consumption and prevention of cirrhosis: in support of the caffeine hypothesis. *Gene Expr.* 2018;18(1):1-3.
90. Duke JA. *Handbook of Medicinal Herbs.* Boca Raton, FL: CRC Handbook Press; 1988. p. 131-2.
91. Dunne DW, Resnick D, Greenberg J, Krieger M, Joiner KA. The type I macrophage scavenger receptor binds to gram-positive bacteria and recognizes lipoteichoic acid. *Proc Natl Acad Sci U S A.* 1994;91(5):1863-7.
92. Dunwiddie TV, Masino SA. The role and regulation of adenosine in the central nervous system. *Annu Rev Neurosci.* 2001;24:31-55.
93. Duryee MJ, Freeman TL, Willis MS, Hunter CD, Hamilton BC, 3rd, Suzuki H, et al. Scavenger receptors on sinusoidal liver endothelial cells are involved in the uptake of aldehyde-modified proteins. *Mol Pharmacol.* 2005;68(5):1423-30.
94. Ehara S, Ueda M, Naruko T, Haze K, Itoh A, Otsuka M, et al. Elevated levels of oxidized low density lipoprotein show a positive relationship with the severity of acute coronary syndromes. *Circulation.* 2001;103(15):1955-60.
95. Ellis EF. Theophylline toxicity. *J Allergy Clin Immunol.* 1985;76(2 Pt 2):297-301.
96. Elvevold K, Simon-Santamaria J, Hasvold H, McCourt P, Smedsrod B, Sorensen KK. Liver sinusoidal endothelial cells depend on mannose receptor-mediated recruitment of lysosomal enzymes for normal degradation capacity. *Hepatology.* 2008;48(6):2007-15.

97. Elvevold KH, Nedredal GI, Revhaug A, Smedsrod B. Scavenger properties of cultivated pig liver endothelial cells. *Comp Hepatol*. 2004;3(1):4.
98. Endesfelder U, Heilemann M. Art and artifacts in single-molecule localization microscopy: beyond attractive images. *Nat Methods*. 2014;11(3):235-8.
99. Endo Y, Nakamura M. The effect of lipopolysaccharide, interleukin-1 and tumour necrosis factor on the hepatic accumulation of 5-hydroxytryptamine and platelets in the mouse. *Br J Pharmacol*. 1992;105(3):613-9.
100. Enomoto M, Sakaguchi H, Ominami M, Iwai S, Morikawa H, Tamori A, et al. Sildenafil-induced severe cholestatic hepatotoxicity. *Am J Gastroenterol*. 2009;104(1):254-5.
101. Erfle H. *Super-Resolution Microscopy: Methods and Protocols*: Springer; 2017.
102. Erni R, Rossell MD, Kisielowski C, Dahmen U. Atomic-resolution imaging with a sub-50-pm electron probe. *Phys Rev Lett*. 2009;102(9):096101.
103. Esterbauer H, Dieber-Rotheneder M, Waeg G, Striegl G, Jurgens G. Biochemical, structural, and functional properties of oxidized low-density lipoprotein. *Chem Res Toxicol*. 1990;3(2):77-92.
104. Esterbauer H, Gebicki J, Puhl H, Jurgens G. The role of lipid peroxidation and antioxidants in oxidative modification of LDL. *Free Radic Biol Med*. 1992;13(4):341-90.
105. Eweka A, Eweka A. The effects of sildenafil citrate on the liver and kidneys of adult wistar rats (*Rattus norvegicus*) - a histological study. In: Azita G, editor. *Sexual dysfunctions - special issues*: IntechOpen; 2011. p. 59-65.
106. Ezekowitz RA, Sastry K, Bailly P, Warner A. Molecular characterization of the human macrophage mannose receptor: demonstration of multiple carbohydrate recognition-like domains and phagocytosis of yeasts in Cos-1 cells. *J Exp Med*. 1990;172(6):1785-94.
107. Faggiotto A, Ross R. Studies of hypercholesterolemia in the nonhuman primate. II. Fatty streak conversion to fibrous plaque. *Arteriosclerosis*. 1984;4(4):341-56.
108. Faggiotto A, Ross R, Harker L. Studies of hypercholesterolemia in the nonhuman primate. I. Changes that lead to fatty streak formation. *Arteriosclerosis*. 1984;4(4):323-40.
109. Falkowska-Hansen B, Falkowski M, Metharom P, Krunic D, Goerd S. Clathrin-coated vesicles form a unique net-like structure in liver sinusoidal endothelial cells by assembling along undisrupted microtubules. *Exp Cell Res*. 2007;313(9):1745-57.
110. Falkowski M, Schledzewski K, Hansen B, Goerd S. Expression of stabilin-2, a novel fasciclin-like hyaluronan receptor protein, in murine sinusoidal endothelia, avascular tissues, and at solid/liquid interfaces. *Histochem Cell Biol*. 2003;120(5):361-9.
111. Febbraio M, Hajjar DP, Silverstein RL. CD36: a class B scavenger receptor involved in angiogenesis, atherosclerosis, inflammation, and lipid metabolism. *J Clin Invest*. 2001;108(6):785-91.
112. Febbraio M, Silverstein RL. CD36: implications in cardiovascular disease. *Int J Biochem Cell Biol*. 2007;39(11):2012-30.
113. Feng H, Wang X, Xu Z, Zhang X, Gao Y. Super-Resolution Fluorescence Microscopy for Single Cell Imaging. *Adv Exp Med Biol*. 2018;1068:59-71.
114. Ferri S, Sesso A. Ultrastructural study of the endothelial cells in teleost liver sinusoids under normal and experimental conditions. *Cell Tissue Res*. 1981;219(3):649-57.
115. Festing M, Lovell D, editors. *Domestication and development of the mouse as a laboratory animal*. Symposia of the Zoological Society of London; 1981.

116. Fiete DJ, Beranek MC, Baenziger JU. A cysteine-rich domain of the "mannose" receptor mediates GalNAc-4-SO₄ binding. *Proc Natl Acad Sci U S A*. 1998;95(5):2089-93.
117. Finbloom DS, Plotz PH. Studies of reticuloendothelial function in the mouse with model immune complexes. I. Serum clearance and tissue uptake in normal C3H mice. *J Immunol*. 1979;123(4):1594-9.
118. Fisone G, Borgkvist A, Usiello A. Caffeine as a psychomotor stimulant: mechanism of action. *Cell Mol Life Sci*. 2004;61(7-8):857-72.
119. Foukas LC, Daniele N, Ktori C, Anderson KE, Jensen J, Shepherd PR. Direct effects of caffeine and theophylline on p110 delta and other phosphoinositide 3-kinases. Differential effects on lipid kinase and protein kinase activities. *J Biol Chem*. 2002;277(40):37124-30.
120. Fraser R, Bosanquet AG, Day WA. Filtration of chylomicrons by the liver may influence cholesterol metabolism and atherosclerosis. *Atherosclerosis*. 1978;29(2):113-23.
121. Fraser R, Bowler LM, Day WA. Damage of rat liver sinusoidal endothelium by ethanol. *Pathology*. 1980;12(3):371-6.
122. Fraser R, Bowler LM, Wisse E. Agents related to fibrosis, such as alcohol and carbon tetrachloride, acutely effect endothelial fenestrae which cause fatty liver. *Connective Tissue Normal Fibrotic Hum Liver*. 1982:159-60.
123. Fraser R, Clark SA, Day WA, Murray FE. Nicotine decreases the porosity of the rat liver sieve: a possible mechanism for hypercholesterolaemia. *Br J Exp Pathol*. 1988;69(3):345-50.
124. Fraser R, Cogger VC, Dobbs B, Jamieson H, Warren A, Hilmer SN, et al. The liver sieve and atherosclerosis. *Pathology*. 2012;44(3):181-6.
125. Fraser R, Day WA, Fernando NS. Atherosclerosis and the liver sieve. Cells of the hepatic sinusoid. 1986;1:317-22.
126. Fraser R, Dobbs BR, Rogers GW. Lipoproteins and the liver sieve: the role of the fenestrated sinusoidal endothelium in lipoprotein metabolism, atherosclerosis, and cirrhosis. *Hepatology*. 1995;21(3):863-74.
127. Fraser R, Heslop VR, Murray FE, Day WA. Ultrastructural studies of the portal transport of fat in chickens. *Br J Exp Pathol*. 1986;67(6):783-91.
128. Fredholm BB, Battig K, Holmen J, Nehlig A, Zvartau EE. Actions of caffeine in the brain with special reference to factors that contribute to its widespread use. *Pharmacol Rev*. 1999;51(1):83-133.
129. Frenkel D, Wilkinson K, Zhao L, Hickman SE, Means TK, Puckett L, et al. Scara1 deficiency impairs clearance of soluble amyloid-beta by mononuclear phagocytes and accelerates Alzheimer's-like disease progression. *Nat Commun*. 2013;4:2030.
130. Frenzel H, Hucker H, Kremer B. [The liver sinusoids in rats following fractionated local telecobalt-irradiation. A transmission and scanning electron microscopic study (author's transl)]. *Virchows Arch A Pathol Anat Histol*. 1977;375(1):37-51.
131. Fujita H, Tamaru T, Miyagawa J. Fine structural characteristics of the hepatic sinusoidal walls of the goldfish (*Carassius auratus*). *Arch Histol Jpn*. 1980;43(3):265-73.
132. Galbraith CG, Galbraith JA. Super-resolution microscopy at a glance. *J Cell Sci*. 2011;124(Pt 10):1607-11.
133. Ganesan LP, Kim J, Wu Y, Mohanty S, Phillips GS, Birmingham DJ, et al. FcgammaRIIb on liver sinusoidal endothelium clears small immune complexes. *J Immunol*. 2012;189(10):4981-8.

134. Ganesan LP, Mates JM, Cheplowitz AM, Avila CL, Zimmerer JM, Yao Z, et al. Scavenger receptor B1, the HDL receptor, is expressed abundantly in liver sinusoidal endothelial cells. *Sci Rep.* 2016;6:20646.
135. Ganesan LP, Mohanty S, Kim J, Clark KR, Robinson JM, Anderson CL. Rapid and efficient clearance of blood-borne virus by liver sinusoidal endothelium. *PLoS Pathog.* 2011;7(9):e1002281.
136. Gardella R, Carpenter F, Yü L, Yu L. The classic of tea by Lu Yü. *Journal of the American Oriental Society.* 1976;96:474.
137. Garlanda C, Dejana E. Heterogeneity of endothelial cells. Specific markers. *Arterioscler Thromb Vasc Biol.* 1997;17(7):1193-202.
138. Geraghty R, Capes-Davis A, Davis J, Downward J, Freshney R, Knezevic I, et al. Guidelines for the use of cell lines in biomedical research. *British journal of cancer.* 2014;111(6):1021-46.
139. Germann A, Schulz JC, Kemp-Kamke B, Zimmermann H, von Briesen H. Standardized Serum-Free Cryomedia Maintain Peripheral Blood Mononuclear Cell Viability, Recovery, and Antigen-Specific T-Cell Response Compared to Fetal Calf Serum-Based Medium. *Biopreserv Biobank.* 2011;9(3):229-36.
140. Glass CK, Witztum JL. Atherosclerosis. the road ahead. *Cell.* 2001;104(4):503-16.
141. Goerdt S, Walsh LJ, Murphy GF, Pober JS. Identification of a novel high molecular weight protein preferentially expressed by sinusoidal endothelial cells in normal human tissues. *J Cell Biol.* 1991;113(6):1425-37.
142. Goldstein I, Tseng LJ, Creanga D, Stecher V, Kaminetsky JC. Efficacy and Safety of Sildenafil by Age in Men With Erectile Dysfunction. *J Sex Med.* 2016;13(5):852-9.
143. Goldstein JL, Ho YK, Basu SK, Brown MS. Binding site on macrophages that mediates uptake and degradation of acetylated low density lipoprotein, producing massive cholesterol deposition. *Proc Natl Acad Sci U S A.* 1979;76(1):333-7.
144. Graziano S, Montana A, Zaami S, Rotolo MC, Minutillo A, Busardo FP, et al. Sildenafil-associated hepatotoxicity: a review of the literature. *Eur Rev Med Pharmacol Sci.* 2017;21(1 Suppl):17-22.
145. Greenwalt DE, Scheck SH, Rhinehart-Jones T. Heart CD36 expression is increased in murine models of diabetes and in mice fed a high fat diet. *J Clin Invest.* 1995;96(3):1382-8.
146. Gressner OA, Lahme B, Siluschek M, Gressner AM. Identification of paraxanthine as the most potent caffeine-derived inhibitor of connective tissue growth factor expression in liver parenchymal cells. *Liver Int.* 2009;29(6):886-97.
147. Gustafsson MG. Surpassing the lateral resolution limit by a factor of two using structured illumination microscopy. *J Microsc.* 2000;198(Pt 2):82-7.
148. Gustafsson MG. Nonlinear structured-illumination microscopy: wide-field fluorescence imaging with theoretically unlimited resolution. *Proc Natl Acad Sci U S A.* 2005;102(37):13081-6.
149. Gustafsson MG, Shao L, Carlton PM, Wang CJ, Golubovskaya IN, Cande WZ, et al. Three-dimensional resolution doubling in wide-field fluorescence microscopy by structured illumination. *Biophys J.* 2008;94(12):4957-70.
150. Guzik TJ, West NE, Pillai R, Taggart DP, Channon KM. Nitric oxide modulates superoxide release and peroxynitrite formation in human blood vessels. *Hypertension.* 2002;39(6):1088-94.
151. Gyoneva S, Shapiro L, Lazo C, Garnier-Amblard E, Smith Y, Miller GW, et al. Adenosine A2A receptor antagonism reverses inflammation-induced impairment of

microglial process extension in a model of Parkinson's disease. *Neurobiol Dis.* 2014;67:191-202.

152. Hampton RY, Golenbock DT, Penman M, Krieger M, Raetz CR. Recognition and plasma clearance of endotoxin by scavenger receptors. *Nature.* 1991;352(6333):342-4.

153. Han R, Li Z, Fan Y, Jiang Y. Recent advances in super-resolution fluorescence imaging and its applications in biology. *J Genet Genomics.* 2013;40(12):583-95.

154. Hansen B, Arteta B, Smedsrod B. The physiological scavenger receptor function of hepatic sinusoidal endothelial and Kupffer cells is independent of scavenger receptor class A type I and II. *Mol Cell Biochem.* 2002;240(1-2):1-8.

155. Hansen B, Longati P, Elvevold K, Nedredal GI, Schledzewski K, Olsen R, et al. Stabilin-1 and stabilin-2 are both directed into the early endocytic pathway in hepatic sinusoidal endothelium via interactions with clathrin/AP-2, independent of ligand binding. *Exp Cell Res.* 2005;303(1):160-73.

156. Hansen B, Svistounov D, Olsen R, Nagai R, Horiuchi S, Smedsrod B. Advanced glycation end products impair the scavenger function of rat hepatic sinusoidal endothelial cells. *Diabetologia.* 2002;45(10):1379-88.

157. Hauser M, Wojcik M, Kim D, Mahmoudi M, Li W, Xu K. Correlative Super-Resolution Microscopy: New Dimensions and New Opportunities. *Chem Rev.* 2017;117(11):7428-56.

158. He P, Noda Y, Sugiyama K. Suppressive effect of coffee on lipopolysaccharide-induced hepatitis in D-galactosamine-sensitized rats. *Biosci Biotechnol Biochem.* 2001;65(8):1924-7.

159. Hebert LA. The clearance of immune complexes from the circulation of man and other primates. *Am J Kidney Dis.* 1991;17(3):352-61.

160. Heilemann M, van de Linde S, Mukherjee A, Sauer M. Super-resolution imaging with small organic fluorophores. *Angew Chem Int Ed Engl.* 2009;48(37):6903-8.

161. Heilemann M, van de Linde S, Schuttpelz M, Kasper R, Seefeldt B, Mukherjee A, et al. Subdiffraction-resolution fluorescence imaging with conventional fluorescent probes. *Angew Chem Int Ed Engl.* 2008;47(33):6172-6.

162. Heintzmann R, Cremer CG, editors. Laterally modulated excitation microscopy: improvement of resolution by using a diffraction grating. *Optical Biopsies and Microscopic Techniques III*; 1999: International Society for Optics and Photonics.

163. Heintzmann R, Jovin TM, Cremer C. Saturated patterned excitation microscopy-a concept for optical resolution improvement. *J Opt Soc Am A Opt Image Sci Vis.* 2002;19(8):1599-609.

164. Hell SW. Microscopy and its focal switch. *Nat Methods.* 2009;6(1):24-32.

165. Hell SW, Wichmann J. Breaking the diffraction resolution limit by stimulated emission: stimulated-emission-depletion fluorescence microscopy. *Opt Lett.* 1994;19(11):780-2.

166. Herz J, Hamann U, Rogne S, Myklebost O, Gausepohl H, Stanley KK. Surface location and high affinity for calcium of a 500-kd liver membrane protein closely related to the LDL-receptor suggest a physiological role as lipoprotein receptor. *EMBO J.* 1988;7(13):4119-27.

167. Herz J, Strickland DK. LRP: a multifunctional scavenger and signaling receptor. *J Clin Invest.* 2001;108(6):779-84.

168. Hess ST, Girirajan TP, Mason MD. Ultra-high resolution imaging by fluorescence photoactivation localization microscopy. *Biophys J.* 2006;91(11):4258-72.

169. Hevonoja T, Pentikainen MO, Hyvonen MT, Kovanen PT, Ala-Korpela M. Structure of low density lipoprotein (LDL) particles: basis for understanding molecular changes in modified LDL. *Biochim Biophys Acta.* 2000;1488(3):189-210.

170. Hickman R, Parker JR, Saunders SJ, Terblanche J. Platelet adherence in the pig liver perfused with human blood. *Transplantation*. 1972;13(2):195-8.
171. Hilmer SN, Cogger VC, Fraser R, McLean AJ, Sullivan D, Le Couteur DG. Age-related changes in the hepatic sinusoidal endothelium impede lipoprotein transfer in the rat. *Hepatology*. 2005;42(6):1349-54.
172. Hilmer SN, Shenfield GM, Le Couteur DG. Clinical implications of changes in hepatic drug metabolism in older people. *Ther Clin Risk Manag*. 2005;1(2):151-6.
173. Hiltunen TP, Gough PJ, Greaves DR, Gordon S, Yla-Herttuala S. Rabbit atherosclerotic lesions express scavenger receptor AIII mRNA, a naturally occurring splice variant that encodes a non-functional, dominant negative form of the macrophage scavenger receptor. *Atherosclerosis*. 2001;154(2):415-9.
174. Hinton DE, Pool CR. Ultrastructure of the liver in channel catfish *Ictalurus punctatus* (Rafinesque). *Journal of Fish Biology*. 1976;8(3):209-19.
175. Hofer M, Pospisil M, Dusek L, Hoferova Z, Komurkova D. Lack of adenosine A3 receptors causes defects in mouse peripheral blood parameters. *Purinergic Signal*. 2014;10(3):509-14.
176. Hoff HF, Whitaker TE, O'Neil J. Oxidation of low density lipoprotein leads to particle aggregation and altered macrophage recognition. *J Biol Chem*. 1992;267(1):602-9.
177. Holden SJ, Uphoff S, Kapanidis AN. DAOSTORM: an algorithm for high-density super-resolution microscopy. *Nat Methods*. 2011;8(4):279-80.
178. Holm T, Klein T, Loschberger A, Klamp T, Wiebusch G, van de Linde S, et al. A blueprint for cost-efficient localization microscopy. *Chemphyschem*. 2014;15(4):651-4.
179. Holvoet P, Perez G, Zhao Z, Brouwers E, Bernar H, Collen D. Malondialdehyde-modified low density lipoproteins in patients with atherosclerotic disease. *J Clin Invest*. 1995;95(6):2611-9.
180. Holvoet P, Stassen JM, Van Cleemput J, Collen D, Vanhaecke J. Oxidized low density lipoproteins in patients with transplant-associated coronary artery disease. *Arterioscler Thromb Vasc Biol*. 1998;18(1):100-7.
181. Holvoet P, Vanhaecke J, Janssens S, Van de Werf F, Collen D. Oxidized LDL and malondialdehyde-modified LDL in patients with acute coronary syndromes and stable coronary artery disease. *Circulation*. 1998;98(15):1487-94.
182. Horiuchi N, Suda T, Sasaki S, Takahashi H, Shimazawa E, Ogata E. Absence of regulatory effects of $1\alpha, 25$ -dihydroxyvitamin D₃ on 25-hydroxyvitamin D₃ metabolism in rats constantly infused with parathyroid hormone. *Biochemical and Biophysical Research Communications*. 1976;73(4):869-75.
183. Horn T, Christoffersen P, Henriksen JH. Alcoholic liver injury: defenestration in noncirrhotic livers--a scanning electron microscopic study. *Hepatology*. 1987;7(1):77-82.
184. Hsu SJ, Lee FY, Wang SS, Hsin IF, Lin TY, Huang HC, et al. Caffeine ameliorates hemodynamic derangements and portosystemic collaterals in cirrhotic rats. *Hepatology*. 2015;61(5):1672-84.
185. Huang B. Super-resolution optical microscopy: multiple choices. *Curr Opin Chem Biol*. 2010;14(1):10-4.
186. Hughes DA, Fraser IP, Gordon S. Murine macrophage scavenger receptor: in vivo expression and function as receptor for macrophage adhesion in lymphoid and non-lymphoid organs. *Eur J Immunol*. 1995;25(2):466-73.
187. Hunt NJ, Lockwood GP, Warren A, Mao H, McCourt PAG, Le Couteur DG, et al. Manipulating fenestrations in young and old liver sinusoidal endothelial cells. *Am J Physiol Gastrointest Liver Physiol*. 2019;316(1):G144-G54.

188. Hussain MM, Strickland DK, Bakillah A. The mammalian low-density lipoprotein receptor family. *Annu Rev Nutr.* 1999;19:141-72.
189. Ignarro LJ. Physiology and pathophysiology of nitric oxide. *Kidney Int Suppl.* 1996;55:S2-5.
190. Ingersoll MA, Spanbroek R, Lottaz C, Gautier EL, Frankenberger M, Hoffmann R, et al. Comparison of gene expression profiles between human and mouse monocyte subsets. *Blood.* 2010;115(3):e10-9.
191. Israilov S, Baniel J, Shmueli J, Niv E, Engelstein D, Segenreich E, et al. Treatment program for erectile dysfunction in patients with cardiovascular diseases. *Am J Cardiol.* 2004;93(6):689-93.
192. Itabe H. Oxidized low-density lipoproteins: what is understood and what remains to be clarified. *Biol Pharm Bull.* 2003;26(1):1-9.
193. Itabe H, Takano T. Oxidized low density lipoprotein: the occurrence and metabolism in circulation and in foam cells. *J Atheroscler Thromb.* 2000;7(3):123-31.
194. Iwakiri Y, Kim MY. Nitric oxide in liver diseases. *Trends Pharmacol Sci.* 2015;36(8):524-36.
195. Jackson G, Benjamin N, Jackson N, Allen MJ. Effects of sildenafil citrate on human hemodynamics. *Am J Cardiol.* 1999;83(5A):13C-20C.
196. Jain NC. A scanning electron microscopic study of platelets of certain animal species. *Thromb Diath Haemorrh.* 1975;33(3):501-7.
197. Jamieson HA, Hilmer SN, Cogger VC, Warren A, Cheluvappa R, Abernethy DR, et al. Caloric restriction reduces age-related pseudocapillarization of the hepatic sinusoid. *Exp Gerontol.* 2007;42(4):374-8.
198. Jay AG, Hamilton JA. The enigmatic membrane fatty acid transporter CD36: New insights into fatty acid binding and their effects on uptake of oxidized LDL. *Prostaglandins Leukot Essent Fatty Acids.* 2018;138:64-70.
199. Jessup W, Kritharides L. Metabolism of oxidized LDL by macrophages. *Curr Opin Lipidol.* 2000;11(5):473-81.
200. Jialal I, Devaraj S. The role of oxidized low density lipoprotein in atherogenesis. *J Nutr.* 1996;126(4 Suppl):1053S-7S.
201. Johansson AG, Lovdal T, Magnusson KE, Berg T, Skogh T. Liver cell uptake and degradation of soluble immunoglobulin G immune complexes in vivo and in vitro in rats. *Hepatology.* 1996;24(1):169-75.
202. Jones AW. Review of Caffeine-Related Fatalities along with Postmortem Blood Concentrations in 51 Poisoning Deaths. *J Anal Toxicol.* 2017;41(3):167-72.
203. Jungermann K, Katz N. Functional hepatocellular heterogeneity. *Hepatology.* 1982;2(3):385-95.
204. Juul K, Nielsen LB, Munkholm K, Stender S, Nordestgaard BG. Oxidation of plasma low-density lipoprotein accelerates its accumulation and degradation in the arterial wall in vivo. *Circulation.* 1996;94(7):1698-704.
205. Kankaanpaa J, Turunen SP, Moilanen V, Horkko S, Remes AM. Cerebrospinal fluid antibodies to oxidized LDL are increased in Alzheimer's disease. *Neurobiol Dis.* 2009;33(3):467-72.
206. Kasuya Y, Miyata H, Watanabe M. Toxicological studies on the chloroquine-melanin affinity in vivo and in vitro in relation to the chloroquine retinopathy. *The Journal of Toxicological Sciences.* 1976;1(1):32-8.
207. Kawasaki T, Murata S, Takahashi K, Nozaki R, Ohshiro Y, Ikeda N, et al. Activation of human liver sinusoidal endothelial cell by human platelets induces hepatocyte proliferation. *J Hepatol.* 2010;53(4):648-54.

208. Kjekken R, Mousavi SA, Brech A, Gjoen T, Berg T. Fluid phase endocytosis of [125I]iodixanol in rat liver parenchymal, endothelial and Kupffer cells. *Cell Tissue Res.* 2001;304(2):221-30.
209. Knook DL, Sleyster EC. Separation of Kupffer and endothelial cells of the rat liver by centrifugal elutriation. *Exp Cell Res.* 1976;99(2):444-9.
210. Knowles RG, Moncada S. Nitric oxide synthases in mammals. *Biochem J.* 1994;298 (Pt 2):249-58.
211. Kobiyama K, Ley K. Atherosclerosis. *Circ Res.* 2018;123(10):1118-20.
212. Kodama T, Freeman M, Rohrer L, Zabrecky J, Matsudaira P, Krieger M. Type I macrophage scavenger receptor contains alpha-helical and collagen-like coiled coils. *Nature.* 1990;343(6258):531-5.
213. Kojda G, Harrison D. Interactions between NO and reactive oxygen species: pathophysiological importance in atherosclerosis, hypertension, diabetes and heart failure. *Cardiovasc Res.* 1999;43(3):562-71.
214. Kozarsky KF, Donahee MH, Rigotti A, Iqbal SN, Edelman ER, Krieger M. Overexpression of the HDL receptor SR-BI alters plasma HDL and bile cholesterol levels. *Nature.* 1997;387(6631):414-7.
215. Krieger M. The other side of scavenger receptors: pattern recognition for host defense. *Curr Opin Lipidol.* 1997;8(5):275-80.
216. Kulkarni PB, Dorand RD. Caffeine toxicity in a neonate. *Pediatrics.* 1979;64(2):254-5.
217. Kunjathoor VV, Febbraio M, Podrez EA, Moore KJ, Andersson L, Koehn S, et al. Scavenger receptors class A-I/II and CD36 are the principal receptors responsible for the uptake of modified low density lipoprotein leading to lipid loading in macrophages. *J Biol Chem.* 2002;277(51):49982-8.
218. Kurokawa T, Ohkohchi N. Platelets in liver disease, cancer and regeneration. *World J Gastroenterol.* 2017;23(18):3228-39.
219. Kurokawa T, Zheng YW, Ohkohchi N. Novel functions of platelets in the liver. *J Gastroenterol Hepatol.* 2016;31(4):745-51.
220. Kwakwa K, Savell A, Davies T, Munro I, Parrinello S, Purbhoo MA, et al. easySTORM: a robust, lower-cost approach to localisation and TIRF microscopy. *J Biophotonics.* 2016;9(9):948-57.
221. Kzhyshkowska J, Workman G, Cardo-Vila M, Arap W, Pasqualini R, Gratchev A, et al. Novel function of alternatively activated macrophages: stabilin-1-mediated clearance of SPARC. *J Immunol.* 2006;176(10):5825-32.
222. Le Couteur DG, Cogger VC, Markus AM, Harvey PJ, Yin ZL, Ansell AD, et al. Pseudocapillarization and associated energy limitation in the aged rat liver. *Hepatology.* 2001;33(3):537-43.
223. Le Couteur DG, Fraser R, Cogger VC, McLean AJ. Hepatic pseudocapillarisation and atherosclerosis in ageing. *Lancet.* 2002;359(9317):1612-5.
224. Le Couteur DG, Warren A, Cogger VC, Smedsrod B, Sorensen KK, De Cabo R, et al. Old age and the hepatic sinusoid. *Anat Rec.* 2008;291(6):672-83.
225. Lee SJ, Evers S, Roeder D, Parlow AF, Risteli J, Risteli L, et al. Mannose receptor-mediated regulation of serum glycoprotein homeostasis. *Science.* 2002;295(5561):1898-901.
226. Lelo A, Birkett DJ, Robson RA, Miners JO. Comparative pharmacokinetics of caffeine and its primary demethylated metabolites paraxanthine, theobromine and theophylline in man. *Br J Clin Pharmacol.* 1986;22(2):177-82.

227. Lelo A, Kjellen G, Birkett DJ, Miners JO. Paraxanthine metabolism in humans: determination of metabolic partial clearances and effects of allopurinol and cimetidine. *J Pharmacol Exp Ther.* 1989;248(1):315-9.
228. Lermen D, Schmitt D, Bartel-Steinbach M, Schroter-Kermani C, Kolossa-Gehring M, von Briesen H, et al. A new approach to standardize multicenter studies: mobile lab technology for the German Environmental Specimen Bank. *Plos One.* 2014;9(8):e105401.
229. Leung BO, Chou KC. Review of super-resolution fluorescence microscopy for biology. *Appl Spectrosc.* 2011;65(9):967-80.
230. Levitan I, Volkov S, Subbaiah PV. Oxidized LDL: diversity, patterns of recognition, and pathophysiology. *Antioxid Redox Signal.* 2010;13(1):39-75.
231. Li DY, Zhang YC, Philips MI, Sawamura T, Mehta JL. Upregulation of endothelial receptor for oxidized low-density lipoprotein (LOX-1) in cultured human coronary artery endothelial cells by angiotensin II type 1 receptor activation. *Circ Res.* 1999;84(9):1043-9.
232. Li R, McCourt P, Schledzewski K, Goerdts S, Moldenhauer G, Liu X, et al. Endocytosis of advanced glycation end-products in bovine choriocapillaris endothelial cells. *Microcirculation.* 2009;16(7):640-55.
233. Li R, Oteiza A, Sorensen KK, McCourt P, Olsen R, Smedsrod B, et al. Role of liver sinusoidal endothelial cells and stabilins in elimination of oxidized low-density lipoproteins. *Am J Physiol Gastrointest Liver Physiol.* 2011;300(1):G71-81.
234. Libby P. Inflammation in atherosclerosis. *Nature.* 2002;420(6917):868-74.
235. Lin Y, Long JJ, Huang F, Duim WC, Kirschbaum S, Zhang Y, et al. Quantifying and optimizing single-molecule switching nanoscopy at high speeds. *Plos One.* 2015;10(5):e0128135.
236. Linehan SA, Martinez-Pomares L, Stahl PD, Gordon S. Mannose receptor and its putative ligands in normal murine lymphoid and nonlymphoid organs: In situ expression of mannose receptor by selected macrophages, endothelial cells, perivascular microglia, and mesangial cells, but not dendritic cells. *J Exp Med.* 1999;189(12):1961-72.
237. Linehan SA, Weber R, McKercher S, Ripley RM, Gordon S, Martin P. Enhanced expression of the mannose receptor by endothelial cells of the liver and spleen microvascular beds in the macrophage-deficient PU.1 null mouse. *Histochem Cell Biol.* 2005;123(4-5):365-76.
238. Ling W, Loughheed M, Suzuki H, Buchan A, Kodama T, Steinbrecher UP. Oxidized or acetylated low density lipoproteins are rapidly cleared by the liver in mice with disruption of the scavenger receptor class A type I/II gene. *J Clin Invest.* 1997;100(2):244-52.
239. Liu J, Hughes TE, Sessa WC. The first 35 amino acids and fatty acylation sites determine the molecular targeting of endothelial nitric oxide synthase into the Golgi region of cells: a green fluorescent protein study. *J Cell Biol.* 1997;137(7):1525-35.
240. Liu JH, Tang Q, Liu XX, Qi J, Zeng RX, Zhu ZW, et al. Analysis of transcriptome sequencing of sciatic nerves in Sprague-Dawley rats of different ages. *Neural Regen Res.* 2018;13(12):2182-90.
241. Lombardi T, Montesano R, Furie MB, Silverstein SC, Orci L. In vitro modulation of endothelial fenestrae: opposing effects of retinoic acid and transforming growth factor beta. *J Cell Sci.* 1988;91 (Pt 2):313-8.
242. Lopes-Virella MF, Virella G, Orchard TJ, Koskinen S, Evans RW, Becker DJ, et al. Antibodies to oxidized LDL and LDL-containing immune complexes as risk factors for coronary artery disease in diabetes mellitus. *Clin Immunol.* 1999;90(2):165-72.

243. Lovdal T, Berg T. Transcription of Fc(γ) receptors in different rat liver cells. *Cell Biol Int*. 2001;25(8):821-4.
244. Lovelock JE, Bishop MW. Prevention of freezing damage to living cells by dimethyl sulphoxide. *Nature*. 1959;183(4672):1394-5.
245. Lu H, Daugherty A. Atherosclerosis. *Arterioscler Thromb Vasc Biol*. 2015;35(3):485-91.
246. Lusis AJ. Atherosclerosis. *Nature*. 2000;407(6801):233-41.
247. Ma H, Fu R, Xu J, Liu Y. A simple and cost-effective setup for super-resolution localization microscopy. *Sci Rep*. 2017;7(1):1542.
248. Ma H, Liu Y. Super-resolution localization microscopy: Toward high throughput, high quality, and low cost. *APL Photonics*. 2020;5(6):060902.
249. Machlus KR, Thon JN, Italiano JE, Jr. Interpreting the developmental dance of the megakaryocyte: a review of the cellular and molecular processes mediating platelet formation. *Br J Haematol*. 2014;165(2):227-36.
250. MacPhee PJ, Schmidt EE, Groom AC. Intermittence of blood flow in liver sinusoids, studied by high-resolution in vivo microscopy. *Am J Physiol*. 1995;269(5 Pt 1):G692-8.
251. Madarame T, Nagaoka T, Inomata M, Suzuki K, Sato S, Kanno S, et al. Basement membrane-like structure may play a role in the alteration of endothelial fenestration. *Cells of the hepatic sinusoid*. 1991;3:98-101.
252. Magnusson S, Berg T. Extremely rapid endocytosis mediated by the mannose receptor of sinusoidal endothelial rat liver cells. *Biochem J*. 1989;257(3):651-6.
253. Mak KM, Lieber CS. Alterations in endothelial fenestrations in liver sinusoids of baboons fed alcohol: a scanning electron microscopic study. *Hepatology*. 1984;4(3):386-91.
254. Malerod L, Juvet K, Gjoen T, Berg T. The expression of scavenger receptor class B, type I (SR-BI) and caveolin-1 in parenchymal and nonparenchymal liver cells. *Cell Tissue Res*. 2002;307(2):173-80.
255. Malovic I, Sorensen KK, Elvevold KH, Nedredal GI, Paulsen S, Erofeev AV, et al. The mannose receptor on murine liver sinusoidal endothelial cells is the main denatured collagen clearance receptor. *Hepatology*. 2007;45(6):1454-61.
256. Mao H, Diekmann R, Liang HPH, Cogger VC, Couteur DGL, Lockwood GP, et al. Cost-efficient nanoscopy reveals nanoscale architecture of liver cells and platelets. *Nanophotonics*. 2019;8(7):1299.
257. March S, Hui EE, Underhill GH, Khetani S, Bhatia SN. Microenvironmental regulation of the sinusoidal endothelial cell phenotype in vitro. *Hepatology*. 2009;50(3):920-8.
258. Marieb ENH, K. N. *Human Anatomy & Physiology with Modified MasteringA&P with Pearson eText*. 9th ed. United States: Benjamin-Cummings Publishing Company; 2012.
259. Martens JH, Kzhyshkowska J, Falkowski-Hansen M, Schledzewski K, Gratchev A, Mansmann U, et al. Differential expression of a gene signature for scavenger/lectin receptors by endothelial cells and macrophages in human lymph node sinuses, the primary sites of regional metastasis. *J Pathol*. 2006;208(4):574-89.
260. Martin WB, Sicard R, Namin SM, Ganey T. *Methods of Cryoprotectant Preservation: Allogeneic Cellular Bone Grafts and Potential Effects*. *Biomed Res Int*. 2019;2019:5025398.
261. Martin-Armas M, Simon-Santamaria J, Pettersen I, Moens U, Smedsrod B, Sveinbjornsson B. Toll-like receptor 9 (TLR9) is present in murine liver sinusoidal

- endothelial cells (LSECs) and mediates the effect of CpG-oligonucleotides. *J Hepatol.* 2006;44(5):939-46.
262. Martinez I, Nedredal GI, Oie CI, Warren A, Johansen O, Le Couteur DG, et al. The influence of oxygen tension on the structure and function of isolated liver sinusoidal endothelial cells. *Comp Hepatol.* 2008;7:4.
263. Martinez-Pomares L, Gordon S. Antigen presentation the macrophage way. *Cell.* 2007;131(4):641-3.
264. Martinez-Pomares L, Wienke D, Stillion R, McKenzie EJ, Arnold JN, Harris J, et al. Carbohydrate-independent recognition of collagens by the macrophage mannose receptor. *Eur J Immunol.* 2006;36(5):1074-82.
265. Marttila-Ichihara F, Turja R, Miiluniemi M, Karikoski M, Maksimow M, Niemela J, et al. Macrophage mannose receptor on lymphatics controls cell trafficking. *Blood.* 2008;112(1):64-72.
266. Mason CG. Ocular accumulation and toxicity of certain systemically administered drugs. *J Toxicol Environ Health.* 1977;2(5):977-95.
267. Masuda J, Ross R. Atherogenesis during low level hypercholesterolemia in the nonhuman primate. II. Fatty streak conversion to fibrous plaque. *Arteriosclerosis.* 1990;10(2):178-87.
268. Masuda J, Ross R. Atherogenesis during low level hypercholesterolemia in the nonhuman primate. I. Fatty streak formation. *Arteriosclerosis.* 1990;10(2):164-77.
269. Mathew RP, Venkatesh SK. Liver vascular anatomy: a refresher. *Abdom Radiol (NY).* 2018;43(8):1886-95.
270. Matsumoto A, Naito M, Itakura H, Ikemoto S, Asaoka H, Hayakawa I, et al. Human macrophage scavenger receptors: primary structure, expression, and localization in atherosclerotic lesions. *Proc Natl Acad Sci U S A.* 1990;87(23):9133-7.
271. Matsuo R, Nakano Y, Ohkohchi N. Platelet administration via the portal vein promotes liver regeneration in rats after 70% hepatectomy. *Ann Surg.* 2011;253(4):759-63.
272. Maxey DM, Ivy DD, Ogawa MT, Feinstein JA. Food and Drug Administration (FDA) postmarket reported side effects and adverse events associated with pulmonary hypertension therapy in pediatric patients. *Pediatr Cardiol.* 2013;34(7):1628-36.
273. Mayorga-Gross AL, Esquivel P. Impact of Cocoa Products Intake on Plasma and Urine Metabolites: A Review of Targeted and Non-Targeted Studies in Humans. *Nutrients.* 2019;11(5).
274. Mazur P. Kinetics of water loss from cells at subzero temperatures and the likelihood of intracellular freezing. *J Gen Physiol.* 1963;47:347-69.
275. Mazur P. Principles of cryobiology. In: Fuller B, Lane N, Benson EE, editors. *Life in the frozen state.* Boca Raton, FL: CRC Press; 2004. p. 3-66.
276. Mazur P, Leibo SP, Chu EH. A two-factor hypothesis of freezing injury. Evidence from Chinese hamster tissue-culture cells. *Exp Cell Res.* 1972;71(2):345-55.
277. Mazzafera P. Catabolism of caffeine in plants and microorganisms. *Front Biosci.* 2004;9:1348-59.
278. Mazzucco L, Borzini P, Gope R. Platelet-derived factors involved in tissue repair-from signal to function. *Transfus Med Rev.* 2010;24(3):218-34.
279. McChesney E, Fitch C. *Antimalarial Drug II: Current Antimalarial and New Drug Developments.* Berlin Heidelberg: Springer; 1984.
280. McChesney EW. Animal toxicity and pharmacokinetics of hydroxychloroquine sulfate. *Am J Med.* 1983;75(1A):11-8.

281. McCourt PA, Smedsrod BH, Melkko J, Johansson S. Characterization of a hyaluronan receptor on rat sinusoidal liver endothelial cells and its functional relationship to scavenger receptors. *Hepatology*. 1999;30(5):1276-86.
282. McCuskey PA, Kan Z, Wallace S. An electron microscopy study of Kupffer cells in livers of mice having Friend erythroleukemia hepatic metastases. *Clin Exp Metastasis*. 1994;12(6):416-26.
283. McCuskey PA, McCuskey R, Hinton D. Electron microscopy of cells of the hepatic sinusoids in rainbow trout (*Salmo gairdneri*). *Cells of the Hepatic Sinusoid*. 1986;1:489-94.
284. McLane MP, Black PR, Law WR, Raymond RM. Adenosine reversal of in vivo hepatic responsiveness to insulin. *Diabetes*. 1990;39(1):62-9.
285. McLean AJ, Cogger VC, Chong GC, Warren A, Markus AM, Dahlstrom JE, et al. Age-related pseudocapillarization of the human liver. *J Pathol*. 2003;200(1):112-7.
286. Medvinsky AL, Gan OI, Semenova ML, Samoylina NL. Development of day-8 colony-forming unit-spleen hematopoietic progenitors during early murine embryogenesis: spatial and temporal mapping. *Blood*. 1996;87(2):557-66.
287. Meryman HT. Preservation of living cells. *Fed Proc*. 1963;22:81-9.
288. Meyer J, Lejmi E, Fontana P, Morel P, Gonelle-Gispert C, Buhler L. A focus on the role of platelets in liver regeneration: Do platelet-endothelial cell interactions initiate the regenerative process? *J Hepatol*. 2015;63(5):1263-71.
289. Michelson AD. *Platelets*. San Diego ; London: Academic Press; 2002. xliii, 956 p. p.
290. Minkowski O. Über theocin (theophyllin) als diureticum. *Ther Gegenwart*. 1902;43:490-3.
291. Miyao M, Kotani H, Ishida T, Kawai C, Manabe S, Abiru H, et al. Pivotal role of liver sinusoidal endothelial cells in NAFLD/NASH progression. *Lab Invest*. 2015;95(10):1130-44.
292. Mönkemöller V, Mao H, Hubner W, Dumitriu G, Heimann P, Levy G, et al. Primary rat LSECs preserve their characteristic phenotype after cryopreservation. *Sci Rep*. 2018;8(1):14657.
293. Mönkemöller V, Øie C, Hubner W, Huser T, McCourt P. Multimodal super-resolution optical microscopy visualizes the close connection between membrane and the cytoskeleton in liver sinusoidal endothelial cell fenestrations. *Sci Rep*. 2015;5:16279.
294. Mönkemöller V, Schuttpelz M, McCourt P, Sorensen K, Smedsrod B, Huser T. Imaging fenestrations in liver sinusoidal endothelial cells by optical localization microscopy. *Phys Chem Chem Phys*. 2014;16(24):12576-81.
295. Mori T, Okanoue T, Sawa Y, Hori N, Ohta M, Kagawa K. Defenestration of the sinusoidal endothelial cell in a rat model of cirrhosis. *Hepatology*. 1993;17(5):891-7.
296. Morsiani E, Mazzoni M, Aleotti A, Gorini P, Ricci D. Increased sinusoidal wall permeability and liver fatty change after two-thirds hepatectomy: an ultrastructural study in the rat. *Hepatology*. 1995;21(2):539-44.
297. Mousavi SA, Sporstol M, Fladeby C, Kjekken R, Barois N, Berg T. Receptor-mediated endocytosis of immune complexes in rat liver sinusoidal endothelial cells is mediated by FcγRIIb2. *Hepatology*. 2007;46(3):871-84.
298. Muirhead GJ, Rance DJ, Walker DK, Wastall P. Comparative human pharmacokinetics and metabolism of single-dose oral and intravenous sildenafil. *Br J Clin Pharmacol*. 2002;53 Suppl 1:13S-20S.
299. Mumford GK, Benowitz NL, Evans SM, Kaminski BJ, Preston KL, Sannerud CA, et al. Absorption rate of methylxanthines following capsules, cola and chocolate. *Eur J Clin Pharmacol*. 1996;51(3-4):319-25.

300. Murata S, Ohkohchi N, Matsuo R, Ikeda O, Myronovych A, Hoshi R. Platelets promote liver regeneration in early period after hepatectomy in mice. *World J Surg.* 2007;31(4):808-16.
301. Nagelkerke JF, Barto KP, van Berkel TJ. In vivo and in vitro uptake and degradation of acetylated low density lipoprotein by rat liver endothelial, Kupffer, and parenchymal cells. *J Biol Chem.* 1983;258(20):12221-7.
302. Nahidiazar L, Agronskaia AV, Broertjes J, van den Broek B, Jalink K. Optimizing Imaging Conditions for Demanding Multi-Color Super Resolution Localization Microscopy. *Plos One.* 2016;11(7):e0158884.
303. Naito M, Wisse E. Observations on the fine structure and cytochemistry of sinusoidal cells in fetal and neonatal rat liver 1977.
304. Nakamura M, Shibazaki M, Nitta Y, Endo Y. Translocation of platelets into Disse spaces and their entry into hepatocytes in response to lipopolysaccharides, interleukin-1 and tumour necrosis factor: the role of Kupffer cells. *J Hepatol.* 1998;28(6):991-9.
305. Napper CE, Drickamer K, Taylor ME. Collagen binding by the mannose receptor mediated through the fibronectin type II domain. *Biochem J.* 2006;395(3):579-86.
306. Naumann H, Schröder G, Löffler-Mang M. *Handbuch bauelemente der optik: Grundlagen, werkstoffe, geräte, messtechnik: Carl Hanser Verlag GmbH Co KG;* 2014.
307. Nawrot P, Jordan S, Eastwood J, Rotstein J, Hugenholtz A, Feeley M. Effects of caffeine on human health. *Food Addit Contam.* 2003;20(1):1-30.
308. Neuman KC, Chadd EH, Liou GF, Bergman K, Block SM. Characterization of photodamage to *Escherichia coli* in optical traps. *Biophys J.* 1999;77(5):2856-63.
309. Nielson CP, Vestal RE, Sturm RJ, Heaslip R. Effects of selective phosphodiesterase inhibitors on the polymorphonuclear leukocyte respiratory burst. *J Allergy Clin Immunol.* 1990;86(5):801-8.
310. Noble RP. Electrophoretic separation of plasma lipoproteins in agarose gel. *J Lipid Res.* 1968;9(6):693-700.
311. Nopanitaya W, Carson JL, Grisham JW, Aghajanian JG. New observations on the fine structure of the liver in goldfish (*Carassius auratus*). *Cell Tissue Res.* 1979;196(2):249-61.
312. Nowatari T, Murata S, Fukunaga K, Ohkohchi N. Role of platelets in chronic liver disease and acute liver injury. *Hepatol Res.* 2014;44(2):165-72.
313. Nowatari T, Murata S, Nakayama K, Sano N, Maruyama T, Nozaki R, et al. Sphingosine 1-phosphate has anti-apoptotic effect on liver sinusoidal endothelial cells and proliferative effect on hepatocytes in a paracrine manner in human. *Hepatol Res.* 2015;45(11):1136-45.
314. Nurden AT. Platelets, inflammation and tissue regeneration. *Thromb Haemost.* 2011;105 Suppl 1:S13-33.
315. Nurden AT, Nurden P, Sanchez M, Andia I, Anitua E. Platelets and wound healing. *Front Biosci.* 2008;13:3532-48.
316. O'Reilly JN, Cogger VC, Fraser R, Le Couteur DG. The effect of feeding and fasting on fenestrations in the liver sinusoidal endothelial cell. *Pathology.* 2010;42(3):255-8.
317. O'Reilly JN, Cogger VC, Le Couteur DG. Old age is associated with ultrastructural changes in isolated rat liver sinusoidal endothelial cells. *J Electron Microsc (Tokyo).* 2010;59(1):65-9.
318. Oda M, Kazemoto S, Kaneko H. Involvement of Ca⁺⁺-calmodulin-actomyosin system in contractility of hepatic sinusoidal endothelial fenestrae. *Cells of the Hepatic Sinusoid.* 1993;4:174-8.

319. Ogura S, Kakino A, Sato Y, Fujita Y, Iwamoto S, Otsui K, et al. Lox-1: the multifunctional receptor underlying cardiovascular dysfunction. *Circ J*. 2009;73(11):1993-9.
320. Ohata M, Tanuma Y, Ito T. A transmission electron microscopic study on sinusoidal cells of guinea pig liver, with special reference to the occurrence of a canalicular system and "pored domes" in the endothelium. *Arch Histol Jpn*. 1984;47(4):359-76.
321. Ohtaki Y, Shimauchi H, Yokochi T, Takada H, Endo Y. In vivo platelet response to lipopolysaccharide in mice: Proposed method for evaluating new antiplatelet drugs. *Thrombosis research*. 2003;108:303-9.
322. Øie CI, Appa RS, Hilden I, Petersen HH, Gruhler A, Smedsrod B, et al. Rat liver sinusoidal endothelial cells (LSECs) express functional low density lipoprotein receptor-related protein-1 (LRP-1). *J Hepatol*. 2011;55(6):1346-52.
323. Øie CI, Mönkemöller V, Hübner W, Schüttpelz M, Mao H, Ahluwalia BS, et al. New ways of looking at very small holes – using optical nanoscopy to visualize liver sinusoidal endothelial cell fenestrations. *Nanophotonics*. 2018;7(3):575-96.
324. Øie CI, Wolfson DL, Yasunori T, Dumitriu G, Sorensen KK, McCourt PA, et al. Liver sinusoidal endothelial cells contribute to the uptake and degradation of entero bacterial viruses. *Sci Rep*. 2020;10(1):898.
325. Ono C, Yamada M, Tanaka M. Absorption, distribution and excretion of ¹⁴C-chloroquine after single oral administration in albino and pigmented rats: binding characteristics of chloroquine-related radioactivity to melanin in-vivo. *J Pharm Pharmacol*. 2003;55(12):1647-54.
326. Orru M, Guitart X, Karcz-Kubicha M, Solinas M, Justinova Z, Barodia SK, et al. Psychostimulant pharmacological profile of paraxanthine, the main metabolite of caffeine in humans. *Neuropharmacology*. 2013;67:476-84.
327. Oteiza A, Li R, McCuskey RS, Smedsrod B, Sorensen KK. Effects of oxidized low-density lipoproteins on the hepatic microvasculature. *Am J Physiol Gastrointest Liver Physiol*. 2011;301(4):G684-93.
328. Ottnad E, Via DP, Frubis J, Sinn H, Friedrich E, Ziegler R, et al. Differentiation of binding sites on reconstituted hepatic scavenger receptors using oxidized low-density lipoprotein. *Biochem J*. 1992;281 (Pt 3):745-51.
329. Ovesny M, Krizek P, Borkovec J, Svindrych Z, Hagen GM. ThunderSTORM: a comprehensive ImageJ plug-in for PALM and STORM data analysis and super-resolution imaging. *Bioinformatics*. 2014;30(16):2389-90.
330. Paigen B, Holmes PA, Mitchell D, Albee D. Comparison of atherosclerotic lesions and HDL-lipid levels in male, female, and testosterone-treated female mice from strains C57BL/6, BALB/c, and C3H. *Atherosclerosis*. 1987;64(2-3):215-21.
331. Palinski W, Rosenfeld ME, Yla-Herttuala S, Gurtner GC, Socher SS, Butler SW, et al. Low density lipoprotein undergoes oxidative modification in vivo. *Proc Natl Acad Sci U S A*. 1989;86(4):1372-6.
332. Pandey E, Nour AS, Harris EN. Prominent Receptors of Liver Sinusoidal Endothelial Cells in Liver Homeostasis and Disease. *Front Physiol*. 2020;11:873.
333. Patterson G, Davidson M, Manley S, Lippincott-Schwartz J. Superresolution imaging using single-molecule localization. *Annu Rev Phys Chem*. 2010;61:345-67.
334. Paulus JM. Platelet size in man. *Blood*. 1975;46(3):321-36.
335. Pegg DE. Principles of cryopreservation. *Methods Mol Biol*. 2007;368:39-57.
336. Pencek RR, Battram D, Shearer J, James FD, Lacy DB, Jabbour K, et al. Portal vein caffeine infusion enhances net hepatic glucose uptake during a glucose load in conscious dogs. *J Nutr*. 2004;134(11):3042-6.

337. Pettenuzzo LF, Noschang C, von Pozzer Toigo E, Fachin A, Vendite D, Dalmaz C. Effects of chronic administration of caffeine and stress on feeding behavior of rats. *Physiol Behav.* 2008;95(3):295-301.
338. Pietrzak WS, Eppley BL. Platelet rich plasma: biology and new technology. *J Craniofac Surg.* 2005;16(6):1043-54.
339. Poisson J, Lemoine S, Boulanger C, Durand F, Moreau R, Valla D, et al. Liver sinusoidal endothelial cells: Physiology and role in liver diseases. *J Hepatol.* 2017;66(1):212-27.
340. Politz O, Gratchev A, McCourt PA, Schledzewski K, Guillot P, Johansson S, et al. Stabilin-1 and -2 constitute a novel family of fasciclin-like hyaluronan receptor homologues. *Biochem J.* 2002;362(Pt 1):155-64.
341. Porto ML, Lima LC, Pereira TM, Nogueira BV, Tonini CL, Campagnaro BP, et al. Mononuclear cell therapy attenuates atherosclerosis in apoE KO mice. *Lipids Health Dis.* 2011;10:155.
342. PrabhuDas MR, Baldwin CL, Bollyky PL, Bowdish DME, Drickamer K, Febbraio M, et al. A consensus definitive classification of scavenger receptors and their roles in health and disease. *J Immunol.* 2017;198(10):3775-89.
343. Prasad JM, Young PA, Strickland DK. High affinity binding of the receptor-associated protein D1D2 domains with the low density lipoprotein receptor-related protein (LRP1) involves bivalent complex formation: CRITICAL ROLES OF LYSINES 60 AND 191. *J Biol Chem.* 2016;291(35):18430-9.
344. Prevo R, Banerji S, Ni J, Jackson DG. Rapid plasma membrane-endosomal trafficking of the lymph node sinus and high endothelial venule scavenger receptor/homing receptor stabilin-1 (FEEL-1/CLEVER-1). *J Biol Chem.* 2004;279(50):52580-92.
345. Qiu Y, Liu S, Chen HT, Yu CH, Teng XD, Yao HT, et al. Upregulation of caveolin-1 and SR-B1 in mice with non-alcoholic fatty liver disease. *Hepatobiliary Pancreat Dis Int.* 2013;12(6):630-6.
346. Rader DJ, Daugherty A. Translating molecular discoveries into new therapies for atherosclerosis. *Nature.* 2008;451(7181):904-13.
347. Rail T. Central nervous system stimulants: The xanthines. The pharmacological basis of therapeutics. 1980:592-607.
348. Rajman I, Eacho PI, Chowienczyk PJ, Ritter JM. LDL particle size: an important drug target? *Br J Clin Pharmacol.* 1999;48(2):125-33.
349. Rappaport AM, Borowy ZJ, Loughheed WM, Lotto WN. Subdivision of hexagonal liver lobules into a structural and functional unit; role in hepatic physiology and pathology. *Anat Rec.* 1954;119(1):11-33.
350. Rasnik I, McKinney SA, Ha T. Nonblinking and long-lasting single-molecule fluorescence imaging. *Nat Methods.* 2006;3(11):891-3.
351. Rego EH, Shao L, Macklin JJ, Winoto L, Johansson GA, Kamps-Hughes N, et al. Nonlinear structured-illumination microscopy with a photoswitchable protein reveals cellular structures at 50-nm resolution. *Proc Natl Acad Sci U S A.* 2012;109(3):E135-43.
352. Resman BH, Blumenthal P, Jusko WJ. Breast milk distribution of theobromine from chocolate. *J Pediatr.* 1977;91(3):477-80.
353. Reynolds JEF, Martindale W. *Martindale : the extra pharmacopoeia.* London: Pharmaceutical P; 1993.
354. Ritsch A, Tancevski I, Schgoer W, Pfeifhofer C, Gander R, Eller P, et al. Molecular characterization of rabbit scavenger receptor class B types I and II: portal to central vein gradient of expression in the liver. *J Lipid Res.* 2004;45(2):214-22.

355. Robertson EJ. Embryo-derived stem cell lines. In: Robertson EJ, editor. Teratocarcinomas and embryonic stem cells: a practical approach. Oxford, UK: IRL Press; 1987. p. 71-112.
356. Rodrigues BP, Campagnaro BP, Balarini CM, Pereira TM, Meyrelles SS, Vasquez EC. Sildenafil ameliorates biomarkers of genotoxicity in an experimental model of spontaneous atherosclerosis. *Lipids Health Dis.* 2013;12:128.
357. Rohrer L, Freeman M, Kodama T, Penman M, Krieger M. Coiled-coil fibrous domains mediate ligand binding by macrophage scavenger receptor type II. *Nature.* 1990;343(6258):570-2.
358. Ross R. Atherosclerosis--an inflammatory disease. *N Engl J Med.* 1999;340(2):115-26.
359. Ross R. The pathogenesis of atherosclerosis: a perspective for the 1990s. *Nature.* 1993;362(6423):801-9.
360. Rowe DJF, Watson ID, Williams J, Berry DJ. The Clinical Use and Measurement of Theophylline. *Annals of Clinical Biochemistry.* 1988;25(1):4-26.
361. Rust MJ, Bates M, Zhuang X. Sub-diffraction-limit imaging by stochastic optical reconstruction microscopy (STORM). *Nat Methods.* 2006;3(10):793-5.
362. Sakano E, Fujita H. Comparative aspects on the fine structure of the teleost liver. *Okajimas Folia Anat Jpn.* 1982;58(4-6):501-20.
363. Salama Y, Lin SY, Dhahri D, Hattori K, Heissig B. The fibrinolytic factor tPA drives LRP1-mediated melanoma growth and metastasis. *Faseb J.* 2019;33(3):3465-80.
364. Sambu S. A Bayesian approach to optimizing cryopreservation protocols. *PeerJ.* 2015;3:e1039.
365. Sanderson J. *Understanding light microscopy*: John Wiley & Sons; 2019.
366. Savill J, Hogg N, Haslett C. Macrophage vitronectin receptor, CD36, and thrombospondin cooperate in recognition of neutrophils undergoing programmed cell death. *Chest.* 1991;99(3 Suppl):6S-7S.
367. Sawamura T, Kume N, Aoyama T, Moriwaki H, Hoshikawa H, Aiba Y, et al. An endothelial receptor for oxidized low-density lipoprotein. *Nature.* 1997;386(6620):73-7.
368. Sawynok J, Yaksh TL. Caffeine as an analgesic adjuvant: a review of pharmacology and mechanisms of action. *Pharmacol Rev.* 1993;45(1):43-85.
369. Schiffer CA, Aisner J, Dutcher JP. Platelet cryopreservation using dimethyl sulfoxide. *Ann N Y Acad Sci.* 1983;411:161-9.
370. Schledzewski K, Geraud C, Arnold B, Wang S, Grone HJ, Kempf T, et al. Deficiency of liver sinusoidal scavenger receptors stabilin-1 and -2 in mice causes glomerulofibrotic nephropathy via impaired hepatic clearance of noxious blood factors. *J Clin Invest.* 2011;121(2):703-14.
371. Schmidt T, Schutz GJ, Baumgartner W, Gruber HJ, Schindler H. Imaging of single molecule diffusion. *Proc Natl Acad Sci U S A.* 1996;93(7):2926-9.
372. Schreyer SA, Wilson DL, LeBoeuf RC. C57BL/6 mice fed high fat diets as models for diabetes-accelerated atherosclerosis. *Atherosclerosis.* 1998;136(1):17-24.
373. Schultze-Werninghaus G, Meier-Sydow J. The clinical and pharmacological history of theophylline: first report on the bronchospasmolytic action in man by S. R. Hirsch in Frankfurt (Main) 1922. *Clin Allergy.* 1982;12(2):211-5.
374. Schvartz T, Aloush N, Goliand I, Segal I, Nachmias D, Arbely E, et al. Direct fluorescent-dye labeling of alpha-tubulin in mammalian cells for live cell and superresolution imaging. *Mol Biol Cell.* 2017;28(21):2747-56.
375. Schwartz CJ, Valente AJ, Sprague EA, Kelley JL, Nerem RM. The pathogenesis of atherosclerosis: an overview. *Clin Cardiol.* 1991;14(2 Suppl 1):11-16.

376. Semple JW, Italiano JE, Jr., Freedman J. Platelets and the immune continuum. *Nat Rev Immunol.* 2011;11(4):264-74.
377. Seternes T, Sorensen K, Smedsrod B. Scavenger endothelial cells of vertebrates: a nonperipheral leukocyte system for high-capacity elimination of waste macromolecules. *Proc Natl Acad Sci U S A.* 2002;99(11):7594-7.
378. Shetty S, Lalor PF, Adams DH. Liver sinusoidal endothelial cells - gatekeepers of hepatic immunity. *Nat Rev Gastroenterol Hepatol.* 2018;15(9):555-67.
379. Shim SG, Jun DW, Kim EK, Saeed WK, Lee KN, Lee HL, et al. Caffeine attenuates liver fibrosis via defective adhesion of hepatic stellate cells in cirrhotic model. *J Gastroenterol Hepatol.* 2013;28(12):1877-84.
380. Shively CA, Tarka SM, Jr. Methylxanthine composition and consumption patterns of cocoa and chocolate products. *Prog Clin Biol Res.* 1984;158:149-78.
381. Silva BR, Pernomian L, Bendhack LM. Contribution of oxidative stress to endothelial dysfunction in hypertension. *Front Physiol.* 2012;3:441.
382. Simionescu M, Simionescu N. Proatherosclerotic events: pathobiochemical changes occurring in the arterial wall before monocyte migration. *Faseb J.* 1993;7(14):1359-66.
383. Simon-Santamaria J, Rinaldo CH, Kardas P, Li R, Malovic I, Elvevold K, et al. Efficient uptake of blood-borne BK and JC polyomavirus-like particles in endothelial cells of liver sinusoids and renal vasa recta. *Plos One.* 2014;9(11):e111762.
384. Skogh T, Blomhoff R, Eskild W, Berg T. Hepatic uptake of circulating IgG immune complexes. *Immunology.* 1985;55(4):585-94.
385. Sleyster EC, Knook DL. Relation between localization and function of rat liver Kupffer cells. *Lab Invest.* 1982;47(5):484-90.
386. Smedsrod B. Clearance function of scavenger endothelial cells. *Comp Hepatol.* 2004;3 Suppl 1:S22.
387. Smedsrød B, Malmgren M, Ericsson J, Laurent TC. Morphological studies on endocytosis of chondroitin sulphate proteoglycan by rat liver endothelial cells. *Cell Tissue Res.* 1988;253(1):39-45.
388. Smedsrød B, Melkko J, Araki N, Sano H, Horiuchi S. Advanced glycation end products are eliminated by scavenger-receptor-mediated endocytosis in hepatic sinusoidal Kupffer and endothelial cells. *Biochem J.* 1997;322 (Pt 2):567-73.
389. Smedsrod B, Pertoft H, Eggertsen G, Sundstrom C. Functional and morphological characterization of cultures of Kupffer cells and liver endothelial cells prepared by means of density separation in Percoll, and selective substrate adherence. *Cell Tissue Res.* 1985;241(3):639-49.
390. Smedsrød B, Pertoft H, Eriksson S, Fraser JR, Laurent TC. Studies in vitro on the uptake and degradation of sodium hyaluronate in rat liver endothelial cells. *Biochem J.* 1984;223(3):617-26.
391. Smedsrød B, Pertoft H, Gustafson S, Laurent TC. Scavenger functions of the liver endothelial cell. *Biochem J.* 1990;266(2):313-27.
392. Smedsrød B, S. E, Fraser JRE, Laurent TC, Pertoft H. Properties of liver endothelial cells in primary monolayer cultures. In: Knook DL, Wisse E, editors. *Sinusoidal Liver Cells.* Amsterdam: Elsevier Biomedical Press; 1982. p. 263-70.
393. Sommer C, Straehle C, Kothe U, Hamprecht FA. Ilastik: Interactive Learning and Segmentation Toolkit. 2011 8th Ieee International Symposium on Biomedical Imaging: From Nano to Macro. 2011:230-3.
394. Sorensen KK, McCourt P, Berg T, Crossley C, Le Couteur D, Wake K, et al. The scavenger endothelial cell: a new player in homeostasis and immunity. *Am J Physiol Regul Integr Comp Physiol.* 2012;303(12):R1217-30.

395. Sorensen KK, Simon-Santamaria J, McCuskey RS, Smedsrod B. Liver Sinusoidal Endothelial Cells. *Compr Physiol*. 2015;5(4):1751-74.
396. Stahl P, Schlesinger PH, Rodman JS, Doebber T. Recognition of lysosomal glycosidases in vivo inhibited by modified glycoproteins. *Nature*. 1976;264(5581):86-8.
397. Stahl PD, Ezekowitz RA. The mannose receptor is a pattern recognition receptor involved in host defense. *Curr Opin Immunol*. 1998;10(1):50-5.
398. Stavric B. Methylxanthines: toxicity to humans. 1. Theophylline. *Food Chem Toxicol*. 1988;26(6):541-65.
399. Stavric B. Methylxanthines: toxicity to humans. 2. Caffeine. *Food Chem Toxicol*. 1988;26(7):645-62.
400. Stavric B. Methylxanthines: toxicity to humans. 3. Theobromine, paraxanthine and the combined effects of methylxanthines. *Food Chem Toxicol*. 1988;26(8):725-33.
401. Steffan AM, Gendrault JL, Kirn A. Increase in the number of fenestrae in mouse endothelial liver cells by altering the cytoskeleton with cytochalasin B. *Hepatology*. 1987;7(6):1230-8.
402. Steinberg D. Low density lipoprotein oxidation and its pathobiological significance. *J Biol Chem*. 1997;272(34):20963-6.
403. Steinberg D. The LDL modification hypothesis of atherogenesis: an update. *J Lipid Res*. 2009;50 Suppl:S376-81.
404. Steinberg D, Parthasarathy S, Carew TE, Khoo JC, Witztum JL. Beyond cholesterol. Modifications of low-density lipoprotein that increase its atherogenicity. *N Engl J Med*. 1989;320(14):915-24.
405. Steinbrecher UP, Witztum JL, Parthasarathy S, Steinberg D. Decrease in reactive amino groups during oxidation or endothelial cell modification of LDL. Correlation with changes in receptor-mediated catabolism. *Arteriosclerosis*. 1987;7(2):135-43.
406. Strauss O, Phillips A, Ruggiero K, Bartlett A, Dunbar PR. Immunofluorescence identifies distinct subsets of endothelial cells in the human liver. *Sci Rep*. 2017;7:44356.
407. Supinski GS, Deal EC, Jr., Kelsen SG. The effects of caffeine and theophylline on diaphragm contractility. *Am Rev Respir Dis*. 1984;130(3):429-33.
408. Suzuki H, Kurihara Y, Takeya M, Kamada N, Kataoka M, Jishage K, et al. A role for macrophage scavenger receptors in atherosclerosis and susceptibility to infection. *Nature*. 1997;386(6622):292-6.
409. Svistounov D, Oteiza A, Zykova SN, Sorensen KK, McCourt P, McLachlan AJ, et al. Hepatic disposal of advanced glycation end products during maturation and aging. *Exp Gerontol*. 2013;48(6):549-56.
410. Svistounov D, Warren A, McNerney GP, Owen DM, Zencak D, Zykova SN, et al. The Relationship between fenestrations, sieve plates and rafts in liver sinusoidal endothelial cells. *Plos One*. 2012;7(9):e46134.
411. Swarbrick J. Clarke's isolation and identification of drugs. *Journal of Pharmaceutical Sciences*. 1987;76(5):420-1.
412. Takamatsu H, Rubinsky B. Viability of deformed cells. *Cryobiology*. 1999;39(3):243-51.
413. Talle MA, Rao PE, Westberg E, Allegar N, Makowski M, Mittler RS, et al. Patterns of antigenic expression on human monocytes as defined by monoclonal antibodies. *Cell Immunol*. 1983;78(1):83-99.
414. Tandon NN, Lipsky RH, Burgess WH, Jamieson GA. Isolation and characterization of platelet glycoprotein IV (CD36). *J Biol Chem*. 1989;264(13):7570-5.
415. Tang WH, Zhuang XJ, Ma LL, Hong K, Zhao LM, Liu DF, et al. Effect of sildenafil on erectile dysfunction and improvement in the quality of sexual life in China: a multi-center study. *Int J Clin Exp Med*. 2015;8(7):11539-43.

416. Tanigawa H, Miura S, Zhang B, Uehara Y, Matsuo Y, Fujino M, et al. Low-density lipoprotein oxidized to various degrees activates ERK1/2 through Lox-1. *Atherosclerosis*. 2006;188(2):245-50.
417. Tanuma Y, Ito T. Electron microscope study on the hepatic sinusoidal wall and fat-storing cells in the bat. *Arch Histol Jpn*. 1978;41(1):1-39.
418. Tanuma Y, Ito T. Electron microscopic study on the sinusoidal wall of the liver of the crucian, *Carassius carassius*, with special remarks on the fat-storing cell (FSC). *Arch Histol Jpn*. 1980;43(3):241-63.
419. Tanuma Y, Ohata M, Ito T. An electron microscopic study of the kitten liver with special reference to fat-storing cells. *Arch Histol Jpn*. 1981;44(1):23-49.
420. Tanuma Y, Ohata M, Ito T. Electron microscopic study on the sinusoidal wall of the liver in the flatfish, *Kareius bicoloratus*: demonstration of numerous desmosomes along the sinusoidal wall. *Arch Histol Jpn*. 1982;45(5):453-71.
421. Taylor ME, Bezouska K, Drickamer K. Contribution to ligand binding by multiple carbohydrate-recognition domains in the macrophage mannose receptor. *J Biol Chem*. 1992;267(3):1719-26.
422. Terrett NK, Bell AS, Brown D, Ellis P. Sildenafil (VIAGRAM), a potent and selective inhibitor of type 5 cGMP phosphodiesterase with utility for the treatment of male erectile dysfunction. *Bioorg Med Chem Lett*. 1996;6(15):1819-24.
423. Thompson RE, Larson DR, Webb WW. Precise nanometer localization analysis for individual fluorescent probes. *Biophys J*. 2002;82(5):2775-83.
424. Thomson JA, Itskovitz-Eldor J, Shapiro SS, Waknitz MA, Swiergiel JJ, Marshall VS, et al. Embryonic stem cell lines derived from human blastocysts. *Science*. 1998;282(5391):1145-7.
425. Tomikawa M, Hashizume M, Highashi H, Ohta M, Sugimachi K. The role of the spleen, platelets, and plasma hepatocyte growth factor activity on hepatic regeneration in rats. *J Am Coll Surg*. 1996;182(1):12-6.
426. Tonini CL, Campagnaro BP, Louro LP, Pereira TM, Vasquez EC, Meyrelles SS. Effects of aging and hypercholesterolemia on oxidative stress and DNA damage in bone marrow mononuclear cells in apolipoprotein E-deficient mice. *Int J Mol Sci*. 2013;14(2):3325-42.
427. Tsukada H, Sawada N, Mitaka T, Gotoh M. Effects of liver-tumor promoters on phalloidin sensitivity of rat hepatocytes. *Carcinogenesis*. 1986;7(2):335-7.
428. Umemura T, Ueda K, Nishioka K, Hidaka T, Takemoto H, Nakamura S, et al. Effects of acute administration of caffeine on vascular function. *Am J Cardiol*. 2006;98(11):1538-41.
429. Van Berkel TJ, De Rijke YB, Kruijt JK. Different fate in vivo of oxidatively modified low density lipoprotein and acetylated low density lipoprotein in rats. Recognition by various scavenger receptors on Kupffer and endothelial liver cells. *J Biol Chem*. 1991;266(4):2282-9.
430. Van Berkel TJ, Van Velzen A, Kruijt JK, Suzuki H, Kodama T. Uptake and catabolism of modified LDL in scavenger-receptor class A type I/II knock-out mice. *Biochem J*. 1998;331 (Pt 1):29-35.
431. Van de Linde S, Heilemann M, Sauer M. Live-cell super-resolution imaging with synthetic fluorophores. *Annu Rev Phys Chem*. 2012;63:519-40.
432. Van de Linde S, Loschberger A, Klein T, Heidbreder M, Wolter S, Heilemann M, et al. Direct stochastic optical reconstruction microscopy with standard fluorescent probes. *Nat Protoc*. 2011;6(7):991-1009.
433. Van de Linde S, Sauer M. How to switch a fluorophore: from undesired blinking to controlled photoswitching. *Chem Soc Rev*. 2014;43(4):1076-87.

434. Van den Bogaard B, Draijer R, Westerhof BE, van den Meiracker AH, van Montfrans GA, van den Born BJ. Effects on peripheral and central blood pressure of cocoa with natural or high-dose theobromine: a randomized, double-blind crossover trial. *Hypertension*. 2010;56(5):839-46.
435. Van der Sluijs P, Bootsma HP, Postema B, Moolenaar F, Meijer DK. Drug targeting to the liver with lactosylated albumins: does the glycoprotein target the drug or is the drug targeting the glycoprotein? *Hepatology*. 1986;6(4):723-8.
436. Vandenberghe JG. Use of house mice in biomedical research. *ILAR Journal*. 2000;41(3):133-5.
437. Vangindertael J, Camacho R, Sempels W, Mizuno H, Dedecker P, Janssen KPF. An introduction to optical super-resolution microscopy for the adventurous biologist. *Methods Appl Fluoresc*. 2018;6(2):022003.
438. Varban ML, Rinninger F, Wang N, Fairchild-Huntress V, Dunmore JH, Fang Q, et al. Targeted mutation reveals a central role for SR-BI in hepatic selective uptake of high density lipoprotein cholesterol. *Proc Natl Acad Sci U S A*. 1998;95(8):4619-24.
439. Vasquez EC, Peotta VA, Meyrelles SS. Cardiovascular autonomic imbalance and baroreflex dysfunction in the apolipoprotein E-deficient mouse. *Cell Physiol Biochem*. 2012;29(5-6):635-46.
440. Vidal-Vanaclocha F, Alonso-Varona A, Ayala R, Barbera-Guillem E. Functional variations in liver tissue during the implantation process of metastatic tumour cells. *Virchows Arch A Pathol Anat Histopathol*. 1990;416(3):189-95.
441. Vidal-Vanaclocha F, Barbera-Guillem E. Fenestration patterns in endothelial cells of rat liver sinusoids. *J Ultrastruct Res*. 1985;90(2):115-23.
442. Vincenzi F, Targa M, Romagnoli R, Merighi S, Gessi S, Baraldi PG, et al. TRR469, a potent A(1) adenosine receptor allosteric modulator, exhibits anti-nociceptive properties in acute and neuropathic pain models in mice. *Neuropharmacology*. 2014;81:6-14.
443. Vogelsang J, Kasper R, Steinhauer C, Person B, Heilemann M, Sauer M, et al. A reducing and oxidizing system minimizes photobleaching and blinking of fluorescent dyes. *Angew Chem Int Ed Engl*. 2008;47(29):5465-9.
444. Vogelsang J, Steinhauer C, Forthmann C, Stein IH, Person-Skegro B, Cordes T, et al. Make them blink: probes for super-resolution microscopy. *Chemphyschem*. 2010;11(12):2475-90.
445. Von Hundelshausen P, Weber C. Platelets as immune cells: bridging inflammation and cardiovascular disease. *Circ Res*. 2007;100(1):27-40.
446. Voyta JC, Via DP, Butterfield CE, Zetter BR. Identification and isolation of endothelial cells based on their increased uptake of acetylated-low density lipoprotein. *J Cell Biol*. 1984;99(6):2034-40.
447. Wack KE, Ross MA, Zegarra V, Sysko LR, Watkins SC, Stolz DB. Sinusoidal ultrastructure evaluated during the revascularization of regenerating rat liver. *Hepatology*. 2001;33(2):363-78.
448. Wake K. Perisinusoidal stellate cells (fat-storing cells, interstitial cells, lipocytes), their related structure in and around the liver sinusoids, and vitamin A-storing cells in extrahepatic organs. *Int Rev Cytol*. 1980;66:303-53.
449. Walker BA, Rocchini C, Boone RH, Ip S, Jacobson MA. Adenosine A2a receptor activation delays apoptosis in human neutrophils. *J Immunol*. 1997;158(6):2926-31.
450. Walker DK, Ackland MJ, James GC, Muirhead GJ, Rance DJ, Wastall P, et al. Pharmacokinetics and metabolism of sildenafil in mouse, rat, rabbit, dog and man. *Xenobiotica*. 1999;29(3):297-310.

451. Warren A, Bertolino P, Cogger VC, McLean AJ, Fraser R, Le Couteur DG. Hepatic pseudocapillarization in aged mice. *Exp Gerontol*. 2005;40(10):807-12.
452. Warren A, Chaberek S, Ostrowski K, Cogger VC, Hilmer SN, McCuskey RS, et al. Effects of old age on vascular complexity and dispersion of the hepatic sinusoidal network. *Microcirculation*. 2008;15(3):191-202.
453. Watson AD, Leitinger N, Navab M, Faull KF, Horkko S, Witztum JL, et al. Structural identification by mass spectrometry of oxidized phospholipids in minimally oxidized low density lipoprotein that induce monocyte/endothelial interactions and evidence for their presence in vivo. *J Biol Chem*. 1997;272(21):13597-607.
454. Webb NR, Connell PM, Graf GA, Smart EJ, de Villiers WJ, de Beer FC, et al. SR-BII, an isoform of the scavenger receptor BI containing an alternate cytoplasmic tail, mediates lipid transfer between high density lipoprotein and cells. *J Biol Chem*. 1998;273(24):15241-8.
455. Wilkinson K, El Khoury J. Microglial scavenger receptors and their roles in the pathogenesis of Alzheimer's disease. *Int J Alzheimers Dis*. 2012;2012:489456.
456. Willnow TE, Nykjaer A, Herz J. Lipoprotein receptors: new roles for ancient proteins. *Nat Cell Biol*. 1999;1(6):E157-62.
457. Wisse E. An ultrastructural characterization of the endothelial cell in the rat liver sinusoid under normal and various experimental conditions, as a contribution to the distinction between endothelial and Kupffer cells. *J Ultrastruct Res*. 1972;38(5):528-62.
458. Wisse E. Ultrastructure and function of Kupffer cells and other sinusoidal cells in the liver. *Med Chir Dig*. 1977;6(7):409-18.
459. Wisse E. Kupffer cell reactions in rat liver under various conditions as observed in the electron microscope. *J Ultrastruct Res*. 1974;46(3):499-520.
460. Wisse E. An electron microscopic study of the fenestrated endothelial lining of rat liver sinusoids. *J Ultrastruct Res*. 1970;31(1):125-50.
461. Wisse E, Braet F, Duimel H, Vreuls C, Koek G, Olde Damink SW, et al. Fixation methods for electron microscopy of human and other liver. *World J Gastroenterol*. 2010;16(23):2851-66.
462. Wisse E, De Zanger RB, Charels K, Van Der Smissen P, McCuskey RS. The liver sieve: considerations concerning the structure and function of endothelial fenestrae, the sinusoidal wall and the space of Disse. *Hepatology*. 1985;5(4):683-92.
463. Wisse E, De Zanger RB, Jacobs R, McCuskey RS. Scanning electron microscope observations on the structure of portal veins, sinusoids and central veins in rat liver. *Scan Electron Microsc*. 1983(Pt 3):1441-52.
464. Wisse E, van't Noordende JM, van der Meulen J, Daems WT. The pit cell: description of a new type of cell occurring in rat liver sinusoids and peripheral blood. *Cell Tissue Res*. 1976;173(4):423-35.
465. Witztum JL, Steinberg D. Role of oxidized low density lipoprotein in atherogenesis. *J Clin Invest*. 1991;88(6):1785-92.
466. Wolfhagen FH, Vermeulen HG, de Man RA, Lesterhuis W. Initially obscure hepatotoxicity attributed to sildenafil. *Eur J Gastroenterol Hepatol*. 2008;20(7):710-2.
467. Wright P, Smith K, Day W, Fraser R. Small liver fenestrae may explain the susceptibility of rabbits to atherosclerosis. *Arteriosclerosis: An Official Journal of the American Heart Association, Inc*. 1983;3(4):344-8.
468. Wright PL, Smith KF, Day WA, Fraser R. Hepatic sinusoidal endothelium in sheep: an ultrastructural reinvestigation. *Anat Rec*. 1983;206(4):385-90.
469. Xie G, Wang L, Wang X, Wang L, DeLeve LD. Isolation of periportal, midlobular, and centrilobular rat liver sinusoidal endothelial cells enables study of zoned drug toxicity. *Am J Physiol Gastrointest Liver Physiol*. 2010;299(5):G1204-10.

470. Xiu-Qin W, Sonoda Y, Sasaki K. Scanning and transmission electron microscopic studies on sinusoidal endothelium in the embryonic, neonatal and adult mouse liver. *Kawasaki medical journal*. 1998;24(2):69-77.
471. Xu X, Zhu F, Zhang M, Zeng D, Luo D, Liu G, et al. Stromal cell-derived factor-1 enhances wound healing through recruiting bone marrow-derived mesenchymal stem cells to the wound area and promoting neovascularization. *Cells Tissues Organs*. 2013;197(2):103-13.
472. Yamanaka M, Smith NI, Fujita K. Introduction to super-resolution microscopy. *Microscopy (Oxf)*. 2014;63(3):177-92.
473. Yang PF, Hua TC, Tsung HC, Cheng QK, Cao YL. Effective cryopreservation of human embryonic stem cells by programmed freezing. *Conf Proc IEEE Eng Med Biol Soc*. 2005;2006:482-5.
474. Yardimci S, Bostanci EB, Ozer I, Dalgic T, Surmelioglu A, Aydog G, et al. Sildenafil accelerates liver regeneration after partial hepatectomy in rats. *Transplant Proc*. 2012;44(6):1747-50.
475. Yaseen H, Darwich M, Hamdy H. Is sildenafil an effective therapy in the management of persistent pulmonary hypertension? *J Clin Neonatol*. 2012;1(4):171-5.
476. Yasui K, Agematsu K, Shinozaki K, Hokibara S, Nagumo H, Yamada S, et al. Effects of theophylline on human eosinophil functions: comparative study with neutrophil functions. *J Leukoc Biol*. 2000;68(2):194-200.
477. Yasui K, Hu B, Nakazawa T, Agematsu K, Komiyama A. Theophylline accelerates human granulocyte apoptosis not via phosphodiesterase inhibition. *J Clin Invest*. 1997;100(7):1677-84.
478. Yildiz A, Forkey JN, McKinney SA, Ha T, Goldman YE, Selvin PR. Myosin V walks hand-over-hand: single fluorophore imaging with 1.5-nm localization. *Science*. 2003;300(5628):2061-5.
479. Yla-Herttuala S, Palinski W, Rosenfeld ME, Parthasarathy S, Carew TE, Butler S, et al. Evidence for the presence of oxidatively modified low density lipoprotein in atherosclerotic lesions of rabbit and man. *J Clin Invest*. 1989;84(4):1086-95.
480. Yoshida H, Kondratenko N, Green S, Steinberg D, Quehenberger O. Identification of the lectin-like receptor for oxidized low-density lipoprotein in human macrophages and its potential role as a scavenger receptor. *Biochem J*. 1998;334 (Pt 1):9-13.
481. Yoshida M, Nishikawa Y, Omori Y, Yoshioka T, Tokairin T, McCourt P, et al. Involvement of signaling of VEGF and TGF-beta in differentiation of sinusoidal endothelial cells during culture of fetal rat liver cells. *Cell Tissue Res*. 2007;329(2):273-82.
482. Yoshimoto R, Fujita Y, Kakino A, Iwamoto S, Takaya T, Sawamura T. The discovery of LOX-1, its ligands and clinical significance. *Cardiovasc Drugs Ther*. 2011;25(5):379-91.
483. Young IS, McEneny J. Lipoprotein oxidation and atherosclerosis. *Biochem Soc Trans*. 2001;29(Pt 2):358-62.
484. Yu KC, Cooper AD. Postprandial lipoproteins and atherosclerosis. *Front Biosci*. 2001;6:D332-54.

Paper I





Research article

Hong Mao^{a,*}, Robin Diekmann^a, Hai Po H. Liang, Victoria C. Cogger, David G. Le Couteur, Glen P. Lockwood, Nicholas J. Hunt, Mark Schüttpelz, Thomas R. Huser, Vivien M. Chen and Peter A.G. McCourt

Cost-efficient nanoscopy reveals nanoscale architecture of liver cells and platelets

<https://doi.org/10.1515/nanoph-2019-0066>

Received February 28, 2019; revised June 10, 2019; accepted June 11, 2019

Abstract: Single-molecule localization microscopy (SMLM) provides a powerful toolkit to specifically resolve intracellular structures on the nanometer scale, even approaching resolution classically reserved for electron microscopy (EM). Although instruments for SMLM are technically simple to implement, researchers tend to stick to commercial microscopes for SMLM implementations. Here we report the construction and use of a “custom-built” multi-color channel SMLM system to study liver sinusoidal endothelial cells (LSECs) and platelets, which costs significantly less than a commercial system.

^a**Hong Mao and Robin Diekmann:** These authors contributed equally to this work.

***Corresponding author: Hong Mao,** Faculty of Health Sciences, Department of Medical Biology, University of Tromsø-The Arctic University of Norway, Hansine Hansens veg 18, Tromsø 9037, Norway, e-mail: hong.mao@uit.no, marcomao1018@gmail.com. <https://orcid.org/0000-0003-4266-3550>

Robin Diekmann: EMBL Heidelberg, Cell Biology and Biophysics Unit, 69117 Heidelberg, Germany. <https://orcid.org/0000-0002-5290-9123>

Hai Po H. Liang: ANZAC Research Institute, Concord Repatriation General Hospital, Concord, NSW, Australia

Victoria C. Cogger, David G. Le Couteur, Glen P. Lockwood and Nicholas J. Hunt: ANZAC Research Institute, Concord Repatriation General Hospital, Concord, NSW, Australia; and The University of Sydney, Charles Perkins Centre, Nutritional Ecology and Physiology Lab, Sydney, NSW, Australia

Mark Schüttpelz: Department of Physics, Bielefeld University, 33615 Bielefeld, Germany

Thomas R. Huser: Department of Physics, Bielefeld University, 33615 Bielefeld, Germany; and Department of Internal Medicine and NSF Center for Biophotonics, University of California, Davis, Sacramento, CA 95817, USA

Vivien M. Chen: ANZAC Research Institute, Concord Repatriation General Hospital, Concord, NSW, Australia; and Department of Haematology, University of Sydney, Concord, NSW, Australia

Peter A.G. McCourt: Department of Medical Biology, University of Tromsø-The Arctic University of Norway, 9037 Tromsø, Norway

This microscope allows the introduction of highly affordable and low-maintenance SMLM hardware and methods to laboratories that, for example, lack access to core facilities housing high-end commercial microscopes for SMLM and EM. Using our custom-built microscope and freely available software from image acquisition to analysis, we image LSECs and platelets with lateral resolution down to about 50 nm. Furthermore, we use this microscope to examine the effect of drugs and toxins on cellular morphology.

Keywords: liver; endothelium; optical nanoscopy; fenestration; platelet.

1 Introduction

The diffraction limit of visible light (~200 nm for blue wavelengths) prevents our use of conventional light microscopy to study a number of biological structures, such as fenestrations (cellular pores ≤ 200 nm that allow free passage of molecules through cells), mitochondrial ultrastructure, super-fine filopodia, the clustering of filamentous proteins, membrane channels, and many other structures. Previously, such structures were only visible through the use of electron microscopy (EM) on fixed and dehydrated samples, resulting in conclusions where their relevance to hydrated or possibly even living cells is often questionable. Such ultrastructures are of particular biological relevance for the liver and general physiology.

In the human liver, fenestrated liver sinusoidal endothelial cells (LSECs) are an abundant cell type with a total surface area matching that of a tennis court. The fenestrations, which are arranged in groups within “sieve plates,” act as plasma filters allowing the passage of nanoparticles, such as lipoproteins, as well as biomolecules and drugs from the plasma for processing by the surrounding hepatocytes [1, 2]. Products secreted by hepatocytes, such as albumin, need to pass through LSECs in the reverse direction to be released to the plasma. As we age, our

LSEC fenestrations become smaller and fewer during age-related defenestration/pseudo capillarization [3]. In addition, a number of compounds/toxins increase/decrease fenestration size or ablate them completely [4, 5]. LSECs also interact with circulating cells such as T-lymphocytes [6] and leukocytes [7], and LSEC fenestrations allow interactions between the villi of circulating T-lymphocytes and the underlying hepatocytes [6]. Platelets, on the other hand, have been proposed to improve liver fibrosis and accelerate liver regeneration [8, 9] via interactions with liver sinusoidal cells.

Platelet interactions with hepatocyte Ashwell-Morell receptors have been proposed as regulating hepatic thrombopoietin production [10]. For this to occur, these platelets would necessarily need to interact first with LSECs to reach the underlying hepatocytes. Indeed, Li et al. [11] proposed a model whereby platelets in liver sinusoids interact with hepatocyte microvilli penetrating LSEC fenestrations. The same authors proposed that Kupffer cells (liver sinusoidal resident macrophages) clear desialylated platelets bound to LSECs in this manner.

Multiple agents can affect LSECs and their fenestrations, for example, in sizes or numbers. Nicotinamide mononucleotide (NMN) is a metabolite crucial for the regulation of nicotinamide adenine dinucleotide (NAD⁺) biosynthesis through the NAD⁺ salvage pathway [12, 13]. Sildenafil is a medication used to remedy erectile dysfunction and pulmonary arterial hypertension [14]. A previous LSEC study showed increased frequency of fenestrations with NMN and sildenafil treatment, as well as an increased proportion of small fenestrations, suggesting the formation of new fenestrations [15].

Typically, fenestrations and microvilli are studied using methods such as transmission and scanning EM [16–18]. These methods are very powerful but require large and expensive equipment, and considerable technical expertise. In addition, while the morphological information from EM methods is exquisite, it is often challenging to identify proteins within the revealed structures using methods such as immune-EM. Therefore, to study primary LSECs and platelets below the optical diffraction limit, we have developed a low-cost and small, custom-built single-molecule localization microscopy (SMLM) [19–21] instrument capable of visualizing cellular structures simultaneously in two colors and down to about 50 nm resolution.

Multiple groups have developed approaches for cost-efficient super-resolution optical microscopy. Studies have either focused mainly on cost reduction associated with SMLM equipment [22–24], for example, by characterizing highly affordable cameras [25, 26], by using the complementary super-resolution modality super-resolution

optical fluctuation imaging [27], or by focusing on single particle tracking [28]. These developments have even included multi-color imaging using sophisticated temporal multiplexing techniques [24] or spectral unmixing [25]. Specific biological applications have mainly been limited to proof-of-concept studies, typically resolving the cytoskeleton or mitochondrial ultrastructure of cultured cells lines. In contrast, we present a cost-efficient setup for SMLM using two low-cost cameras that enable traditional dual-color imaging of spectrally distinct channels at 488 and 647 nm excitation. These channels allow the use of established protocols for sample preparation and a wide selection of fluorescent labels. We apply low-cost SMLM, in the form of direct stochastic optical reconstruction microscopy (dSTORM), to resolve the ultrastructure and the structural response of primary cells to specific treatments. The microscope achieves a good compromise of low cost and small size together with high mechanical stability, low maintenance, and reliable, long-term operation. We show the versatility of this setup by imaging the primary cell types LSECs and platelets with SMLM and the effects of agents/activation on their morphology. This SMLM setup is thus a tool for the cost-efficient super-resolution study of two cell types with a vital role in liver physiology and regeneration.

2 Materials and methods

2.1 Mouse and rat LSEC production

Sprague Dawley male rats and C57/B16 male mice (Animal Resource Centre, Murdoch, Western Australia) were kept under standard conditions and fed standard chow *ad libitum* (Glen Forrest, Western Australia). The experimental protocols were approved by the ethics committee of the Sydney Local Health District Animal Welfare Committee (Approval 2017/012A). All experiments were performed in accordance with relevant approved guidelines and regulations.

2.2 Cell culture protocols, fixation

Male rats (body weight 300–400 g) and mice (~20 g) were anesthetized with a mixture of 10 mg/kg xylazine (Bayer Health Care, CA, USA) and 100 mg/kg ketamine (Ketalar, Pfizer, New York, NY, USA) in saline, and LSECs were isolated and purified as described [29] and plated in serum-free RPMI-1640 (Sigma-Aldrich, Sydney, AU) at 0.2×10^6

cells/cm² on fibronectin-coated (Sigma-Aldrich, Sydney, AU) 16-well chambered #1.5 coverslips (Grace Bio-Labs CultureWell™ removable chambered coverglass, Sigma-Aldrich, Sydney, AU) for 3 h in RPMI-1640. LSECs were then fixed with 4% paraformaldehyde (ProSciTech, Pty Ltd, Thuringowa, AU) in phosphate buffered saline (PBS) and 0.02M sucrose (Sigma-Aldrich, Sydney, AU), pH 7.2, for 15 min, and stored under PBS. After fixation, the cells were prepared for visualization prior to applying on dSTORM [30].

2.3 Platelet preparation

Blood from healthy human donors (ethical approval: Concord RG Hospital Ethics Board no. HREC/15/CRGH/54) was collected from antecubital fossa via a 21G butterfly needle into 3.2% citrate-containing tubes (Becton Dickinson, Sydney, AU). Washed platelets were prepared from citrated blood as described [31]. Briefly, platelet-rich plasma was isolated by brake-free centrifugation for 10 min at 200×g and mixed gently by inversion in a 1:1 ratio with Tyrode's buffer (137 mM NaCl, 2.5 mM KCl, 0.5 mM MgCl₂, 12 mM NaHCO₃, 0.36 mM Na₂HPO₄, 10 mM HEPES, 5.5 mM glucose, and 0.25% human serum albumin, pH 7.5) containing 1 μM prostaglandin E1 (PGE₁), (Sigma-Aldrich, Sydney, AU). Platelets were then pelleted by brake-free centrifugation for 15 min at 650×g, washed once with Tyrode's buffer, and pelleted again, before resuspension in Tyrode's buffer to 1×10⁶ platelets per 100 μl. The platelets were allowed to rest for 20 min before further manipulation. The platelets were then plated in removable chambered coverglass wells (see above) in Tyrode's buffer. After platelet wash, 2 U/ml of thrombin (Sigma-Aldrich, Sydney, AU) was added for 10 min at room temperature (RT) to stimulate the platelets, followed by fixation as above.

2.4 Cell staining

All fixed samples were washed with PBS. For membrane staining, cells were stained with Vybrant DiD (1:200, ThermoFisher) for 20 min, or Cell Mask Green (1:1000, ThermoFisher) for 10 min at RT, or BODIPY FL C5-Ganglioside GM1(1:200, ThermoFisher) for 15 min at RT.

For cytoskeleton staining, cells were permeabilized for 90 s with 0.5% Triton-X100 and washed two to three times with PBS. Non-specific binding was blocked with 5% bovin serum albumin in PBS for 45 min at RT. Cells were incubated with the primary antibody (1:500, monoclonal

anti- α -tubulin, Sigma-Aldrich, Sydney, AU) for 1 h at RT, and then washed three times for 10 min with 0.1% PBS Tween-20. The secondary antibody (1:1000, Anti-mouse IgG, AlexaFluor 647 or 488 conjugate, CellSignaling, Arundel, AU) was applied for 1 h at RT. The staining solution was removed and the cells were then washed with 0.1% PBS Tween-20 (Sigma-Aldrich, Sydney, AU) (three times for 10 min) then PBS. Phalloidin AlexaFluor 488 (AF488) or AlexaFluor 647 (AF647) (1:40, ThermoFisher, Sydney, AU) was applied for 20 min at RT. Cells were washed with PBS.

All samples were mounted in imaging buffer (see imaging conditions and composition of buffers in Supplementary Tables 1 and 2, respectively). We used either OxEA [Oxyrase-based oxygen depletion supplemented with β -mercaptoethylamine (MEA), Sigma-Aldrich, Sydney, AU] buffer [32] [3% (v/v) Oxyfluor, Oxyrase Inc. Mansfield, 40.5 units/ml], GODCAT-1 (glucose oxidase and catalase-based oxygen depletion and hydrogen peroxide depletion) buffer [33] [50 μg/ml glucose oxidase (Sigma-Aldrich, Sydney, AU), 1 μg/ml (50 units) catalase (Sigma-Aldrich, Sydney, AU), 40 mg/ml glucose (Sigma-Aldrich, Sydney, AU), 1.25 mM KCl and 1 mM Tris] including 100 mM MEA, 2.5% glycerol (Sigma-Aldrich, Sydney, AU) and 200 μM Tris (2-carboxyethyl) phosphine hydrochloride (Sigma-Aldrich, Sydney, AU), or GODCAT-2 buffer (50 mM MEA, 0.5 mg/ml glucose oxidase, 40 mg/ml catalase). After the buffer was applied in the cell chamber, excess buffer was removed by sliding a coverslip onto the chamber to prevent oxygen permeation.

2.5 Imaging

Rat (Figures 1D, 3, 4) and mouse (Figures 1C, 5) LSECs were imaged on the custom-built dSTORM setup described below, using 488 and 647 nm lasers (Coherent, Santa Clara, CA, USA) and two CMOS cameras (IDS-Imaging Development Systems, Obersulm, DE). A 60×/NA=1.49 oil immersion total internal reflection fluorescence (TIRF) objective lens (Olympus, Center Valley, PA, US) or a 60×/NA=1.4 oil immersion objective lens (Olympus, Center Valley, PA, US) was used. For dual-color images, first the deep red channel (647 nm excitation) was imaged, followed by the green (488 nm excitation) channel. In general, 20,000 to 45,000 frames were collected at 50 to 100 fps with image sizes of 344×344 or 400×400 pixels for rat LSECs, and 144×144 or 200×200 pixels for platelets. CMOS cameras were controlled via Micro Manager [34], using a modified device adapter [26]. The lasers were controlled using the manufacturer's software.

2.6 Optical setup

Our custom-built wide-field dSTORM microscope uses two solid-state lasers of 488 and 647 nm wavelengths (Figure 1). The latter is fiber-coupled to allow for easy handling. After adjusting the beam diameters using a collimation lens and/or telescopes, the beams are overlaid via a dichroic mirror and focused onto the back focal plane of the objective lens for sample illumination. Mounting the relevant parts of the illumination unit on a translatable stage allows for easy switching between epi-fluorescence (epi), highly inclined and laminated optical sheet (HILO) [35], and TIRF [36] configuration. The

system has sufficient degrees of freedom such that both lasers can be optimally aligned to illuminate a sample mounted on an xy-stage. Focusing is performed manually by a precise z-translation stage holding objective lens. The fluorescence emission is separated from excitation by a dichroic mirror and the emission is further separated by emission wavelength using a second dichroic mirror. A detailed part list together with assembly and alignment instructions is supplied in the Supplementary material.

We placed a separate tube lens into every detection path behind the dichroic excitation beam splitter. In doing so, the collimated, but not focused, part of the

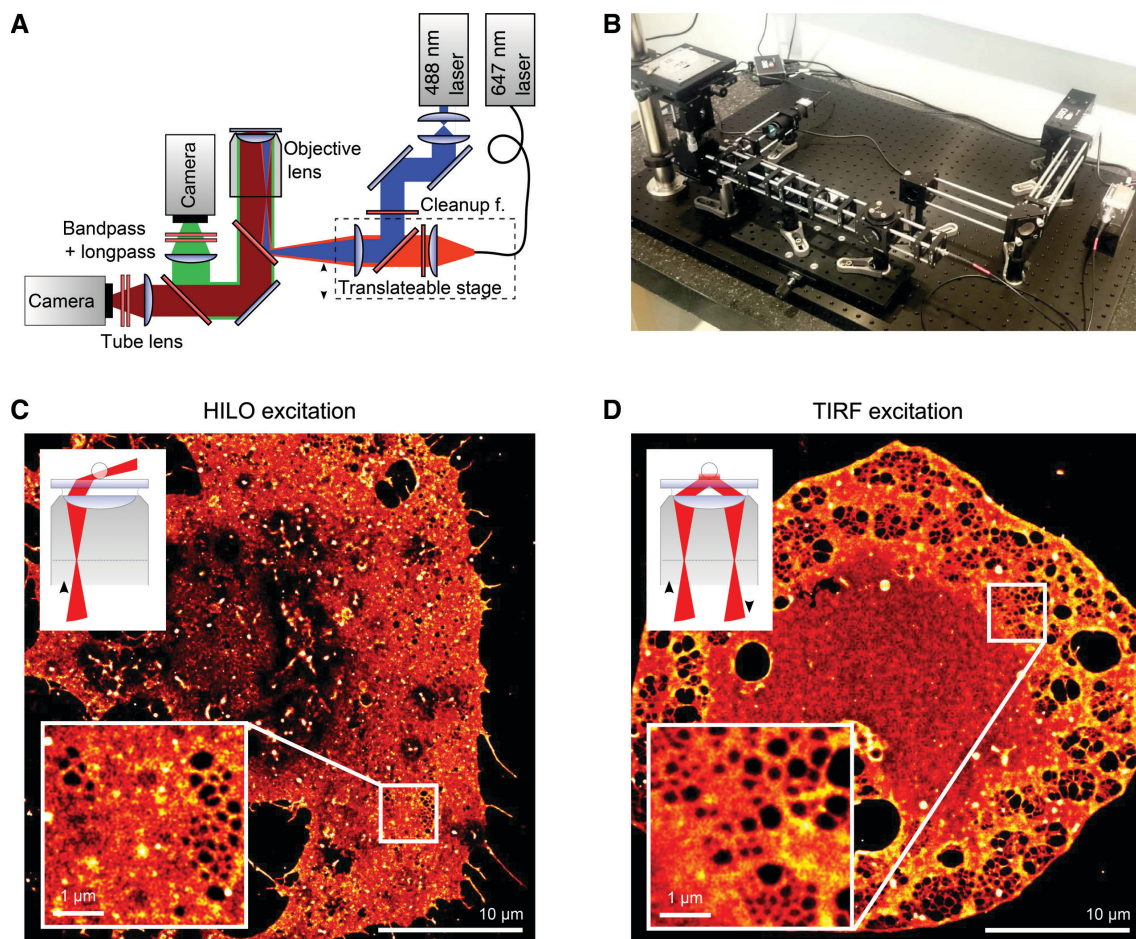


Figure 1: The cost-efficient dual-color dSTORM microscope.

Schematic (A) and photograph (B) of the microscope showing the free standing 488 nm and fiber pig-tailed 647 nm laser that are combined by a dichroic mirror. The lasers are focused to the back focal plane of the high NA objective lens, while a translatable stage allows for shifting the focus in the back focal plane and therefore to conveniently switch between epi, HILO (C), and TIRF (D) illumination. The fluorescence collected by the objective lens is separated from the excitation and spectrally split onto two CMOS cameras. (B) Mounting the optical components into a cage system results in high mechanical stability. Open space on the black breadboard shows that the 0.5 m² used could in principle have been reduced by a factor of about 2. However, this layout was chosen to provide the option of including further lasers of different wavelengths. dSTORM images of both (C) Vybrant DiD stained mouse LSECs using HILO illumination (inset) and (D) Vybrant DiD stained rat LSECs using TIRF illumination visualize sub-diffraction limit sized membrane fenestrations at high image quality. Insets in (C) and (D) show fenestrations within sieve plates in more detail.

beam is transmitted through the dichroic beam splitter. In contrast, using a single tube lens for both channels would require its placement before the dichroic beam splitter. Arimoto and Murray showed that a tilted glass plate can cause serious aberrations when transmitting a focused beam in a medium of a different refractive index [37]. This effect is avoided in our setup, where the dichroic beam splitter results in a minor lateral displacement of the beam, but does not lead to serious optical distortions.

Raw data were acquired using a dedicated industry-grade CMOS camera in each color channel. Multiple industry-grade CMOS cameras that feature sufficiently low noise and high sensitivity are available [22, 25]. We chose a camera model using the Sony IMX174 sensor (UI-3060CP Rev.2; IDS-Imaging Development Systems, Obersulm, DE), which we previously characterized extensively and found to perform close to a commonly applied scientific-grade camera, but at a fraction of the cost [26]. The quantum efficiency of the sensor is about 77% at 520 nm and about 45% at 676 nm [26]. The detector characterization was performed using multiple thousands of frames recorded at different light levels as described by Huang et al. [38] and Diekmann et al. [26]. Data for the cameras used in this study can be found in the Supplementary information of Diekmann et al. [26] (Supplementary Figures 2–4, CMOS 2 and CMOS 3). To provide an impression of the quality of the raw data we collected, we provide 500 frames each for the images shown in Figures 3A, E, 5H and 6A as Supplementary data.

2.7 Image reconstruction

The freely available software package Fiji [39] was used for image processing and analysis, including dSTORM reconstruction [40], registration of multi-color images (bUnwarpJ plugin [41]), super-resolution image analysis (SQUIRREL plugin [42]) particle size measurement, line profile measurements, application of look-up tables, cropping, and image export.

The projected pixel size was determined by a calibration sample and deviated less than 2% from the theoretical value of 109.9 nm. After finding the single-molecule positions with sub-pixel accuracy using the single emitter fitter of ThunderSTORM, post-processing with drift correction (ThunderSTORM, using the image cross-correlation algorithm, number of bins=3–7; magnification=5) was applied if necessary. Localization merging within subsequent frames and spatial proximity as well as filters based on the localization table was applied subsequently, if necessary. Other super-resolved

images were reconstructed using the free software rapidSTORM [43] (Figure 4A–F and H, I, K, L). In rapidSTORM, we used the same pixel size as ThunderSTORM. rapidSTORM is stand-alone software requiring the user to specify the workflow of the fitting and reconstruction algorithm by choosing certain modules. To do so, the “Count localizations,” “Display progress,” and “Cache localization” modules were added under the “dSTORM engine output” module to process the data and the “Expression filter” output module was added under the “Cache localization” module to allow for filtering based on the individual localization properties such as photon count. Furthermore, the “Localizations file” and “Image display” modules were displayed under the “Expression filter” module to have the data stored and the image displayed accordingly.

2.8 Fenestration and actin quantification

Fenestration detection and actin stress fiber detection were performed using the pixel classification workflow in the freely available machine learning image processing software Ilastik [44]. For the fenestration size analysis, the two classes of fenestrations and membranes were manually annotated and iteratively refined in a few locations for every cell, but the same classification was used for all cells. The automatically segmented fenestrations were then exported to Fiji [39]. The size was determined using Fiji’s “Analyze Particles” plugin with a circularity of 0.6–1.0. The resulting table was imported into MATLAB (Mathworks); the area was translated to the diameter of a corresponding circle of the same area and filtered for diameters ranging from 54 to 401 nm prior to binning. For the actin stress fiber analysis, the three classes of actin stress fibers, other actin fibers, and background were manually annotated and iteratively refined in a few locations for every cell, but the same classification was used for all cells. The segmentation was exported to Fiji and the area covered by the stress fibers and the entire actin network was determined from the segmentation.

3 Results

3.1 Schematic of the low-cost microscope for SMLM

Our custom-built microscope is shown in Figure 1A and B. A full list of all components, their suppliers/

catalogue numbers, cost, and detailed assembly instructions is provided in the Supplementary material. Fluorescence is excited with 488 and 647 nm lasers and the emission is split into two cameras for conventional dual-color imaging. The optical breadboard (Figure 1B) has sufficient “free real estate” to house more lasers and cameras if desired, and the dichroic filter used allows for the additional inclusion of, for example, 405 and 532 nm lasers.

3.2 Cost-saving features

We evaluated the use of available objective lenses from our obsolete microscope park to reduce costs even further. We anticipate that many biomedical laboratories face a similar situation, where spare, high-quality objective lenses (e.g. from obsolete confocal microscopes) are available. Directing the lasers via a translatable stage into our microscope (Figure 1A) allows the use of standard (i.e. non-TIRF) objectives for epi and HILO illumination. Using an oil-immersion $60\times/\text{NA}=1.40$ objective lens from an obsolete Olympus microscope, individual fenestrations of mouse LSECs were resolvable with dSTORM [30] (Figure 1C, inset). Due to diffraction-limited resolution, fenestrations sized below 200 nm cannot be visualized in conventional wide-field imaging with the same objective. For comparison, a TIRF lens on the same microscope can similarly be used to resolve individual fenestrations of rat LSECs (Figure 1D). Given that the $60\times$ TIRF objective we acquired specifically for this microscope costs €6350, using spare objectives instead would represent significant savings.

In many cases, SMLM microscopes are set up on vibration dampened optical tables. If these microscopes are not mechanically isolated, oscillations from the environment (e.g. air conditioning units, etc.) can easily exceed the spatial resolution this microscopy can achieve and thus attenuate the quality of the super-resolution images. To mechanically isolate our microscope, without the cost of a dampened optical table, we set the microscope up on an aluminum breadboard placed on an inflated bicycle inner tube at a relative pressure of 0.5 bar (Figure 2A). Inclusion of this inner tube significantly reduced vibrations, as shown by the repeated localization of the center of bright, fluorescent beads of 100 nm diameter (Tetraspeck; ThermoFisher) (Figure 2B). The achieved full-width-at-half-maximum (FWHM) values for the localization cloud from one bead of 7.9 nm correspond to an effective precision of about 3.3 nm. This precision is much better than what we achieved localizing

single molecules in dSTORM experiments (Figure 3); hence potential remaining vibrations are not a major resolution-limiting factor.

For further savings, we chose not to build the microscope around a costly conventional microscope body, but set up the microscope using almost exclusively off-the-shelf optics and optomechanical components. This provided us the flexibility to plan and build it such that high mechanical stability with very low lateral drift of less than 50 nm over more than 1 h was achieved (Figure 2C). Additional axial drift can lead to the loss of the focus over time. We tested multiple options for high mechanical stability without the need for costly active components (such as piezo actuators and position sensors) and found a z-translator that achieved almost perfect focal stability. Our 2D imaging experiments do not allow us to access the z-position directly, but the high focal stability is indicated by the median value of the point spread function FWHM remaining almost constant over more than 1 h (Figure 2D). Although lateral drift in particular could not be prevented entirely in all experiments, a conventional drift correction routine was able to correct for the residual drift and restore fine image details such as fenestrations in LSECs (Supplementary Figure 2C and D). Other image reconstructions did not require drift correction at all (Figure 3A and B). Noticeably, the image shown in Figure 3A was recorded 11 months after the microscope was originally set up and no further optical realignment had been performed during this time. This is another indicator for the high mechanical stability of the microscope, not only allowing for long-term SMLM image acquisitions but also resulting in low maintenance requirements.

While a UV laser (such as 405 nm) is a preferred choice for active photo-switching of dyes to the fluorescent on-state in SMLM modalities such as dSTORM, we did not include it in our setup to reduce costs and complexity. However, the existing 488 nm laser can also be used for effective photo-switching of organic dye molecules that are excited using the 647 nm laser (Figure 2E). The 488 nm laser can therefore serve the two purposes of (1) exciting dyes in the green spectral region and (2) photo-switching dyes of the far-red spectral region.

For dual-color imaging, the excitation profiles can be optically well aligned to illuminate the same part of the sample (Figure 2F). On the other hand, optical alignment alone of the two emission channels left residual deviations of more than 400 nm locally (Figure 2G), giving rise to the need of post-acquisition registration which, however, is a standard procedure in traditional multi-color imaging.

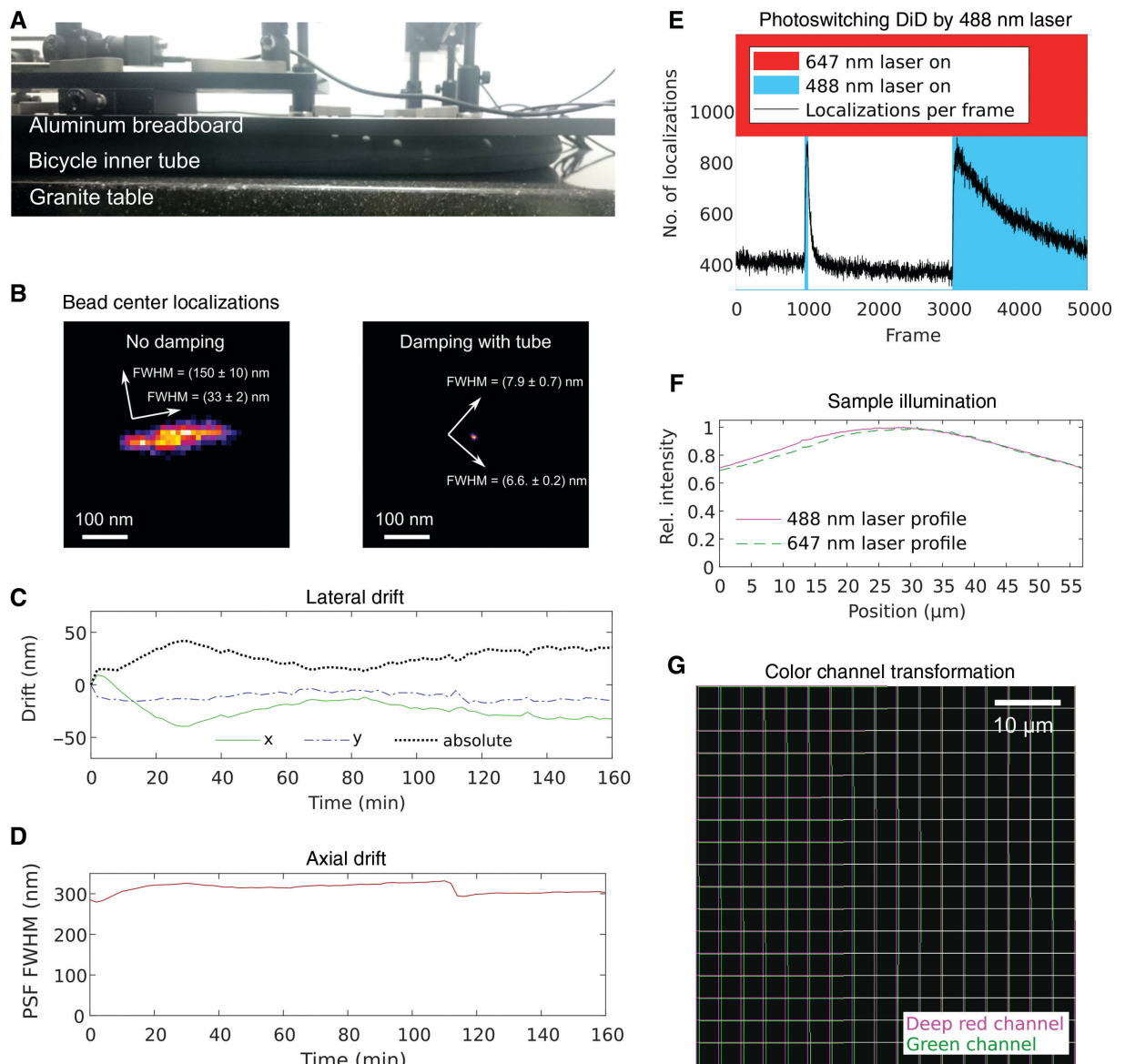


Figure 2: Mechanical and optical characterization of the custom-built dSTORM microscope.

(A) Side view of the microscope setup showing the bicycle inner tube for vibration damping. (B) The vibrations of the microscope are characterized by the repeated, high frame rate localization of the center of a sub-diffraction limit sized fluorescent bead. When damping the vibration with the inner tube in place, the remaining motion blur is well below the resolution of the microscope. (C) Plot of lateral drift as a function of time for repeated localizations of a fluorescent bead shows that the drift is below 50 nm over more than 1 h. (D) The point spread function width does not considerably change during this time, indicating high focus stability. (E) Vybrant DiD localizations as a function of time when using the 647 nm for fluorescence excitation and the 488 nm laser for photo-switching to the on-state in defined time intervals. (F) The different lasers are well overlaid for sample illumination using a beam profile that maintains about 80% of its peak intensity over a disk of 40 μm in diameter. (G) The color channel transformation between the two channels (transforming the green onto the deep red channel) measured by beads simultaneously emitting in both channels.

3.3 Visualizing the nanoscale architecture of LSEC plasma membranes and the actin cytoskeleton

LSEC membranes (and the fenestrations within) as well as the cytoskeleton have previously been visualized by dSTORM super-resolution microscopy using Cell Mask

Deep Red, Vybrant DiD, and antibodies or phalloidin conjugated with AlexaFluor 647 (AF647), AlexaFluor 488 (AF488), or Atto488 [45–47]. We tested a variety of buffers and stains on LSECs and platelets (Supplementary Note 1). Phalloidin-AF488 in OxEA buffer resulted in actin images of high quality (Figure 3A–D), while Vybrant DiD in GODCAT buffer resulted in membrane images of high quality (Figure

3E–H). These are indicated by SQUIRREL analyses [42] showing a resolution-scaled Pearson coefficient better than 0.9 (Figure 3C and G). The resolution-scaled error (RSE) particularly increases in regions of higher actin density (Figure 3C) and membrane structures distant from sieve plates, both possibly because of multi-emitter artifacts due to the relatively high emitter density (Figure 3I). However, the low RSE values in regions of sieve plates confirm the ability of analyzing the fenestration size at high confidence [46]. Due to the relatively low quantum efficiency of the industry-grade CMOS cameras in our microscope, observed photon counts per localization (Figure 3J) as well as background signal (Figure 3K) were not as high as in former studies [46] and [45], resulting in average localization precisions of 20 to 24 nm (Figure 3L). The particularly good Fourier ring correlation (FRC) resolution [48] of down to 38 nm (Figure 3H) correlates with regions of bad RSE values (Figure 3G), confirming other researchers' findings that the FRC resolution might be an inferior resolution metric in SMLM [49, 50]. As suggested by Legant et al. [49], we additionally calculated the geometric sum of 2.4 times the mean localization precision (i.e. inferring the best possible resolution from the localization precision) equal to 57.8 nm and the 10 times oversampled Nyquist-limited resolution equal to 10.4 nm that we estimated from the localization sampling of the plasma membrane of 3 million localizations per $81 \mu\text{m}^2$ (Figure 3F). The resulting estimated resolution is 58.7 nm. As the resolution can be locally slightly increased, we

conclude that we can measure fenestration sizes down to approximately 54 nm in our dSTORM images.

The dense localization sampling of the plasma membrane that allows for this high Nyquist resolution is particularly challenging for the SMLM fitting and reconstruction software. The SMLM community has produced a magnificent amount of different software solutions for SMLM data reconstruction, post-processing, and analysis [51, 52]. While it is beyond the scope of our work to extensively compare and evaluate the broad variety of software packages, we would like to point out the two software packages we used for image reconstruction in this study. ThunderSTORM [40] is a good option for inexperienced users since it comes as an ImageJ/Fiji plugin [39]. The user can therefore navigate in an environment already familiar to many researchers in the field of fluorescence microscopy. While ThunderSTORM also offers experienced users the options to tweak many parameters of the reconstruction pipeline, its default settings often yield respectable results, making it a good choice even for inexperienced users. However, reconstructing images of LSEC membranes is a particularly challenging task due to the high localization density. A lot of single emitter events must first be fitted for one reconstruction of high quality and then also be stored in the memory. Unfortunately, ThunderSTORM runs relatively slowly during the fitting algorithm and demands a lot of memory, easily filling the memory even for a high-end desktop computer. We therefore used rapidSTORM [43] as a complementary

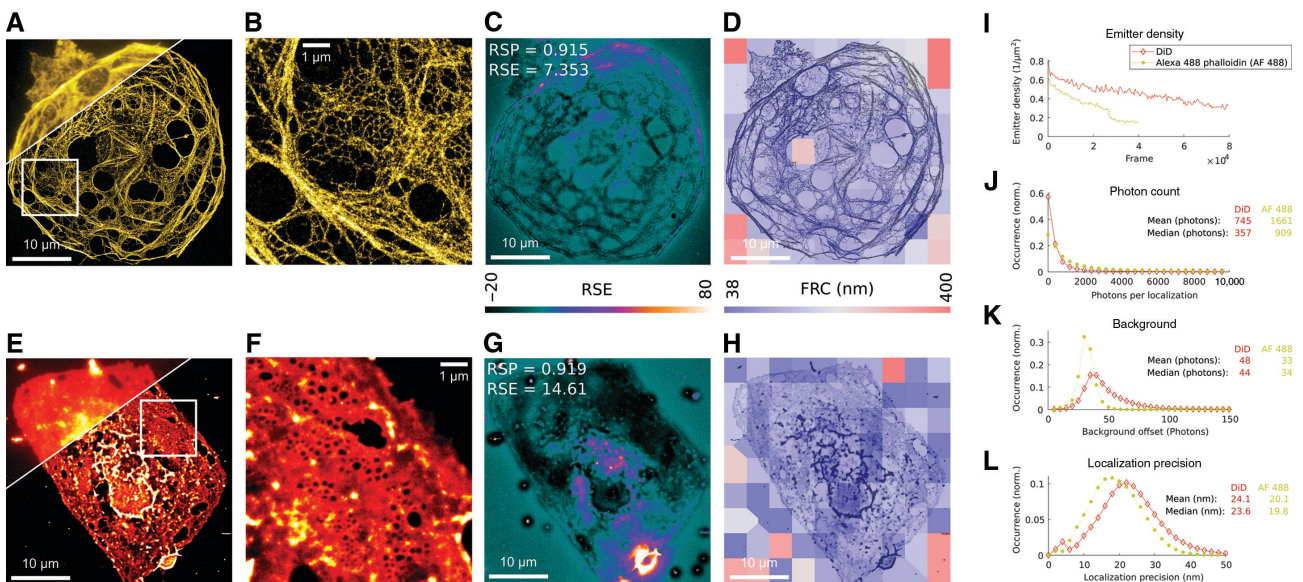


Figure 3: dSTORM imaging quality characterization.

Rat LSEC diffraction limited (A, E, upper left) and dSTORM images of actin (A, B) stained with AF488-phalloidin and membrane (E, F) stained with Vybrant DiD. Spatially dependent dSTORM image quality metrics of RSE (C, G) and FRC resolution (D, H) determined by SQUIRREL. (I) Emitter density in the ROI of (B, F) as a function of the frame. (J–L) The single molecule localization statistics (AF488 and DiD) as photon counts per localization, background and localization precision.

option for SMLM data reconstruction. As suggested by its name, it runs relatively quickly during the reconstruction and furthermore is relatively memory efficient. This made it our preferred choice for reconstruction of the membrane structure. The two different software packages ThunderSTORM and rapidSTORM produced comparable results when reconstructing the same data set of immunostained tubulin recorded with our microscope (Supplementary Figure 1B and C). Both reconstructions show the significant resolution improvement as compared to the diffraction-limited wide-field image that we recorded before acquiring the dSTORM data (Supplementary Figure 1D).

3.4 dSTORM imaging of LSECs challenged with exogenous agents

Recently, a number of agents (NMN and sildenafil among others) were demonstrated to enhance fenestrations size and number in LSECs from aging mice, as visualized with scanning EM [15]. We tested these agents in our optical super-resolution microscope (Figure 4) and visualized changes in the actin cytoskeleton in cells treated with NMN (Figure 4B and E) and sildenafil (Figure 4C and F). Especially on sildenafil treatment, actin stress fibers became clearly pronounced (Figure 4M) as measured in a machine learning assisted workflow (Methods, Supplementary Figure 4). F-actin in the sildenafil-treated cells appears to be generally more condensed, and the actin rings (arrows, Figure 4E and F) that typically delineate fenestrations [47] are more pronounced in both NMN and sildenafil-treated cells. We also noted similar changes in fenestration size (Figure 4H, I, K, L) as reported in [15]. NMN and sildenafil increased the median fenestration diameter by 5% and 30%, respectively (Figure 4N). While the use of EM for the quantitative analysis of fenestration morphology is a well-established tool, the use of dSTORM for the same purpose makes certain steps in the workflow (such as sample preparation) much easier, and, in particular when using a low-cost implementation as presented here, drastically lowers the instrument cost. Furthermore, the use of fluorescence super-resolution microscopy combines high resolution with specificity such that the users can get the best of both worlds, which makes quantitative actin analysis accessible.

3.5 Super-resolution imaging of lipid rafts on LSECs

Svistounov et al. [53] previously demonstrated the presence of lipid rafts on LSECs and proposed that these

play a role in the regulation of fenestration size. Using our microscope, we found that Bodipy FL C5-ganglioside GM1 (BodipyGM1), a lipid raft stain, photo-switches in GODCAT-1 buffer. This confirms the work of Bittel et al. [54], who recently reported photo-switching of Bodipy FL for dSTORM. Interestingly, the C5-ganglioside GM1 conjugated form of Bodipy FL not only visualized lipid rafts but also stained all of the LSEC plasma membrane, with some areas of higher localization density probably being indicative of lipid rafts (Figure 5A and B). We achieved a sufficiently low blinking density to allow for high-resolution dSTORM imaging of the LSEC plasma membrane (Figure 5B and C), at a mean photon count of 831 photons per localization (Figure 5D), together with a mean background of 102 photons (Figure 5E), resulting in an average localization precision of about 19 nm (Figure 5F). The mean on-state lifetime was 1.7 frames per fluorophore (Figure 5G) when using single frame exposure times of 20 ms. Interestingly, fenestrations were also visible with BodipyGM1 staining (Figure 5B, H, and I), allowing the simultaneous imaging of fenestrations and structures (lipid rafts) that are proposed to regulate their size [53]. Choosing a look-up table with high contrast throughout a large scale, Figure 5H shows how the low-density BodipyGM1 staining (blue) is distributed over the entire cell and visualizes fenestrations. The high-density of BodipyGM1 staining (green to white) is distributed throughout the cell in discrete points, long sinuous structures, or patches. Figure 5I shows one such patch (arrow) adjacent to a sieve plate (dashed circle), which also contains some discrete punctuated BodipyGM1 staining within. The long sinuous patches have been reported previously on BodipyGM1-stained LSECs using TIRF microscopy [53]. We attempted double staining of LSECs with Vybrant DiD and BodipyGM1 on our setup, but were not successful. However, we achieved this co-staining using structured illumination microscopy (not shown) where we saw some overlap of BodipyGM1 and Vybrant DiD staining. This is to be expected since lipid rafts are membrane structures, but there were areas where BodipyGM1 staining was elevated relative to Vybrant DiD staining, and therefore indicative of elevated lipid raft membrane components.

3.6 Imaging platelets by dSTORM

Given that platelets play an active role in the resolution of hepatic fibrosis and liver regeneration [8, 9], we also investigated the utility of our microscope for the study of these cells. We successfully tested phalloidin-AF647 (actin stain) and Vybrant DiD (membrane stain) (Figure 6, Supplementary Figure 5). Unstimulated discoid platelets

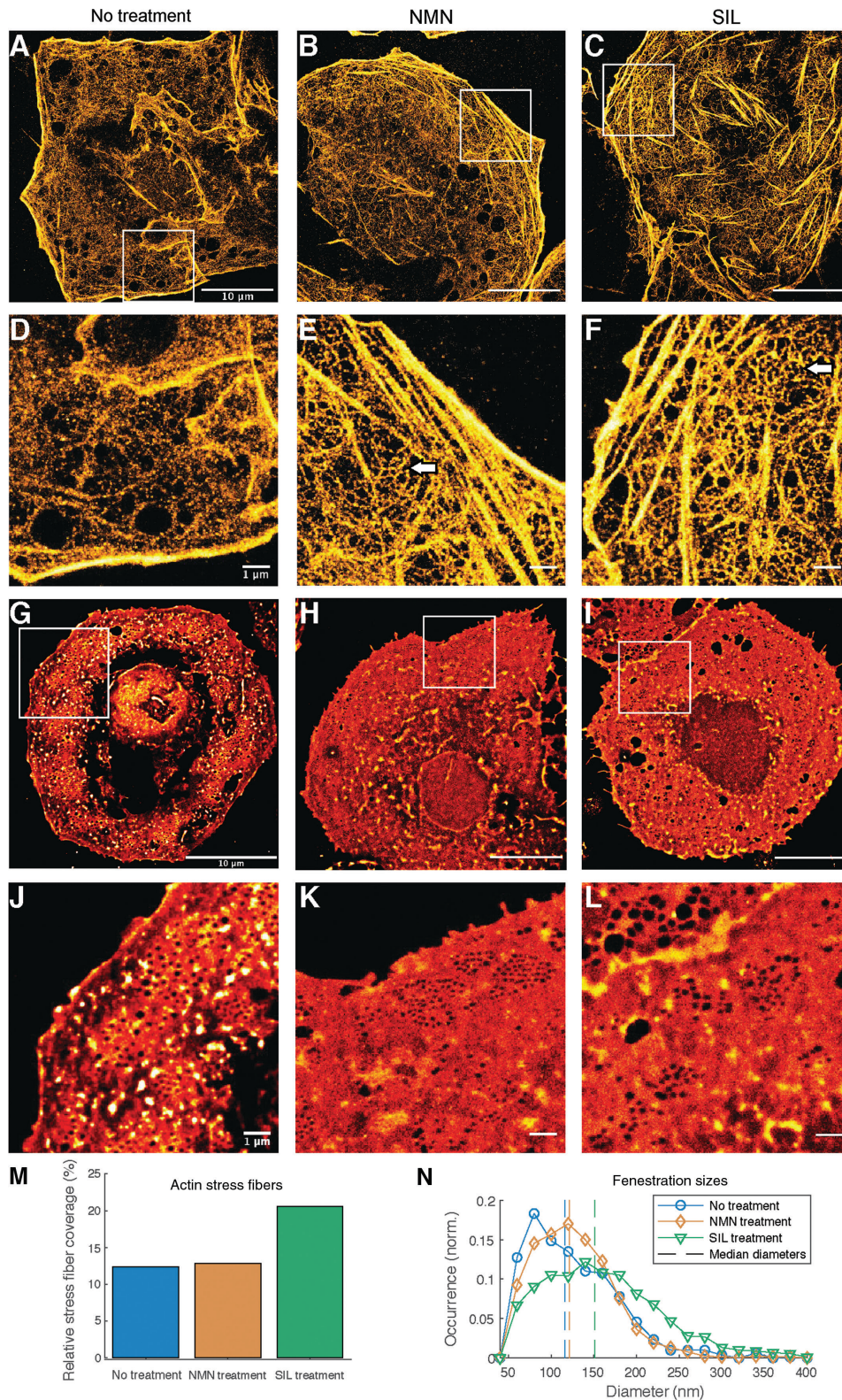


Figure 4: Membrane and actin staining in LSECs treated with NMN and sildenafil. (A–F) dSTORM images of drug-treated rat LSECs in OxEA buffer, stained for actin with phalloidin-AF488: (A, D) Control; (B, E) 333 $\mu\text{g}/\text{ml}$ NMN; (C, F) 60 ng/ml SIL. Insets (D–F) show a detailed comparison of drug effects compared to controls. Arrows in E and F indicate actin rings that typically delineate fenestrations. (G–I) Images of drug-treated rat LSECs, stained with Vybrant DiD in GODCAT-1 buffer, (G, J) Control; (H, K) NMN; (I, L) SIL. (M) Plot of relative percentage of stress fibers as a total of actin staining vs. control, NMN and SIL treatment ($n=1$ for each point). The relative proportion of stress fiber actin within total actin increases particularly upon SIL treatment. (N) Histogram of occurrence vs. fenestration size after challenge with NMN and SIL. Fenestration size increases after NMN and SIL treatment. All imaging was in TIRF mode.

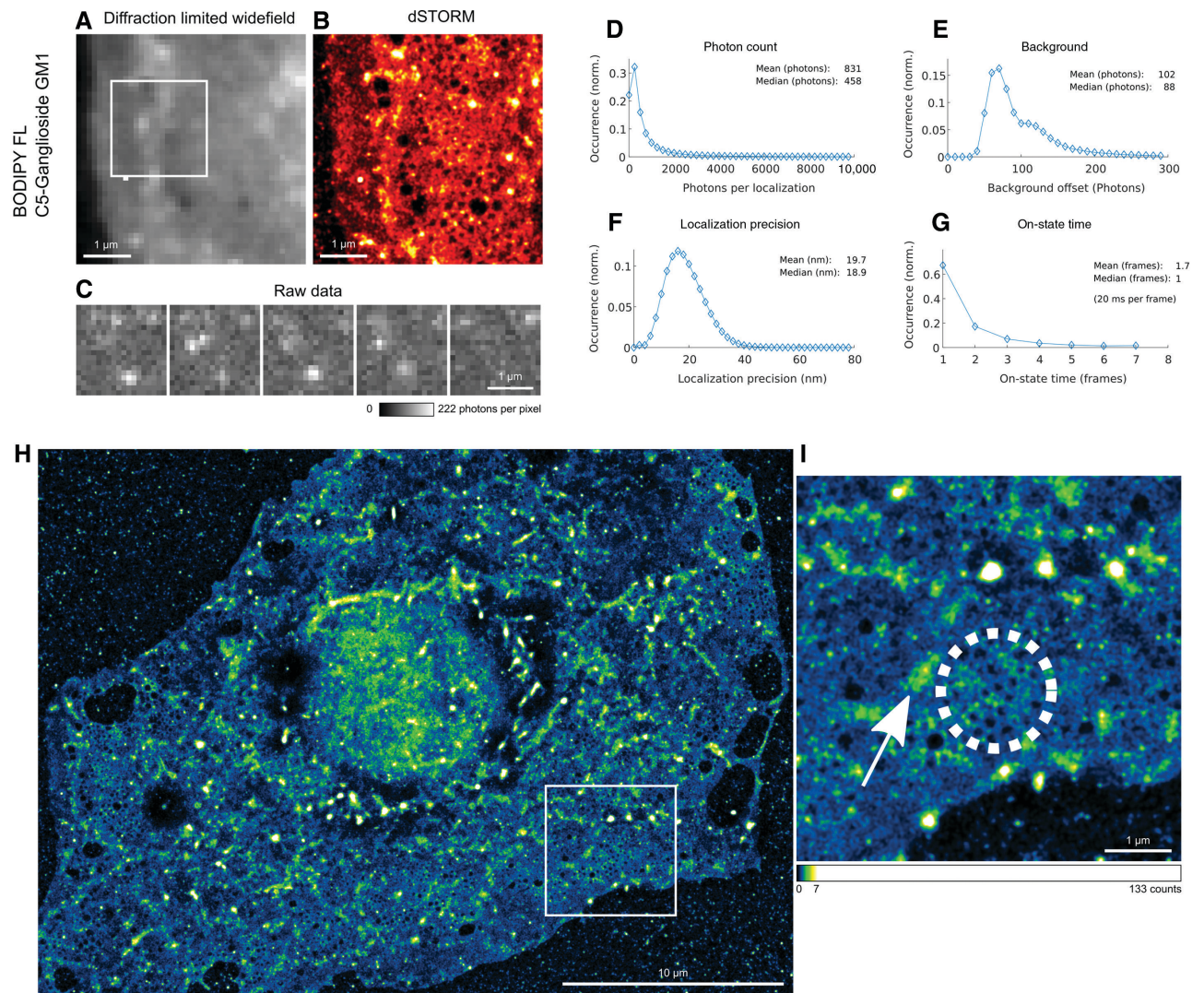


Figure 5: Bodipy FL C5-ganglioside GM1 visualizes lipid rafts and fenestrations.

(A) Diffraction limited and (B) dSTORM images of BodipyGM1-stained mouse LSECs show the resolution enhancement in the dSTORM image, where membrane fenestrations become visible. (C) Representative raw data of photo-switching BodipyGM1 in subsequent frames of the area indicated by the box in (A). (D–G) show the single molecule (Bodipy) localization statistics as photon counts per localization, background, localization precision and on-state-lifetime histograms. (H) An entire LSEC stained with BodipyGM1 processed with a high-contrast look-up table. Blue indicates low-density BodipyGM1 staining, while green to white indicates high-density BodipyGM1 staining. (I) The inset from (H) shows the proximity of a sieve plate (encircled with white dashes) to a putative lipid raft (indicated by a white arrow).

adopt a round shape on contact with imaging surface (Figure 6H–J, Supplementary Figure 5A and B). After thrombin stimulation, platelets begin to spread and actin-rich cell protrusions (filopodia) forming a spindle-like morphology appeared (Figure 6K–M, Supplementary Figure 5C and D). Up to 7 μm long and about 100 nm wide filopodia were often seen emanating from the platelet plasma membrane in thrombin-stimulated platelets (Figure 6M). Filopodia are characterized by organized actin fibers arranged in parallel bundles, while lamellipodia are intermediate areas between individual filopodia in which the actin is orthogonal to the membrane. These structures have previously been reported in EM studies

of platelets [55]. Double staining allows the relationship between actin and membrane to be visualized in these structures (Figure 6M).

3.7 Evaluation of double-staining methodologies with our microscope

By screening a combination of dyes allowing for multi-color dSTORM imaging of platelets, we discovered that the membrane stain Cell Mask Green (Figure 6A) photo-switches in GODCAT-1 buffer. To the best of our knowledge, photo-switching of Cell Mask Green has not been

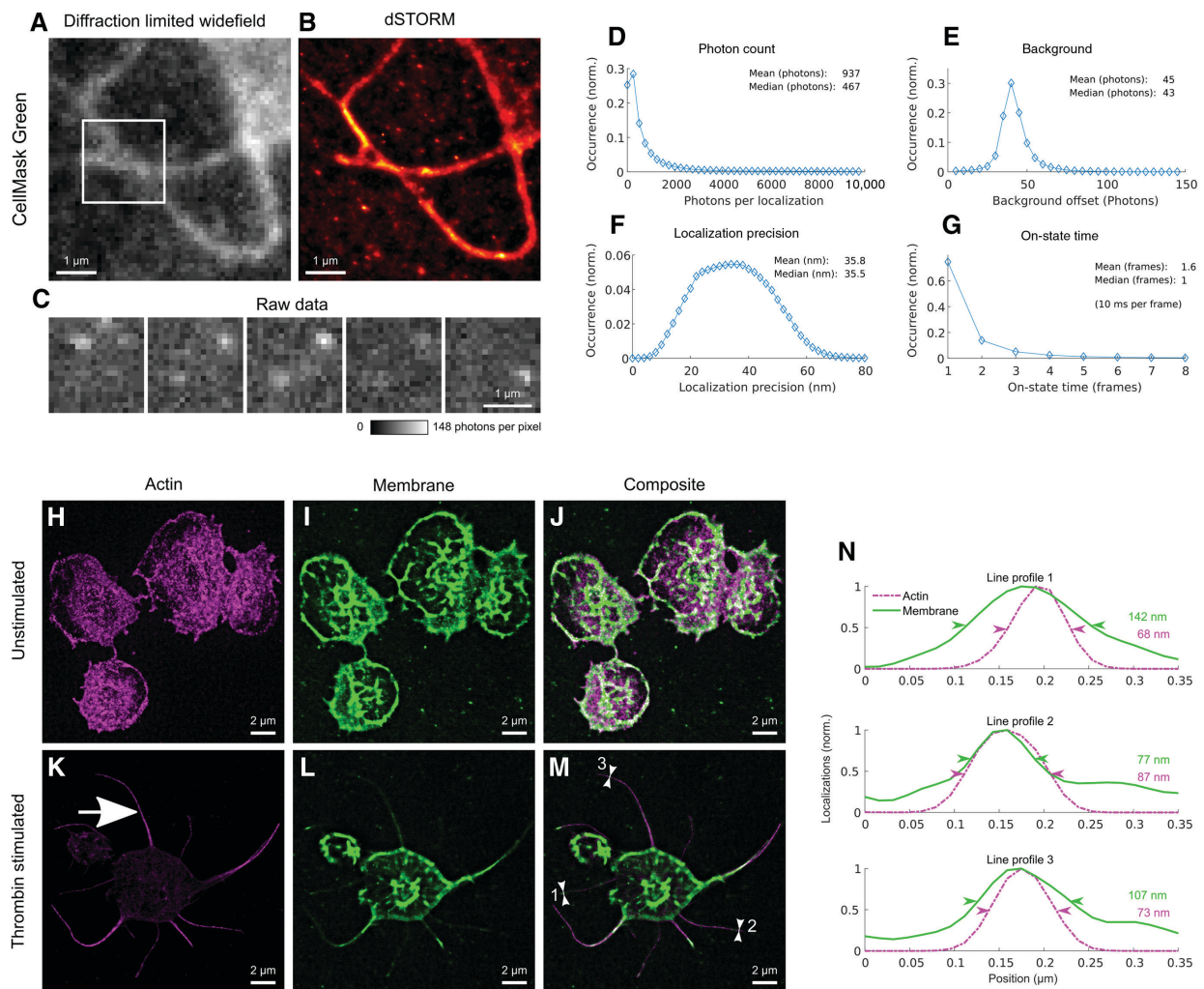


Figure 6: Dual color staining of human platelets.

(A) Diffraction limited and (B) dSTORM images of Cell Mask Green stained thrombin-stimulated platelet plasma membrane extensions. (C) Representative raw data of photo-switching Cell Mask Green in subsequent frames of the area indicated by the box in (A). (D–G) The single molecule localization statistics (Cell Mask Green) as photon counts per localization, background, localization precision and on-state-lifetime histograms. (H–M) Dual-color dSTORM images of human unstimulated (H–J) and thrombin stimulated (K–M) platelets stained with phalloidin AF647 (H, K) (purple) and Cell Mask Green (I, L) (green). (J, M) merged phalloidin AF647 and Cell Mask Green images. (N) The line profile analysis of (M) regions 1, 2, and 3 indicated within the figure shows that the ultra-thin membrane projections contain polymerized actin (white arrow in (K)). The numbers report the FWHM values of the membrane and actin structures, respectively. Imaging was performed in TIRF mode.

reported previously, and this enabled dSTORM imaging of the platelet membrane (Figure 6B). Sparse single-molecule blinking occurred at illumination intensities of 620–2330 W/cm² from the 488 nm laser (Figure 6C). Single molecules were detected at a mean photon count of 937 photons per localization (Figure 6D) and a mean background of 45 photons (Figure 6E). The resulting average localization precision was 36 nm (Figure 6F) and the mean on-state lifetime was 1.6 frames per fluorophore when using single frame exposure times of 10 ms (Figure 6G). We used Cell Mask Green to co-stain and simultaneously image actin using phalloidin AF647 in the same buffer (Figure 6H, J, K and M). Using this strategy for dSTORM, we found

that the ultra-thin membrane projections (Figure 6M) contained a scaffold of polymerized actin (Figure 6K–N).

4 Discussion

In this work we demonstrate a simple and cost-effective dSTORM microscope using off-the-shelf components. The total cost of the microscope, including the new TIRF objective lens, was about €30,000 (Supplementary material). Using objective lenses from obsolete microscopes, and low-end lasers [23], this can be reduced to about €15,000. However, we chose higher quality lasers to guarantee stability and

low maintenance for microscope users with little experience in handling lasers and other optical components. Furthermore, air tables costing in the range of €7000–15,000 are unnecessary, as using a bicycle inner tube under our breadboard was sufficient to isolate building vibrations.

With our custom-built SMLM microscope, we resolved LSEC fenestrations from mice and rat livers. Mouse and rat LSEC fenestrations are highly similar in morphology and organization, and are similarly difficult structures to visualize, as it is the absence of staining that visualizes a fenestration. In this context, background staining can obscure the structure. Background staining and other sources of noise therefore require extra attention. That said, the industrial CMOS cameras used in this study provided sufficient wide-field fluorescence image data, easily detected single blinking fluorescent molecules, and the read noise of about 6.4 electrons per pixel was not an issue. While the performance of this particular CMOS camera was extensively evaluated in a previous study [26], we note that there are other, even cheaper industry-grade cameras available [22, 25]. Additionally, other microscope components such as optomechanics might in principle be replaced by other manufacturers' solutions or custom-made parts. This opens up the possibility of choosing the ideal hardware for the specific applications of advanced users.

Advanced users can also easily start from our build (which is documented in detail in the Supplementary material) and modify it according to their needs. Many groups have described solutions for cost-effective, small, and accessible microscopes for SMLM [22–25, 28, 56]. We would like to encourage advanced users to gather inspiration from the broad variety of suggested options and decide what suits best for their particular application – just as we did for this work. While other researchers have presented significantly cheaper and/or smaller microscopes for SMLM, our aim was to achieve sufficient image quality particularly for the task of studying the cell types described in this study and using traditional multi-color imaging at high mechanical stability and low maintenance on a particularly easy to use microscope, even for users with little SMLM experience. While achieving these goals, the microscope is significantly cheaper than commercially available SMLM microscopes.

Intracellular structures were easily visualized at super-resolution with our microscope. The LSEC actin cytoskeleton was also easy to visualize, and the resolution of our microscope enabled us to see structures resembling fenestrations, which are encircled by a ring of actin [47]. In a previous study [15] (which used this microscope for actin analysis), NMN and sildenafil were shown to increase the fenestration size, and the actin cytoskeleton is greatly affected by these agents. We report here the full

description of the setup and confirm the findings, namely the dramatic condensation of the actin cytoskeleton into stress fibers, and rings of actin became more defined after NMN and sildenafil treatment.

Svistounov et al. [53] proposed that lipid rafts play an integral role in the regulation of fenestration size by pulling or pushing on LSEC sieve plates. We assessed the functionality of the lipid raft stain BodipyGM1 to stain LSECs in the dSTORM context. This stain binds GM1 glycolipids present in lipid rafts, but using single-molecule imaging, we found that it stained all the plasma membrane on LSECs. Some areas of the LSECs stained more intensely with this dye, probably indicative of lipid rafts, but the apparent non-specificity of the stain was initially disappointing. However, further careful analysis of the output revealed that fenestrations were fortuitously also visualized with this lipid raft stain (Figure 5). An explanation for this is that the BodipyGM1 stain, like other commercially available lipid raft stains, is based on the cholera toxin B (CT-B) subunit, which binds GM1 gangliosides. However, a limitation of CT-B is that it binds other cell surface sugars such as galactose [57, 58]. We thus propose that this binding to other cell surface sugars is what we see as background staining (that fortuitously reveals fenestrations), making the BodipyGM1 stain an exciting tool to simultaneously study the relationship between fenestrations and lipid rafts at super-resolution using only one color channel.

We also investigated primary cultures of platelets. Features which particularly captured our interest were super-fine filaments, some thinner than 100 nm, emanating from their plasma membranes. These filaments were membrane structures with an actin skeleton and would be sufficiently long and thin to pass through LSEC fenestrae and, for example, interact with the underlying hepatocytes in the *in vivo* context. Similar interactions of lymphocyte villi with hepatocytes via LSEC fenestrations and vice versa have been shown by Warren et al. [6]. Given that platelets have a role in resolution of fibrosis [8, 9], this super-resolution microscope will be a useful tool to study the platelet: LSEC “synapse” in future studies.

This work thus demonstrates the effectiveness of a custom-built SMLM microscope to perform super-resolution imaging of primary cells for only a small fraction of the cost of a commercial microscope for SMLM. We believe that our work will contribute to the strong current movement of democratizing the access to super-resolution microscopy, making super-resolution available to a wide range of laboratories as a routine lab microscope.

Acknowledgments: The authors are grateful to Marcel Müller for his support with the Micro-Manager-based

camera control. This project was funded by the McKnight Bequest via the Sydney Medical School Foundation and the Ageing and Alzheimers Institute. The publication charges for this article have been funded by a grant from the publication fund of the University of Tromsø – The Arctic University of Norway.

References

- [1] Fraser R, Cogger VC, Dobbs B, et al. The liver sieve and atherosclerosis. *Pathology* 2012;44:181–6.
- [2] Sorensen KK, Simon-Santamaria J, McCuskey RS, Smedsrod B. Liver sinusoidal endothelial cells. *Compr Physiol* 2015;5:1751–74.
- [3] McLean AJ, Cogger VC, Chong GC, et al. Age-related pseudocapillarization of the human liver. *J Pathol* 2003;200:112–7.
- [4] Braet F, Wisse E. Structural and functional aspects of liver sinusoidal endothelial cell fenestrae: a review. *Comp Hepatol* 2002;1:1.
- [5] Mohamad M, Mitchell SJ, Wu LE, et al. Ultrastructure of the liver microcirculation influences hepatic and systemic insulin activity and provides a mechanism for age-related insulin resistance. *Aging Cell* 2016;15:706–15.
- [6] Warren A, Le Couteur DG, Fraser R, Bowen DG, McCaughan GW, Bertolino P. T lymphocytes interact with hepatocytes through fenestrations in murine liver sinusoidal endothelial cells. *Hepatology* 2006;44:1182–90.
- [7] Oteiza A, Li R, McCuskey RS, Smedsrod B, Sorensen KK. Effects of oxidized low-density lipoproteins on the hepatic microvasculature. *Am J Physiol Gastrointest Liver Physiol* 2011;301:G684–93.
- [8] Kurokawa T, Ohkohchi N. Platelets in liver disease, cancer and regeneration. *World J Gastroenterol* 2017;23:3228–39.
- [9] Kurokawa T, Zheng YW, Ohkohchi N. Novel functions of platelets in the liver. *J Gastroenterol Hepatol* 2016;31:745–51.
- [10] Grozovsky R, Begonja AJ, Liu K, et al. The Ashwell-Morell receptor regulates hepatic thrombopoietin production via JAK2-STAT3 signaling. *Nat Med* 2015;21:47–54.
- [11] Li Y, Fu J, Ling Y, et al. Sialylation on O-glycans protects platelets from clearance by liver Kupffer cells. *Proc Natl Acad Sci USA* 2017;114:8360–5.
- [12] Bonkowski MS, Sinclair DA. Slowing ageing by design: the rise of NAD(+) and sirtuin-activating compounds. *Nat Rev Mol Cell Biol* 2016;17:679–90.
- [13] Revollo JR, Korner A, Mills KF, et al. Nampt/PBEF/Visfatin regulates insulin secretion in beta cells as a systemic NAD biosynthetic enzyme. *Cell Metab* 2007;6:363–75.
- [14] Boolell M, Allen MJ, Ballard SA, et al. Sildenafil: an orally active type 5 cyclic GMP-specific phosphodiesterase inhibitor for the treatment of penile erectile dysfunction. *Int J Impot Res* 1996;8:47–52.
- [15] Hunt NJ, Lockwood GP, Warren A, et al. Manipulating fenestrations in young and old liver sinusoidal endothelial cells. *Am J Physiol Gastrointest Liver Physiol* 2019;316:G144–54.
- [16] Wisse E. An electron microscopic study of the fenestrated endothelial lining of rat liver sinusoids. *J Ultrastruct Res* 1970;31:125–50.
- [17] Wisse E. An ultrastructural characterization of the endothelial cell in the rat liver sinusoid under normal and various experimental conditions, as a contribution to the distinction between endothelial and Kupffer cells. *J Ultrastruct Res* 1972;38:528–62.
- [18] Wisse E, De Zanger RB, Jacobs R, McCuskey RS. Scanning electron microscope observations on the structure of portal veins, sinusoids and central veins in rat liver. *Scan Electron Microsc* 1983(Pt 3):1441–52.
- [19] Betzig E, Patterson GH, Sougrat R, et al. Imaging intracellular fluorescent proteins at nanometer resolution. *Science* 2006;313:1642–5.
- [20] Hess ST, Girirajan TP, Mason MD. Ultra-high resolution imaging by fluorescence photoactivation localization microscopy. *Biophys J* 2006;91:4258–72.
- [21] Rust MJ, Bates M, Zhuang X. Sub-diffraction-limit imaging by stochastic optical reconstruction microscopy (STORM). *Nat Methods* 2006;3:793–5.
- [22] Ma H, Fu R, Xu J, Liu Y. A simple and cost-effective setup for super-resolution localization microscopy. *Sci Rep* 2017;7:1542.
- [23] Holm T, Klein T, Loschberger A, et al. A blueprint for cost-efficient localization microscopy. *Chemphyschem* 2014;15:651–4.
- [24] Auer A, Schlichthaerle T, Woehrstein JB, et al. Nanometer-scale multiplexed super-resolution imaging with an economic 3D-DNA-PAINT microscope. *Chemphyschem* 2018;19:3024–34.
- [25] Babcock HP. Multiplane and spectrally-resolved single molecule localization microscopy with industrial grade CMOS cameras. *Sci Rep* 2018;8:1726.
- [26] Diekmann R, Till K, Muller M, Simonis M, Schuttpelz M, Huser T. Characterization of an industry-grade CMOS camera well suited for single molecule localization microscopy – high performance super-resolution at low cost. *Sci Rep* 2017;7:14425.
- [27] Van den Eynde R, Sandmeyer A, Vandenberg W, et al. A cost-effective approach to Super-resolution Optical Fluctuation (SOFI) microscopy using an industry-grade CMOS camera. *bioRxiv* 2018;413179. <https://doi.org/10.1101/413179>.
- [28] Martens KJA, van Beljouw S, van der Els S, et al. An open microscopy framework suited for tracking dCas9 in live bacteria. *bioRxiv* 2018;437137. <https://doi.org/10.1101/437137>.
- [29] Smedsrod B, Pertoft H. Preparation of pure hepatocytes and reticuloendothelial cells in high yield from a single rat liver by means of Percoll centrifugation and selective adherence. *J Leukoc Biol* 1985;38:213–30.
- [30] Heilemann M, van de Linde S, Schuttpelz M, et al. Subdiffraction-resolution fluorescence imaging with conventional fluorescent probes. *Angew Chem Int Ed Engl* 2008;47:6172–6.
- [31] Hua VM, Abeynaik L, Glaros E, et al. Necrotic platelets provide a procoagulant surface during thrombosis. *Blood* 2015;126:2852–62.
- [32] Nahidiazar L, Agronskaia AV, Broertjes J, van den Broek B, Jalink K. Optimizing imaging conditions for demanding multi-color super resolution localization microscopy. *PLoS One* 2016;11:e0158884.
- [33] Dempsey GT, Vaughan JC, Chen KH, Bates M, Zhuang X. Evaluation of fluorophores for optimal performance in localization-based super-resolution imaging. *Nat Methods* 2011;8:1027–36.
- [34] Edelstein A, Amodaj N, Hoover K, Vale R, Stuurman N. Computer control of microscopes using microManager. *Curr Protoc Mol Biol* 2010;Chapter 14:Unit14 20.

- [35] Tokunaga M, Imamoto N, Sakata-Sogawa K. Highly inclined thin illumination enables clear single-molecule imaging in cells. *Nat Methods* 2008;5:159–61.
- [36] Axelrod D. Cell-substrate contacts illuminated by total internal reflection fluorescence. *J Cell Biol* 1981;89:141–5.
- [37] Arimoto R, Murray JM. A common aberration with water-immersion objective lenses. *J Microsc* 2004;216(Pt 1):49–51.
- [38] Huang F, Hartwich TM, Rivera-Molina FE, et al. Video-rate nanoscopy using sCMOS camera-specific single-molecule localization algorithms. *Nat Methods* 2013;10:653–8.
- [39] Schindelin J, Arganda-Carreras I, Frise E, et al. Fiji: an open-source platform for biological-image analysis. *Nat Methods* 2012;9:676–82.
- [40] Ovesny M, Krizek P, Borkovec J, Svindrych Z, Hagen GM. ThunderSTORM: a comprehensive ImageJ plug-in for PALM and STORM data analysis and super-resolution imaging. *Bioinformatics* 2014;30:2389–90.
- [41] Arganda-Carreras I, Sorzano COS, Marabini R, Carazo JM, Ortiz-De-Solorzano C, Kybic J. Consistent and elastic registration of histological sections using vector-spline regularization. *Lect Notes Comput Sci* 2006;4241:85–95.
- [42] Culley S, Albrecht D, Jacobs C, et al. Quantitative mapping and minimization of super-resolution optical imaging artifacts. *Nat Methods* 2018;15:263–6.
- [43] Wolter S, Loschberger A, Holm T, et al. rapidSTORM: accurate, fast open-source software for localization microscopy. *Nat Methods* 2012;9:1040–1.
- [44] Sommer C, Straehle C, Kothe U, Hamprecht FA. Ilastik: Interactive Learning and Segmentation Toolkit. 2011 8th IEEE International Symposium on Biomedical Imaging: From Nano to Macro. 2011:230–3.
- [45] Diekmann R, Helle OI, Oie CI, et al. Chip-based wide field-of-view nanoscopy. *Nat Photonics* 2017;11:322.
- [46] Mönkemöller V, Schuttpelz M, McCourt P, Sorensen K, Smedsrod B, Huser T. Imaging fenestrations in liver sinusoidal endothelial cells by optical localization microscopy. *Phys Chem Chem Phys* 2014;16:12576–81.
- [47] Mönkemöller V, Oie C, Hubner W, Huser T, McCourt P. Multi-modal super-resolution optical microscopy visualizes the close connection between membrane and the cytoskeleton in liver sinusoidal endothelial cell fenestrations. *Sci Rep* 2015;5:16279.
- [48] Banterle N, Bui KH, Lemke EA, Beck M. Fourier ring correlation as a resolution criterion for super-resolution microscopy. *J Struct Biol* 2013;183:363–7.
- [49] Legant WR, Shao L, Grimm JB, et al. High-density three-dimensional localization microscopy across large volumes. *Nat Methods* 2016;13:359–65.
- [50] Kiuchi T, Higuchi M, Takamura A, Maruoka M, Watanabe N. Multitarget super-resolution microscopy with high-density labeling by exchangeable probes. *Nat Methods* 2015;12:743–6.
- [51] Sage D, Kirshner H, Pengo T, et al. Quantitative evaluation of software packages for single-molecule localization microscopy. *Nat Methods* 2015;12:717–24.
- [52] Sage D, Pham T-A, Babcock H, et al. Super-resolution fight club: assessment of 2D and 3D single-molecule localization microscopy software. *Nat Methods* 2019;16:387–95.
- [53] Svistounov D, Warren A, McEnerney GP, et al. The relationship between fenestrations, sieve plates and rafts in liver sinusoidal endothelial cells. *PLoS One* 2012;7:e46134.
- [54] Bittel AM, Saldivar IS, Dolman NJ, Nan X, Gibbs SL. Superresolution microscopy with novel BODIPY-based fluorophores. *PLoS One* 2018;13:e0206104.
- [55] Bettache N, Baisamy L, Baghdiguian S, Payrastré B, Mangeat P, Bienvenue A. Mechanical constraint imposed on plasma membrane through transverse phospholipid imbalance induces reversible actin polymerization via phosphoinositide 3-kinase activation. *J Cell Sci* 2003;116(Pt 11):2277–84.
- [56] Kwakwa K, Savell A, Davies T, et al. easySTORM: a robust, lower-cost approach to localisation and TIRF microscopy. *J Biophotonics* 2016;9:948–57.
- [57] Munro S. Lipid rafts: elusive or illusive? *Cell* 2003;115:377–88.
- [58] Uesaka Y, Otsuka Y, Lin Z, et al. Simple method of purification of *Escherichia coli* heat-labile enterotoxin and cholera toxin using immobilized galactose. *Microb Pathog* 1994;16:71–6.

Supplementary Material: The online version of this article offers supplementary material (<https://doi.org/10.1515/nanoph-2019-0066>).

Supplementary Note 1:**Comparison of buffers and stains for dSTORM visualization of cellular structures**

One of the challenges of dSTORM microscopy is choosing the correct match between the fluorescent probe and the imaging buffer system to enable blinking for each fluorophore. Supplementary Fig. 3 shows LSEC stained with phalloidin AF488 to visualize actin (Supplementary Fig. 3A, C), and Vybrant DiD to visualize the plasma membrane (Supplementary Fig. 3B, D) using GODCAT (Supplementary Fig. 3A, B) or OxEA [32] (Supplementary Fig. 3C, D) buffer. The results confirm other groups' findings [32, 48] that GODCAT-1 /-2 and Oxyrase systems function well with phalloidin AlexaFluor 488 to produce high quality actin filament staining on LSEC (Supplementary Fig. 3A, C). GODCAT-1 /-2 worked well with Vybrant DiD in the visualization of fenestrations (Supplementary Fig. 3B). However, we found that the OxEA/ Vybrant DiD combination resolved fenestrations poorly (Supplementary Fig. 3D).

Supplementary Table 1:

	TX-100	Blocking	Incubation time	dSTORM Buffer Tested	Cell type	Excitation intensity
Membrane stains:						
BodipyGM1 FL 5µg/ml (1:200)	-	-	15m	GODCAT-1	mLSEC	910-1190 W/cm ²
Vybrant DiD 5µg/ml (1:200)	-	-	20m	GODCAT-1&2	m&rLSEC	290-870 W/cm ²
Cell Mask Green 5µg/ml (1:1000)	-	-	10m	GODCAT-1	platelet	620-2330 W/cm ²
Cytoskeleton stains:						
Phalloidin AF647/488 165nM	1m 30s	45m	20m	GODCAT-1&2, OxEA	m&rLSEC, platelet	870-1760 W/cm ²
1° anti-tubulin 1:500*			1° - 1h			
2° anti-mouse AF647/488 1:1000*	1m 30s	45m	2° - 1h	GODCAT-1&2, OxEA	mLSEC, platelet	870-1760 W/cm ²

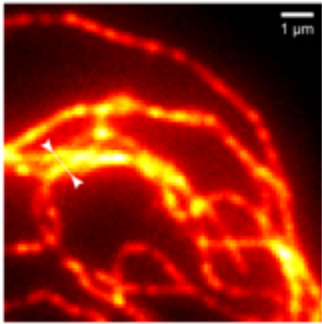
List of stains and conditions for dSTORM. Abbreviations: m/r LSEC = mouse/rat liver sinusoidal endothelial cells. GODCAT = glucose oxidase/catalase. OxEA = Oxyrase/ β-MercaptoEthylAmine. TX= Triton X-100. AF = Alexa Flour; *actual concentration not supplied by vendor

Supplementary Table 2: Composition of the imaging buffers:

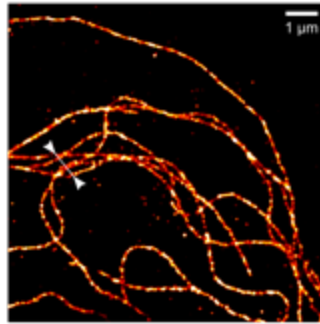
<p>GODCAT (glucose oxidase/catalase) or GLOX (glucose oxidase-based oxygen scavenger) buffer-1:</p>	<p>GODCAT buffer-2:</p>	<p>OxEA buffer:</p>
<ul style="list-style-type: none"> • 1 µg/ml (50 units) Catalase (≥30,000 units/mg) (Sigma-Aldrich) • 40 mg/ml glucose (Sigma-Aldrich) • 50 µg/ml glucose oxidase (≥100,000 units/g solid) (Sigma-Aldrich) • 2.5% glycerol (Sigma-Aldrich) • 1.25 mM KCl • 100 mM MEA-HCl (Mercaptoethylamine-HCl) (Sigma-Aldrich) • 200 µM TCEP (Tris (2-carboxyelthyl) phosphine hydrochloride) (Sigma-Aldrich) • 1 mM Tris <p>in PBS</p>	<ul style="list-style-type: none"> • 50 mM MEA-HCl • 10% (v/v) of a 250 g/l solution of glucose • 0.5 mg/ml (≥100,000 units/g solid) glucose oxidase • 40 mg/ml catalase <p>in PBS, pH 7.6</p>	<ul style="list-style-type: none"> • 50 mM MEA-HCl • 3% (v/v) OxyFlour™ (40.5 units/ml) (Oxyrase Inc. Mansfield) • 20% (v/v) of sodium DL-lactate solution (Sigma-Aldrich) <p>in PBS, pH adjusted to 8–8.5 with NaOH</p>

Supplementary Figure 1

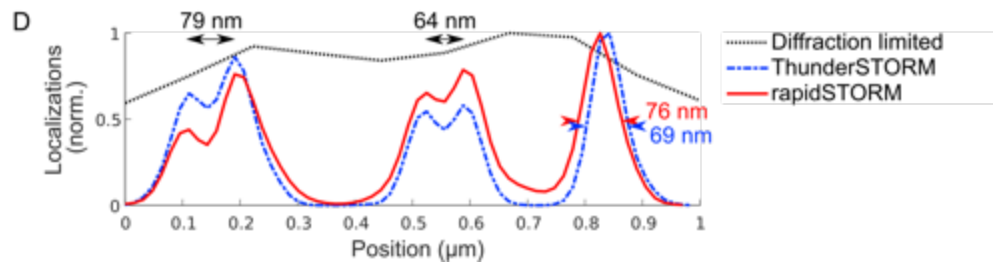
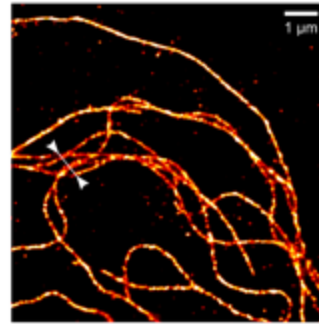
A Diffraction limited image



B ThunderSTORM
+ ImageJ/FIJI plugin
+ default settings work
well for most data



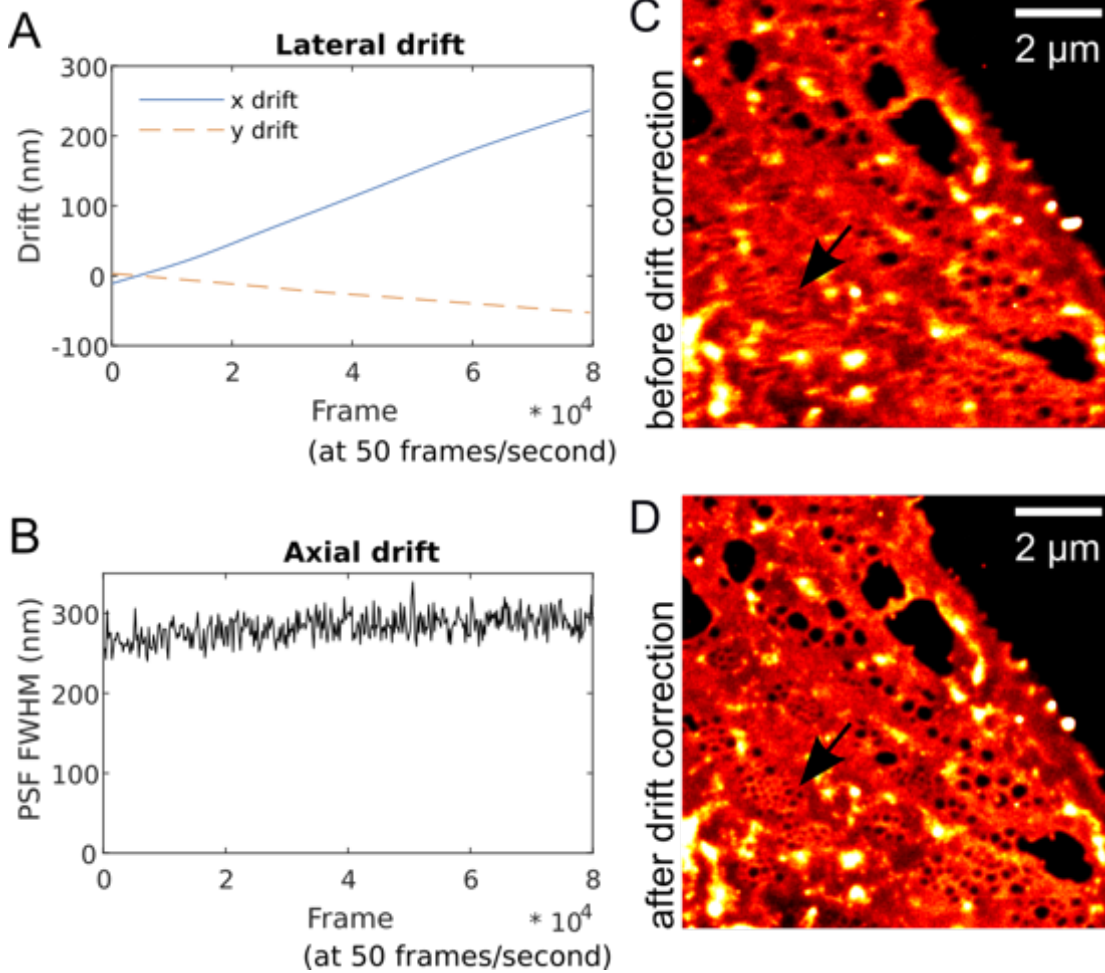
C rapidSTORM
+ very fast
+ memory efficient



Reconstruction with different software tools

(A) Diffraction limited image of mouse LSEC immunostained for tubulin filaments. (B, C) dSTORM imaging of the same sample as in (A) shows that adjacent tubulin filaments closer than the diffraction limit can be resolved. (D) Line profiles of adjacent microtubules show the obtained resolution and similar quality of the reconstruction from the two software packages, while each software features different strengths.

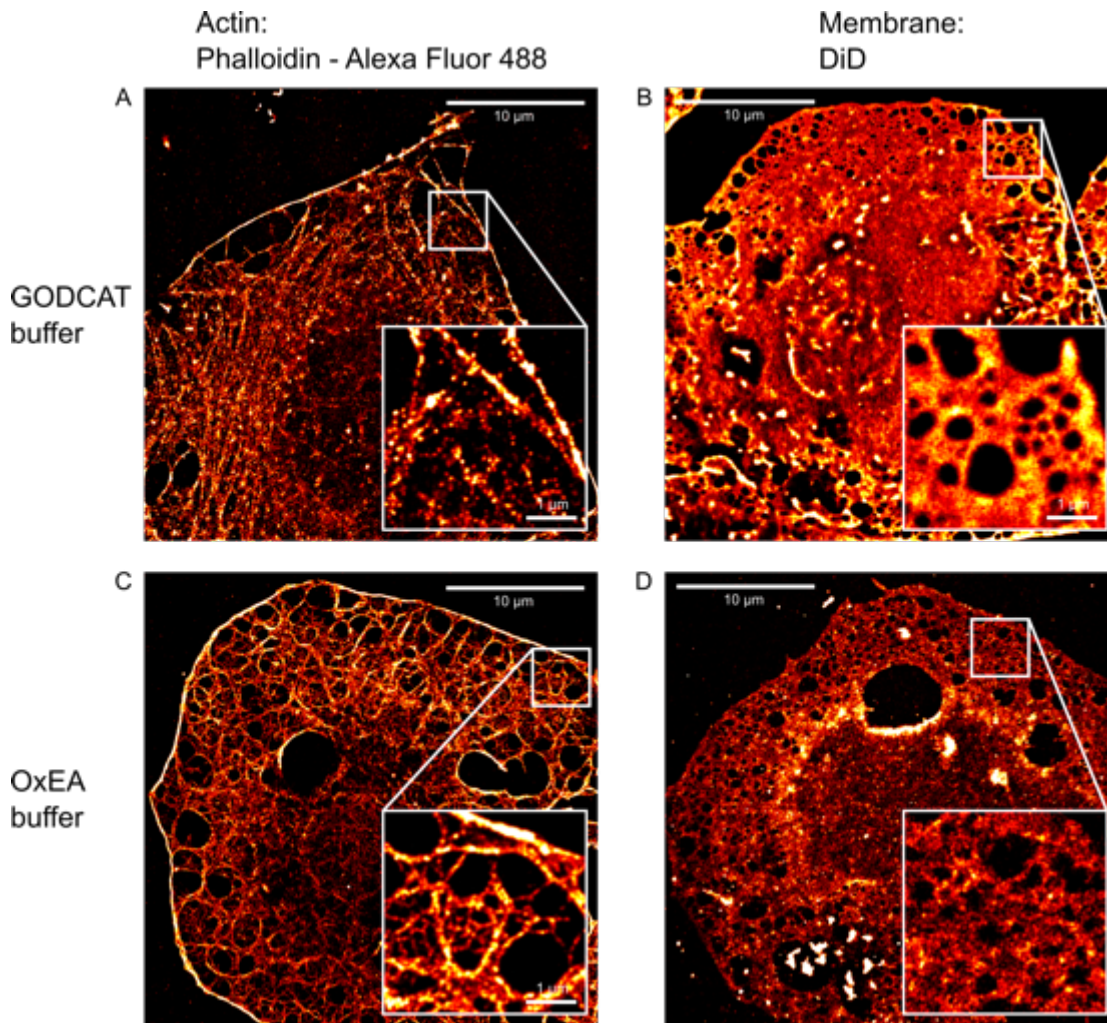
Supplementary Figure 2



Drift correction of dSTORM image acquisition

Vybrant DiD stained rat LSEC: the smooth lateral drift (A,C) can easily be corrected for (D), and smaller membrane fenestrations become visible (black arrow). (B) The point spread function width does not considerably change during the acquisition, indicating high focus stability.

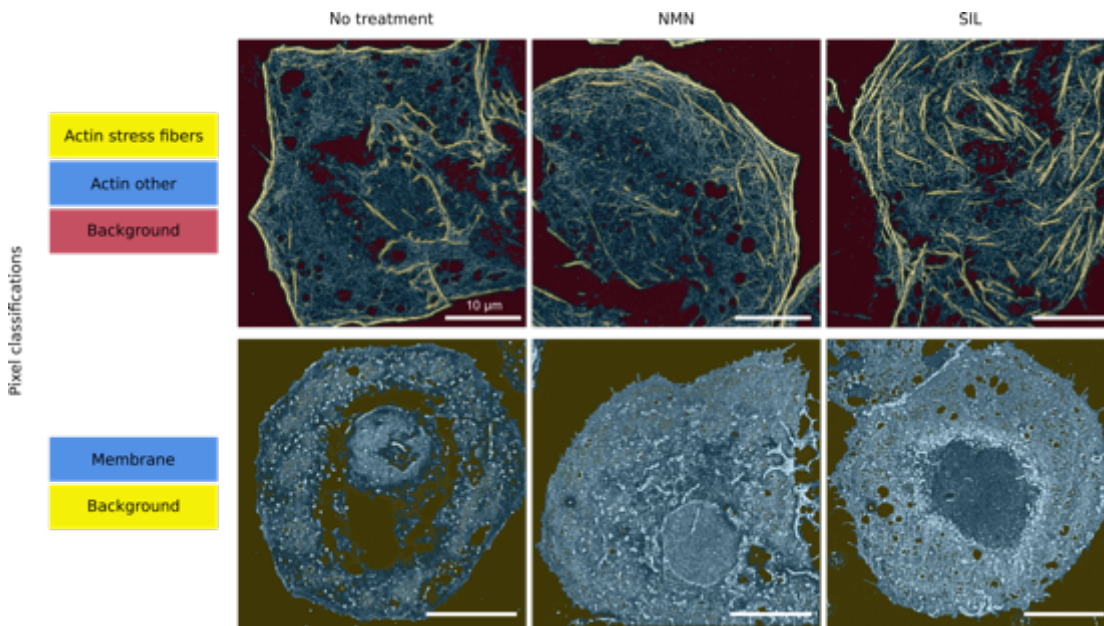
Supplementary Figure 3



dSTORM imaging of mouse and rat LSEC with different buffers

dSTORM images of mouse (A, no treatment) and rat (B-D, 1mg/ml AGE treatment*) LSEC with stained for actin (AF647-phalloidin) (A,C) and membrane (Vybrant DiD) (B,D) showing which buffer are optimal for each dye.*AGE is advanced glycation end-product protein used as a functional marker for LSEC and similar cells. It had no effects on LSEC morphology in this study.

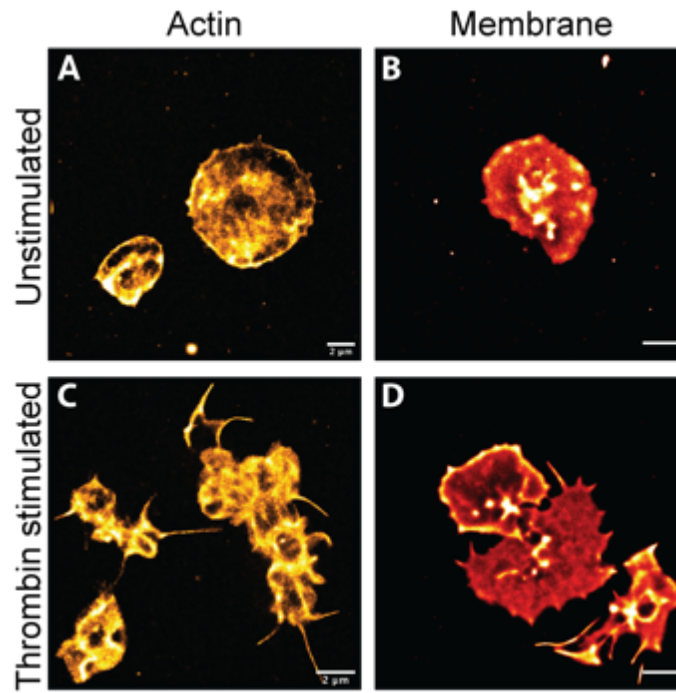
Supplementary Figure 4



Pixel classification for automated actin and fenestration analysis

Results of the pixel classification workflow of the Ilastik software. For the actin images (upper row), three different classes were used while for the membrane images (lower row), two different classes were used.

Supplementary Figure 5



Staining of human platelets (unstimulated and thrombin stimulated)

Plated human platelets \pm challenge with thrombin were stained with (A, C) Phalloidin-AF647 (actin); (B, D) Vybrant DiD (membrane). (A, B) Unstimulated platelets; (C, D) thrombin stimulated platelets. Imaging was in TIRF mode.

Supplementary Material

Custom-built dSTORM



Microscope construction protocol

Hong Mao*, Robin Diekmann*, Helena Hai Po Liang, Victoria C. Cogger, David G. Le Couteur, Glen P. Lockwood, Nicholas J. Hunt, Mark Schüttpeiz, Thomas R. Huser, Vivien M. Chen, Peter A.G. McCourt

Microscope construction protocol

The microscope parts list can be found online at:

https://docs.google.com/spreadsheets/d/1hvrnPTvSZmYkHC3xNXGYsR_a2GfpmK2dHhe4n9T49A/edit?usp=sharing

You will need the following equipment not mentioned in the microscope parts list:

- 30 cm ruler
- Small sheet of graph paper
- Laser safety equipment according to your institute's standards.
- A coverslip with fluorescent beads that can be excited using 488 nm and 647 nm and emit around 550 nm and 700 nm (e.g. 100 nm sized Tetraspeck beads from ThermoFisher).

Two parts need to be custom made:

- Connector of the Thorlabs 30 cm cage system to the microscope stage.
- The sample holder

We tried to use as many commercially available parts as possible but could not find good solutions for exactly these two parts. Since we had access to a mechanical workshop, we had them custom made there. The CAD drawings are attached at the end of this document. However, we think it is possible to find solutions based on commercially available parts, such as using a Thorlabs cage plate (e.g. CP02T/M) and gluing it to the stage as the connector to the rod system. For the sample holder, a metal plate with a hole in the center could work. Please note that these alternatives have not been tested by us though. We have used the parts as specified by the CAD drawings for the microscope described in this work.

Assembly and alignment instructions

(Please see below for pictures of the assembled microscope):

Breadboard

- Inflate the bicycle inner tube and place the breadboard on top. If you have vibration issues, try different air pressures.

Upright microscope body

- Fix a post mounting clamp (C1498/M) to the X-Y stage (KT 90-D56-EP).
- Fix the custom-made adaptor plate from the Thorlabs 30 mm cage rod system to the X-Y stage.
- Connect four 4" cage rods (ER4-P4) to the adaptor plate.
- Extend the 4" cage rods by 1/2" long cage rods (ER05-P4).
- Screw the SM1 to RMS adaptor (SM1A3) into the Z-Translator (SM1Z).
- Slide the Z-Translator onto the rods.
- Slide the cage cube (C6W) onto the rods.
- Screw the end cap (SM1CP2) into the cage cube on the side of the post mounting clamp.
- Slide the cage plate to post adaptor (CPTR10/M) onto the rods.
- Mount a post (TRA30/M) to the cage plate to post adaptor.
- To the other side of the post, mount a post mounting clamp (C1498/M). Extend the post by multiple washers (W8S038) such that the post mounting clamp is flush with the post mounting clamp attached to the stage. Fine adjustment of the length can be made by sliding the post in or out the cage plate to the post adaptor.
- Fix the elliptical mirror (BBE1-E02) inside the right-angle mirror mount (KCB1EC/M).
- Mount the post clamp (RM1B/M) to the mirror holder.
- Place the dynamically damped post (DP14A/M) in the corner of the breadboard (MB4590/M) and fix it using 4 screws.
- Slide the assembled part onto the post.
- Place the pillar post (RS3P/M) inside the post clamp.

Detection beam path

- Mount the 1" long cage rods (ER1-P4) to the cage cube (C4W).
- Slide the cage plate (CP02/M) onto the rods.
- Screw the aluminum post (TRA30/M) into the cage plate.
- Screw the end cap (SM1CP2) into the side of the cage cube.
- Do the following twice, i.e. for two remaining open sides of the cage cube:
 - Fix three of the 6" long cage rods (ER6-P4) to the cage cube. You should have two cage rods on the bottom and one on the top.
 - Put the $f=160$ mm lens (G063204000) into the lens mount (G06104700) and fix it.
 - Slide the lens mount onto the cage rods.
 - Screw the lens tube (SM1L10) into the cage plate (CP02/M).
 - Slide the cage plate onto the rods. Leave approx. 1 cm space to later fit one more cage plate and fix it.
 - Screw the aluminum post (TRA30/M) into the cage plate.
 - Slide one 4" long cage rod into the remaining hole of the cage plate such that it is flush with the end of the 6" long cage rods and fix it.
- Fix the 1" long cage rods of the assembled parts to the right-angle mirror mount of the upright microscope body and fix the three aluminum posts to the breadboard using one pedestal post holder (PH20E/M) and clamping fork for each post. The height of the aluminum posts can be adjusted by sliding them further into or out of the pedestal post holders.

647 nm laser, laser combiner and TIRF module

- Always stick to the laser safety instructions when working with the lasers, including wearing safety goggles where necessary.
- Connect the laser to the computer following the manufacturer's instructions.
- Place the laser (1193844) on the heat sink (1193289).
- Make sure the laser is working.
- All optical components will be held by the Thorlabs cage system rods. Connect the rods (ER3-P4) to the cage cube (C4W) that will later be used for laser combining.
- Mount the cover plate (B4C/M) to the bottom of the cage cube.
- Mount a post (TRA50/M) to the cover plate, and fix it to the small breadboard (MB1030/M) using a pedestal post holder (PH20E/M) and a clamping fork.
- The 647 nm laser will come out of the fiber as a diverging beam. To get it collimated, place the fiber in the fiber adapter plate (S1FCA) and hold the plate by the cage plate (CP02/M). Then place the $f = 35$ mm lens (La1027-A-ML) at a distance of approx. 35 mm in front of it, holding the lens by the cage plate (CP02/M). Vary the distance of the lens to the fiber output until the laser is collimated (i.e., the beam diameter does not change with its distance from the lens). Hold graph paper into the laser beam at different distances to check its diameter as a function of the distance.
- Put the 647 nm cleanup filter (LL01-647-12.5) in the SM05-to-SM1 adaptor (SM1A6T) and screw it into the cage cube at the side of the laser source.
- Screw the cage rods (E12) into the other side of the cage cube.
- Put the $f=120$ mm lens (G063202000) into the lens mount (G062047000), fix the lens using a pin (G06101100) and slide it onto the rods.
- Screw the $f=-75$ mm lens (LC1582-A-ML) into the cage plate (CP02/M) and place it onto the rods.
- Slide a cage plate to post adaptor (CPTR20/M) onto the rods, connect a post to its bottom, and fix it to the small breadboard using a pedestal post holder (PH20E/M) and a clamping fork.
- Slide a lens mount (G061047000) onto the rods, but do not put in the lens yet.
- Place the two lenses ($f=120$ mm and $f=-75$ mm) at approx. 45 mm distance and slide the lens mount of the former along the rails of the former until the beam is collimated. Then fix the lenses to the cage rods.
- Fix the single axis translation (PT1B/M) stage to the large breadboard. Fix the small breadboard holding the assembled parts on top of the translation stage.
- Adjust the height of the laser beam. To do so, slide the aluminum posts further into or out of the pedestal post holders. The height should be adjusted such that the beam goes centered through the cage cube. To see the position of the beam, temporarily screw an alignment disk (DG10-1500-H1-MD) to its entry side.

- Put in the main dichroic and align it:
 - Mount the filter holder (FFM1) to the cage cube platform (B4C/M).
 - Mount the dichroic (Di03-R405/488/532/635) to the filter holder. Note: Though we are only using the 488 nm and 647 nm lasers in this study, we have selected this dichroic for potential upgrades to UV (e.g. 405 nm) or green (532 nm) lasers.
 - Place the cage cube platform inside the cage cube such that the mirror is at an angle of 45° with the reflective side towards the laser.
 - Slightly rotate the cage cube platform such that the laser hits the Z-translator in the center. To view the laser beam, temporarily mount the RMS-to-SM1-adaptor (SM1A4) and an alignment disk (DG10-1500-H1-MD) in the Z-translator.
 - Now the 647 nm laser has been roughly aligned. For fine alignment, the 647 nm laser has to hit the Z-translator (which will later hold the objective lens) both in the center as well as perpendicular. This requirement has to be fulfilled for both the x as well as the y direction. We therefore need four degrees of freedom in the setup.
 - For the Y-axis, the rotating angle of the dichroic can be changed by
 - (Y1) rotating the cage cube platform inside the cage cube (this changes the angle of the beam); and
 - (Y2) the height of the laser beam entering the cage cube can be changed by slightly lifting or lowering the aluminum post holding the laser cage cube rods inside the pedestal post holders (this changes the position of the beam). To make (Y2) easier, use the slip-on post collars to temporarily "store" the post height. To do so, place the slip-on post collars on the two posts, slide them all the way down and fix them.
 - For the X-axis, the beam entering the cage cube can be changed by
 - (X1) temporarily loosening the clamping fork holding the aluminum post closest to the fiber output while rotating it around the other aluminum post (this changes the angle of the beam); and
 - (X2) moving the 1 axis translation stage (this changes the position of the beam).
 - Using the two alignment possibilities per axis, iteratively align the beam at the Z-translator position:
 - Use steps (Y2) and (X2) to make the laser beam hitting the alignment disk in the Z-translator in the center.
 - Afterwards, remove the alignment disk from the Z-translator. Instead, screw in the two SM1 extension tubes (SM1E60) and screw in an alignment disk at the top.
 - Use steps (Y1) and (X1) to make the laser beam hitting the alignment disk in the two extension tubes in the center.
 - Afterwards, remove the SM1 extension tubes, screw the alignment disk back directly into the Z-translator and go back to the first step.
 - Repeat these steps until the laser hits the alignment disk at both positions in the center.

488 nm laser

- Connect the laser to the computer following the manufacturer's instructions.
- Place the laser (1226420) on the heat sink (1193289).
- Make sure the laser is working.
- Place the laser on two posts (TRA75/M-P5), hold the posts by pedestal post holders (PH40E/M) and fix them to the breadboard using clamping forks (CF175C/M). It will be fine-positioned later.
- Assemble the cage system that will adjust the 488 nm laser beam-width and allow for its alignment:
 - Place the mirrors (BB1-E02) mirrors inside the mirror mounts (KCB1C/M)
 - Connect the ER3-P4 rods to the ER6-P4 rods to form 9-inch long rods and connect them to a mirror mount on one side.
 - Slide the lens mount (G061047000) onto the rods.
 - Slide a cage plate (CP11/M) onto the rods.
 - Connect the two mirror mounts using the ER6-P4 rods.
 - Connect three posts (TRA75/M-P5) to the mirror mounts as well as the cage plate. Fix them to the breadboard using the pedestal post holders (PH50E/M) and clamping forks.
 - Position the cage system in front of the 488 nm laser such that the beam travels straight through it. To do so, temporarily place an additional cage plate (CP02/M) at the entry side of the rod system.

- Temporarily screw one alignment disk (DG10-1500-H1-MD) into the temporarily placed cage plate at the entry side and another alignment disk (DG10-1500-H1-MD) into the entry side of the first mirror mount.
- Place the cage system in front of the 488 nm laser and vary its position until the laser hits both alignment disks in the center. You might make use of the small holes in the center of the alignment disks and/or iteratively mount and unmount them, until both are being hit in the center.
 - To vary the height and angle of the cage system, loosen the screws on the pedestal post holders and slide the posts further in or out.
 - To vary the position of the cage system on the breadboard, loosen the clamping forks and slide the pedestal post holders on the breadboard.
- As soon as the laser goes straight through the first part of the cage system, place the lenses inside the lens mount (G063205000) and the cage plate (LA1560-A-ML). The cage plate can be fixed at the end of the rods.
- Slide the lens mount almost all the way towards the mirror mount.
- Direct the 488 nm laser beam through the two lenses and collimate it by sliding the lens mount along the rail. Fix it once the beam is collimated.
- Place the 488 nm laser cage system at the side of the cage cube of the TIRF module.
- Place the 488 nm laser such that it goes straight through the lenses and enters the first mirror holder centered. To do so, you can either make use of the alignment disks at different positions or slide the cage system alignment plates (CPA1) along the rails to different positions.
- Make sure that the 488 nm laser beam goes straight through the center of the cage cube. To do so, iteratively follow these steps:
 - Temporarily screw an alignment disk into the cage cube and align the laser to its center using the first mirror.
 - Afterwards, screw the two SM1 extension tubes into the other side of the cage cube and screw the alignment disk to the exit side. Use the second mirror to align the laser beam to the center of the alignment disk.
 - Remove the SM1 extension tubes and iteratively repeat the two steps until the beam has been aligned.
- Put in the dichroic to combine the two lasers and re-align the 488 nm laser:
 - Mount the 488 nm laser clean up filter (LL01-488-12.5) in the SM1 to SM05 adaptor (SM1A6T) and screw it into the side-port of the cage cube that will hold the dichroic for combining the two lasers.
 - Mount the filter holder (FFM1) to the cage cube platform (B4C/M).
 - Mount the dichroic (FF499-Di01-25x36) to the filter holder.
- Place the cage cube platform inside the cage cube such that the mirror is at an angle of 45° with the reflective side towards the 488 nm laser.
- Slightly rotate the cage cube platform such that the 488 nm laser hits the Z-translator in the center. To view the laser beam, temporarily mount the RMS-to-SM1-adaptor (SM1A4) and an alignment disk (DG10-1500-H1-MD) in the Z-translator.
- Now the 488 nm laser has been roughly aligned. For fine alignment, the 488 nm laser has to hit the Z-translator (which will later hold the objective lens) both in the center as well as perpendicular. This requirement has to be fulfilled for both the x as well as the y direction. We therefore need four degrees of freedom in the setup.
 - For the Y-axis, the rotating angle of the dichroic can be changed by
 - The first mirror of the 488 nm cage cube system provides 2 degrees of freedom.
 - The second mirror of the 488 nm cage cube system provides 2 degrees of freedom.
- Using the two alignment possibilities per mirror, iteratively align the beam at the Z-translator position:
 - Use the first mirror of the 488 nm cage cube system to make the laser beam hitting the alignment disk in the Z-translator in the center.
 - Afterwards, remove the alignment disk from the Z-translator. Screw the two SM1 extension tubes (SM1E60) into the Z-translator and screw in an alignment disk at the top.
 - Use the second mirror of the 488 nm cage cube system to make the laser beam hit the alignment disk in the two extension tubes in the center.
 - Afterwards, remove the SM1 extension tubes, screw the alignment disk back directly into the Z-translator and go back to the first step.
- Repeat these steps until the laser hits the alignment disk at both positions in the center.

- Now both lasers should be aligned to the same positions. To check if both lasers are aligned to the same position, turn both lasers on and check if they are well overlaid at different positions of the beam path. If not, reiterate the alignment of the 488 nm laser using the two mirrors in the 488 nm cage cube system. If this does not work, realign the rotation of the dichroic combining the two lasers.

Epiillumination

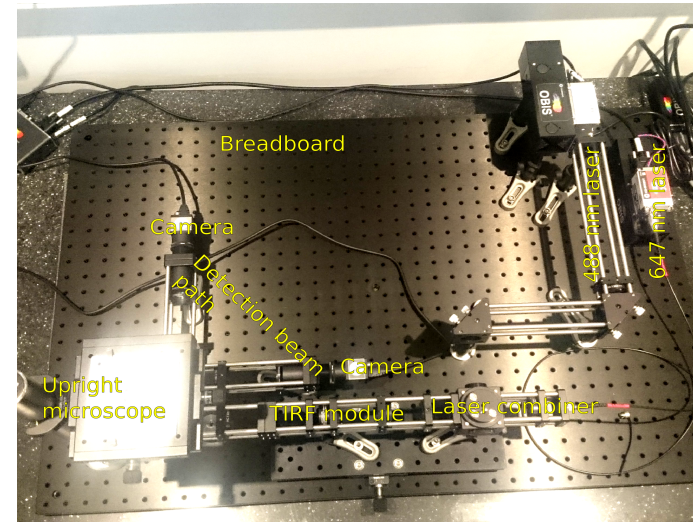
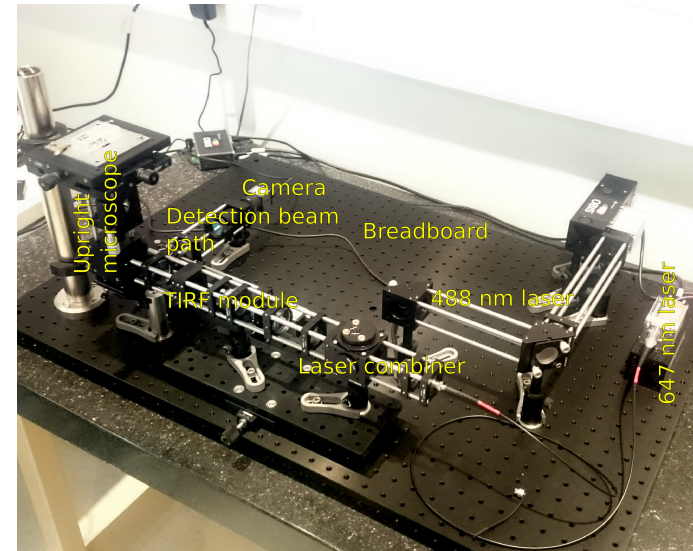
- Screw the objective lens (1-U2B617) into the Z-translator. If not in place, use the thread adaptor (SM1A3).
- Put the f=200 mm lens (G063205000) into the empty lens mount in the TIRF module.
- Turn on a laser and slide the lens mount along the rail system until the laser comes out of the objective lens as a collimated beam.
- Fix the lens mount to the rail system.
- To later change the illumination mode from widefield epi illumination to HILO or TIRF, drive the 1 axis translation stage hosting the TIRF module.

Cameras

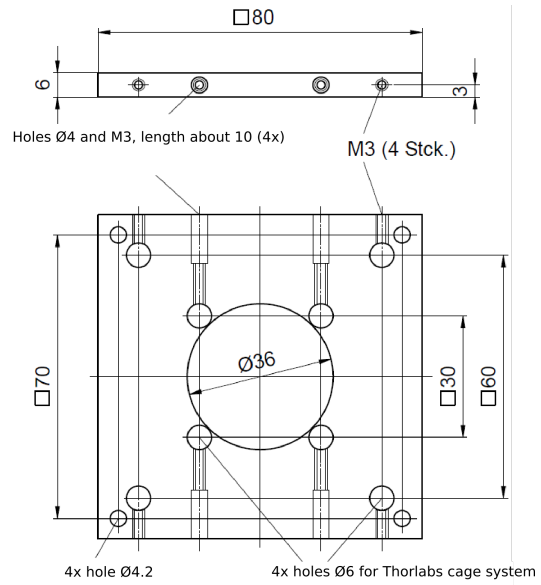
- Do this twice, i.e. for each camera:
 - Screw the thread adaptor (SM1A9) into the camera (AB00604).
 - Screw the SM1 coupler into the thread adaptor (SM1T10).
 - Screw the SM1 coupler into the cage cube, such that the inner thread is about half way filled by the SM1 coupler.
 - Make sure the camera is at an angle of 0° by rotating it. Then fix the angle by screwing a retaining ring into the other side of the cage cube.
 - Slide the cage plate holding the camera onto the cage rods such that it touches the other cage plate and fix it.
 - Slide the lens mount on the cage rods such that is approx. 170 mm away from the center of the camera. This is going to hold the tube lens.
- Install Micro-Manager 1.4.22 on your computer.
- Download the latest release of the IDS device adaptor from <https://github.com/biophotonics-bielefeld/ids-device-adaptor/releases> and use it to replace the mmgr_dal_ids_ueye.dll in the Micro Manager root directory.
- Download the IDS driver software from the manufacturer's webpage.
- Connect one camera to the computer via USB 3.0 and make sure it is working using the acquisition software provided by the manufacturer.
- Use the camera manager software provided by the manufacturer to change the ID of the camera from 1 to 2.
- Connect the other camera to the computer via USB 3.0 and make sure it is working using the acquisition software of the manufacturer.
- Start Micro-Manager and create a hardware configuration with both cameras. To do so, change the ID of one camera to 2 in the hardware configuration wizard.
- Save the hardware configuration and go to the live mode to view the camera image of the camera on the straight beam path.
- Use the device properties panel or create an according group in Micro-Manager to switch between the cameras.
- In the device properties, do the following:
 - Change to the value of the pixel clock to the maximum value.
 - Change the value of USB reconnect maximum tries to the maximum value.
 - Change the exposure time to 100 ms.
 - Change the value of the framerate to the maximum value.
 - For changing the exposure time or changing the ROI, repeat the last steps. You can save the settings via the group editor for convenience.
- Put the 700/75 bandpass filter (F47-700) into the filter holder (G06103100) and place it in the cage system before the camera of the straight beam path.
- Put the 647 nm long-pass (BLP01-647R-25) filter into the filter holder (G061031000) and place it in the cage system before the camera of the straight beam path.

- Make sure the correction collar of the objective lens is set to the nominal value, e.g. 0.17 when using #1.5 coverslips.
- If necessary, adjust the height of the Z-Translator such that the objective lens just does not touch a coverslip that will be placed on the sample holder.
- Apply immersion oil to the objective lens.
- Put the coverslip with fluorescent beads onto the sample holder.
- Turn on the 647 nm laser at low power.
- Focus onto the beads using the Z-Translator. If the travel range of the Z-Translator is not large enough to do so, put it to its middle position and carefully slide the Z-Translator along the cage rods until the focus is approximately reached and fix it. Then use the Z-Translator to find the focus.
- Find the correct position of the tube lens by minimizing spherical aberrations:
 - Use the Z-Translator to defocus to both directions (above and below the focal plane) and see if the three-dimensional point spread function (PSF) looks symmetric. In this case, you should see rings on both sides of the focus. If the PSF is not yet symmetric, you see very prominent rings on one side of the focus and blur on the other side of the focus.
 - In case of an asymmetric PSF, move the tube lens by a few millimeters on the rails, refocus using the z-Translator, and check the symmetry of the PSF again. If it gets better, continue moving the tube lens in the same direction. If it gets worse, move the tube lens in the opposite direction.
- Repeat these steps until the PSF looks similar to both sides of the focus.
 - Turn off the 647 nm laser.
- Put the 550/88 bandpass filter (FF01-550/88-25) into the filter holder (G061031000) and place it in the cage systems before the other camera.
- Put in the dichroic that separates the two emission channels and align it:
 - Mount the filter holder (FFM1) to the cage cube platform (B4C/M).
 - Mount the dichroic (FF640-FDi01-25x36) to the filter holder.
 - Place the cage cube platform inside the cage cube such that the mirror is at an angle of 45° with the reflective side facing the laser.
- Turn on the 488 nm laser at low power.
- Slightly rotate the cage cube platform such that the beads image becomes visible on the camera.
- Turn on the 647 nm laser.
- Using both cameras simultaneously, rotate the cage cube platform such that the images of both colors roughly overlap. Perfect overlap cannot be achieved anyway. Image registration should be handled later on in the post-processing.
- Turn off the lasers.
- Add multiple caps to shield the beam path:
 - Place the SM1-Threaded End Cap (SM1CP2) at the free side of the dichroic holder for combination of the two lasers. If you later want to realign the 488 nm laser, you will have to temporarily remove this cap.
 - Add the blank cover plate (B1C/M) at the free side of the dichroic holder in the upright microscope part.
 - Place the SM1-Threaded End Cap (SM1CP2) at the free side of the dichroic holder in the detection beam path.

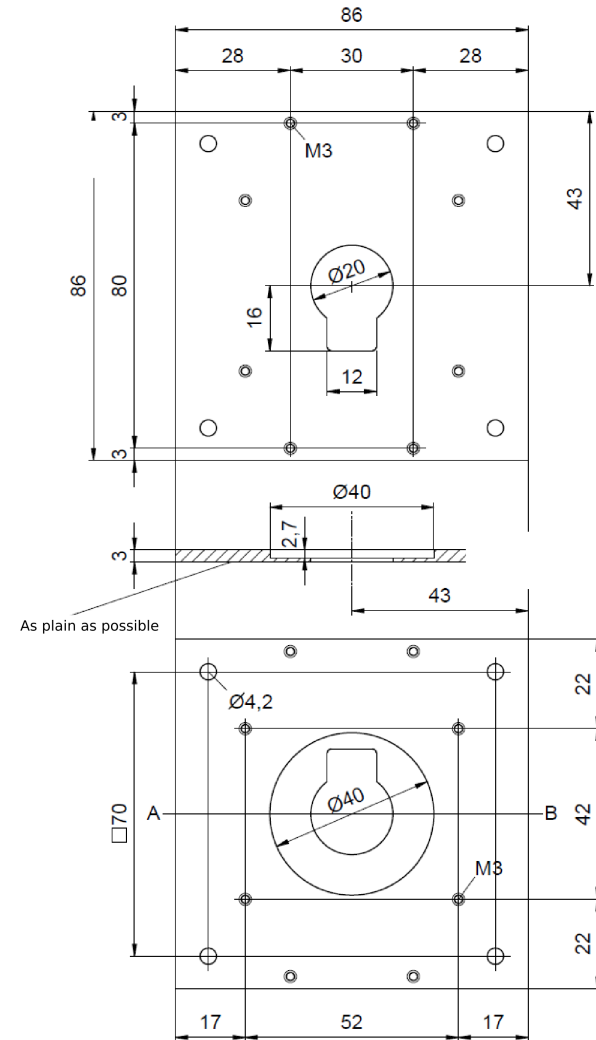
Pictures of assembled microscope



Connector of the Thorlabs 30 cm cage system to the microscope stage



Sample holder



Shopping list:

Custom-built dSTORM

Items	No.	Approx. total price	Supplier	Details
Part: 647 nm Laser				
Laser 647 (1193844)	1	€ 5 039.70	Coherent	OBIS 647 nm LX 100 mW laser, fiber pigtail
Laser cooling (1193289)	1	€ 437.84	Coherent	OBIS heat sink mount with fan
Fiber outcoupling holder (S1FCA)	1	€ 29.75	Thorlabs	Ø1" FC/APC Fiber Adapter Plate Without Thread
Frame for fiber outcoupling holder (CP02T/M)	1	€ 19.50	Thorlabs	SM1-Threaded 30 mm Cage Plate, 0.5" Thick, 2 Retaining Rings, Metric
Frame for holding collimating lens (CP02/M)	1	€ 14.90	Thorlabs	SM1-Threaded 30 mm Cage Plate, 0.35" Thick, 2 Retaining Rings, Metric
Collimating lens (LA1027-A-ML)	1	€ 41.25	Thorlabs	Ø1" N-BK7 Plano-Convex Lens, SM1-Threaded Mount, f = 35.0 mm, ARC:350-700 nm
Cage rods connecting 647 nm lens (ER3-P4)	1	€ 22.80	Thorlabs	Cage Assembly Rod, 3" Long, Ø6 mm, 4 Pack
Part: 488 nm Laser				
Laser 488 nm (1226420)	1	€ 7 374.01	Coherent	OBIS 488 nm LS 100 mW laser
Laser cooling (1193289)	1	€ 437.84	Coherent	OBIS heat sink mount with fan
Post holder for 488 nm laser construction (PH40E/M)	2	€ 42.80	Thorlabs	Ø12.7 mm Pedestal Post Holder, Spring-Loaded Hex-Locking Thumbscrew, L=44.7 mm

Post holder for 488 nm laser construction (PH50E/M)	3	€ 65.40	Thorlabs	Ø12.7 mm Pedestal Post Holder, Spring-Loaded Hex-Locking Thumbscrew, L=54.7 mm
Post for 488 nm construction (TRA75/M-P5)	1	€ 21.95	Thorlabs	Ø12.7 mm Aluminum Post, M4 Setscrew, M6 Tap, L = 75 mm, 5 Pack
Cage rods for 488 nm telescope, total length: 22.5 cm (ER3-P4)	1	€ 22.80	Thorlabs	Cage Assembly Rod, 3" Long, Ø6 mm, 4 Pack
Cage rods for 488 nm telescope, total length: 22.5 cm (ER6-P4)	1	€ 29.23	Thorlabs	Cage Assembly Rod, 6" Long, Ø6 mm, 4 Pack
Cage rods connecting 488 nm alignment mirrors (ER6-P4)	1	€ 29.23	Thorlabs	Cage Assembly Rod, 6" Long, Ø6 mm, 4 Pack
First lens in 488 nm telescope (CP11/M)	1	€ 14.90	Thorlabs	SM05-Threaded 30 mm Cage Plate, 0.35" Thick, Two Retaining Rings, M4 Tap
First lens in 488 nm telescope (LA1560-A-ML)	1	€ 39.75	Thorlabs	Ø1/2" N-BK7 Plano-Convex Lens, SM05-Threaded Mount, f = 25.0 mm, ARC: 350-700 nm
Second lens in 488 nm telescope-a (G063205000)	1	€ 147.00	Qioptiq	Achr. VIS ARB2; D=31.5; F=200; gefasst
Second lens in 488 nm telescope-b (G061047000)	1	€ 28.00	Qioptiq	Mount for 35mm Linos lens
Mirror holder for 488 nm alignment (KCB1C/M)	2	€ 260.00	Thorlabs	30 mm Cage Right-Angle Kinematic Mirror Mount with Smooth Cage Rod Bores
Mirror for 488 nm alignment (BB1-E02)	2	€ 135.18	Thorlabs	Ø1" Broadband Dielectric Mirror, 400 - 750 nm
Optional: frame for ND filter in 488 nm beam path (CPTR10/M)	1	€ 32.25	Thorlabs	Cage Plate to Ø1/2" Post Adapter, 10 mm Spacing, Metric
Optional: ND filter in 488 nm beam path (NE13A)	1	€ 44.50	Thorlabs	Ø25 mm Absorptive ND Filter, SM1-Threaded Mount, Optical Density: 1.3
Optional: post holder for ND filter in 488 nm beam path (PH40E/M)	1	€ 21.40	Thorlabs	Ø12.7 mm Pedestal Post Holder, Spring-Loaded Hex-Locking Thumbscrew, L=44.7 mm

Optional: post for ND filter in 488 nm beam path (TRA75/M)	1	€ 6.70	Thorlabs	Ø12.7 mm Aluminum Post, M4 Setscrew, M6 Tap, L = 75 mm
--	---	--------	----------	--

Part: Laser Combiner

Cage cube for laser overlay (C4W)	1	€ 53.75	Thorlabs	30 mm cage cube
Holder for 647 nm cleanup filter (SM1A6T)	1	€ 18.40	Thorlabs	Adapter with External SM1 Threads and Internal SM05 Threads, 0.15" Thick
647 nm cleanup filter (LL01-647-12.5)	1	€ 258.64	Semrock	647 nm MaxLine laser clean-up filter Laser Wavelength 647 nm 12.5 mm x 3.5 mm
Holder for 488 nm cleanup filter (SM1A6T)	1	€ 18.40	Thorlabs	Adapter with External SM1 Threads and Internal SM05 Threads, 0.15" Thick
488 nm cleanup filter (LL01-488-12.5)	1	€ 258.64	Semrock	488 nm MaxLine laser clean-up filter Laser Wavelength 488 nm 12.5 mm x 3.5 mm
Alignment for Dichroic (B4C/M)	1	€ 87.75	Thorlabs	Kinematic Cage Cube Platform for C4W/C6W, Metric
Cover plate on left (SM1CP2)	1	€ 15.80	Thorlabs	Externally SM1-Threaded End Cap
Cover plate on bottom (B1C/M)	1	€ 16.70	Thorlabs	Blank Cover Plate, Metric
Dichroic combining 647 nm and 488 nm laser (FF499-Di01-25x36)	1	€ 216.24	Semrock	488 nm edge BrightLine single-edge dichroic beamsplitter
Filter holder for dichroic (FFM1)	1	€ 52.25	Thorlabs	Cage-Compatible Rectangular Filter Holder

Part: TIRF Model

Breadboard holding TIRF unit (MB1030/M)	1	€ 58.50	Thorlabs	Aluminum Breadboard, 100 mm x 300 mm x 12.7 mm, M6 Taps
Translation stage for TRIF unit (PT1B/M)	1	€ 191.00	Thorlabs	Single-Axis Translation Stage
Cage rods holding multiple frames, connected to cage cube combining 647 nm and 488 nm lasers (ER12)	4	€ 61.20	Thorlabs	Cage Assembly Rod, 12" Long, Ø6 mm

Post holder (PH20E/M)	2	€ 41.80	Thorlabs	Ø12.7 mm Pedestal Post Holder, Spring-Loaded Hex-Locking Thumbscrew, L=25 mm
Post holder (TRA50/M)	2	€ 12.80	Thorlabs	Ø12.7 mm Aluminum Post, M4 Setscrew, M6 Tap, L = 50 mm
Post clamp for comfortable alignment (R2/M)	2	€ 9.00	Thorlabs	R2/M - Slip-On Post Collar for Ø1/2" Posts, Metric
First lens in beam diameter adjustment telescope (G0632020009)	1	€ 147.00	Qioptiq	Achr. VIS ARB2; D=31.5; F=120; gefasst
Frame for first lens in beam diameter adjustment telescope (G061047000)	1	€ 28.00	Qioptiq	Mount for 35mm Linos lens
Second lens in beam diameter adjustment telescope (LC1582-A-ML)	1	€ 38.75	Thorlabs	Ø1" N-BK7 Plano-Concave Lens, SM1-Threaded Mount, f = -75 mm, ARC: 350-700 nm
Frame for second lens in beam diameter adjustment telescope (CP02/M)	1	€ 14.90	Thorlabs	SM1-Threaded 30 mm Cage Plate, 0.35" Thick, 2 Retaining Rings, M4 Tap
Frame holding cage rods and connecting to post (CPTR20/M)	1	€ 32.25	Thorlabs	Cage Plate to Ø1/2" Post Adapter, 20 mm Spacing, Metric
Lens focusing lasers onto back-focal-plane of objective lens (G063205000)	1	€ 147.00	Qioptiq	Achr. VIS ARB2; D=31.5; F=200; gefasst
Frame for lens focusing lasers onto back-focal-plane of objective lens (G061047000)	1	€ 28.00	Qioptiq	Mount for 35mm Linos lens

Part: Upright Microscope

Big post holding the imaging part (DP14A/M)	1	€ 185.00	Thorlabs	Ø1.5" Dynamically Damped Post, 14" Long, Metric
Mounting clamp to big post (C1498/M)	2	€ 57.00	Thorlabs	Post mounting clamp

Microscope stage (KT 90-D56-EP)	1	€ 800.00	OWIS	X-Y stage with 20 mm travel
Z-focusing unit (SM1Z)	1	€ 173.00	Thorlabs	Z-Translator for Cage System
Thread adaptor from z-focusing unit to Olympus objective lens (SM1A3)	1	€ 15.60	Thorlabs	Adapter with External SM1 Threads and Internal RMS Threads
60x TIRF lens (1-U2B617)	1	€ 6 352.00	Olympus	Olympus APO N 60x / 1.49 TIRF objective for BX & IX microscopes
Cage rods connecting microscope stage and c6w cage cube holding the dichroic (ER4-P4)	1	€ 24.51	Thorlabs	Cage Assembly Rod, 4" Long, Ø6 mm, 4 Pack
Cage cube holding the dichroic (C6W)	1	€ 56.75	Thorlabs	30 mm Cage Cube with ER Clearance Holes
End cap on cage cube (SM1CP2)	1	€ 15.80	Thorlabs	Externally SM1-Threaded End Cap
Alignment stage for dichroic (B4C/M)	1	€ 87.75	Thorlabs	Kinematic Cage Cube Platform for C4W/C6W, Metric
Imaging dichroic (Di03-R405/488/532/635)	1	€ 504.56	Semrock	405/488/532/635 nm lasers BrightLine® quad-edge super-resolution laser dichroic
Filter holder for dichroic (FFM1)	1	€ 52.25	Thorlabs	Cage-Compatible Rectangular Filter Holder
Cover plate on cage cube (B1C/M)	1	€ 16.70	Thorlabs	Blank Cover Plate, Metric
Frame connecting imaging part to big post (CPTR10/M)	1	€ 32.25	Thorlabs	Cage Plate to Ø1/2" Post Adapter, 10 mm Spacing, Metric
Post connecting CPTR10/M to mounting clamp to big post (TRA30/M)	1	€ 5.95	Thorlabs	Ø12.7 mm Aluminum Post, M4 Setscrew, M6 Tap, L = 30 mm
Cage rods connecting cage cube to elliptical mirror holder (ER05-P4)	1	€ 17.45	Thorlabs	Cage Assembly Rod, 1/2" Long, Ø6 mm, 4 Pack

Elliptical mirror holder in fluorescence detection path (KCB1EC/M)	1	€ 184.00	Thorlabs	Right-Angle Kinematic Elliptical Mirror Mount with Smooth Cage Rod Bores, 30 mm Cage System and SM1 Compatible, M4 and M6 Mounting Holes
Elliptical mirror in fluorescence detection path (BBE1-E02)	1	€ 85.25	Thorlabs	1" Broadband Dielectric Elliptical Mirror, 400 - 750 nm
Mounting clamp connecting elliptical mirror holder and small post (RM1B/M)	1	€ 45.00	Thorlabs	Ø25.0 mm Post Clamp, M4 Tap, M4 Threaded Stud
Small post supporting imaging part (RS3P/M)	1	€ 26.50	Thorlabs	Ø25.0 mm Pedestal Pillar Post, M6 Taps, L = 75 mm
Custom made adaptor form Thorlabs cage rod system to X-Y stage	1			
Custom made sample holder	1			

Part: Detection Beam Path

Cage cube for emission splitting (C4W)	1	€ 53.75	Thorlabs	30 mm cage cube
Post holder for frame close to cage cube in fluorescence detection (PH20E/M)	1	€ 20.90	Thorlabs	Ø12.7 mm Pedestal Post Holder, Spring-Loaded Hex-Locking Thumbscrew, L=25 mm
Post for frame close to cage cube in fluorescence detection (TRA30/M)	1	€ 5.95	Thorlabs	Ø12.7 mm Aluminum Post, M4 Setscrew, M6 Tap, L = 30 mm
Frame connecting post and cage rods (CP02/M)	1	€ 14.90	Thorlabs	SM1-Threaded 30 mm Cage Plate, 0.35" Thick, 2 Retaining Rings, M4 Tap
Cage rods connecting elliptical mirror holder to cage cube in fluorescence detection (ER1-P4)	1	€ 17.45	Thorlabs	Cage Assembly Rod, 1" Long, Ø6 mm, 4 Pack

Cage plate on cage cube (SM1CP2)	1	€ 15.80	Thorlabs	Externally SM1-Threaded End Cap
Alignment platform for dichroic mirror (B4C/M)	1	€ 87.75	Thorlabs	Kinematic Cage Cube Platform for C4W/C6W, Metric
Dichroic mirror in fluorescence path (FF640-FDi01-25x36)	1	€ 284.08	Semrock	640 nm edge BrightLine single-edge imaging-flat dichroic beamsplitter 25.2x35.6x1.1mm
Dichroic mirror holder (FFM1)	1	€ 52.25	Thorlabs	Cage-Compatible Rectangular Filter Holder

Part: Camera (647 nm)

Cage rods connecting cage cube and camera (ER6-P4)	1	€ 29.23	Thorlabs	Cage Assembly Rod, 6" Long, Ø6 mm, 4 Pack, only 3 are being used
Cage rods (ER2-P4)	1	€ 21.09	Thorlabs	Cage Assembly Rod, 2" Long, Ø6 mm, 4 Pack, 2 rod cage, screwed together mounted to the camera, leaving a hole to remove the filters conveniently
Tube lens for 647 nm camera (G063204000)	1	€ 147.00	Qioptiq	Achr. VIS ARB2; D=31.5; F=160; gefasst
Frame for tube lens (G061047000)	1	€ 28.00	Qioptiq	Mount for 35mm Linos lens
647 nm bandpass filter (F47-700)	1	€ 339.00	AHF	700/75 ET Bandpass AOI 0° Diameter 25 mm
647 nm longpass filter (BLP01-647R-25)	1	€ 301.04	Semrock	647 nm EdgeBasic best-value long-pass edge filter
Filter holders (G061031000)	2	€ 56.00	Qioptiq	Filter holder before camera
Frame connecting cage system to post (CP02/M)	1	€ 14.90	Thorlabs	SM1-Threaded 30 mm Cage Plate, 0.35" Thick, 2 Retaining Rings, M4 Tap
Post holder for frame supporting cage system (PH20E/M)	1	€ 20.90	Thorlabs	Ø12.7 mm Pedestal Post Holder, Spring-Loaded Hex-Locking Thumbscrew, L=25 mm
Post for frame supporting cage system (TRA30/M)	1	€ 5.95	Thorlabs	Ø12.7 mm Aluminum Post, M4 Setscrew, M6 Tap, L = 30 mm

Lens tube connected to frame before camera (SM1L10)	1	€ 12.83	Thorlabs	SM1 Lens Tube, 1" Thread Depth, One Retaining Ring Included
Frame connecting camera to cage system (CP02/M)	1	€ 14.90	Thorlabs	SM1-Threaded 30 mm Cage Plate, 0.35" Thick, 2 Retaining Rings, M4 Tap
Camera to tube adapter thread (SM1A9)	1	€ 17.40	Thorlabs	Adapter with External C-Mount Threads and Internal SM1 Threads
Tube connecting camera to frame (SM1T10)	1	€ 18.60	Thorlabs	SM1 (1.035"-40) Coupler, External Threads, 1" Long
USB 3.0 cable	1	€ 6.00		
647 nm camera (AB00604)	1	€ 587.66	IDS	iDS imaging monochrome CMOS camera UI-3060CP-M-GL Rev.2

Part: Camera (488 nm)

Cage rods connecting cage cube and camera (ER6-P4)	1	€ 29.23	Thorlabs	Cage Assembly Rod, 6" Long, Ø6 mm, 4 Pack, only 3 are being used
Tube lens for 488 nm camera (G063204000)	1	€ 147.00	Qioptiq	Achr. VIS ARB2; D=31.5; F=160; gefasst
Frame for tube lens (G061047000)	1	€ 28.00	Qioptiq	Mount for 35 mm Linos lens
550/88 nm single-band bandpass filter (FF01-550/88-25)	1	€ 301.04	Semrock	550/88 nm BrightLine® single-band bandpass filter
Filter holders (G061031000)	1	€ 28.00	Qioptiq	Filter holder before camera
Frame connecting cage system to post (CP02/M)	1	€ 14.90	Thorlabs	SM1-Threaded 30 mm Cage Plate, 0.35" Thick, 2 Retaining Rings, M4 Tap
Post holder for frame supporting cage system (PH20E/M)	1	€ 20.90	Thorlabs	Ø12.7 mm Pedestal Post Holder, Spring-Loaded Hex-Locking Thumbscrew, L=25 mm
Post for frame supporting cage system (TRA30/M)	1	€ 5.95	Thorlabs	Ø12.7 mm Aluminum Post, M4 Setscrew, M6 Tap, L = 30 mm
Lens tube connected to frame before camera (SM1L10)	1	€ 12.83	Thorlabs	SM1 Lens Tube, 1" Thread Depth, One Retaining Ring Included

Frame connecting camera to cage system (CP02/M)	1	€ 14.90	Thorlabs	SM1-Threaded 30 mm Cage Plate, 0.35" Thick, 2 Retaining Rings, M4 Tap
Camera to tube adapter thread (SM1A9)	1	€ 17.40	Thorlabs	Adapter with External C-Mount Threads and Internal SM1 Threads
Tube connecting camera to frame (SM1T10)	1	€ 18.60	Thorlabs	SM1 (1.035"-40) Coupler, External Threads, 1" Long
USB 3.0 cable	1	€ 6.00		
488 nm camera (AB00604)	1	€ 587.66	IDS	iDS imaging monochrome CMOS camera UI-3060CP-M-GL Rev.2

Misc.

Small clamping forks (CF125C/M)	7	€ 68.25	Thorlabs	Clamping Fork, 1.24" Counterbored Slot, 1/4"-20 Captive Screw
Big clamping forks (CF175C/M)	4	€ 42.80	Thorlabs	Clamping Fork, 1.76" Counterbored Slot, 1/4"-20 Captive Screw
Screws (SH4MS06)	1	€ 5.75	Thorlabs	M4 x 0.7 Stainless Steel Cap Screw, 6 mm Long, Pack of 50
Screws (SH4MS10)	1	€ 6.00	Thorlabs	M4 x 0.7 Stainless Steel Cap Screw, 10 mm Long, Pack of 50
Screws (SH4MS16)	1	€ 6.30	Thorlabs	M4 x 0.7 Stainless Steel Cap Screw, 16 mm Long, Pack of 50
Screws (W8S038)	1	€ 3.02	Thorlabs	#8 Washer, M4 Compatible, Stainless Steel, Pack of 100
Screws (SH6MS06)	1	€ 11.50	Thorlabs	M6 x 1.0 Stainless Steel Cap Screw, 6 mm Long, Pack of 25
Screws (SH6MS10)	1	€ 7.00	Thorlabs	M6 x 1.0 Stainless Steel Cap Screw, 10 mm Long, Pack of 25
Screws (SH6MS16)	1	€ 7.45	Thorlabs	M6 x 1.0 Stainless Steel Cap Screw, 16 mm Long, Pack of 25
Screws (SH6MS25)	1	€ 8.85	Thorlabs	M6 x 1.0 Stainless Steel Cap Screw, 25 mm Long, Pack of 25

Screws (W25S050)	1	€ 4.18	Thorlabs	1/4" Washer, M6 Compatible, Stainless Steel, Pack of 100
Set of Threaded Pins (G061011000)	1	€ 13	Qioptiq	Set of Threaded Pins M2.3x3, 150 ea.
DV Immersion oil kit (29163068)	1	€ 176.38	GE Healthcare	different immersion oil for correction of spherical aberrations
Screw into frames etc. for alignment (SM1L20)	1	€ 14.85	Thorlabs	SM1 Lens Tube, 2" Thread Depth, One Retaining Ring Included
Opaque target for alignment (DG10-1500-H1-MD)	2	€ 58.50	Thorlabs	Ø1" SM1-Mounted Frosted Glass Alignment Disk w/Ø1 mm Hole
Screw-in target for alignment (SM1A7)	1	€ 22.90	Thorlabs	SM1 Series Alignment Disk
Target for alignment to be put onto cage rod system (CPA1)	2	€ 22.80	Thorlabs	30 mm Cage System Alignment Plate with Ø1 mm Hole
Screw into objective lens holder etc. for alignment (SM1E60)	2	€ 82.00	Thorlabs	SM1 Extension Tube, 6" Long, 1" Thread Depth, One Retaining Ring Included
Adapter for objective lens holder (SM1A4)	1	€ 21.40	Thorlabs	Adapter with External RMS Threads and Internal SM1 Threads
Lens tissue for cleaning (MC-5)	3	€ 27.30	Thorlabs	Lens Tissues, 25 Sheets per Booklet, 5 Booklets
Tool (CCHK/M)	1	€ 20.90	Thorlabs	9-piece hex key set metric
Tool (CCHK)	1	€ 20.90	Thorlabs	11-Piece Color-Coded Hex Key Set, Imperial
Tool (TC3/M)	1	€ 78.00	Thorlabs	15-piece balldriver kit
Tool (PSS7)	1	€ 52.00	Thorlabs	7-piece precision screw-driver set
Big breadboard (MB4590/M)	1	€ 508.00	Thorlabs	Aluminum Breadboard 450 mm x 900 mm x 12.7 mm M6 taps

Total € 29 598.56

Paper II



Effect of caffeine, theobromine and other xanthines on liver sinusoidal endothelial cell ultrastructure

Hong Mao¹, Karolina Szafrńska¹, Deanna L. Wolfson², Balpreet Singh Ahluwalia², Cynthia B. Whitechurch³, Glen P. Lockwood⁴, Robin Diekmann⁵, David Le Couteur⁴, Victoria C. Cogger⁴, Peter A.G. McCourt¹

¹ Vascular Biology Research Group, Department of Medical Biology, Faculty of Health Sciences, University of Tromsø-The Arctic University of Norway, Tromsø, Norway

² Optical Nanoscopy Research Group, Department of Physics and Technology, Faculty of Science and Technology, University of Tromsø-The Arctic University of Norway, Tromsø, Norway

³ Microbial Imaging Facility. the itthree institute, University of Technology Sydney, Ultimo, NSW, Australia

⁴ ANZAC Research Institute, Concord Repatriation General Hospital, Concord, NSW, Australia; and The University of Sydney, Charles Perkins Centre, Nutritional Ecology and Physiology Lab, Sydney, NSW, Australia

⁵ Cell Biology and Biophysics Unit, European Molecular Biology Laboratory (EMBL), Heidelberg, Germany

Corresponding author:

Peter A.G. McCourt

Vascular Biology Research Group,

Department of Medical Biology,

Faculty of Health Sciences,

University of Tromsø-The Arctic University of Norway

9037 Tromsø, Norway

Phone: +47 77646391

E-mail: peter.mccourt@uit.no

Keyword:

Liver sinusoidal endothelial cell, caffeine, theobromine, fenestration, ultrastructure

ABSTRACT

Objectives: Xanthines such as caffeine and theobromine are among the most consumed psychoactive stimulants in the world, either as natural components of coffee, tea and chocolate, or as food additives. Caffeine has been reported to have anti-fibrotic effects in the liver. The present study aimed to assess if xanthines are of any benefit for liver sinusoidal endothelial cells (LSECs).

Methods: Cultured primary rat LSECs were challenged with xanthines at concentrations that can be obtained by upper normal consumption of xanthine containing beverages and food stuff (in vivo “physiological” concentrations), and at in vivo toxic concentrations. The cell cultures were examined with scanning electron microscopy and structured illumination microscopy. LSEC viability was monitored with endocytosis assays.

Results: With the exception of toxic concentrations of theobromine, all xanthine challenges had no negative effects on LSEC ultrastructure as judged by LSEC fenestration status, and function as judged by endocytosis studies. In most xanthine challenges, the fenestration diameter was reduced, while there was a simultaneous tendency to increased fenestration frequency. Theobromine at physiological concentrations and theophylline at toxic concentrations induced significantly increased LSEC porosity, which is a function of both fenestration frequency and diameter.

Conclusion: Theobromine (~8 µg/mL) increases the porosity of rat LSEC *in vitro*. This concentration can be attained in human plasma from the daily consumption of 40-80 g of dark chocolate. If theobromine can induce similar changes *in vivo*, theobromine treatment might be of benefit for elderly people who have reduced LSEC porosity. Further *in vivo* studies are therefore needed to determine if theobromine can be an intervention of benefit for liver health.

INTRODUCTION

The liver, as the body's largest organ, has the major role of detoxifying various metabolites in the human body. Liver sinusoidal endothelial cells (LSECs), located in hepatic sinusoids, play a fundamental role in maintaining homeostasis and metabolic integrity of the liver (59), and their distinct dynamic morphological character – fenestrations - enable bidirectional transportation (according to the size of substrates) between the blood and the underlying hepatocytes. Fenestrations are non-diaphragmed pores with diameters of 50-300 nm (12, 29), typically grouped in clusters called “sieve plates” (64, 65). The structural integrity of fenestrations is believed to be vital for the maintenance of regular exchange between the liver and the blood, and the alteration of fenestrations can have adverse effects on hepatocytes and liver function (65). The regulation of fenestration size and frequency is assumed to be via the effects of nitric oxide (NO) via a vascular endothelial growth factor (VEGF)-related & independent pathways (63, 66), and a previous study has demonstrated that sildenafil acts on this pathway to enhance fenestrations size (31). It should be noted however that other pathways may also be involved in the regulation of fenestration size (e.g. those mediated by calcium, and by alpha and beta adrenergic receptors among others (28). Moreover, LSECs are the most effective scavenger of blood-borne waste, regulate the sinusoidal blood flow (39), trigger liver regeneration and contribute to hepatic complications, such as liver fibrosis and liver metastasis (21, 46, 59).

Caffeine is a stimulant compound in the xanthine class of chemicals, and is primarily metabolized in the liver to theobromine, theophylline and paraxanthine. In the human liver paraxanthine is the main metabolite, accounting for approximately 80% of the metabolites in caffeine biotransformation (2, 51). In rats, all three main metabolites of caffeine are roughly present in similar amounts, which demonstrates the differences in caffeine metabolism among species (3, 7, 44). Overall, more than 25 metabolites have been identified in humans after caffeine metabolism (16, 57). All the aforementioned primary metabolites are pharmacologically active and their plasma concentration may exceed that of caffeine in some stages due to their respective rate of metabolism and clearance(1), although paraxanthine has a potentially lower toxicity than caffeine (44).

Nowadays, caffeine as the most widely consumed psychostimulant in the world, is generally considered to be safe in moderate amounts (≤ 400 mg /day) in healthy adults (20, 43). The plasma concentrations of caffeine are usually between 2-10 $\mu\text{g/mL}$ (approximately 10-50 μM , rarely exceeding 50-60 μM during normal human consumption in adults (26), with toxic effects occurring at plasma caffeine concentrations more than 40 $\mu\text{g/mL}$ (26, 33). The adverse effects of very large doses of caffeine have been noted from early times, and these include nervousness, anxiety, insomnia, irregular heartbeats, excess stomach acid and heartburn (22). If consumed with adequate quantities, it can cause significant toxicity and even be fatal (10 g/person) (32, 43).

For theophylline to achieve adequate control of adult asthma, the required plasma concentration is 8-20 $\mu\text{g}/\text{mL}$ in humans (5, 8, 10, 49). Chocolate contains two methylated xanthine derivatives (caffeine and theobromine), which may contribute to its reinforcing effects (4). It was reported that 370 mg theobromine from 82g chocolate (40-80g of dark chocolate or 110g of regular milk chocolate) was rapidly absorbed in humans and produces a plasma concentration of 8.05 $\mu\text{g}/\text{mL}$ after 2hours (38, 42, 47).

Though caffeine is widely used all over the world, its effects on LSEC have not been investigated. Here, we investigated the effect of caffeine and its major xanthine metabolites at their physiological plasma doses on rat LSEC using super-resolution methods such as electron microscopy and structured illumination microscopy. Of all the tested xanthines, theobromine enhanced the fenestration porosity of cultured rat LSEC at a dose physiologically relevant for humans.

MATERIALS AND METHODS

Rat LSEC production and Cell culture

Sprague Dawley male rats (Animal Resource Centre, Murdoch, Western Australia) were kept under standard conditions and fed standard chow ad libitum (Glen Forrest, Western Australia). The experimental protocols were approved by the ethics committee of the Sydney Local Health District Animal Welfare Committee (Approval 2017/012A). All experiments were performed in accordance with relevant approved guidelines and regulations.

Reagents included caffeine (Cat No. C0750; Sigma-Aldrich, Oslo, Norway), sildenafil citrate (Cat No. PHR1807, Sigma-Aldrich, Oslo, Norway), theobromine (Cat No. T4500; Sigma-Aldrich, Oslo, Norway), theophylline (Cat No. T1633; Sigma-Aldrich, Oslo, Norway), paraxanthine (Cat No. P6148; Sigma-Aldrich, Oslo, Norway). Fibronectin was isolated from human plasma using gelatin-Sepharose (GE Healthcare, Sydney, Australia) according manufacturer's instructions. All reagents were dissolved in serum-free RPMI media. All experiments were performed in triplicate. Caffeine (8 and 150 µg/mL) [physiologically relevant plasma and high dosages were selected based on previous works (26, 33)]. Metabolites of caffeine: theobromine (8 and 150 µg/mL), theophylline (49) (20/30 and 150 µg/mL), paraxanthine(8 and 150 µg/mL) were applied at physiologically relevant and high dosages as for caffeine. The NO pathway was elicited with sildenafil (0.6 and 0.06 µg/mL) [dosages based on previous works (31, 37), in mice and rats respectively, for method validation purposes]. CellMask Green (Cat No. C37608; Fisher Scientific, Oslo, Norway)

Male rats (body weight 300-400 g) were anesthetized with a mixture of 10 mg/kg Xylazine (Bayer Health Care, California, USA) and 100 mg/kg ketamine (Ketalar, Pfizer, New York, USA) and LSECs were isolated and purified as described Smedsrod, *et al.* (55), several fractions of cells were prepared for each of the methodologies: for EM and endocytosis; for SIM observation, cells are plated on 0.2 mg/mL fibronectin [purified from human plasma by affinity chromatography on Gelatin Sepharose 4B as described by the manufacturer (GE Healthcare, Uppsala, Sweden)] coated #1.5 coverslips (Sigma-Aldrich, Sydney, Australia) cultured (37°C, 5% CO₂) for 3 h in serum-free RPMI-1640 (with 10,000 U/mL Penicillin, 10 mg/mL Streptomycin, 1:100) (Sigma-Aldrich, Sydney, Australia) at a density of 0.2×10^6 cells/cm². Fibronectin coating was performed using just enough volume to completely cover the surface area. After 10 min of incubation at room temperature (RT), the fibronectin was washed off with PBS and then the cells were seeded. The LSECs were treated with various agents for 30 min to determine effects on fenestrations, then fixed with 4% formaldehyde (FA) in phosphate buffered saline (PBS) and 0.02 M sucrose (Sigma-Aldrich, Sydney, Australia), pH 7.2 for 15 min, and stored in PBS until visualization on a structured illumination microscope (SIM) or a scanning electron microscope (SEM).

Structured illumination microscope (SIM)

After fixation, the cells were stained with CellMask Green (1:1000 in serum-free RPMI) for 10 minutes or Alexa Fluor 488 phalloidin (1:40 in serum free RPMI) for 20 minutes, and mounted in VECTASHIELD antifade mounting medium (Vectro Laboratories, Burlingame, California) and imaged using a commercial super-resolving SIM (DeltaVision/OMXv4.0 BLAZE, GE Healthcare) with a 60X 1.42NA oil-immersion objective (Olympus). 3D-SIM images stacks of 1 μm were acquired with a z-distance of 125 nm and with 15 raw images per plane (five phases, three angles). Raw datasets were computationally reconstructed using SoftWoRx software (GE Healthcare). The datasets were further analyzed using the pixel classification workflow in the freely available machine learning image processing software Ilastik (6, 58). Fenestration detection steps were described in our previous study (37), notably, the diameters ranged from 50–300 nm for filtering prior to binning for SIM images.

Scanning electron microscopy (SEM)

For SEM preparation, cryopreserved rat LSECs were used, the thawing and culturing protocols are described in our previous study (40). The treatments of agents are as mentioned above. The treated cells were fixed overnight in McDowell's or 4% formaldehyde (FA), 2.5% glutaraldehyde (GA) in cacodylic buffer. After washes with PBS, the coverslips containing the cells were treated with freshly made 1% tannic acid in 0.15 mol/l cacodylic buffer for 1 hour, 1% OsO₄ in 0.1 mol/l cacodylic buffer for 1 hour, dehydrated in ethanol (30%, 60%, 90% for 5 minutes each, 5 times 100% ethanol for 4 minutes), and incubated twice in hexamethyldisilazane for 2 minutes each (Sigma-Aldrich, Oslo, Norway), before coating with 10-nm gold/palladium alloys. Specimens were examined using a commercial SEM (Sigma HV0307, Zeiss). Large fields of view containing several/individual cells were randomly acquired in specific location (see next paragraph) on the stubs to determine cell culture condition and cell size, and high-resolution SEM images of cell at magnification of 15k were randomly acquired to assess fenestration size, porosity and frequency. Measurements of fenestration size, porosity and frequency were done using the public domain software Fiji (<https://imagej.net/Fiji>)(52).

Fenestration size, porosity and frequency were assessed in SEM images from each cell culture selected from different areas. Fenestrations and gaps were defined as open pores with diameters between 50–300 nm and larger than 300 nm, respectively. Porosity was defined as the sum area of fenestrations per total area of the cell in the micrograph. Frequency was denoted as the total number of fenestrations per sum area of the cell exclude the sum area of gaps. The measurements in Fiji software were performed according to our previous study (40).

Endocytosis and degradation assay.

For quantitative studies of endocytosis and degradation, fully confluent cultures of cryopreserved rat LSECs (approx. $0.2\text{--}0.25 \times 10^6$ cells/cm²) established in 24-well culture dishes coated with fibronectin, were treated with different agents mentioned above for 30 minutes at 37 °C, subsequently incubated in 0.2 mL serum-free RPMI containing 0.1% human serum albumin and $2\text{--}3 \times 10^4$ cpm ¹²⁵I-FSA for 2 h. Thereafter, the cell-associated and degraded FSA fractions were assayed according to (35). The radioactivity was measured using a Cobra II, Auto-Gamma detector (Packard Instruments, Laborel, Oslo, Norway). Cell association and degradation of ligands in each treatment for endocytosis were respectively analyzed with one-way ANOVA performed using the GraphPad Prism 8 (La Jolla, USA, www.graphpad.com), the post hoc tests were used with Dunnett's multiple comparisons test for each treatment with RPMI control.

Statistical analysis

Fenestration diameters, porosities, frequencies and cell association/degradation of ligands in each treatment for endocytosis were respectively analyzed with one-way ANOVA performed using the GraphPad Prism 8, the post hoc tests were used with Dunnett's multiple comparisons test for each treatment with RPMI control. Two-tailed Welch's t-test was used to assess between-group differences within a treatment (i.e. physiological and high doses) for fenestration porosity and frequency comparisons. Differences were considered significant if $p < 0.05$.

RESULTS

SEM data with the analyzed number of cells and fenestration diameter, porosity and frequency following various treatments are shown in Table 1. The average diameter of the fenestrae from different treatments ranged from 175-190 nm (roughly 7200-69000 holes were analyzed, see Table 1), average porosity and frequency (about 17-157 cells were assessed) ranged from 5.4-8.5 % and 1.9-3.0 / μm^2 , respectively.

The shape of cells from different treatment groups in culture was observed with no differences: typical “fried-egg” like shape, and presence of unique morphological feature of LSECs—fenestrations (Fig. 1) which indicate healthy cell status/condition. The holes were present in all treatment groups in clusters (>5) called sieve plates, small groups (<5) or alone.

Effects of exogenous xanthine on fenestrations

Differences were observed in the responses of LSECs to certain xanthines and doses: the mean diameter of fenestrae tended to decrease slightly ($\leq 7\%$) with all xanthine agents except paraxanthine (150 $\mu\text{g}/\text{mL}$), with no physiologically relevant change from the control group. Frequency changes, in general, were increased with all xanthine treatment groups. Porosity changes tended to increase except caffeine (8 $\mu\text{g}/\text{mL}$) and theobromine (150 $\mu\text{g}/\text{mL}$) (Table 1; Fig. 1C and 1F). The physiological dose of theobromine (8 $\mu\text{g}/\text{mL}$) was significantly associated with increased fenestration porosity and frequency (Table 1; Fig. 1E), and there was a significant increase in frequency (number of fenestra) with high doses of theophylline (150 $\mu\text{g}/\text{mL}$), resulting in an increase in porosity in the same condition (Table 1; Fig. 1H). The sildenafil group was tested for comparison with an earlier study in mice (31). Higher dosages of sildenafil (0.6 $\mu\text{g}/\text{mL}$) did not promote greater changes in fenestration porosity or frequency in LSEC from young mice, which is consistent with previous findings (31). However, there was a reduction (5.3%) of fenestration diameter in this dosage in our findings (Table 1). Furthermore, a sildenafil dosage of 0.06 $\mu\text{g}/\text{mL}$ did not increase fenestration diameter (Table 1 & Fig. 1B inset).

There were effects of xanthine treatments on the frequency distribution of fenestration diameter. Caffeine (8 $\mu\text{g}/\text{mL}$) induced an increase ($\sim 3\%$ and 29% , respectively) in <200 nm and a $\sim 38\%$ reduction in >200 nm region. However, an $\sim 57\%$ increase in <200 nm region and a $\sim 22\%$ decrease in >200 nm-sized fenestrations occurred in the high dose of caffeine (150 $\mu\text{g}/\text{mL}$). Both treatments tended to elicit smaller fenestrations (Fig. 2B, CA8&150). Theobromine (8 $\mu\text{g}/\text{mL}$) elicited an increase in <200 nm fenestrations, and the higher dose (150 $\mu\text{g}/\text{mL}$) of theobromine resulted in $\sim 95\%$ increase of small fenestrations at <100 nm and $\sim 15\%$ decrease in large fenestrations (>200 nm) (Fig. 2B, TB8&150). Theophylline (20 $\mu\text{g}/\text{mL}$) produced an $\sim 10\%$ increase of fenestrations in <200 nm, while a higher dose of theophylline (150 $\mu\text{g}/\text{mL}$) yielded 26% more fenestrations in <200 nm and 34% fewer fenestrations in the >200 nm region, which

altered average diameter to around 180.0 nm (Fig. 2B TP20&150). Paraxanthine (8 $\mu\text{g}/\text{mL}$) produced $\sim 30\%$ increase in <200 nm fenestrations, and 34% reduction of fenestrae in >200 nm area. Higher doses of paraxanthine elicited an $\sim 23\%$ increase in <100 nm, a $\sim 5\%$ reduction in 100-200 nm fenestrations and a slight increase in >200 nm-sized fenestrae (Fig. 2B, PA8&150). Sildenafil (0.06 $\mu\text{g}/\text{mL}$) was associated with an 11% increase in >200 nm fenestrations, which elevated the average diameter to 191.3 nm. Higher doses resulted in a 71% increase of smaller fenestrations at <100 nm and $\sim 13\%$ reduction in >200 nm, resulting the average diameter in 180.0 nm (Fig. 2B, SIL 0.06&0.6).

Porosity was increased primarily as a result of increased number (frequency) rather than the size of fenestrations (Fig. 2C). Porosity changes (Fig. 2D) show LSEC treated with caffeine (8 $\mu\text{g}/\text{mL}$) and theobromine (150 $\mu\text{g}/\text{mL}$) resulted in a decrease in average porosity, the rest of treatments overall tended to elicit higher porosity compared with control, with theobromine (8 $\mu\text{g}/\text{mL}$) causing a significant increase (39%) in porosity over control cells. Within caffeine treatments, the increase of dose from 8 $\mu\text{g}/\text{mL}$ to 150 $\mu\text{g}/\text{mL}$, significantly increased the porosity by 28% ($P < 0.05$, $n = 33$ and 34, respectively). Frequency changes (Fig. 2E) exhibit a general increase in all treatments compared with control. However, only high doses of theobromine and theophylline (150 $\mu\text{g}/\text{mL}$) give a significant rise (47% and 40%, respectively) in fenestration numbers compared with the control group. Within theobromine treatments, the high dose (150 $\mu\text{g}/\text{mL}$) resulted in a significant reduction (32%) of fenestration numbers in contrast to the low dose (8 $\mu\text{g}/\text{mL}$). And in theophylline treatments, on the other hand, the high dose (150 $\mu\text{g}/\text{mL}$) significantly increased 27% of the fenestration number compared with the low dose (20 $\mu\text{g}/\text{mL}$).

To validate our findings, we also assessed the fenestrations with some treatments on SIM (Fig. 3, only caffeine 150 $\mu\text{g}/\text{mL}$ and theophylline 30 $\mu\text{g}/\text{mL}$ are shown for comparison). Similarly, to the SEM observations, LSECs featured numerous fenestrations which were clustered as sieve plates (Fig. 3). Further assessment of the diameter of fenestrations (Fig 3, insets) was conducted in a machine learning assisted workflow, which as used in a previous study (37). By comparing the mean fenestration diameter in our dehydrated SEM result in a wet SIM one-time measurement, the latter resulted in a 23% smaller size for the control group. The selected shown groups of SIM results are noted with a similar change in fenestration size as our findings from SEM (Fig. C); a high dose of caffeine (150 $\mu\text{g}/\text{mL}$) tended to elicit more and smaller fenestrations (consistent with finding from Table 1) and with pronounced sieve plate areas throughout the plasma membrane compared with the control group (Fig 3A), the mean fenestrations diameter decreased by 13%; interestingly, the 1.5 fold higher (than physiological) dose of theophylline (30 $\mu\text{g}/\text{mL}$) elicited an increase in fenestration diameter, in contrast to the physiological dose in the SEM result (Table 1); at this higher dose the mean fenestration size increased by 39% compared with control (Fig. 3D), the plot curve result tends to shift towards the

direction of large size of fenestrations. Large gaps occurred in the up-left corner of the membrane (Fig. 3B).

Endocytosis

The endocytic ability of rLSECs with the treatment of high doses of xanthines and sildenafil was tested by challenge with radiolabeled formaldehyde-treated serum albumin (¹²⁵I-FSA) in culture (Fig. 4). With three replicates tested on LSECs, results demonstrated virtually identical uptake and degradation ability among all treatments except for high dose of caffeine, which showed a significant decrease (22%, $P < 0.05$, $n = 4$) in degradation compared with the control group.

DISCUSSION

For SEM, the acquired resolution of images is much higher than that imaged via optical microscopes; thus, the quality is well within the range for statistical analysis (34). However, the preparation of samples is a series of fixation and dehydration procedures that generate artifacts, such as cracks, shrinkage of the specimen and alteration of tissue structure (19). To analyze under such conditions, the design of the experiment was followed as previous study (41), morphometric measurements were conducted on coded pictures to control the observer bias, as well as the imaging process was blinded for each treatment. For further SEM data analysis, only cells without clear artifacts in the images were analyzed while blinded with treatment information. Therefore, the final number of cells (≥ 17) from each assessed treatment was not identical, though they were prepared and imaged with the same number during designing. The control group is the largest as there was a triplicate within each biological group (3 biological groups in total, no significant differences between each biological control group were shown prior to pooling them as one total control group). The rest of the treatment groups were repeated among the 3 biological groups.

It was noted that high doses (150 $\mu\text{g}/\text{mL}$) of theobromine treatment samples produced the fewest measurable cell images for porosity and frequency, and relatively few cell images in physiological dose compared with other treatments as well. That might be due to rats are generally are not exposed to theobromine, which has been reported to be toxic in other animals such as dogs (27, 60, 61). Therefore, further dose response studies might be needed to test the toxicity of each compound.

LSEC fenestration morphology is responsive to xanthine and sildenafil challenge. Consistent with previous studies, a sildenafil dose of 0.6 $\mu\text{g}/\text{mL}$ produced no greater changes in fenestration frequency or porosity (31); and a sildenafil dose of 0.06 $\mu\text{g}/\text{mL}$ slightly increased fenestration diameter (Table 1 & Fig. 1B inset) in a study using Vybrant DiD membrane stains (37). This confirms the validity of our “blinding” methods and data analysis. However, such slight changes probably have no physiological relevance for the passage of substances such as chylomicron remnants via fenestrae from the plasma to the hepatocytes. The regulation of LSEC fenestrations is speculated to be mediated by VEGF and NO pathways (21), and sildenafil can lead to increased NO availability (18, 50). As expected, sildenafil was found to increase fenestration diameter (31), also confirming our findings showing increased fenestration diameter at sildenafil doses at 0.06 $\mu\text{g}/\text{mL}$. Notably, our findings show that changes in fenestration diameter do not necessarily cause alteration of porosity or frequency in one treatment. This conclusion was further verified by correlating with all the data in the control group (Fig. 2C), showing porosity is primarily correlated to frequency rather than fenestration diameter. Another example is caffeine challenge at high doses, which elicited a decrease in fenestration diameter combined with a tendency towards increased fenestration number and porosity in LSECs. This indicates that porosity is a function of fenestration number rather than diameter.

Caffeine at lower doses induced lower porosity while the higher dose gave higher porosity compared to control; a similar case for theobromine treatment, suggesting that xanthine dose differences can elicit opposite responses compared to control, depending on the xanthine used and dose (Fig. 2D&E).

As for chocolate consumption, sensory pleasures are explained by chocolate taste and texture. However, the combination of caffeine and theobromine may also play a psychoactive role. Both compounds are reported to present in sufficient concentrations to act as psychoactive effects in chocolate (4). Though caffeine presents ~8-10 times less than theobromine in chocolate (13), caffeine penetrates the blood-brain barrier more readily than theobromine (62). Additionally, theobromine has a lower affinity (2-3 times) than caffeine for adenosine receptors (14, 15, 24-26, 54, 56), which has less inhibitory effects on the central nervous system than caffeine (23, 45). On the other hand, theobromine is a more potent cardiac stimulant than caffeine. Thus, theobromine is more likely to appear in the circulation, which is relevant to our LSEC clearance system in the liver. Our study demonstrated theobromine may increase the porosity and frequency in LSECs, which may further affect hepatocyte metabolism and xenobiotic detoxification. For instance, due to fenestration loss associated with ageing, some drug dosages safe for young individuals may be toxic for elderly people. If the results in this study translate to the *in vivo* context, theobromine could improve liver function by improving the bi-directional exchange of substrates between the plasma and the hepatocytes that surround LSEC, for example in the elderly who have reduced LSEC porosity. Daily consumption of 40-80 g of dark chocolate or 110 g of regular milk chocolate yields a plasma theobromine concentration of 4-8 $\mu\text{g}/\text{mL}$ in humans, which is within the region that elicits increased porosity in rat LSEC *in vitro* (38, 47, 48). However, *in vivo* studies are therefore needed to determine if theobromine can be an intervention of benefit for liver health.

The general morphology of cultured cells was observed by super-resolution SIM and SEM (Fig. 1&3). Though not as high resolution as SEM, the SIM technique gives a resolution double that obtained via conventional light microscopy. The average diameter of fenestrations is well discerned within the range (17). For SIM, the samples can be studied in wet conditions – for example, cells can be imaged under culture conditions, with the potential for live imaging (11, 53). Moreover, dehydration is not required for SIM, avoiding the generation of artifacts from dehydration. 3D-SIM was used in our study to image fenestrations in fixed rat LSECs in Vectashield mounted samples. Importantly, the limitation of the linear SIM technique, is that only fenestrations with a diameter around 100 nm or more are resolved. As mentioned in the results sections, by comparing the results of the control group from both methods, the mean fenestration diameter was larger in SEM processed samples, which might be due to dehydration in SEM preparation. Notably, due to the resolution limit of SIM being around 100 nm, the real data of diameter analyzed from SIM images was in the same magnitude (Fig. 3D).

Furthermore, the analysis of porosity of SIM images in such magnitude is not very accurate to be compared with SEM results.

Similar to fenestrations as the gold standard for intact ultrastructural LSEC-specific identity, the functional hallmark of LSEC is their specific and effective uptake of soluble macromolecules via LSEC signature receptors (clathrin-mediated endocytosis) (59). In past decades, studies have established the uptake of LSEC for FSA was mostly endocytosed on stabilin-1 and stabilin-2 (9, 36). When recognized by these receptors, the macromolecules are rapidly trafficked to the endolysosomal compartments, and efficiently degraded there. This assay permits precise quantification of the amount of ligand that is taken up by the cells. The high dose of caffeine treatment may have some inhibitory effect on LSEC with less degradation function. Though our result is an *in vitro* cell culture-based, the dose is a much higher dose than the highest reported physiological dose (26, 33). Thus, there is always a consideration regarding the *in vivo* result consistency with *in vitro* application on drug delivery. Recent studies have suggested the high plasma concentration need for effect can be avoided if therapies are directly delivered to LSECs via nanoparticles, and may result in similar *in vivo* effects as observed *in vitro* (30). In any case, further studies are required to determine if caffeine affects fenestrations *in vivo*.

In conclusion, we have shown *in vitro* xanthine treatments with caffeine, theobromine, theophylline and paraxanthine elicit changes in fenestration size, porosity and frequency in rat LSECs. Caffeine in high doses may have an inhibitory impact on the uptake of soluble macromolecules, and increase smaller-sized fenestrations in LSECs. Theobromine in physiological dose increases fenestration frequency and porosity in rat LSECs. These findings remain to be confirmed *in vivo*. However, if theobromine elicits similar effects in animal studies, it might prove to be useful (and simple) intervention - via chocolate - to improve LSEC porosity in elderly people.

ACKNOWLEDGEMENT

This study was supported by grants from the Tromsø Research Foundation/Trond Mohn, the University of Tromsø-The Arctic University of Norway, the Research Council of Norway FRIMED grant no. 262538, and Marie Skłodowska-Curie Grant Agreement No. 766181, project: DeLIVER.

REFERENCES

1. Arnaud M. Metabolism of caffeine and other components of coffee. *Caffeine, Coffee and Health*. 1993:43-95.
2. Arnaud MJ. Pharmacokinetics and metabolism of natural methylxanthines in animal and man. *Handb Exp Pharmacol*. 2011(200):33-91.
3. Arnaud MJ. Comparative metabolic disposition of [1-Me¹⁴C]caffeine in rats, mice, and Chinese hamsters. *Drug Metab Dispos*. 1985;13(4):471-8.
4. Baggott MJ, Childs E, Hart AB, de Bruin E, Palmer AA, Wilkinson JE, et al. Psychopharmacology of theobromine in healthy volunteers. *Psychopharmacology (Berl)*. 2013;228(1):109-18.
5. Barnes PJ. Theophylline for COPD. *Thorax*. 2006;61(9):742-4.
6. Berg S, Kutra D, Kroeger T, Straehle CN, Kausler BX, Haubold C, et al. ilastik: interactive machine learning for (bio)image analysis. *Nat Methods*. 2019;16(12):1226-32.
7. Berthou F, Ratanasavanh D, Alix D, Carlhant D, Riche C, Guillouzo A. Caffeine and theophylline metabolism in newborn and adult human hepatocytes; comparison with adult rat hepatocytes. *Biochem Pharmacol*. 1988;37(19):3691-700.
8. Blanchard J, Harvey S, Morgan WJ. Variability of the serum protein binding of theophylline in patients with asthma and cystic fibrosis. *Br J Clin Pharmacol*. 1992;33(6):653-6.
9. Blomhoff R, Drevon CA, Eskild W, Helgerud P, Norum KR, Berg T. Clearance of acetyl low density lipoprotein by rat liver endothelial cells. Implications for hepatic cholesterol metabolism. *J Biol Chem*. 1984;259(14):8898-903.
10. Boison D. Methylxanthines, seizures, and excitotoxicity. *Handb Exp Pharmacol*. 2011(200):251-66.
11. Bottomley AL, Turnbull L, Whitchurch CB, Harry EJ. Immobilization Techniques of Bacteria for Live Super-resolution Imaging Using Structured Illumination Microscopy. *Methods Mol Biol*. 2017;1535:197-209.
12. Braet F, Wisse E. Structural and functional aspects of liver sinusoidal endothelial cell fenestrae: a review. *Comp Hepatol*. 2002;1(1):1.
13. Bruinsma K, Taren DL. Chocolate: food or drug? *J Am Diet Assoc*. 1999;99(10):1249-56.
14. Carney JM. Effects of caffeine, theophylline and theobromine on scheduled controlled responding in rats. *Br J Pharmacol*. 1982;75(3):451-4.
15. Carney JM, Holloway FA, Modrow HE. Discriminative stimulus properties of methylxanthines and their metabolites in rats. *Life Sci*. 1985;36(10):913-20.
16. Carrillo JA, Benitez J. Clinically significant pharmacokinetic interactions between dietary caffeine and medications. *Clin Pharmacokinet*. 2000;39(2):127-53.
17. Cogger VC, McNerney GP, Nyunt T, DeLeve LD, McCourt P, Smedsrod B, et al. Three-dimensional structured illumination microscopy of liver sinusoidal endothelial cell fenestrations. *J Struct Biol*. 2010;171(3):382-8.
18. Corbin JD, Francis SH. Cyclic GMP phosphodiesterase-5: target of sildenafil. *J Biol Chem*. 1999;274(20):13729-32.
19. Crang RFEK, K. L. Artifacts in Biological Electron Microscopy Science. 1988;242(4876):309.
20. Curatolo PW, Robertson D. The health consequences of caffeine. *Ann Intern Med*. 1983;98(5 Pt 1):641-53.
21. DeLeve LD. Liver sinusoidal endothelial cells in hepatic fibrosis. *Hepatology*. 2015;61(5):1740-6.

22. Duke JA. Handbook of Medicinal Herbs. Boca Raton, FL: CRC Handbook Press; 1988. p. 131-2.
23. Dunwiddie TV, Masino SA. The role and regulation of adenosine in the central nervous system. *Annu Rev Neurosci.* 2001;24:31-55.
24. Ferre S. An update on the mechanisms of the psychostimulant effects of caffeine. *J Neurochem.* 2008;105(4):1067-79.
25. Fredholm BB. Adenosine, an endogenous distress signal, modulates tissue damage and repair. *Cell Death Differ.* 2007;14(7):1315-23.
26. Fredholm BB, Battig K, Holmen J, Nehlig A, Zvartau EE. Actions of caffeine in the brain with special reference to factors that contribute to its widespread use. *Pharmacol Rev.* 1999;51(1):83-133.
27. Gans JH, Korson R, Cater MR, Ackerly CC. Effects of short-term and long-term theobromine administration to male dogs. *Toxicol Appl Pharmacol.* 1980;53(3):481-96.
28. Gatmaitan Z, Varticovski L, Ling L, Mikkelsen R, Steffan AM, Arias IM. Studies on fenestral contraction in rat liver endothelial cells in culture. *Am J Pathol.* 1996;148(6):2027-41.
29. Horn T, Christoffersen P, Henriksen JH. Alcoholic liver injury: defenestration in noncirrhotic livers--a scanning electron microscopic study. *Hepatology.* 1987;7(1):77-82.
30. Hunt BJ, Neal MD, Stensballe J. Reversing anti-factor Xa agents and the unmet needs in trauma patients. *Blood.* 2018;132(23):2441-5.
31. Hunt NJ, Lockwood GP, Warren A, Mao H, McCourt PAG, Le Couteur DG, et al. Manipulating fenestrations in young and old liver sinusoidal endothelial cells. *Am J Physiol Gastrointest Liver Physiol.* 2019;316(1):G144-G54.
32. Jones AW. Review of Caffeine-Related Fatalities along with Postmortem Blood Concentrations in 51 Poisoning Deaths. *J Anal Toxicol.* 2017;41(3):167-72.
33. Kulkarni PB, Dorand RD. Caffeine toxicity in a neonate. *Pediatrics.* 1979;64(2):254-5.
34. Leung BO, Chou KC. Review of super-resolution fluorescence microscopy for biology. *Appl Spectrosc.* 2011;65(9):967-80.
35. Li R, McCourt P, Schledzewski K, Goerdts S, Moldenhauer G, Liu X, et al. Endocytosis of advanced glycation end-products in bovine choriocapillaris endothelial cells. *Microcirculation.* 2009;16(7):640-55.
36. Li R, Oteiza A, Sorensen KK, McCourt P, Olsen R, Smedsrod B, et al. Role of liver sinusoidal endothelial cells and stabilins in elimination of oxidized low-density lipoproteins. *Am J Physiol Gastrointest Liver Physiol.* 2011;300(1):G71-81.
37. Mao H, Diekmann R, Liang HPH, Cogger VC, Couteur DGL, Lockwood GP, et al. Cost-efficient nanoscopy reveals nanoscale architecture of liver cells and platelets. *Nanophotonics.* 2019;8(7):1299.
38. Mayorga-Gross AL, Esquivel P. Impact of Cocoa Products Intake on Plasma and Urine Metabolites: A Review of Targeted and Non-Targeted Studies in Humans. *Nutrients.* 2019;11(5).
39. McCuskey RS. Morphological mechanisms for regulating blood flow through hepatic sinusoids. *Liver.* 2000;20(1):3-7.
40. Mönkemöller V, Mao H, Hübner W, Dumitriu G, Heimann P, Levy G, et al. Primary rat LSECs preserve their characteristic phenotype after cryopreservation. *Sci Rep.* 2018;8(1):14657.
41. Morsiani E, Mazzoni M, Aleotti A, Gorini P, Ricci D. Increased sinusoidal wall permeability and liver fatty change after two-thirds hepatectomy: an ultrastructural study in the rat. *Hepatology.* 1995;21(2):539-44.

42. Mumford GK, Benowitz NL, Evans SM, Kaminski BJ, Preston KL, Sannerud CA, et al. Absorption rate of methylxanthines following capsules, cola and chocolate. *Eur J Clin Pharmacol.* 1996;51(3-4):319-25.
43. Nawrot P, Jordan S, Eastwood J, Rotstein J, Hugenholtz A, Feeley M. Effects of caffeine on human health. *Food Addit Contam.* 2003;20(1):1-30.
44. Orru M, Guitart X, Karcz-Kubicha M, Solinas M, Justinova Z, Barodia SK, et al. Psychostimulant pharmacological profile of paraxanthine, the main metabolite of caffeine in humans. *Neuropharmacology.* 2013;67:476-84.
45. Pettenuzzo LF, Noschang C, von Pozzer Toigo E, Fachin A, Vendite D, Dalmaz C. Effects of chronic administration of caffeine and stress on feeding behavior of rats. *Physiol Behav.* 2008;95(3):295-301.
46. Poisson J, Lemoine S, Boulanger C, Durand F, Moreau R, Valla D, et al. Liver sinusoidal endothelial cells: Physiology and role in liver diseases. *J Hepatol.* 2017;66(1):212-27.
47. Resman BH, Blumenthal P, Jusko WJ. Breast milk distribution of theobromine from chocolate. *J Pediatr.* 1977;91(3):477-80.
48. Richelle M, Tavazzi I, Enslin M, Offord EA. Plasma kinetics in man of epicatechin from black chocolate. *Eur J Clin Nutr.* 1999;53(1):22-6.
49. Rowe DJF, Watson ID, Williams J, Berry DJ. The Clinical Use and Measurement of Theophylline. *Annals of Clinical Biochemistry.* 1988;25(1):4-26.
50. Rybalkin SD, Rybalkina IG, Feil R, Hofmann F, Beavo JA. Regulation of cGMP-specific phosphodiesterase (PDE5) phosphorylation in smooth muscle cells. *J Biol Chem.* 2002;277(5):3310-7.
51. Sawynok J, Yaksh TL. Caffeine as an analgesic adjuvant: a review of pharmacology and mechanisms of action. *Pharmacol Rev.* 1993;45(1):43-85.
52. Schindelin J, Arganda-Carreras I, Frise E, Kaynig V, Longair M, Pietzsch T, et al. Fiji: an open-source platform for biological-image analysis. *Nat Methods.* 2012;9(7):676-82.
53. Schvartz T, Aloush N, Goliand I, Segal I, Nachmias D, Arbely E, et al. Direct fluorescent-dye labeling of alpha-tubulin in mammalian cells for live cell and superresolution imaging. *Mol Biol Cell.* 2017;28(21):2747-56.
54. Shi D, Daly JW. Chronic effects of xanthines on levels of central receptors in mice. *Cell Mol Neurobiol.* 1999;19(6):719-32.
55. Smedsrod B, Pertoft H. Preparation of pure hepatocytes and reticuloendothelial cells in high yield from a single rat liver by means of Percoll centrifugation and selective adherence. *J Leukoc Biol.* 1985;38(2):213-30.
56. Snyder SH, Katims JJ, Annau Z, Bruns RF, Daly JW. Adenosine receptors and behavioral actions of methylxanthines. *Proc Natl Acad Sci U S A.* 1981;78(5):3260-4.
57. Somani SM, Gupta P. Caffeine: a new look at an age-old drug. *Int J Clin Pharmacol Ther Toxicol.* 1988;26(11):521-33.
58. Sommer C, Straehle C, Kothe U, Hamprecht FA. Ilastik: Interactive Learning and Segmentation Toolkit. 2011 8th Ieee International Symposium on Biomedical Imaging: From Nano to Macro. 2011:230-3.
59. Sorensen KK, McCourt P, Berg T, Crossley C, Le Couteur D, Wake K, et al. The scavenger endothelial cell: a new player in homeostasis and immunity. *Am J Physiol Regul Integr Comp Physiol.* 2012;303(12):R1217-30.
60. Stidworthy MF, Bleakley JS, Cheeseman MT, Kelly DF. Chocolate poisoning in dogs. *Vet Rec.* 1997;141(1):28.
61. Strachan ER, Bennett A. Theobromine poisoning in dogs. *Vet Rec.* 1994;134(11):284.

62. Svenningsson P, Nomikos GG, Fredholm BB. The stimulatory action and the development of tolerance to caffeine is associated with alterations in gene expression in specific brain regions. *J Neurosci.* 1999;19(10):4011-22.
63. Svistounov D, Warren A, McNerney GP, Owen DM, Zencak D, Zykova SN, et al. The Relationship between Fenestrations, Sieve Plates and Rafts in Liver Sinusoidal Endothelial Cells. *Plos One.* 2012;7(9):e46134.
64. Wisse E. An electron microscopic study of the fenestrated endothelial lining of rat liver sinusoids. *J Ultrastruct Res.* 1970;31(1):125-50.
65. Wisse E, De Zanger RB, Charels K, Van Der Smissen P, McCuskey RS. The liver sieve: considerations concerning the structure and function of endothelial fenestrae, the sinusoidal wall and the space of Disse. *Hepatology.* 1985;5(4):683-92.
66. Xie G, Wang X, Wang L, Wang L, Atkinson RD, Kanel GC, et al. Role of differentiation of liver sinusoidal endothelial cells in progression and regression of hepatic fibrosis in rats. *Gastroenterology.* 2012;142(4):918-27 e6.

FIGURE LEGENDS

Fig. 1 Representative scanning electron microscopy (SEM) images following xanthines and sildenafil treatments of rat liver sinusoidal endothelial cell (LSEC) fenestration.

A: Control images show fenestrations grouped in sieve plates (inset); B: Sildenafil (SIL, 0.06 $\mu\text{g}/\text{mL}$); C: Caffeine (CA, 8 $\mu\text{g}/\text{mL}$); D: Caffeine (CA, 150 $\mu\text{g}/\text{mL}$); E: Theobromine (TB, 8 $\mu\text{g}/\text{mL}$); F: Theobromine (TB, 150 $\mu\text{g}/\text{mL}$); G: Theophylline (TP, 20 $\mu\text{g}/\text{mL}$); H: Theophylline (TP, 150 $\mu\text{g}/\text{mL}$); I: Paraxanthine (PA, 8 $\mu\text{g}/\text{mL}$); J: Paraxanthine (PA, 150 $\mu\text{g}/\text{mL}$). All challenges were at 37°C, 5% CO₂ for 30 min in RPMI \pm additives. Presented images were taken at a magnification of 15,000. Scale bar: 2 μm and 1 μm (insets).

Fig. 2 Fenestration size, frequency and porosity in LSEC after challenge with xanthines

A: Relative frequency distribution of fenestration size within 50-300 nm, compared to theophylline (150 $\mu\text{g}/\text{mL}$) and control group as an example, more distributions of each treatment are provided in supplementary information. Fenestrae size are divided as three subpopulations for comparison of fenestrae size change in each region: <100 nm is region S (green), 100-200 nm is region M (yellow), and >200 nm is region L (orange). B: Table of subpopulations fenestra changes in distribution of size compared with control group (in percentage), arrow up means increase; arrow down means decrease; C: correlations plot between porosity (%) and frequency (no./ μm^2) in rat LSECs control group; D&E: Box plot showing the porosity and frequency changes within same treatment compared to control group. Dashed line is mean value and solid line is median value. *Statistically significant ($P < 0.05$) difference. Statistics were performed using one-way ANOVA, with post-hoc Dunnett's test to compare each treatment with RPMI control. Two-tailed Welch's t-test was used to assess between-group differences within a treatment for fenestration porosity and frequency comparisons; $n = 3$ for all treatments.

Fig. 3 Structured illumination microscopy (SIM) images following caffeine and theophylline treatments on rat liver sinusoidal endothelial cells (LSECs) fenestration

A: SIM control images show fenestrations grouped in sieve plates (inset); B: Theophylline (TP, 30 $\mu\text{g}/\text{mL}$) treatment; C: Caffeine (CA, 150 $\mu\text{g}/\text{mL}$) treatment; D: Histogram plot of relative frequency vs. fenestration size after challenge with CA and TP. Mean fenestration size increases after TP treatment, and decreases after CA treatment. All images were measured via Ilastik as described in in Material and Methods ($n = 1$),

and samples were incubated at 37°C, 5% CO₂ for 30 min using RPMI ± additives. Scale bars: 2 μm.

Fig. 4 Endocytic ability of rat liver sinusoidal endothelial cells (LSECs) after treatments.

Primary cryopreserved rat LSEC cultures were incubated for 2 h at 37 °C with trace amounts of radiolabeled ligands for the endocytosis receptors (¹²⁵I-FSA for stabilin1/2). Endocytosis was measured as described in Material and Methods. Black bars represent cell-associated ligand, whereas grey bars represent degraded ligand. Total endocytosed radioactivity represents the sum of cell-associated and degraded ligand radioactivity. Results are average of 3-4 independent experiments, are given in percentage of total endocytosed radioactivity. Bars represents mean ± SD. *Statistically significant (P < 0.05) difference. Statistics were performed using one-way ANOVA, with post-hoc Dunnett's test compare each treatment with RPMI control for cell association and degradation of ligands, respectively.

Supplementary Fig.1 Distributions of frequency vs fenestration size

A-E: Relative frequency distributions of fenestration size within 50-300 nm: treatments vs. control (Ctrl) group, A: Caffeine (CA, 8&150 μg/mL); B: Sildenafil (SIL, 0.06&0.6 μg/mL); C: Theophylline (TP, 20&150 μg/mL); D: Theobromine (TB, 8&150 μg/mL); E: Paraxanthine (PA, 8&150 μg/mL). Perpendicular dashed lines indicate interfaces between small/medium fenestrations and medium/large fenestrations. Histogram fenestration distributions show with gaussian fitted lines, dotted line for control, dashed line for physiological dose of treatment, solid line for high dose of treatment.

Table 1. Treatments on rat liver sinusoidal endothelial cells (LSECs) data

Drug Treatment	No. fenestrations measured	Diameter (nm)	No. cells	Porosity (%)	Frequency (No./ μm^2)
Control	68829	190.1 \pm 51.1	157	6.06 \pm 3.10	1.99 \pm 1.08
Caffeine (8 $\mu\text{g}/\text{mL}$)	7235	175.7 \pm 45.7*	33	5.47 \pm 2.71	2.06 \pm 0.95
Caffeine (150 $\mu\text{g}/\text{mL}$)	18844	179.3 \pm 53.1*	34	6.98 \pm 3.36	2.52 \pm 1.06
Theobromine (8 $\mu\text{g}/\text{mL}$)	12771	185.3 \pm 47.8*	20	8.43 \pm 3.89*	2.93 \pm 1.25*
Theobromine (150 $\mu\text{g}/\text{mL}$)	7029	177.2 \pm 57.9*	17	5.58 \pm 4.59	2.00 \pm 1.13
Theophylline (20 $\mu\text{g}/\text{mL}$)	13496	188.1 \pm 50.8*	27	6.51 \pm 2.74	2.19 \pm 0.87
Theophylline (150 $\mu\text{g}/\text{mL}$)	20311	178.0 \pm 47.4*	33	7.43 \pm 3.60	2.78 \pm 1.33*
Paraxanthine (8 $\mu\text{g}/\text{mL}$)	15210	178.4 \pm 45.5*	21	6.76 \pm 2.36	2.38 \pm 0.83
Paraxanthine (150 $\mu\text{g}/\text{mL}$)	16766	189.6 \pm 54.6	36	6.59 \pm 2.69	2.16 \pm 0.87
Sildenafil (0.06 $\mu\text{g}/\text{mL}$)	13857	191.3 \pm 52.3	29	6.77 \pm 2.79	2.19 \pm 0.85
Sildenafil (0.6 $\mu\text{g}/\text{mL}$)	16443	180.0 \pm 55.8*	33	6.08 \pm 2.92	2.17 \pm 1.11

No. animals =3. All data are shown as means \pm SD. *P < 0.05

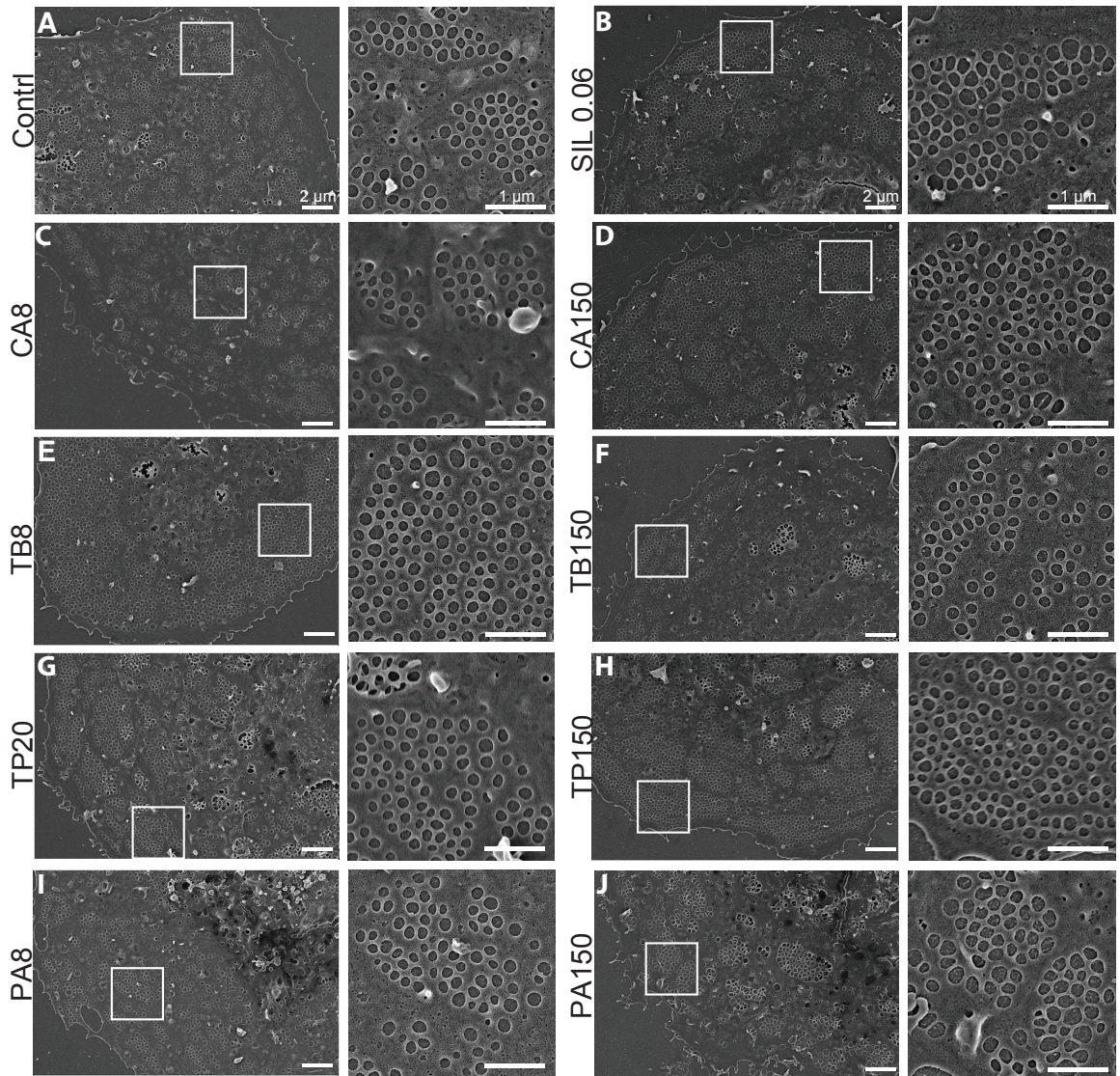


Fig. 1 Representative scanning electron microscopy (SEM) images following xanthines and sildenafil treatment of rat liver sinusoidal endothelial cell (LSEC) fenestration.

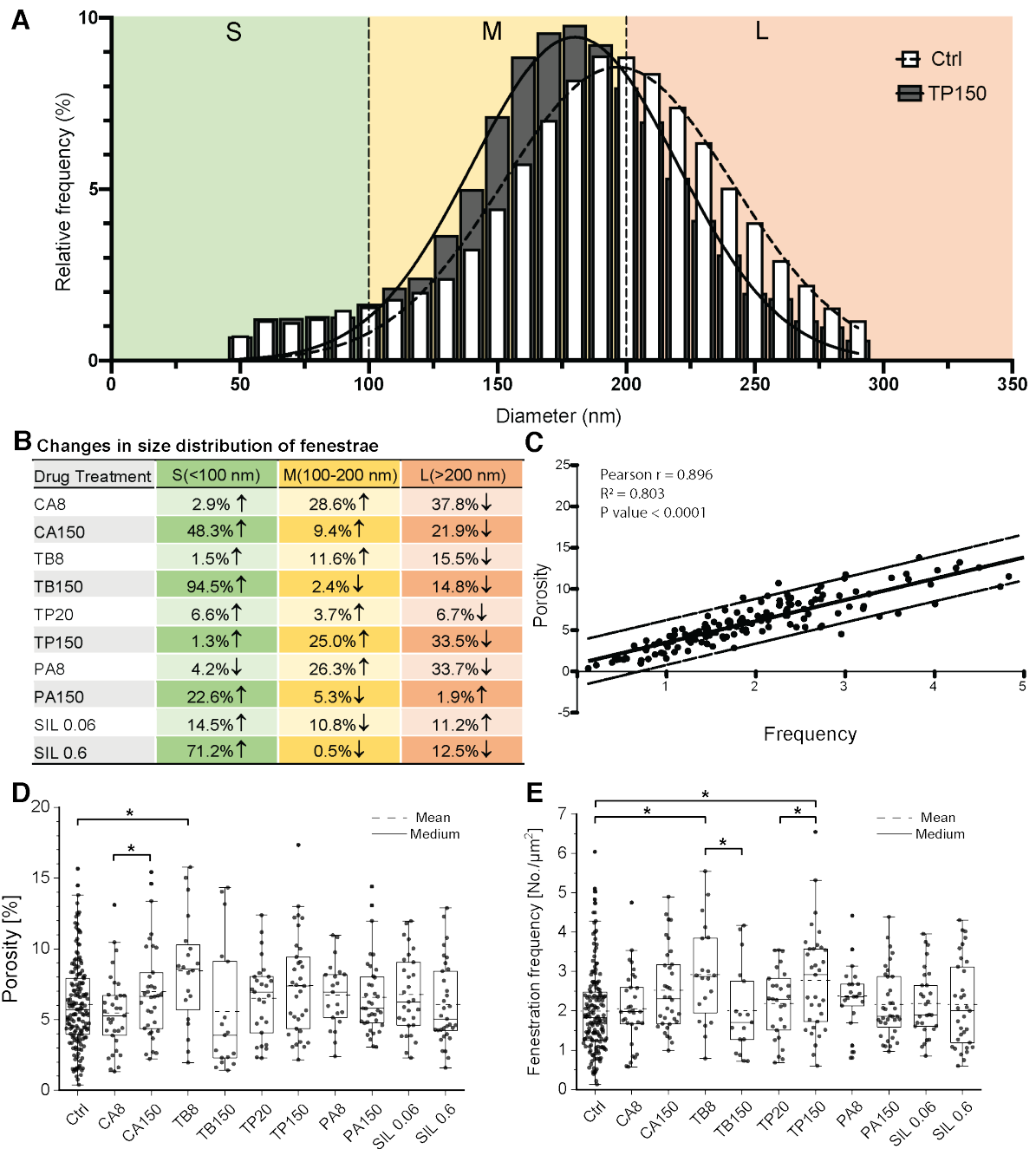


Fig. 2 Fenestration size, frequency and porosity in LSEC after challenge with xanthines.

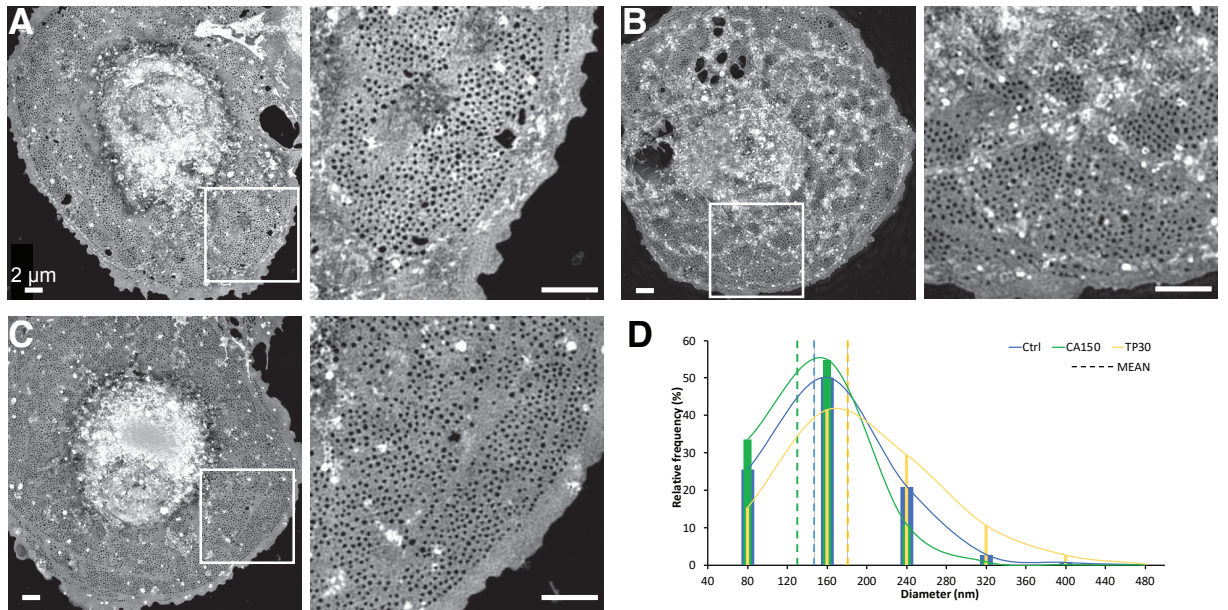


Fig. 3 Structured illumination microscopy (SIM) images following caffeine and theophylline treatments on rat liver sinusoidal endothelial cells (LSECs) fenestration.

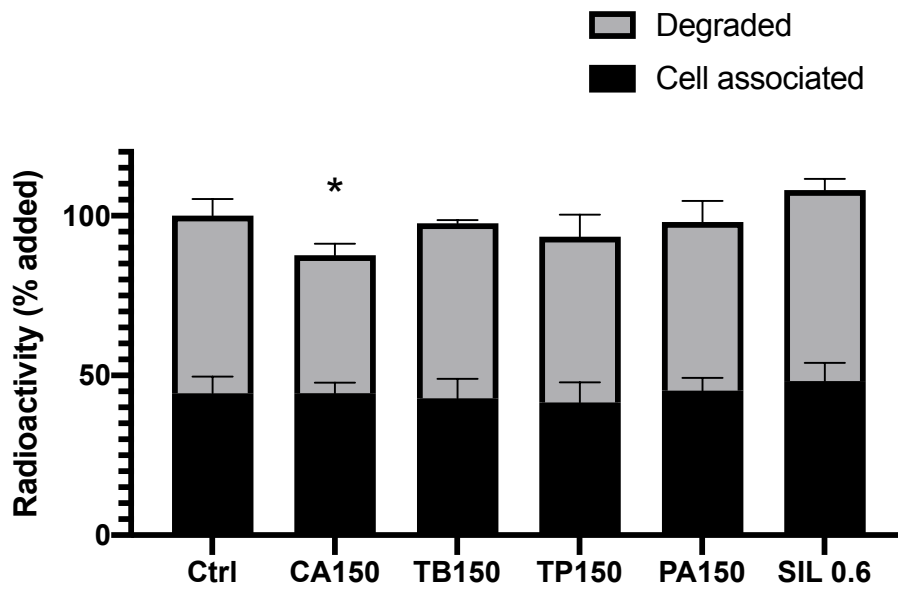
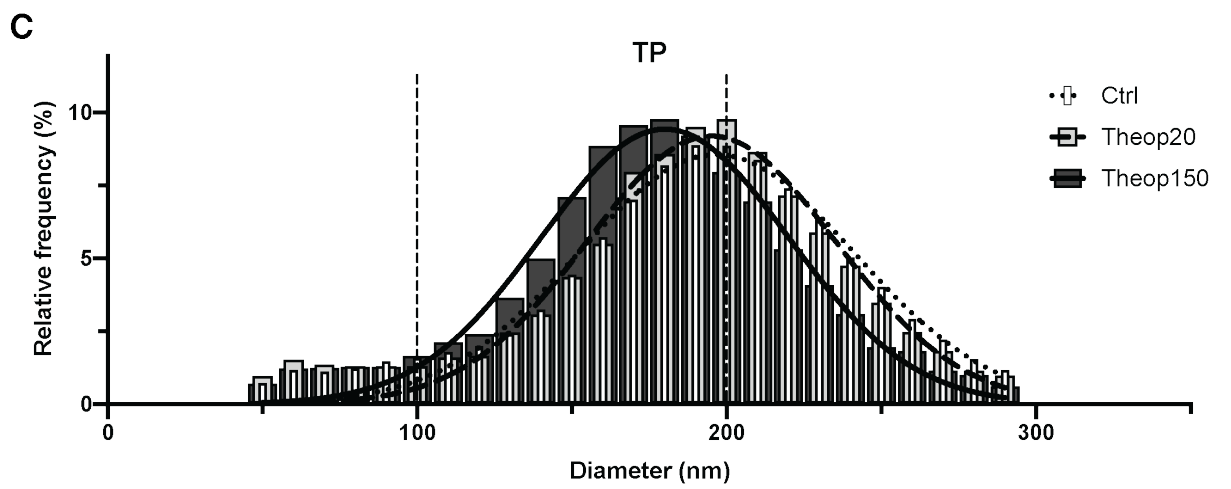
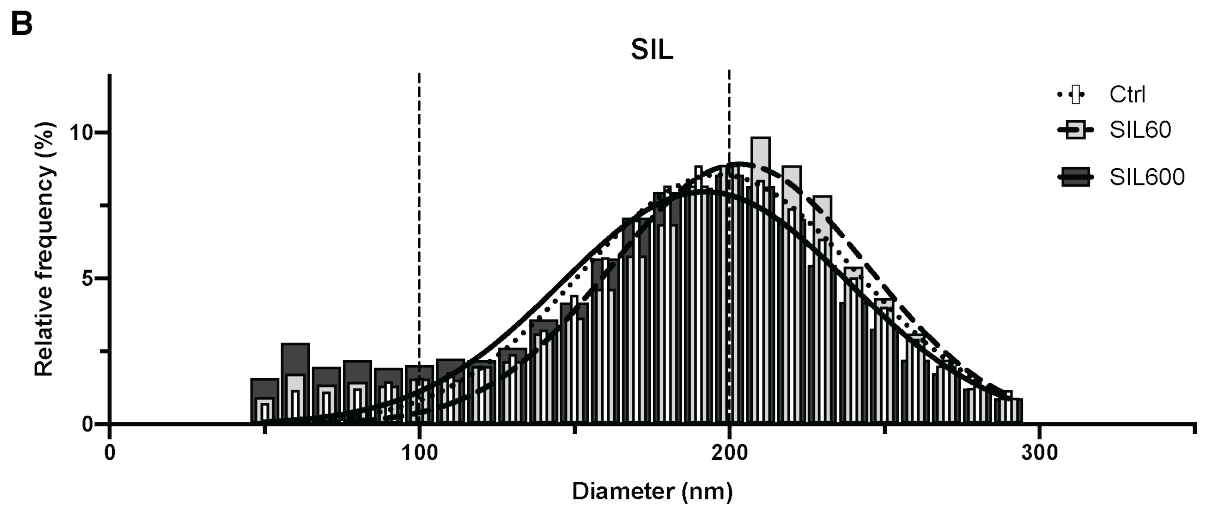
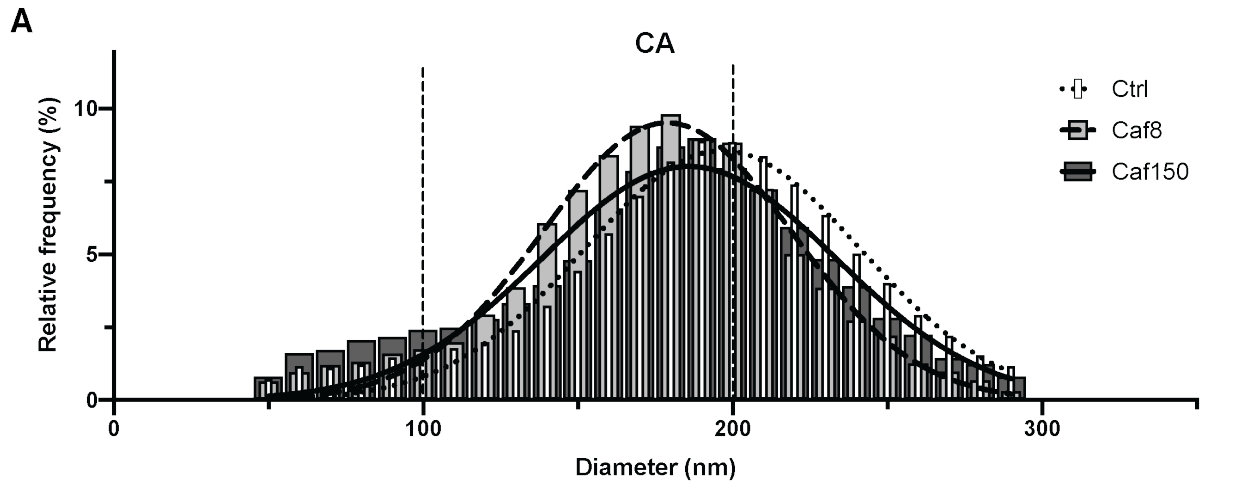
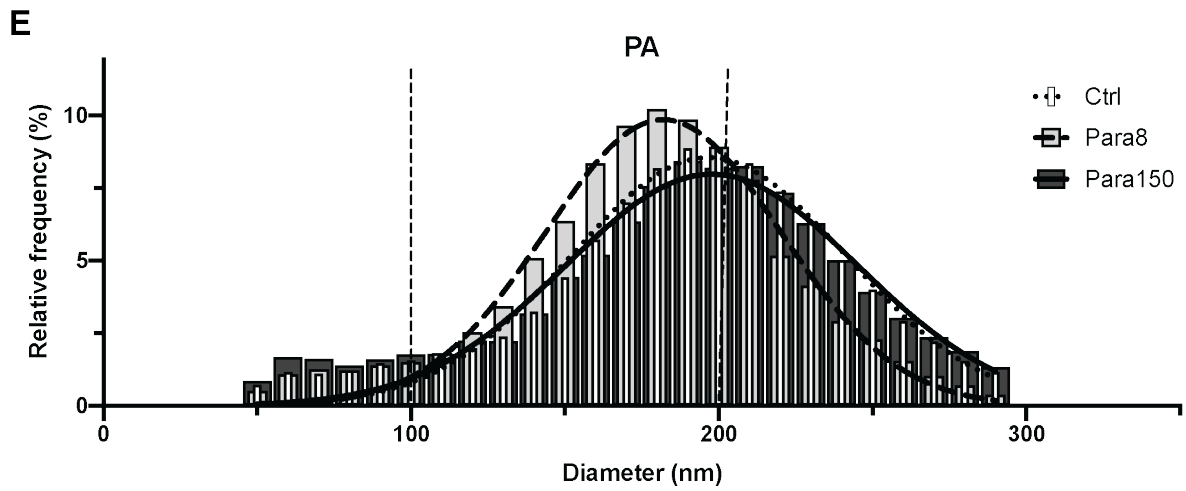
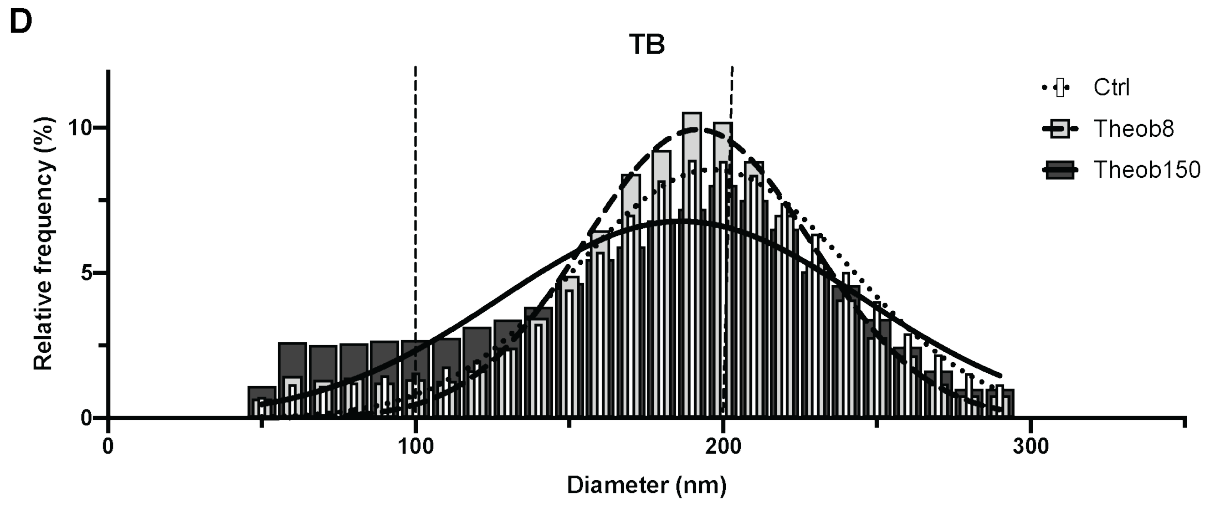


Fig. 4 Endocytic ability of rat liver sinusoidal endothelial cells (LSECs) after treatments.





Supplementary Fig.1 Distributions of frequency vs fenestration size.

Paper III



Impact of oxidized low-density protein on rat liver sinusoidal endothelial cell ultrastructure

Hong Mao¹, Larissa D. Kruse¹, Ruomei Li¹, Ana Oteiza², Victoria C. Cogger³, David Le Couteur³, Balpreet Singh Ahluwalia⁴, Karen K. Sørensen¹, Cristina Øie^{1*}, Peter A. G. McCourt^{1*}

¹ Vascular Biology Research Group, Department of Medical Biology, Faculty of Health Sciences, University of Tromsø-The Arctic University of Norway, Tromsø Norway

² Nuclear Medicine and Radiation Biology Research Group, Department of Clinical Medicine, University of Tromsø -The Arctic University of Norway, Tromsø, Norway and The PET Imaging Center, University Hospital of North Norway, Tromsø, Norway

³ ANZAC Research Institute, Concord Repatriation General Hospital, Concord, NSW, Australia; and The University of Sydney, Charles Perkins Centre, Nutritional Ecology and Physiology Lab, Sydney, NSW, Australia

⁴ Optical Nanoscopy Research Group, Department of Physics and Technology, Faculty of Science and Technology, University of Tromsø-The Arctic University of Norway, Tromsø, Norway

Corresponding author:

Peter A.G. McCourt

Vascular Biology Research Group,

Department of Medical Biology,

Faculty of Health Sciences,

University of Tromsø-The Arctic University of Norway

9037 Tromsø, Norway

Phone: +47 77646391

E-mail: peter.mccourt@uit.no

Keyword:

Liver sinusoidal endothelial cell, oxidized LDL, fenestration, ultrastructure, live SIM

ABSTRACT

Objectives: Atherogenesis is associated with elevated levels of proinflammatory oxidized low-density lipoproteins (oxLDL) in the circulation. *In vivo*, oxLDL causes endothelial swelling in the liver, and disturbs the fenestrae of liver sinusoidal endothelial cells (LSECs). The present study aimed to map the kinetics of these changes *in vitro* using super-resolution microscopy.

Methods: Cultures of freshly isolated and cultured rat LSECs were challenged with oxLDL at various physiological concentrations and at varying levels of oxidation (oxidized for 3h oxLDL₃; and for 24h oxLDL₂₄). The cell cultures were examined with scanning electron microscopy and in real-time with structured illumination microscopy. LSEC viability was monitored with endocytosis and lactate dehydrogenase (LDH) detection assays.

Results: oxLDL challenge disrupted LSEC ultrastructure – increasing oxLDL concentrations and oxidation levels increased the level of disruption which manifested as loss of sieve plates, the fusion of fenestrations within sieve plates, and gap formation in LSECs. Importantly, these effects were not uniform across all LSEC. LSEC maintained the ability to endocytose ligands irrespective of the oxidation level/concentration of oxLDL. However, increasing oxidation levels and concentrations of oxLDL inhibited LSEC mediated degradation of the endocytosed ligands. LDH release was only slightly increased after the oxLDL challenge, irrespective of the type/concentration of oxLDL.

Conclusion: oxLDL disrupts LSEC morphology *in vitro*, manifested as loss of sieve plates, fusion of fenestrations and large gap formation. However, LSEC remains viable and maintain scavenging functionality during oxLDL challenge, suggesting these cells are functionally robust in the presence of this cytotoxic compound.

INTRODUCTION

Low-density lipoproteins (LDL) are the main carrier for the delivery of fat molecules (lipids, including cholesterol) in blood circulation via LDL receptor mediated endocytosis to peripheral tissues (8). Elevated levels of LDL in the circulation are associated with the development of atherosclerosis (15, 16, 30, 31). Studies have suggested the important role of oxidative modification of LDL in the development of these progressions, as non-modified LDL incubated with macrophages does not appear to elicit abnormal cholesterol accumulation (21, 46, 47). LDL may transverse the endothelium at atherosclerotic sites, where they can be modified by oxidation or enzymatic activity, and taken up by macrophages and accumulate in atherosclerotic plaques (38).

The oxidation of LDL can also occur in the plasma of healthy individuals (2, 13, 22, 23, 25). LDL can experience oxidation in the arterial wall (during atherosclerosis) or in the plasma circulation (2, 23, 25, 37). Circulating oxidized LDL (oxLDL) is mainly the mildly form of oxLDL compared to the more heavily oxLDL found in the atherosclerotic plaques. Mildly oxLDL was suggested to be the precursor of heavily oxLDL in the intima. It is a physiological pro-atherogenic molecule in the body (26, 51). The level of oxidative modification of LDLs altered the properties of these molecules and also their pathophysiological functions. Intravenously injected mildly oxLDL showed much slower liver uptake and had longer retention in circulation compared to heavily oxLDL, which may be sufficient to allow it to enter and accumulate in the arterial intima (1). In addition to its key role in the development of atherosclerosis (3, 20, 42, 46, 48, 53), oxLDL has also shown to be associated with the aging process (7).

Circulating oxLDL, as a major atherogenic substance (2, 55), is mainly removed from the blood by the cells lining in the liver sinusoids (29, 49). Previous studies showed that heavily oxLDL was taken up both by Kupffer cells and liver sinusoidal endothelial cells (LSECs) (49), and mildly oxLDL was only recognized by LSECs (28). This indicates that LSECs play an important role in eliminating plasma oxLDLs, which demonstrates the importance of the liver cell clearance system in the prevention of cardiovascular disease (22, 24, 44).

LSEC fenestrations (plasma membrane nanopores of 50-300nm in diameter) regulate the size of lipoproteins trafficking to the space of Disse where they are further metabolized by hepatocytes (17, 19). LSECs thus play a role in mediating the level of lipoproteins in circulation, as defenestrated LSECs leading to the reduction of hepatic uptake of lipoproteins is one of the causes of hyperlipoproteinemia (18). Similarly, the defenestration of LSECs is associated with the progression of non-alcoholic fatty liver disease (NAFLD). Therefore, the dysfunction of LSECs in the early stages of NAFLD might indicate the severity of subsequent progression of NAFLD (33, 43).

In addition to their bi-directional fenestration filter system, LSECs are well equipped with specific receptors for endocytosis, to fulfill their scavenger role in cleaning waste from the blood. For instance, after intravenous administration of formaldehyde-treated serum albumin (FSA), it will distribute nearly exclusively to LSECs and be internalized via SR-H1/2 (also called stabilin-1/2)-mediated endocytosis (5, 14, 28). Therefore, FSA uptake in LSEC has been utilized as a functional biomarker for LSECs (12, 54). Of note, stabilin-1 and -2 also mediate the LSEC uptake of oxLDL, stabilin-1 and -2 having a higher affinity for mildly oxLDL and heavily oxLDL, respectively (Li, 2011).

In an *in vivo* study (36), oxLDL induced acute alterations in the liver microvasculature, such as narrowing of liver sinusoids, more swollen endothelial cells as well as endothelial thickening and reduced fenestration number. These changes can lead to sinusoidal endothelial dysfunction. Here, we studied the *in vitro* effects of oxLDL on LSEC at the cellular level, focusing on ultrastructural morphological alterations in these cells, using scanning electron microscopy (SEM) and structured illumination microscopy (SIM).

MATERIALS AND METHODS

Animals and ethics statements

Sprague Dawley male rats were obtained from Charles River Laboratories (Sulzfeld, Germany). The rats were group-housed (2-3 rats/cage) 2–3 rats per cage) in 135G Eurostandard type IV conventional cages (Tecniplast, Italy) with aspen bedding (Scanbur, Norway) and with nesting material, rat tunnels and aspen chew blocks (Sizzelnest®, Datesand, UK) as environmental enrichment. The rats were kept under controlled environmental conditions ($21^{\circ}\text{C} \pm 1^{\circ}$, relative humidity $55\% \pm 5\%$ and 12 h light/12 h dark cycle), at the specific pathogen free animal research facility at the University of Tromsø (UiT) – The Arctic University of Norway. The rats had free access to water and standard chow (RM1-E, Special Diet Service, UK). The experimental protocols and animal handling were approved by the National Animal Research Authority at the Norwegian Food Safety Authority (approval ID: 8455), and experiments were performed in compliance with the European Convention for the protection of Vertebrate Animals used for Experimental and Other Scientific Purposes. A total of 17 animals were used in the study. All animals were euthanized, and died from exsanguination while in deep surgical anesthesia during the liver perfusion procedure (for anesthesia protocol see section “Rat LSEC isolation and cell culture”).

Material

Collagenase was from Worthington Biochemical Corporation (Lakewood, NJ, USA). Carrier-free Na^{125}I was from PerkinElmer Norge AS (Oslo, Norway). Bovine serum albumin (BSA) was from MP Biomedicals (Solon, OH, USA). Human fibronectin was purified from human plasma by affinity chromatography on Gelatin Sepharose 4B as described by the manufacturer (GE Healthcare, Uppsala, Sweden). Percoll and PD-10 columns (Sephadex G-25) were from GE Healthcare. Serum-free Roswell Park Memorial Institute (RPMI-1640) cell culture medium (supplemented with 20 mM sodium bicarbonate, 0.006% penicillin, and 0.01% streptomycin) and monensin were from Sigma-Aldrich (Oslo, Norway). Culture dishes of 35 mm diameter and #1.5 glass coverslip-bottom were from MatTek Corp. (Ashland, MA, USA). Trichloroacetic acid (TCA) was from Merck (Darmstadt, Germany). Formaldehyde-treated bovine serum albumin (FSA) was prepared by treating BSA with 10% formaldehyde in 0.2 M carbonate buffer, pH 10, for 3 days as described by Mego, *et al.* (32). Ethylenediaminetetraacetic acid (EDTA) was from Sigma Chemical Company (St. Louis, MO, USA). Human serum albumin (HSA) was from Octapharma (Ziegelbrücke, Switzerland). Live cell imaging solution was from ThermoFisher (Oslo, Norway). CellMask™ Green was from Fisher Scientific (Cat No. C37608; Oslo, Norway). Lactate dehydrogenase (LDH) cytotoxicity detection kit was purchased from Clontech Laboratories (CA, USA).

Oxidation of LDL

LDL (density: 1.019-1.063 g/mL) was isolated from fresh human plasma by density gradient ultracentrifugation (39), and preserved in 10% sucrose in 150 mM NaCl with 0.24 mM EDTA (pH 7.4 at -80 °C for ≤6 mo (40)). Sucrose was removed by dialysis at 4°C against phosphate-buffered saline (PBS) before further use. The protein concentration was determined by Nanodrop 2000 Spectrophotometer (Thermo Scientific, Oslo, Norway).

LDL was oxidized with CuSO₄ (10 μM) at 37°C for 3 or 24 h to produce oxLDL₃ and oxLDL₂₄ (mildly and heavily oxidized LDL forms), respectively. The oxidation process was terminated by adding EDTA to a final concentration of 305 μM after which samples were stored under nitrogen at 4°C for ≤1 wk before use to prevent further oxidation. Before use, CuSO₄ and EDTA were removed by extensive dialysis against PBS at 4°C, and oxLDLs were centrifuged (12,000 g) for 20 minutes. Relative electrophoretic mobility (REM) (34) of differently oxLDLs was measured and compared with non-copper sulfate-treated LDL was: oxLDL₃: 1.42 ± 0.20 and oxLDL₂₄ 1.79 ± 0.34; respectively, in 3-4 experiments (means ± SD).

Rat LSEC isolation and cell culture

The rats (body weight 150–300 g) were anesthetized with a mixture (ZRF-mix) of zolazepam /tiletamine hydrochloride 12.9/12.9 mg/mL (Zoletil forte vet, Virbac, Norway), xylazine 1.8 mg/mL (Rompun, Bayer Nordic, Norway) and fentanyl 10.3 μg/mL (Actavis, Norway), injected intraperitoneally. LSECs were isolated and purified as described by Smedsrod, *et al.* (45) and plated on 0.2 mg/mL human fibronectin coated #1.5 coverslips (Sigma-Aldrich) cultured (37°C, 5% CO₂) for 3 h in serum-free RPMI-1640 at a density of 0.2 × 10⁶ cells/cm². Fibronectin coating was performed with just enough volume to completely cover the surface area. After 10 minutes of incubation at room temperature (RT), the redundant fibronectin solution was rinsed with PBS and cells were then seeded. The LSECs were treated with mildly or heavily oxLDLs at 10, 40, or 80 μg/mL, doses were selected based on previous work by (36) for 30 minutes to determine effects on fenestrations, then fixed with 4% formaldehyde (FA) in phosphate buffered saline (PBS) and 0.02 M sucrose (Sigma-Aldrich, Oslo, Norway), pH 7.2 for 15 minutes, and then kept in PBS for visualizing by SIM.

Structured illumination microscopy (SIM)

After fixation, the cells were stained with CellMask™ Green (1:1000 in serum-free RPMI) for 10 minutes, and immediately imaged using a commercial super-resolving SIM (DeltaVision/OMXv4.0 BLAZE, GE Healthcare) with a 60X 1.42NA oil-immersion objective (Olympus). 3D-SIM images stacks of 1 μm were acquired with a z-distance of 125 nm and with 15 raw images per plane (five phases, three angles). Raw datasets were

computationally reconstructed using SoftWoRx software (GE Healthcare). For live cell SIM, LSEC cultures were seeded in human fibronectin (0.2 mg/mL) coated MatTek dishes (35mm Dish /No 1.5 coverslip, Ashland, MA, USA) with RPMI-1640 for 1 h at 37°C. Unattached cells were gently washed away, and LSEC cultures were continued with incubating for 1-2 h to reach the desired confluency prior to imaging.

Fresh working solutions were prepared in a warm live cell imaging solution at 5 µg/mL of CellMask™ Green Plasma Membrane Stain. LSEC cultured dishes were placed on the pre-warmed 36°C SIM holder. RPMI culture media was replaced with the aforementioned imaging solution, and after 5-10 minutes incubation, cells were imaged for 20 frames in 30 minutes.

Scanning electron microscopy (SEM)

For SEM preparation, the treated specimens were fixed overnight in McDowell's fixative (4% formaldehyde (FA), 1% glutaraldehyde (GA), in phosphate buffer, pH 7.2). After washes with 0.1M PHEM buffer, the coverslips containing the cells were treated with 1% tannic acid in 0.15 mol/l cacodylic buffer for 1 hour, 1% OsO₄ in 0.1 mol/l cacodylic buffer for 1 hour, dehydrated in ethanol (30%, 60%, 90% for 5 minutes each, 5 times 100% ethanol for 4 minutes), and incubated twice in hexamethyldisilazane (Sigma-Aldrich, Oslo, Norway) for 2 minutes each, dried, and sputter-coated with 10-nm gold/palladium alloys. Specimens were examined using a commercial SEM (Sigma HV0307, Zeiss), run at 2kV. Large fields of view containing cells were randomly acquired in specific locations on the stubs to show cell culture condition and cell size, and high-resolution SEM images of a cell at magnification of 10-15K were randomly acquired to observe fenestration alterations. Fenestrations were defined as open pores with diameters between 50–300 nm; gaps as open pores with a diameter larger than 300 nm.

Endocytosis and degradation assay.

For quantitative studies of endocytosis and degradation, fully confluent cultures of rat LSECs (approx. $0.2\text{--}0.25 \times 10^6$ cells/cm²) established in 24-well culture dishes coated with human fibronectin, were treated with different oxLDL preparations for 30 minutes at 37 °C, subsequently incubated in 0.2 mL serum-free RPMI containing 0.1% human serum albumin and $2\text{--}3 \times 10^4$ cpm ¹²⁵I-FSA for 2h. Thereafter, the cell-associated and degraded FSA fractions were assayed according to Li, *et al.* (27). The LDH standard protocol assays were performed according to the manufacturer's instructions. Plot of toxicity and endocytosis activities column bar graphs were performed using the GraphPad Prism 8 (La Jolla, USA, www.graphpad.com). Cell association and degradation of ligands in each treatment for endocytosis were respectively analyzed with one-way ANOVA performed using the GraphPad Prism 8, the post hoc tests were used with Dunnett's multiple comparisons test for each treatment with RPMI control. Differences were considered significant if $p < 0.05$.

RESULTS

Cell morphology

SEM and SIM imaging were used to assess cultured LSEC fenestration alterations induced by various oxidation levels and doses of oxLDL (Figs. 1&2). The effects of oxLDL on LSEC were not uniform within the same cell culture, with some LSECs (approximately 5-10%) appearing to be more resistant to oxLDL treatment. LSECs treated with 80 $\mu\text{L}/\text{mL}$ oxLDL_{3/24} induced loss of sieve plates organization (Fig. 1B/C), compared with control cells treated with RPMI cell medium only, which show typical distinct sieve plates with fenestrae (Fig. 1A). Despite the loss of organized sieve plates, the cell surface is still perforated with fenestrations. The loss of sieve plates seems to be more pronounced and with higher LDL oxidation levels. Notably, there is a rather uniform distribution of the fenestrations throughout the entire cell surface in oxLDL₂₄ treated LSEC (Fig. 1C). On the other hand, the same concentration (80 $\mu\text{L}/\text{mL}$) oxLDL_{3/24} can also lead fenestrae in LSECs fusion and appearing with large trans-cytoplasmic gaps (Fig. 1D/E), and again, the occurrence of such gaps escalated with increasing oxidation levels of LDL.

Similarly, parallel to SEM samples, SIM microscopy was applied to monitor wet samples under the same oxLDL challenges to obviate the drying artifacts arising from SEM preparation, as well as to visualize the effects of oxLDLs treatments on the cell membrane in real-time. Fig. 2B shows that the higher LDL oxidation/concentration, the more fusions of fenestrations within the sieve plates, leading to the formation of trans-cytoplasmic gaps of 2-4 μm diameter (Fig. 2A). In general, the oxidation level of LDLs correlates with the fusion of fenestrations within sieve plates, i.e. the higher oxidization levels of LDL cause more damage to LSEC morphology. Interestingly, oxLDL₂₄ in low doses (10 $\mu\text{g}/\text{mL}$) exhibits a unique combination of a fully fenestrated cell surface with scattered large gaps in between (Fig. 2A, oxLDL₂₄ 10 $\mu\text{g}/\text{mL}$). These fenestrations appear to be similar to those observed in the oxLDL₂₄ treated LSECs SEM image (Fig. 1C), which might have become large gaps in LSEC with a longer incubation time.

Live imaging in Fig. 2B provides more detailed progress of large trans-cytoplasmic gap formations. Here, the RPMI cell medium treated LSECs (control) did not elicit obvious fenestrations fusion over 30 minutes (20 time points) of laser exposures. OxLDL_{3/24} treated LSECs were imaged under the same photon load, indicating that any changes, such as trans-cytoplasmic gap formation, are not the result of phototoxicity. Furthermore, we noted that small fenestrations that stand alone tended to disappear (red dashed circles) with oxLDL challenge. During the oxLDL challenge, fenestrations tend to expand further and form large gaps by merging with smaller fenestrations within the same sieve plate (yellow dashed rectangles). From our observations, mildly oxidized oxLDL₃ elicited a slower response than oxLDL₂₄ on LSECs with regard to alterations in morphology.

However, after sufficient time oxLDL₃ would likely elicit similar structural changes as the heavily oxLDL₂₄ does in the early stages.

Viability and scavenger function

To determine if oxLDL was directly toxic for LSEC, we performed viability (lactate dehydrogenase release: LDH) (Fig. 3A) and FSA endocytosis scavenger function assays (Fig. 3B) on cultured LSEC that were challenged with oxLDL. The LDH assay showed that oxLDL₃ and oxLDL₂₄ at the highest concentrations (80 µg/mL) had minimal cytotoxic effects compared to control, non-treated cells, with the LDH readout being roughly double baseline levels in control cultures treated with RPMI alone (Fig. 3A). Treatment of LSEC with 1% Triton X-100, which will cause 100% cell lysis without interfering LDH activity, gave an LDH readout 9-fold higher than baseline. The endocytic ability of LSECs following challenge with oxLDL was tested by incubating the cells with ¹²⁵I-FSA (Fig. 3B). At lower oxLDL concentrations (10 µg/mL) both oxLDL₃ and oxLDL₂₄ had no effects on the endocytosis of ¹²⁵I-FSA, neither at the cell-associated nor the degradation level. However, with increasing oxLDL concentrations and oxidation levels, endocytosis was significantly inhibited by 55, 76 and 89 % (by oxLDL₃ at 80 µg/mL, n=4; oxLDL₂₄ at 40 and 80 µg/mL, respectively, n=2 and 4) compared to RPMI group (n=4). Interestingly, the effects seen were mainly as a reduction in ¹²⁵I-FSA degradation, with the effect being more pronounced with increasing oxidation levels of oxLDL. This would suggest that LSEC maintain the capacity to take up oxLDL irrespective of the concentration and oxidation levels of oxLDL they are challenged with, but at higher concentrations and oxidation levels of oxLDL, the intracellular degradation machinery in LSEC is negatively affected.

DISCUSSION

As a major atherogenic substance, oxLDL exists in atherosclerotic lesions and in the circulation (2, 55), and is mainly removed by cells lining in the liver sinusoids (29, 49). The liver is the main clearance organ for these heterogeneous particles, which may present with different forms in plasma (9, 36). In our study, we tested the effects of mildly (oxLDL₃) and heavily (oxLDL₂₄) oxLDLs. Oxidation of LDL for 20-24 hours induces excessive modification (structural compositions, aggregation and fusion of molecules) of LDL (35), which also gives a more net negative charge to the complex compared to mildly oxLDLs (28). Mildly oxLDL is the main circulating form (9), whereas heavily oxLDL is rarely detected in the circulation of healthy individuals (55). Studies have shown that heavily oxLDL was taken up both by Kupffer cells and LSECs (49), and mildly oxLDL was only recognized by LSECs (28). This indicates that LSECs play an important role in eliminating plasma oxLDLs, which demonstrates the importance of the liver cell clearance system in the prevention of cardiovascular disease (22, 24, 44).

A previous *in vivo* study by Oteiza, *et al.* (36) showed that circulating oxLDL has significant negative effects on its clearance system, in that oxLDL challenge at clinically relevant plasma concentrations on mouse LSECs reduced the number of fenestrations. Our *in vitro* investigation on rat LSECs with relevant concentrations, shows similar negative effects, with more profound alterations on fenestrations (Fig. 2B): smaller fenestrations are disappearing or become smaller, which is consistent with the *in vivo* finding (36). With time, most of them turned into large trans-cytoplasmic gaps, which became more pronounced with increasing oxidation levels and concentrations of oxLDLs. Hence, the morphology of fenestrations in LSECs is clearly responsive to the oxLDL challenge.

Our SEM analysis demonstrated the loss of sieve plates post-oxLDL challenge (Fig. 1A), and this loss of sieve plates was apparent in previous *in vivo* findings but was not discussed by these authors (36). Our SIM investigations showed effects of oxLDL₂₄ at low concentrations, which appeared with loss of sieve plates and perforations with large trans-cytoplasmic gaps for a single cell after oxLDL₂₄ exposure at low concentrations (Fig. 2A oxLDL₂₄, 10 µg/mL). This unique combination of both effects within one single cell might be a further stage after the loss of sieve plates shown in Fig. 1C. The effects of oxLDL on LSECs were not uniform within the cells in the same cell culture, with some LSECs being more resistant to the oxLDL toxicity. While, demonstrating only loss of sieve plates and covered by numerous fenestration in some cells; in others, LSECs were presented with large trans-cytoplasmic gaps. Both effects were more profound with increasing oxidation levels of LDL.

As mentioned above, the effects of oxLDL on LSEC were not uniform within the same cell culture, with some LSECs appearing to be more resistant to oxLDL toxicity. LSECs treated with 80 µL/mL oxLDL_{3/24} induced loss of sieve plates (Fig. 1B/C), compared with

RPMI cell medium treated (control) LSECs, which show typical distinct sieve plates with fenestrae (Fig. 1A). Despite the loss of organized sieve plates, the cell surface is covered by numerous fenestrations. The loss of sieve plates tends to appear more with increasing LDL oxidation levels. Notably, there is a rather uniform distribution of the fenestrations throughout the entire cell surface in oxLDL₂₄ treated LSEC (Fig. 1C). On the other hand, the same concentration (80 μ L/mL) oxLDL_{3/24} can also lead to the formation of large trans-cytoplasmic gaps (Fig. 1D/E), the occurrence of such gaps escalated with increasing oxidation of LDL.

The effect differences on LSEC might be due to the cells being originating from different zones across the areas of liver lobules pre-perfusion (i.e. centrilobular and periportal regions), which show different morphological distributions of fenestrae. Vidal-Vanaclocha, *et al.* (50) showed that clustered and free fenestrae distributed differently in the LSEC of these two regions. In addition, larger and higher numbers of fenestrae from centrilobular sinusoids with greater fenestrae size were reported in several studies (50, 52, 54). Furthermore, a previous study showed that the oxLDL effects were most pronounced in central liver lobule LSEC (36). All these might explain why in our study the oxLDL effects were not uniformly observed on all cells. Further studies might be needed to understand the impact of oxLDL on LSECs from these two different liver zones.

Although SEM allows for high resolution imaging, it is known that SEM sample preparation procedures (e.g. dehydration) may induce artifacts such as alteration of tissue structure and shrinkage of the specimen (Cragg, 1988). For instance, 15-30% shrinkage of the tissue was reported in SEM imaging when using the critical point drying step (52). However, these induced artifacts can be avoided by using the SIM technique, which gives a resolution twice that of conventional light microscopy, which is sufficient to discern the average diameter (≥ 100 nm) of fenestrations on LSECs with SIM (10). Furthermore, samples can be applied in wet conditions, i.e. the cells can be imaged under suitable culture conditions; therefore, fixation and dehydration are not absolute requirements, avoiding the generation of artifacts from dehydration; and a leading advantage of this technique is the potential for imaging living cells (6, 41).

Imaging the LSECs by SIM, we could observe in real-time the effects oxLDL (80 μ g/mL) had on the cell membrane and fenestrations. To avoid excessive photobleaching of our fluorophore, we imaged the cells 20 times during a 30 minutes time-period. Mildly oxLDL₃ in our *in vitro* findings elicited a slower response than heavily oxLDL₂₄ on LSECs with regard to changes in morphology. However, after a sufficient time of incubation with oxLDL₃, it will probably elicit similar structural changes as the heavily oxLDL does at early stages. Thus, we suggest that mildly oxLDL with a longer circulatory life than the heavily oxLDL may have similar proatherogenic effects (29, 49), due to longer exposure time in contact with the vascular endothelial cells (4, 51). Therefore, an effective LSEC clearance of circulating mildly oxLDL is appeared to be also important in the prevention of cardiovascular disease (22, 24, 44).

In addition to being a key component in atherosclerosis development, the modification of LDL turns it into a proinflammatory and cytotoxic substance (47, 53). Importantly, in comparison to heavily oxLDL, the lower net negative charge of mildly oxLDL may have a low affinity for scavenger receptors, which might also explain the slow removal of this ligand from circulation, making it the predominant form present in human plasma (11, 28). Despite the presence of oxLDL in plasma (28), and in this study, LSECs largely remain viable, and are able to function as scavenger cells though with some effects on endocytosis and degradation of FSA resulting from oxLDL challenge. The reason for mildly oxLDL having less effect on FSA degradation might be due to the lower affinity for endocytosis of mildly oxidized compared with heavily oxLDL (28). Heavily oxLDL was shown to be more efficiently taken up by LSECs. Heavily oxLDL challenge of LSEC may thus elicit more rapid disruptions of morphology and inhibition of intracellular degradation pathways. However, the inhibition of FSA degradation was more obvious with increasing concentrations and oxidation levels of oxLDL in endocytosis studies (Fig. 3B). Interestingly, LSEC maintained the ability to take up FSA, irrespective of the concentration or oxidation status of the oxLDL treatment. This would suggest that the early endocytic machinery continues to function as (essentially) normal, but subsequent steps in the endo-lysosomal pathway are inhibited by oxLDL. This might be at the level of intracellular transport from endosomes to lysosomes, such that oxLDL-mediated disruptions to LSEC morphology may disrupt intracellular transport routes. Another possibility is that heavily oxidized oxLDL, with all its chemical modifications, causes lysosomal “indigestion” and renders the lysosome less able to degrade other substrates (such as FSA) as well.

Notably, the dramatic *in vitro* effects on LSECs morphology via oxLDLs do not take into account the other cell types (hepatocytes, Kupffer cells) in the liver, and the mutual effects these cells will have on each other. The same cell types might be less (or more) affected *in vivo*. Co-cultures with multiple liver cell-types are therefore more likely to resemble a functional liver. Further studies based on multiple relevant cell types in co-culture may facilitate a better understanding of the effects at the tissue/organ level of oxLDL challenge.

To conclude, this *in vitro* study addressed the effects of mildly and heavily oxLDL on rat LSEC morphology and function. LSECs remain viable and capable of (largely) functioning as scavenger cells, though with detrimental effects on LSECs morphology including the loss of sieve plates and ruptured fenestrations. Thus, oxLDLs cause adverse effects on LSECs.

ACKNOWLEDGEMENT

This study was supported by grants from the Tromsø Research Foundation/Trond Mohn, the University of Tromsø-The Arctic University of Norway, the Research Council of Norway FRIMED grant no. 262538, and Marie Skłodowska-Curie Grant Agreement No. 766181, project: DeLIVER.

REFERENCES

1. Ahotupa M, Asankari TJ. Baseline diene conjugation in LDL lipids: an indicator of circulating oxidized LDL. *Free Radic Biol Med.* 1999;27(11-12):1141-50.
2. Avogaro P, Bon GB, Cazzolato G. Presence of a modified low density lipoprotein in humans. *Arteriosclerosis.* 1988;8(1):79-87.
3. Berliner JA, Heinecke JW. The role of oxidized lipoproteins in atherogenesis. *Free Radic Biol Med.* 1996;20(5):707-27.
4. Berliner JA, Territo MC, Sevanian A, Ramin S, Kim JA, Bamshad B, et al. Minimally modified low density lipoprotein stimulates monocyte endothelial interactions. *J Clin Invest.* 1990;85(4):1260-6.
5. Blomhoff R, Drevon CA, Eskild W, Helgerud P, Norum KR, Berg T. Clearance of acetyl low density lipoprotein by rat liver endothelial cells. Implications for hepatic cholesterol metabolism. *J Biol Chem.* 1984;259(14):8898-903.
6. Bottomley AL, Turnbull L, Whitchurch CB, Harry EJ. Immobilization Techniques of Bacteria for Live Super-resolution Imaging Using Structured Illumination Microscopy. *Methods Mol Biol.* 2017;1535:197-209.
7. Brinkley TE, Nicklas BJ, Kanaya AM, Satterfield S, Lakatta EG, Simonsick EM, et al. Plasma oxidized low-density lipoprotein levels and arterial stiffness in older adults: the health, aging, and body composition study. *Hypertension.* 2009;53(5):846-52.
8. Brown MS, Goldstein JL. Receptor-mediated endocytosis: insights from the lipoprotein receptor system. *Proc Natl Acad Sci U S A.* 1979;76(7):3330-7.
9. Chang YH, Abdalla DS, Sevanian A. Characterization of cholesterol oxidation products formed by oxidative modification of low density lipoprotein. *Free Radic Biol Med.* 1997;23(2):202-14.
10. Cogger VC, McNerney GP, Nyunt T, DeLeve LD, McCourt P, Smedsrod B, et al. Three-dimensional structured illumination microscopy of liver sinusoidal endothelial cell fenestrations. *J Struct Biol.* 2010;171(3):382-8.
11. De Rijke YB, Biessen EA, Vogelezang CJ, van Berkel TJ. Binding characteristics of scavenger receptors on liver endothelial and Kupffer cells for modified low-density lipoproteins. *Biochem J.* 1994;304 (Pt 1):69-73.
12. DeLeve LD. Liver sinusoidal endothelial cells in hepatic fibrosis. *Hepatology.* 2015;61(5):1740-6.
13. Ehara S, Ueda M, Naruko T, Haze K, Itoh A, Otsuka M, et al. Elevated levels of oxidized low density lipoprotein show a positive relationship with the severity of acute coronary syndromes. *Circulation.* 2001;103(15):1955-60.
14. Elvevold KH, Nedredal GI, Revhaug A, Smedsrod B. Scavenger properties of cultivated pig liver endothelial cells. *Comp Hepatol.* 2004;3(1):4.
15. Faggiotto A, Ross R. Studies of hypercholesterolemia in the nonhuman primate. II. Fatty streak conversion to fibrous plaque. *Arteriosclerosis.* 1984;4(4):341-56.
16. Faggiotto A, Ross R, Harker L. Studies of hypercholesterolemia in the nonhuman primate. I. Changes that lead to fatty streak formation. *Arteriosclerosis.* 1984;4(4):323-40.
17. Fraser R, Bosanquet AG, Day WA. Filtration of chylomicrons by the liver may influence cholesterol metabolism and atherosclerosis. *Atherosclerosis.* 1978;29(2):113-23.
18. Fraser R, Cogger VC, Dobbs B, Jamieson H, Warren A, Hilmer SN, et al. The liver sieve and atherosclerosis. *Pathology.* 2012;44(3):181-6.

19. Fraser R, Dobbs BR, Rogers GW. Lipoproteins and the liver sieve: the role of the fenestrated sinusoidal endothelium in lipoprotein metabolism, atherosclerosis, and cirrhosis. *Hepatology*. 1995;21(3):863-74.
20. Glass CK, Witztum JL. Atherosclerosis. the road ahead. *Cell*. 2001;104(4):503-16.
21. Goldstein JL, Ho YK, Basu SK, Brown MS. Binding site on macrophages that mediates uptake and degradation of acetylated low density lipoprotein, producing massive cholesterol deposition. *Proc Natl Acad Sci U S A*. 1979;76(1):333-7.
22. Holvoet P, Stassen JM, Van Cleemput J, Collen D, Vanhaecke J. Oxidized low density lipoproteins in patients with transplant-associated coronary artery disease. *Arterioscler Thromb Vasc Biol*. 1998;18(1):100-7.
23. Holvoet P, Vanhaecke J, Janssens S, Van de Werf F, Collen D. Oxidized LDL and malondialdehyde-modified LDL in patients with acute coronary syndromes and stable coronary artery disease. *Circulation*. 1998;98(15):1487-94.
24. Itabe H, Mori M, Fujimoto Y, Higashi Y, Takano T. Minimally modified LDL is an oxidized LDL enriched with oxidized phosphatidylcholines. *J Biochem*. 2003;134(3):459-65.
25. Itabe H, Takano T. Oxidized low density lipoprotein: the occurrence and metabolism in circulation and in foam cells. *J Atheroscler Thromb*. 2000;7(3):123-31.
26. Jessup W, Kritharides L. Metabolism of oxidized LDL by macrophages. *Curr Opin Lipidol*. 2000;11(5):473-81.
27. Li R, McCourt P, Schledzewski K, Goerdts S, Moldenhauer G, Liu X, et al. Endocytosis of advanced glycation end-products in bovine choriocapillaris endothelial cells. *Microcirculation*. 2009;16(7):640-55.
28. Li R, Oteiza A, Sorensen KK, McCourt P, Olsen R, Smedsrod B, et al. Role of liver sinusoidal endothelial cells and stabilins in elimination of oxidized low-density lipoproteins. *Am J Physiol Gastrointest Liver Physiol*. 2011;300(1):G71-81.
29. Ling W, Loughheed M, Suzuki H, Buchan A, Kodama T, Steinbrecher UP. Oxidized or acetylated low density lipoproteins are rapidly cleared by the liver in mice with disruption of the scavenger receptor class A type I/II gene. *J Clin Invest*. 1997;100(2):244-52.
30. Masuda J, Ross R. Atherogenesis during low level hypercholesterolemia in the nonhuman primate. I. Fatty streak formation. *Arteriosclerosis*. 1990;10(2):164-77.
31. Masuda J, Ross R. Atherogenesis during low level hypercholesterolemia in the nonhuman primate. II. Fatty streak conversion to fibrous plaque. *Arteriosclerosis*. 1990;10(2):178-87.
32. Mego JL, Bertini F, McQueen JD. The use of formaldehyde-treated 131-I-albumin in the study of digestive vacuoles and some properties of these particles from mouse liver. *J Cell Biol*. 1967;32(3):699-707.
33. Miyao M, Kotani H, Ishida T, Kawai C, Manabe S, Abiru H, et al. Pivotal role of liver sinusoidal endothelial cells in NAFLD/NASH progression. *Lab Invest*. 2015;95(10):1130-44.
34. Noble RP. Electrophoretic separation of plasma lipoproteins in agarose gel. *J Lipid Res*. 1968;9(6):693-700.
35. Oorni K, Pentikainen MO, Ala-Korpela M, Kovanen PT. Aggregation, fusion, and vesicle formation of modified low density lipoprotein particles: molecular mechanisms and effects on matrix interactions. *J Lipid Res*. 2000;41(11):1703-14.
36. Oteiza A, Li R, McCuskey RS, Smedsrod B, Sorensen KK. Effects of oxidized low-density lipoproteins on the hepatic microvasculature. *Am J Physiol Gastrointest Liver Physiol*. 2011;301(4):G684-93.

37. Palinski W, Rosenfeld ME, Yla-Herttuala S, Gurtner GC, Socher SS, Butler SW, et al. Low density lipoprotein undergoes oxidative modification in vivo. *Proc Natl Acad Sci U S A*. 1989;86(4):1372-6.
38. Rader DJ, Daugherty A. Translating molecular discoveries into new therapies for atherosclerosis. *Nature*. 2008;451(7181):904-13.
39. Redgrave TG, Roberts DC, West CE. Separation of plasma lipoproteins by density-gradient ultracentrifugation. *Anal Biochem*. 1975;65(1-2):42-9.
40. Rumsey SC, Galeano NF, Arad Y, Deckelbaum RJ. Cryopreservation with sucrose maintains normal physical and biological properties of human plasma low density lipoproteins. *J Lipid Res*. 1992;33(10):1551-61.
41. Schwartz T, Aloush N, Goliand I, Segal I, Nachmias D, Arbely E, et al. Direct fluorescent-dye labeling of alpha-tubulin in mammalian cells for live cell and superresolution imaging. *Mol Biol Cell*. 2017;28(21):2747-56.
42. Schwartz CJ, Valente AJ, Sprague EA, Kelley JL, Nerem RM. The pathogenesis of atherosclerosis: an overview. *Clin Cardiol*. 1991;14(2 Suppl 1):11-16.
43. Shetty S, Lalor PF, Adams DH. Liver sinusoidal endothelial cells - gatekeepers of hepatic immunity. *Nat Rev Gastroenterol Hepatol*. 2018;15(9):555-67.
44. Smedsrod B. Clearance function of scavenger endothelial cells. *Comp Hepatol*. 2004;3 Suppl 1:S22.
45. Smedsrod B, Pertoft H. Preparation of pure hepatocytes and reticuloendothelial cells in high yield from a single rat liver by means of Percoll centrifugation and selective adherence. *J Leukoc Biol*. 1985;38(2):213-30.
46. Steinberg D. The LDL modification hypothesis of atherogenesis: an update. *J Lipid Res*. 2009;50 Suppl:S376-81.
47. Steinberg D. Low density lipoprotein oxidation and its pathobiological significance. *J Biol Chem*. 1997;272(34):20963-6.
48. Steinberg D, Parthasarathy S, Carew TE, Khoo JC, Witztum JL. Beyond cholesterol. Modifications of low-density lipoprotein that increase its atherogenicity. *N Engl J Med*. 1989;320(14):915-24.
49. Van Berkel TJ, De Rijke YB, Kruijt JK. Different fate in vivo of oxidatively modified low density lipoprotein and acetylated low density lipoprotein in rats. Recognition by various scavenger receptors on Kupffer and endothelial liver cells. *J Biol Chem*. 1991;266(4):2282-9.
50. Vidal-Vanaclocha F, Barbera-Guillem E. Fenestration patterns in endothelial cells of rat liver sinusoids. *J Ultrastruct Res*. 1985;90(2):115-23.
51. Watson AD, Leitinger N, Navab M, Faull KF, Horkko S, Witztum JL, et al. Structural identification by mass spectrometry of oxidized phospholipids in minimally oxidized low density lipoprotein that induce monocyte/endothelial interactions and evidence for their presence in vivo. *J Biol Chem*. 1997;272(21):13597-607.
52. Wisse E, De Zanger RB, Charels K, Van Der Smissen P, McCuskey RS. The liver sieve: considerations concerning the structure and function of endothelial fenestrae, the sinusoidal wall and the space of Disse. *Hepatology*. 1985;5(4):683-92.
53. Witztum JL, Steinberg D. Role of oxidized low density lipoprotein in atherogenesis. *J Clin Invest*. 1991;88(6):1785-92.
54. Xie G, Wang L, Wang X, Wang L, DeLeve LD. Isolation of periportal, midlobular, and centrilobular rat liver sinusoidal endothelial cells enables study of zoned drug toxicity. *Am J Physiol Gastrointest Liver Physiol*. 2010;299(5):G1204-10.
55. Yla-Herttuala S, Palinski W, Rosenfeld ME, Parthasarathy S, Carew TE, Butler S, et al. Evidence for the presence of oxidatively modified low density lipoprotein in atherosclerotic lesions of rabbit and man. *J Clin Invest*. 1989;84(4):1086-95.

FIGURE LEGENDS

Fig. 1 Representative scanning electron microscopy (SEM) images demonstrating loss of sieve plates following mildly/heavily oxidized LDL challenge on rat liver sinusoidal endothelial cells (LSECs).

A: RPMI culture medium incubated LSEC SEM image showing fenestrations grouped in sieve plates. B/C: 3/24-hour copper sulfate-induced oxidized LDL (oxLDL_{3/24}, 80 µg/mL, 30 minutes) treated LSEC SEM images with increasing oxidation levels showing a pronounced loss of sieve plates and uniform fenestration distribution. D/E: oxLDL_{3/24} (30 minutes, 80 µg/mL) treated LSEC SEM images with increasing oxidation levels showing the appearance of large trans-cytoplasmic gaps. Scale bar: 2 µm.

Fig. 2 Structured illumination microscopy (SIM) images of rat liver sinusoidal endothelial cells (LSECs) fenestration following treatments with LDL in different concentrations and degree of oxidation.

A: SIM images on fixed LSECs stained with CellMask Green show the appearance of large trans-cytoplasmic gaps after 30 minutes of various oxLDL challenges: RPMI cell medium, 3-hour copper sulfate-oxidized LDL (oxLDL₃, 10 and 80 µg/mL) and 24-hour copper sulfate-oxidized LDL (oxLDL₂₄, 10 and 80 µg/mL); B: Time-lapse images of live LSEC labeled with CellMask Green showing the effect of respective oxLDLs at 80 µg/mL, fenestration changes occurred in real-time and imaged within 30 minutes (every 1.5 minutes, 20 time-points in total, only 0, 1.5, 15 and 30 minutes are shown here): turning into large trans-cytoplasmic gaps for most of the fenestrations (yellow dashed rectangles) and disappearance of small fenestrations near the periphery (red dashed circle). The results are representative of experiments performed with 3 replicates. Images represent maximum intensity projections of a 1-2 µm 3D SIM z-stack. Scale bar: 2 µm.

Fig. 3 Viability and endocytic ability of rat liver sinusoidal endothelial cells (LSECs) with oxLDLs *in vitro* inhibition.

A: Primary rat LSEC tested with LDH cell viability kit to test the cytotoxicity of oxLDLs, RPMI cell media as control, 3/24-hours copper sulfate-oxidized LDL (oxLDL_{3/24}, 80 µg/mL) and 1% Triton X-100 (TX-100) as a positive control (100% toxicity), n=1. B: Different doses (10/40/80 µg/mL) of oxLDLs treated LSEC cultures were incubated for 2 hours at 37 °C with trace amounts of ¹²⁵I-FSA for the main LSEC endocytosis receptors (stabilin1/2). Endocytosis was measured as presented in Material and Methods. Dark grey bars represent cell-associated ligand, whereas white bars represent degraded ligand. Total endocytosed radioactivity represents the sum of cell-associated and degraded ligand radioactivity. Results are average of 2-4 independent experiments, are given in percentage of total endocytosed radioactivity. Bars represent mean ± SD. * p>0.05 using one-way ANOVA.

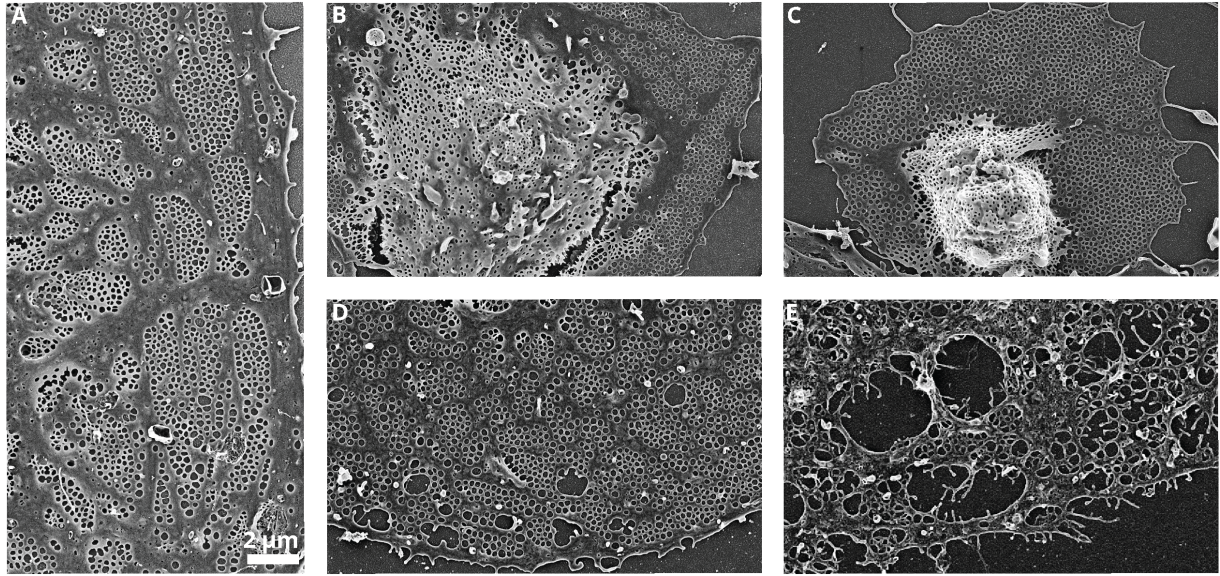


Fig. 1 Representative scanning electron microscopy (SEM) images demonstrating loss of sieve plates following mildly/heavily oxidized LDL challenge on rat liver sinusoidal endothelial cells (LSECs)

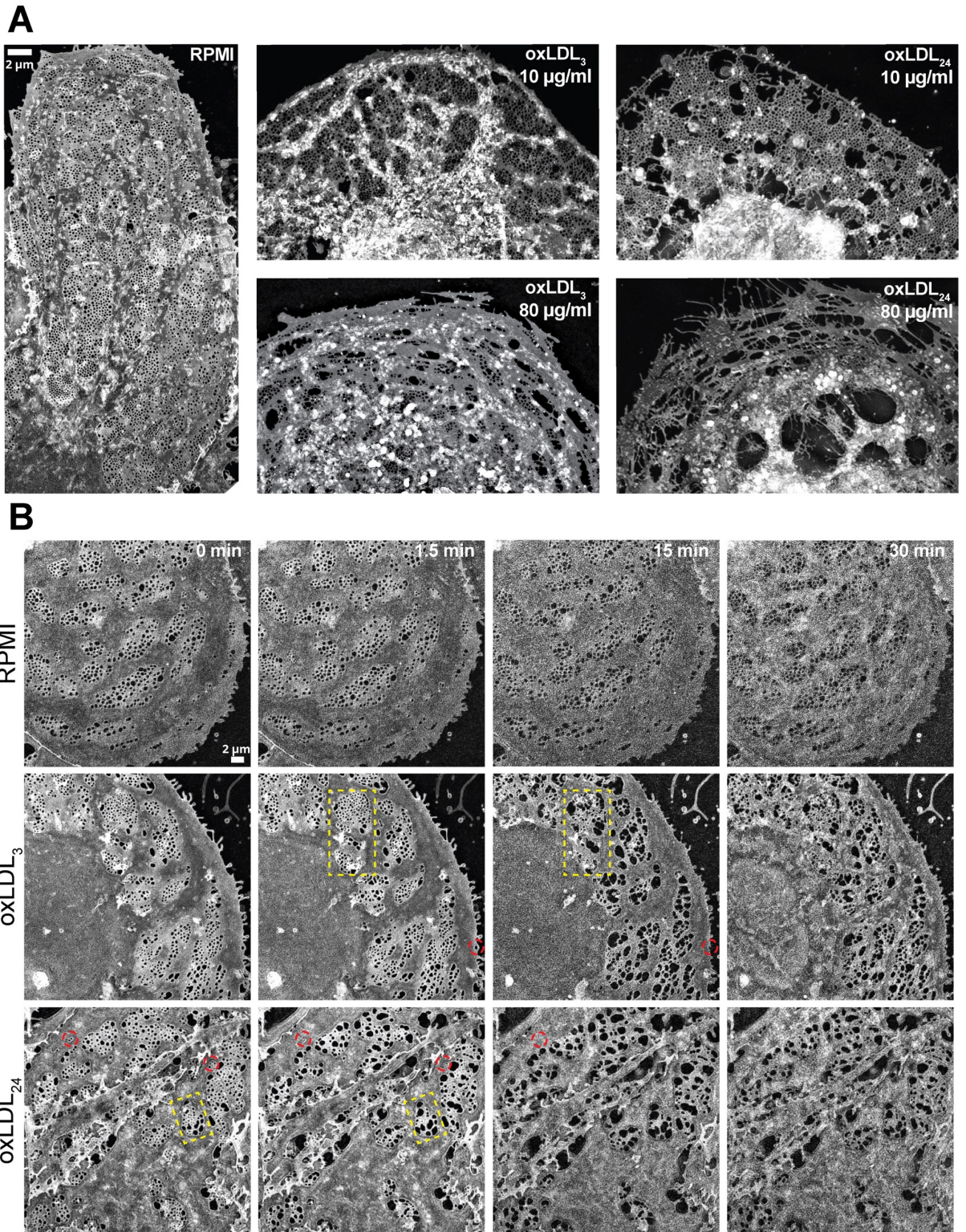


Fig. 2 Structured illumination microscopy (SIM) images of rat liver sinusoidal endothelial cells (LSECs) fenestration following treatments with LDL in different concentrations and degree of oxidation

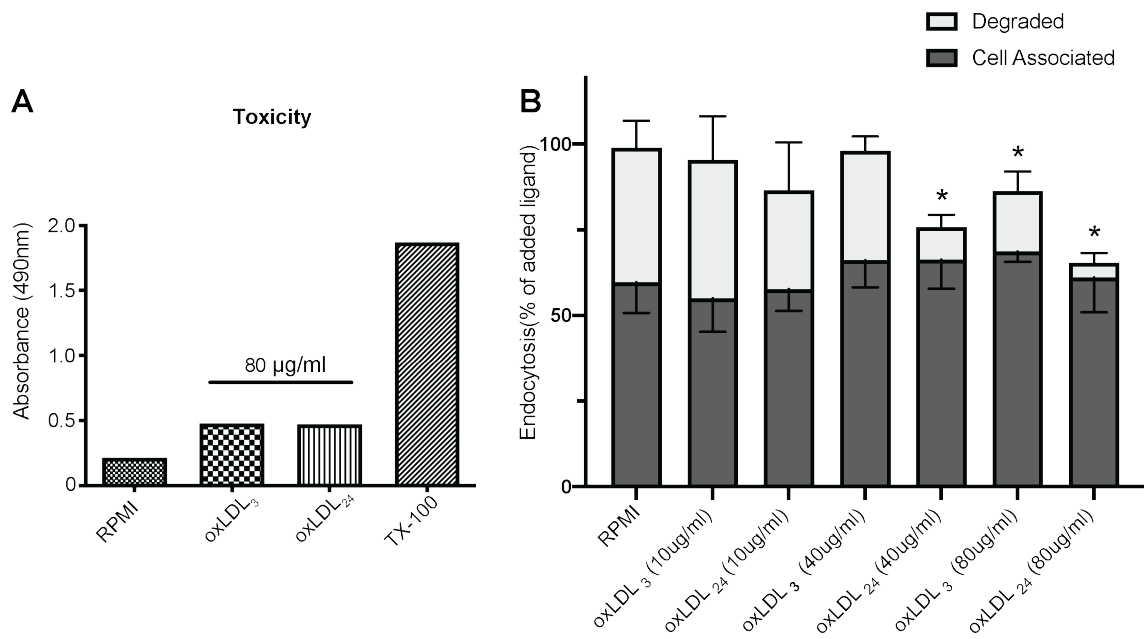


Fig. 3 Viability and ¹²⁵I-FSA endocytic ability of rat liver sinusoidal endothelial cells (LSECs) after oxLDLs *in vitro* inhibition

Paper IV



SCIENTIFIC REPORTS



OPEN

Primary rat LSECs preserve their characteristic phenotype after cryopreservation

Viola Mönkemöller¹, Hong Mao², Wolfgang Hübner¹, Gianina Dumitriu², Peter Heimann³, Gahl Levy², Thomas Huser¹, Barbara Kaltschmidt³, Christian Kaltschmidt³ & Cristina I. Øie²

Liver disease is a leading cause of morbidity and mortality worldwide. Recently, the liver non-parenchymal cells have gained increasing attention for their potential role in the development of liver disease. Liver sinusoidal endothelial cells (LSECs), a specialized type of endothelial cells that have unique morphology and function, play a fundamental role in maintaining liver homeostasis. Current protocols for LSEC isolation and cultivation rely on freshly isolated cells which can only be maintained differentiated in culture for a few days. This creates a limitation in the use of LSECs for research and a need for a consistent and reliable source of these cells. To date, no LSEC cryopreservation protocols have been reported that enable LSECs to retain their functional and morphological characteristics upon thawing and culturing. Here, we report a protocol to cryopreserve rat LSECs that, upon thawing, maintain full LSEC-signature features: fenestrations, scavenger receptor expression and endocytic function on par with freshly isolated cells. We have confirmed these features by a combination of biochemical and functional techniques, and super-resolution microscopy. Our findings offer a means to standardize research using LSECs, opening the prospects for designing pharmacological strategies for various liver diseases, and considering LSECs as a therapeutic target.

The liver is the largest organ in the human body, having essential functions related to maintaining homeostasis and metabolic integrity^{1,2}. Liver disease is one of the leading causes of morbidity and mortality worldwide^{3–5}. For decades, an immense effort has been undertaken to investigate the mechanisms behind various liver diseases and to develop therapeutic avenues. Despite great strides, many liver disease mechanisms have remained elusive^{3,6}. In recent years, the non-parenchymal cells of the liver have gained increasing attention for their potential role in the development of liver disease^{7–9}. Among these, the liver sinusoidal endothelial cells (LSECs) are the most abundant non-parenchymal cells, and play a fundamental role in maintaining liver homeostasis¹⁰. LSECs, the most effective scavengers of blood-borne waste macromolecules in the body^{10,11}, form the walls of the hepatic sinusoids and represent a highly specialized type of endothelial cells whose plasma membrane is perforated by numerous nanosized pores, or fenestrations^{11–13}. These fenestrations, which range between 50 and 300 nm in diameter under normal physiological conditions, facilitate the bi-directional transfer of substrates between the blood and the underlying hepatocytes¹². Liver injury coincides with drastic alterations in the LSEC phenotype, resulting in the loss of fenestrations and the formation of a basement membrane^{13,14}. LSECs have been reported to play a role in regulating sinusoidal flow¹⁵, liver regeneration^{16,17}, hepatic complications such as hepatitis, fibrosis and cirrhosis¹⁸, liver immune regulation^{14,19,20}, and age-related conditions^{21–23}.

Current protocols for isolation and cultivation of LSECs rely on freshly isolating the cells directly from the liver, which must be cultured shortly after isolation due to their rapid dedifferentiation. Their most important *in vivo* features, scavenging function and fenestrations, are severely decreased or disappear completely in LSECs that are kept in culture for more than 1–2 days^{24–26}, in particular in LSECs from small vertebrates like rodents²⁷. This is accompanied by a downregulation of LSEC signature genes²⁸. In addition, the isolation method is time consuming, meaning that to make the *in vitro* experimental conditions reflect the *in vivo* situation the closest (e.g. morphological/functional changes in response to stimuli/drugs), an entire work day may pass before the actual

¹Biomolecular Photonics, Department of Physics, Bielefeld University, Universitätsstr. 25, 33615, Bielefeld, Germany.

²Faculty of Health Sciences, Department of Medical Biology, Vascular Biology Research Group, UiT-The Arctic University of Norway, 9037, Tromsø, Norway. ³Cell Biology and Molecular Neurobiology, Department of Biology, Bielefeld University, Universitätsstr. 25, 33615, Bielefeld, Germany. Viola Mönkemöller and Hong Mao contributed equally. Correspondence and requests for materials should be addressed to C.I.Ø. (email: cristina.ionica.oie@uit.no)

experiment can be carried out. Maintaining functionally intact LSECs in culture for extended periods of time is presently not possible. Approaches to overcome these limitations, such as developing immortalized LSEC lines (reviewed in¹⁸), have had minimal success^{29–31}. These cells lack a proper phenotypic validation, and display very limited LSEC characteristics. The shortage of a consistent source of LSECs has led to the use of alternative cell models, such as non-hepatic ECs^{32–34}. However, alternative EC models lack the fundamental characteristics of LSECs with respect to their most important features in the liver, fenestrations and scavenging function.

To date, no protocols have been reported that enable the cryopreservation of LSECs that retain functional and morphological characteristics upon thawing and culturing. Therefore, we sought to develop a protocol that would allow for the cryopreservation of freshly isolated LSECs with intact phenotype upon thawing, similar to their *in vivo* counterparts. We found that freezing down freshly isolated LSECs (fLSECs) at low concentration is a prerequisite for after-thawing recovery of cryopreserved LSECs (cLSECs) with high viability, and full LSEC-signature features: fenestrations, scavenger receptor expression and endocytic function, on par with freshly isolated cells.

Results and Discussion

Rat LSECs were isolated using the Percoll gradient and selective adherence method^{35,36}. This method usually results in 80–120 million LSECs and >95% purity¹¹, enough to cover the needs for all the LSEC experiments ongoing in our lab. The leftover cells are sometimes frozen down in pellets for use in e.g. Western blot, RNA/gene expression analyses, or, in most cases, they are simply discarded. In this study we have investigated whether freshly isolated LSECs (fLSECs) would survive cryopreservation, and if, upon thawing, they might maintain their characteristic morphology and function. Two cell freezing media were used, containing 20% or 90% FBS in addition to 10% and 5% DMSO, respectively. Upon thawing and before seeding, the cryopreserved LSECs (cLSECs) were spun down once to remove FBS and DMSO. Although with various cell lines this step is omitted in order to avoid further mechanical stress on the cells, we found it to be necessary to remove the serum since it was previously shown to be toxic to rat LSECs in culture, having a major negative effect on the cells' viability and endocytic function^{27,37}. However, during this centrifugation step, about 25% of the cells are lost. The viability of the recovered cells was tested by Trypan Blue exclusion. We found that the LSECs cryopreserved in 20% FBS had very high viability after thawing as compared to the cells cryopreserved in 90% serum (>90% vs <50% viability, respectively). Moreover, the viability was also drastically affected depending on the number of cells to be frozen down. Increasing the cell count to more than 4×10^6 cells per cryotube resulted in less than 50% viability upon thawing, and the ability of the cells to adhere to the substrate in culture was dramatically reduced. After optimization of the method, dozens of vials from dozens of animals were thawed and used for various projects. The viability of the cells in these vials was similar to the one presented here. The thawed cLSECs were seeded in serum-free RPMI on plastic or glass surfaces coated with fibronectin, to allow adhesion and spreading. While fLSECs normally adhere to the substrate and fully expand their cytoplasm within 2 h from the time they were seeded³⁵, the cLSECs required about 1.5 h for optimal adherence, and an additional 1.5 h for spreading of their cytoplasm.

The general morphology of both types of cultured cells was assessed by light microscopy (LM) and, for ultra-structural details, by super-resolution structured illumination microscopy (SR-SIM) and scanning electron microscopy (SEM) (Fig. 1). No differences in cell shape or size were observed between the two groups. The cells had the typical “fried-egg” like shape, and an identical diameter of $29 \pm 7 \mu\text{m}$ in both groups (Fig. 1a–d). The unique morphological characteristic of LSECs, their fenestrations, were present in both fLSECs and cLSECs in culture (Fig. 1e–h). They could be observed clustered in sieve plates, spread throughout the cytoplasm in smaller groups, or standing alone. The average diameter of the fenestrae in fLSECs was similar, and not significantly different between the two cell conditions ($130 \pm 0.2 \text{ nm}$ in fLSECs and $139 \pm 0.4 \text{ nm}$ in cLSECs (reported with standard error of the mean)) (Fig. 2a). Figure 2b compares the distribution of fenestrations in the two cell cultures, grouped in different diameter size ranges. Compared to the fLSECs, the cLSECs had 18% fewer fenestrations with small diameters lying between 50–100 nm. Also, the cLSECs had 27% and 34% more fenestrations with large diameters between 200–250 nm and 250–300 nm, compared to fLSECs. Porosity, defined as the total area covered by fenestrations per total surface area analyzed, was also not significantly altered by cryopreserving the cells ($2.63 \pm 0.19\%$ versus $3.05 \pm 0.35\%$ in fLSECs versus cLSECs, respectively) (Fig. 2c). Fused fenestrations, i.e. adjacent fenestrations which have lost some of the intervening cytoplasm, were not included in the analysis. However, in cLSECs we observed an increase in fenestration distribution in the thicker membranes, close to the nuclear region, as compared to fLSECs (not shown). This nuclear distribution may be due to the fact that the cLSECs required more time for establishment in culture and expansion of their cytoplasm to fully expose the fenestrations in the thin areas of the cytoplasm. Gaps larger than 300 nm were equally observed in both cell groups: $8.5 \text{ gaps}/\mu\text{m}^2$ in the fLSECs versus $9.3 \text{ gaps}/\mu\text{m}^2$ in the cLSECs (Fig. 2d).

Preparation of the samples for SEM requires a series of fixation and dehydration steps that can generate artifacts, such as cracks and/or shrinkage of the specimen and alteration of tissue structure³⁸. To avoid this, we have also assessed the fenestrations in the two cell groups using super-resolution structured illumination microscopy (SR-SIM). This wide-field nanoscopy technique uses patterned illumination from a coherent light source to convert otherwise unobservable structures below the resolution limit of light microscopy into observable ones by generating difference/beat frequencies called Moiré fringes^{39–43}. The reconstructed image then has a resolution two times higher than that obtained by conventional light microscopy, which is well within the average diameter of fenestrations⁴⁴. Compared to SEM, the samples to be imaged by SR-SIM can be wet, meaning that the cells can be observed while in culture medium, and without fixation, thus avoiding dehydration artifacts and providing the greatest potential for live cell imaging^{45,46}. Here, we have used 3D-SIM to image fenestrations in live rat LSECs from both freshly isolated and cryopreserved cultures. Similar to the observations from SEM images, LSECs from both cultures expressed numerous fenestrations (Fig. 1g,h). However, due to the limitation of the linear SR-SIM technique, only fenestrations with a diameter of 100 nm or more are fully resolved.

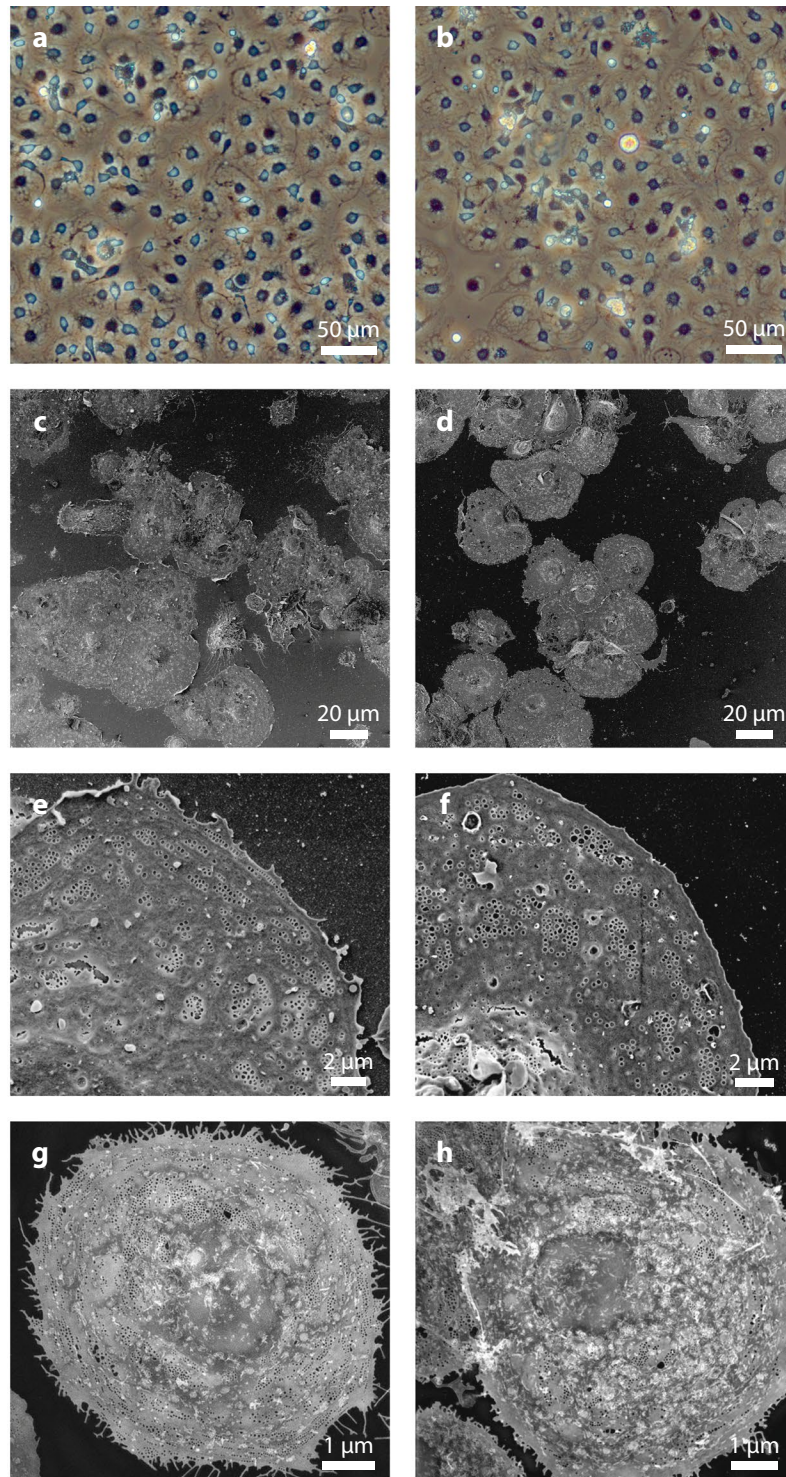


Figure 1. General morphology of fLSECs and cLSECs. In all micrographs, the left panels show images of fLSECs, and the right panels show images of cLSECs. (a) and (b) light microscopy images displaying the general morphology of the live cell cultures. (c) and (d) SEM micrographs of large fields of view of the two fixed cultures. The cells had the typical “fried-egg” shape, and an identical size of $29 \pm 7 \mu\text{m}$ for both fLSECs and cLSECs (Statistical details are presented in Table 2 under Materials and Methods). (e) and (f) High magnification SEM micrographs showing approximately one quarter of an entire LSEC. Numerous fenestrations are visible in both cell conditions, clustered in sieve plates, in smaller groups or standing alone, spread throughout the cytoplasm. (g) and (h) Maximum intensity Z-projections of 3D-SIM images of an entire LSEC from live cultures of fLSECs and cLSECs, respectively. For visualization of the plasma membrane and fenestrations, the fLSECs were stained with Vybrant DiO, and the cLSECs with CellMask Deep Red.

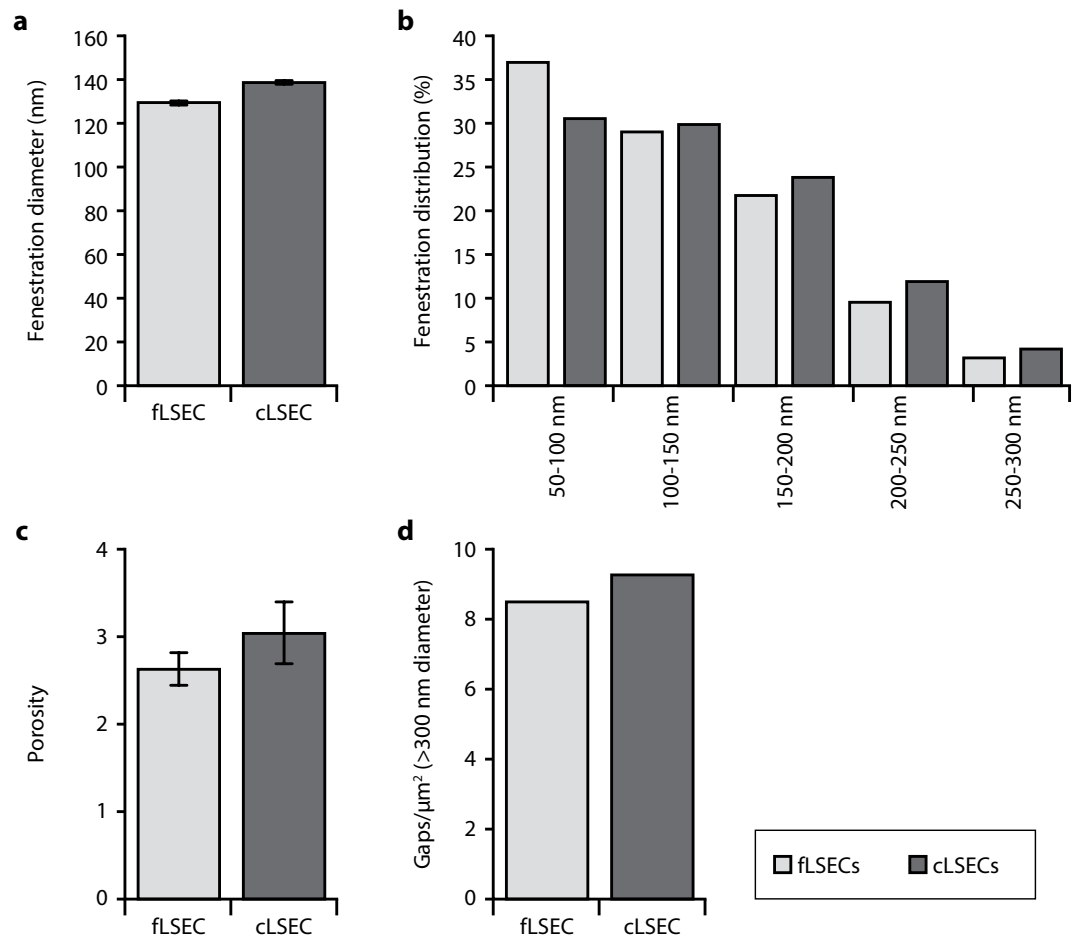


Figure 2. Ultrastructural features of fLSECs and cLSECs. **(a)** Average fenestration diameter. Statistical details are presented in Table 2 under Materials and Methods. **(b)** Frequency distribution of the fenestration diameter in fLSECs (light gray) versus cLSEC (dark gray), respectively. **(c)** Porosity (percentage) = total area covered by fenestrations per total surface area analyzed. **(d)** Number of gaps per μm^2 (holes larger than 300 nm in diameter). Bars represent mean \pm SEM.

Just as fenestrations are the gold standard for intact ultrastructural LSEC-specific identity, the functional hallmark of these cells is their effective uptake of soluble macromolecules that are cleared via clathrin-mediated endocytosis⁴⁷. Studies over the last couple of decades have established that the LSEC endocytic function relies mostly on the stabilin-1 and stabilin-2^{48–50}, mannose receptor (MR)^{10,51,52}, and Fc-gamma receptor IIb2 (Fc γ RIIb2)^{53,54}. The expression of these receptors was tested in cultures of LSECs by immunofluorescence (Fig. 3). Total fluorescence intensity per cell was measured for each receptor protein staining, and we found no significant difference in the expression between the two groups (Fig. 3 right panel).

In fully functional LSECs, the macromolecules that are recognized by these receptors are rapidly trafficked to, and efficiently degraded in the endo-lysosomal compartments. Here, we have tested the endocytic ability of cLSECs and compared it with the endocytic ability of fLSECs, by challenging the cultures with radiolabeled formaldehyde-treated serum albumin (¹²⁵I-FSA), tissue plasminogen activator (¹²⁵I-tPA), and aggregated gamma globulin (¹²⁵I-AGG), ligands specifically recognized by stabilin1/2, MR, and Fc γ RIIb2, respectively^{11,54–56} (Fig. 4). This assay allows precise quantification of the amount of ligand that is taken up by the cells. We found that cLSECs had virtually identical uptake and degradation ability as fLSECs based on all three endocytosis receptors tested.

Conclusion

Here, we have established and optimized a method for cryopreservation of rat LSECs. This cryopreservation method is very simple and reproducible, inexpensive, and readily available at any time point in any laboratory, without having to spend time and resources for expensive cryopreservants and method optimization. Cryopreserving freshly isolated rat LSECs using this method results in unchanged phenotype upon thawing and culturing. The ability to cryopreserve fully functional LSECs will facilitate a significant increase in research using these cells, reducing the number of animals and costs associated with cell isolation, and enable experiments to be conducted within the time frame of a regular working day. Studying LSECs and their implications in most liver diseases¹⁸ is important for our understanding of the natural progress of these diseases, and has the prospect of making LSECs an attractive therapeutic target. Moreover, cLSECs provide an ideal cell type for toxicology studies

Freezing medium containing 70% RPMI, 20% FBS, and 10% DMSO	Freezing medium containing 5% RPMI, 90% FBS, and 5% DMSO
Resuspend the cells in 1–2 ml cold RPMI	Resuspend the cells in 1–2 ml cold FBS
Add cold RPMI to the final calculated volume	Add cold RPMI
Add cold FBS	Add cold FBS to the final calculated volume
Resuspend the cells using a 5 ml pipette	Resuspend the solution using a 5 ml pipette
Dropwise, add the DMSO while rotating the tube containing the cells	Dropwise, add the DMSO while rotating the tube containing the cells
Resuspend the solution using a 5 ml pipette	Resuspend the solution using a 5 ml pipette
Dispense the final solution in 1 ml per cryotube	Disperse the final solution in 1 ml per cryotube

Table 1. Freezing media for cryopreservation of freshly isolated rat LSECs.

and designing pharmacological strategies, since by utilizing fully functional cLSECs one can avoid the limitations with batch-to-batch variability in response to drug therapy, especially when the cells originate from animals with rare conditions or liver diseases.

Materials and Methods

Materials and Reagents. Collagenase P was from Worthington Biochemical (Lakewood, NJ). Human serum albumin (HSA) was from Octapharma (Ziegelbrücke, Switzerland). Culture medium RPMI 1640, supplemented with 20 mM sodium bicarbonate, 0.006% (wt/vol) penicillin, and 0.01% (wt/vol) streptomycin, phosphate buffer saline (PBS), bovine serum albumin (BSA), and fetal bovine serum (FBS) were from Sigma-Aldrich, Oslo, Norway. Human fibronectin was purified from human plasma by affinity chromatography on Gelatin Sepharose 4B as described by the manufacturer. Sephadex G-25 (PD-10 columns) and Percoll were from Amersham Biotech (Uppsala, Sweden). Carrier-free Na^{125}I was from Perkin-Elmer Norge (Oslo, Norway), and 1,3,4,6-tetrachloro-3 α ,6 α -diphenylglycoluril (Iodogen) was from Pierce Chemical (Rockford, IL). Formaldehyde-treated bovine serum albumin (FSA) was prepared as described⁵⁷. Aggregated gamma globulin (AGG) was prepared from human normal immunoglobulin (100 mg/ml); Baxter, Vienna, Austria) by diluting it 1:9 with PBS and incubation at 63 °C in a water bath for 1 hour. Tissue plasminogen activator (tPA) was from American Diagnostica Inc., Stamford, CT, USA. Polyclonal rabbit anti rat stabilin-2 antibody was prepared as described⁵⁰. Polyclonal goat anti human mannose receptor (MR) and polyclonal goat anti human $\text{Fc}\gamma\text{RIIb}$ were from R&D Systems (Minneapolis, MN, USA). Both antibodies against human MR and $\text{Fc}\gamma\text{RIIb}$ also react with rat specimens. Rabbit nonimmune IgG and goat serum were from Sigma-Aldrich, Oslo, Norway. DRAQ5 was from Biostatus Limited (Leicestershire, UK). Vybrant DiO, CellMask Deep Red, Alexa Fluor-488 goat anti rabbit IgG, and Alexa Fluor-488 rabbit anti goat IgG secondary antibodies were from ThermoFisher Scientific, Oslo, Norway.

Labeling procedures. FSA, tPA and AGG (50 mg in 0.1 ml PBS) were labeled with carrier-free Na^{125}I in a direct reaction employing Iodogen as oxidizing agent, as described⁵⁸. Radiolabeled ligands and free iodine were separated by gel filtration on PD-10 columns equilibrated with PBS containing 1% human serum albumin. The specific activities were $3.3\text{--}5.1 \times 10^6$ cpm/ μg for FSA, $1.3\text{--}1.6 \times 10^6$ cpm/ μg for tPA, and $2.8\text{--}3.2 \times 10^6$ cpm/ μg for AGG.

Isolation and culture of rat liver sinusoidal endothelial cells. Sprague Dawley, Crl:CD(SD), male rats (Charles River, Sulzfeld, Germany) were group housed (2–3 rats per cage) in conventional Eurostandard type IV cages with aspen bedding (Tapvei, Estonia) and with nesting material (Sizzelnest, Datesand, UK), rat tunnels (Scanbur, Norway) and aspen chew blocks (Scanbur, Norway) as environmental enrichment. The rats were housed under controlled environmental conditions (21 °C \pm 1°, relative humidity 55% \pm 5% and 12-hour light/12-hour dark cycle). They were fed a standard chow *ad libitum* (RM1-E, Special Diet Service, UK) and tap water *ad libitum*. The rats (body weight 250–350 g) were anesthetized with a mixture (ZRF-mix) of zolazepam/tiletamine hydrochloride 12.9/12.9 mg/ml (Zoletil forte vet, Virbac, Norway), xylazine 1.8 mg/ml (Rompun, Bayer Nordic, Norway) and fentanyl 10.3 $\mu\text{g}/\text{ml}$ (Actavis, Norway). The experimental protocols were approved by the Norwegian Food Safety Authority (approval ID: 8455). Animal handling performed at the University of Bielefeld were approved by and carried out according to local authorities (Bezirksregierung Düsseldorf) and international guidelines. Rat LSECs were isolated and purified from anesthetized rats by Percoll separation and selective adherence³⁵. Briefly, the liver was perfused with collagenase, and the resulting single cell suspension was subjected to velocity and density centrifugations in Percoll gradients to produce purified suspensions of hepatocytes and nonparenchymal cells (NPCs). The NPC suspension was a mixture of Kupffer cells (KCs) and LSECs, and essentially devoid of hepatocytes, red blood cells, and debris. The NPC suspension was seeded directly on plastic in three 25 cm² culture dishes (Nunc, Roskilde, Denmark). Following a 45 min incubation at 37 °C, only KCs attached and spread onto the substrate, resulting in a highly enriched LSEC fraction in the supernatant. LSEC preparations were between 95% and 98% pure. The usual contaminants have been previously reported to be Kupffer cells (KCs; CD163-positive), and Stellate cells (SCs; identified by their content of autofluorescent vitamin A)¹¹. In this study, non-fenestrated cells identified by SEM were considered contaminants. Immediately after isolation, a fraction of the cells was seeded in the respective experimental conditions, and the remaining cells dispensed in cryotubes for cryopreservation.

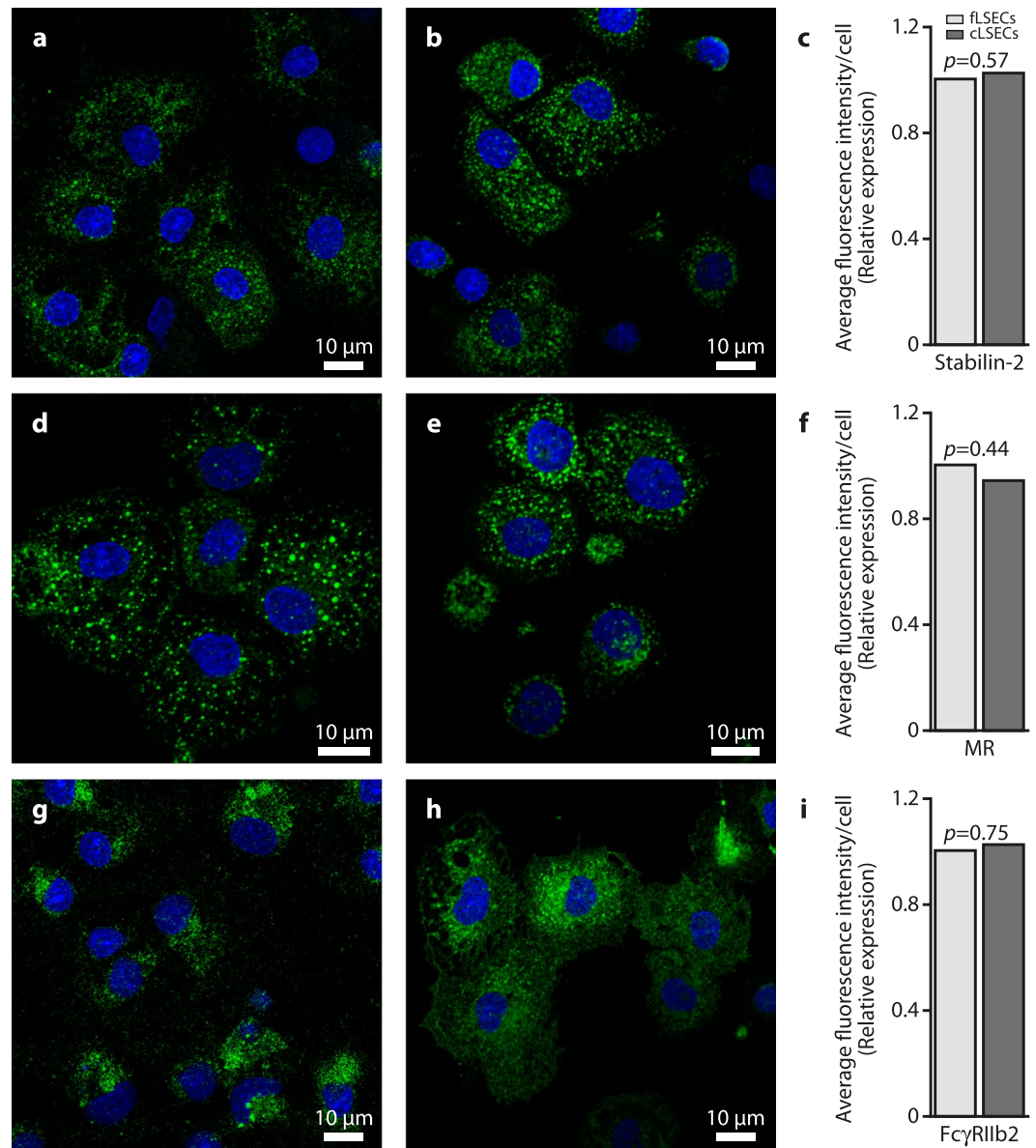


Figure 3. Expression of main endocytosis receptors by fLSEC and cLSECs. In all micrographs, the fLSECs are shown in the left panel and cLSECs in the right panel. The cultures were fixed with paraformaldehyde, permeabilized with Triton X, and immune labeled with antibodies against stabilin-2 (a and b), mannose receptor (MR) (d and e), and Fc γ RIIb2 (g and h). Positive immunolabeling was visualized with Alexa Fluor-488 secondary antibodies (green fluorescence). Cell nuclei were stained with DAPI (blue fluorescence). (g–i) The average fluorescence intensity per cell for each receptor protein was measured and the results expressed as relative expression, where the expression of the different markers in fLSECs equals 1. The *p* value is shown, which was calculated using the Excel two-tailed paired *t*-test assuming unequal variation. Statistical details are presented in Table 2 under Materials and Methods.

Freezing, thawing and culturing rat LSECs. Following the last step of isolation, the cells in suspension were counted using a hemocytometer and the viability assessed by Trypan Blue exclusion (>95%). The cells were then split into two fractions and pelleted by centrifugation for 8 min at 300 G, 4 °C. The supernatant was decanted without disturbing the cell pellet. Each cell pellet was resuspended at a final concentration of 4×10^6 LSECs/ml in the freezing media as described in Table 1. The solution was then dispensed into Nunc CryoTubes (Sigma-Aldrich, Oslo, Norway), and the tubes immediately placed in Mr. Frosty cryo container (ThermoFisher Scientific, Nalgene, Oslo, Norway). The container was transferred to -80 °C until the next day when the cryotubes were transferred to liquid nitrogen for long term storage.

For thawing the cLSECs, the cryotubes were retrieved from the liquid nitrogen tank and immediately placed into a 37 °C water bath. The tubes were swirled until only a small bit of ice was visible. Immediately, the cell suspension was dropwise added to a centrifuge tube containing 40 ml pre-warmed serum-free RPMI. After

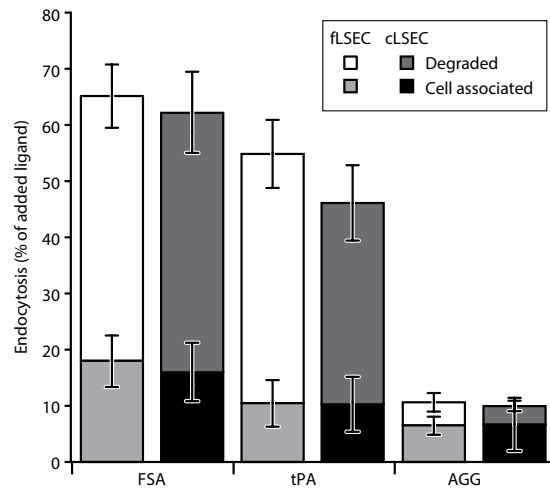


Figure 4. Endocytic ability of flSEC and cLSECs. Confluent cultures of flSEC and cLSECs were established in 24-well plates and incubated for 2 h at 37 °C with trace amounts of radiolabeled ligands for the main endocytosis receptors (^{125}I -FSA for stabilin1/2, ^{125}I -tPA for MR, and ^{125}I -AGG for Fc γ RIIb2). At the end of the incubation time, the amount of cell association radioactivity and degraded radioactivity was measured in the cells and spend medium. Bars represents mean \pm SD. Statistical details are presented in Table 2 under Materials and Methods.

centrifugation for 8 min at 300 G, the supernatant was discarded and the pelleted cells gently resuspended in serum-free RPMI. Cell number and viability was assessed prior seeding the cells in the respective experimental conditions.

Scanning electron microscopy (SEM). Cultures of flSECs and cLSECs from the same isolation were established in serum-free RPMI-1640 at a density of 0.1×10^6 cells/cm² on fibronectin coated plastic 6-well culture plates. The concentration of the fibronectin used was 0.2 mg/ml, and the coating was done using just enough volume to completely cover the surface area. After 10 min of incubation at RT, the fibronectin was washed off with PBS and cells seeded. The cells were fixed overnight in McDowell's or 4% formaldehyde (FA), 2.5% glutaraldehyde (GA) in cacodylic buffer. After washes with PBS, the bottom of the dishes containing the cells were cut off and treated with 1% tannic acid in 0.15 mol/l cacodylic buffer, 1% OsO₄ in 0.1 mol/l cacodylic buffer, dehydrated in ethanol, and incubated in hexamethyldisilazane (Sigma-Aldrich, Oslo, Norway), before coating with 10-nm gold/palladium alloys. Large field of view containing several cells, and high resolution SEM images of individual cells were acquired to assess cell size, fenestrations size and porosity. The iTEM software (Olympus, Asker, Norway) was used for measuring the cell diameter, while measurements of fenestration size and porosity were done using the public domain software Fiji (<https://fiji.sc>)⁵⁹.

Fluorescence microscopy. Cultures of flSECs and cLSECs from the same isolation were established in serum-free RPMI-1640 at a density of 0.1×10^6 cells/cm² on fibronectin coated 13 mm diameter #1.5 glass coverslips (VWR, Oslo, Norway) and #1.5 glass bottom dishes (MatTek, Ashland, MA, USA). Following attachment and spreading of the cytoplasm, the cells were either fixed and immunolabeled for confocal microscopy, or stained and observed live by structured illumination microscopy (SIM). For immunolabeling, the cells were washed and fixed in 4% FA for 15 min at room temperature. After a blocking step of 30 min with PBS containing 1% BSA, the cells were permeabilized in 0.03% Triton X-100 for 4 min and immune labeled by antibodies against stabilin-2, MR, or Fc γ RIIb as described^{50,60}. Rabbit nonimmune IgG and goat serum were used as negative controls. The Positive staining was visualized by using secondary antibodies tagged with Alexa Fluor-488 and DRAQ5 for nuclear staining. Specimens were examined using a Zeiss Laser Scanning Microscope 780 Meta (Carl Zeiss Microimaging GmbH, Göttingen, Germany) with a water-immersion Apochromat 40x/1.4 objective lens. For live super resolution imaging of the fenestrations, the cells were either stained with Vybrant DiO (1:200 in serum-free RPMI) or with CellMask Deep Red (1:5000 in serum-free RPMI) for 10 minutes and immediately imaged using a commercial super-resolving structured illumination microscope (DeltaVision/OMXv4.0 BLAZE, GE Healthcare) equipped with a 60X 1.42NA oil-immersion objective (Olympus). 3D-SIM images stacks of 1 μm were acquired with a z-distance of 125 nm and with 15 raw images per plane (five phases, three angles). Raw datasets were computationally reconstructed using SoftWoRx software (GE Healthcare). For clarity of display, linear changes were made to brightness and contrast of the images. Total fluorescence intensity per cell was measured using the Fiji software.

Endocytosis and degradation assay. For quantitative studies of endocytosis and degradation, fully confluent cultures of flSECs and cLSECs (approx. $0.2\text{--}0.25 \times 10^6$ cells/cm²) established in 24-well culture dishes coated with fibronectin were incubated in 0.2 ml serum-free RPMI containing 0.1% human serum albumin and $2\text{--}3 \times 10^4$ cpm ^{125}I -FSA, ^{125}I -tPA, or ^{125}I -AGG. After 2 h of incubation at 37 °C, the amount of degraded ligands was measured by collecting the spent medium together with one wash volume of 0.5 mL PBS. TCA (0.75 ml, 20%)

Result	No. of rats(separate cryotube)	Repeats	Statistical variation	Figure
Cell size			SD	1c,d
flSECs	5	27 images/449 cells		
cLSECs	3	13 images/281 cells		
flSECFenestration diameter/size distribution/porosity/gaps	4	44 images/137 cells78120 fenestrations6208 gaps	SEM	2a-d
cLSECFenestration diameter/size distribution/porosity/gaps	5	28 images/44 cells26731 fenestrations2107 gaps	SEM	2a-d
Immunocytochemistry Stabilin 2	3		Two tailed paired <i>t</i> -test assuming unequal variation	3
flSECs		103 cells		
cLSECs		79 cells		
Mannose receptor				
flSECs		103 cells		
cLSECs		97 cells		
Fc γ RIIb				
flSECs		97 cells		
cLSECs		66 cells		
Endocytosis assay				
¹²⁵ I-FSA		2-3 repeats (2-3 wells with cells + 1 well-cell free control) for each time an experiment was performed		4
flSECs	7			
cLSECs	5		SD	
¹²⁵ I-tPA				
flSECs	3		SD	
cLSECs	5			
¹²⁵ I-AGG				
flSECs	4			
cLSECs	4		SD	

Table 2. Summary of the repeats for each experiment. Each experiment was performed independently, and in parallel, using cells from 2–3 separate rats/cryotubes.

was added to precipitate intact phages. The amount of TCA-soluble radioactivity measured in the supernatant after centrifugation represented degraded ligands. To determine the amount of cell bound and internalized ligands, the cells were lysed in 0.1% sodium dodecyl sulfate (SDS). The radioactivity was measured using a Cobra II, Auto-Gamma detector (Packard Instruments, Laborel, Oslo, Norway). The amount of non-specific binding and free ¹²⁵I in cell-free wells was subtracted. The total endocytosis represents the sum of cell-associated and acid-soluble radioactivity.

Statistics. Table 2 summarizes the number of animals, the data, and the statistics done for the experiments included in this study. Measurements of cell size, fenestration size, and porosity were done using the SEM images. Only cells with clearly identifiable cellular borders were used for measurement of cell diameters. Fenestration size and porosity were assessed in SEM images from each cell culture selected from different areas (up, right, down, left and middle areas). Fenestrations were defined as open pores with diameters between 50–300 nm. Porosity was defined as the sum area of fenestrations per total area of the cell in the micrograph. Gaps were defined as holes with a diameter larger than 300 nm. Fiji software was used to identify and measure the area of all fenestrations (circularity 0.6–1) and gaps (circularity 0.1–1). Total fluorescence intensity per cell for each receptor staining was measured using Fiji after adjusting for background fluorescence. The results are expressed as relative expression, where the expression of the different markers in flSECs equals 1. Comparison between the two groups was performed using the Excel two-tailed paired *t*-test assuming unequal variation. Differences were considered significant if $p < 0.05$.

References

- Baynes, J. W. & Dominiczak, M. H. *Medical biochemistry* (Elsevier Mosby, 2005).
- Kmiec, Z. Cooperation of liver cells in health and disease. *Adv Anat Embryol Cell Biol* **161**, III–XIII, 1–151 (2001).
- Fotbolcu, H. & Zorlu, E. Nonalcoholic fatty liver disease as a multi-systemic disease. *World J. Gastroenterol.* **22**, 4079–4090 (2016).
- Mokdad, A. A. *et al.* Liver cirrhosis mortality in 187 countries between 1980 and 2010: a systematic analysis. *BMC Med* **12**, 145 (2014).
- Tsochatzis, E. A., Bosch, J. & Burroughs, A. K. Liver cirrhosis. *Lancet* **383**, 1749–1761 (2014).
- Arab, J. P., Arrese, M. & Trauner, M. Recent Insights into the Pathogenesis of Nonalcoholic Fatty Liver Disease. *Annu Rev Pathol Mech Dis* **13**, 321–350 (2018).
- Higashi, T., Friedman, S. L. & Hoshida, Y. Hepatic stellate cells as key target in liver fibrosis. *Adv Drug Deliv Rev* **121**, 27–42 (2017).

8. Ni, Y. *et al.* Pathological process of liver sinusoidal endothelial cells in liver diseases. *World J. Gastroenterol.* **23**, 7666–7677 (2017).
9. Byun, J. S. & Yi, H. S. Hepatic Immune Microenvironment in Alcoholic and Nonalcoholic Liver Disease. *Biomed Res Int* **2017**, 6862439 (2017).
10. Sorensen, K. K. *et al.* The scavenger endothelial cell: a new player in homeostasis and immunity. *Am. J. Physiol. Regul. Integr. Comp. Physiol.* **303**, R1217–30 (2012).
11. Li, R. *et al.* Role of liver sinusoidal endothelial cells and stabilins in elimination of oxidized low-density lipoproteins. *Am. J. Physiol. Gastrointest. Liver Physiol.* **300**, G71–81 (2011).
12. Braet, F. & Wisse, E. Structural and functional aspects of liver sinusoidal endothelial cell fenestrae: a review. *Comp Hepatol* **1**, 1 (2002).
13. Horn, T., Christoffersen, P. & Henriksen, J. H. Alcoholic liver injury: defenestration in noncirrhotic livers—a scanning electron microscopic study. *Hepatology* **7**, 77–82 (1987).
14. Warren, A. *et al.* Marked changes of the hepatic sinusoid in a transgenic mouse model of acute immune-mediated hepatitis. *J. Hepatol.* **46**, 239–246 (2007).
15. McCuskey, R. S. Morphological mechanisms for regulating blood flow through hepatic sinusoids. *Liver* **20**, 3–7 (2000).
16. Moniaux, N. & Faivre, J. Key role of sinusoidal endothelial cells in the triggering of liver regeneration. *J Hepatol* **55**, 488–490 (2011).
17. Ding, B. S. *et al.* Divergent angiocrine signals from vascular niche balance liver regeneration and fibrosis. *Nature* **505**, 97–102 (2014).
18. Poisson, J. *et al.* Liver sinusoidal endothelial cells: Physiology and role in liver diseases. *J Hepatol* **66**, 212–227 (2017).
19. Steinhoff, G., Behrend, M., Schrader, B., Duijvestijn, A. M. & Wonigeit, K. Expression patterns of leukocyte adhesion ligand molecules on human liver endothelia. Lack of ELAM-1 and CD62 inducibility on sinusoidal endothelia and distinct distribution of VCAM-1, ICAM-1, ICAM-2, and LFA-3. *Am. J. Pathol.* **142**, 481–488 (1993).
20. Racanelli, V. & Rehermann, B. The liver as an immunological organ. *Hepatology* **43**, S54–62 (2006).
21. Le Couteur, D. G. *et al.* Old age and the hepatic sinusoid. *Anat. Rec.* **291**, 672–683 (2008).
22. Warren, A. *et al.* Effects of old age on vascular complexity and dispersion of the hepatic sinusoidal network. *Microcirculation* **15**, 191–202 (2008).
23. Simon-Santamaria, J. *et al.* Age-related changes in scavenger receptor-mediated endocytosis in rat liver sinusoidal endothelial cells. *J. Gerontol. A. Biol. Sci. Med. Sci.* **65**, 951–960 (2010).
24. Ohi, N. *et al.* Maintenance of Bad phosphorylation prevents apoptosis of rat hepatic sinusoidal endothelial cells *in vitro* and *in vivo*. *Am. J. Pathol.* **168**, 1097–1106 (2006).
25. Krause, P. *et al.* Hepatocyte-supported serum-free culture of rat liver sinusoidal endothelial cells. *J Hepatol* **32**, 718–726 (2000).
26. Elvevold, K., Nedredal, G. I., Revhaug, A., Bertheussen, K. & Smedsrod, B. Long-term preservation of high endocytic activity in primary cultures of pig liver sinusoidal endothelial cells. *Eur J Cell Biol* **84**, 749–764 (2005).
27. Elvevold, K., Smedsrod, B. & Martinez, I. The liver sinusoidal endothelial cell: a cell type of controversial and confusing identity. *Am. J. Physiol. Liver Physiol.* **294**, G391–G400 (2008).
28. Geraud, C. *et al.* Liver sinusoidal endothelium: a microenvironment-dependent differentiation program in rat including the novel junctional protein liver endothelial differentiation-associated protein-1. *Hepatology* **52**, 313–326 (2010).
29. March, S., Hui, E. E., Underhill, G. H., Khetani, S. & Bhatia, S. N. Microenvironmental regulation of the sinusoidal endothelial cell phenotype *in vitro*. *Hepatology* **50**, 920–928 (2009).
30. Hwa, A. J. *et al.* Rat liver sinusoidal endothelial cells survive without exogenous VEGF in 3D perfused co-cultures with hepatocytes. *FASEB J* **21**, 2564–2579 (2007).
31. Bale, S. S. *et al.* Long-term coculture strategies for primary hepatocytes and liver sinusoidal endothelial cells. *Tissue Eng Part C Methods* **21**, 413–422 (2015).
32. Prodanov, L. *et al.* Long-term maintenance of a microfluidic 3D human liver sinusoid. *Biotechnol Bioeng* **113**, 241–246 (2016).
33. Nahmias, Y., Casali, M., Barbe, L., Berthiaume, F. & Yarmush, M. L. Liver endothelial cells promote LDL-R expression and the uptake of HCV-like particles in primary rat and human hepatocytes. *Hepatology* **43**, 257–265 (2006).
34. Liu, Y., Li, H., Yan, S., Wei, J. & Li, X. Hepatocyte cocultures with endothelial cells and fibroblasts on micropatterned fibrous mats to promote liver-specific functions and capillary formation capabilities. *Biomacromolecules* **15**, 1044–1054 (2014).
35. Smedsrod, B. & Pertoft, H. Preparation of pure hepatocytes and reticuloendothelial cells in high yield from a single rat liver by means of Percoll centrifugation and selective adherence. *J Leukoc Biol* **38**, 213–230 (1985).
36. Pertoft, H. & Smedsrod, B. Separation and characterization of liver cells. Pretlow, T. G. & Pretlow, T. P. N. Y. *eds Cell Sep. Methods Sel. Appl. Vol. 4. Acad. Press* 1–24 (1987).
37. Hansen, B., Melkko, J. & Smedsrod, B. Serum is a rich source of ligands for the scavenger receptor of hepatic sinusoidal endothelial cells. *Mol Cell Biochem* **229**, 63–72 (2002).
38. Crang, R. F. E. & Klomparens, K. L. Artifacts in Biological Electron Microscopy. Crang, R. F. E. & Klomparens, K. L. *Eds Plenum*, New York, 1988. xx, 233 pp., ill. \$45. *Science (80-)*. **242**, 309 (1988).
39. Abrahamsson, S., Ball, G., Wicker, K., Heintzmann, R. & Schermelleh, L. Structured Illumination Microscopy. *Super-Resolution Imaging Biomed. Eds: Albe*, 137–148 (2016).
40. Heintzmann, R. & Huser, T. Super-Resolution Structured Illumination Microscopy. *Chem Rev* **117**, 13890–13908 (2017).
41. Monkemoller, V., Oie, C., Hubner, W., Huser, T. & McCourt, P. Multimodal super-resolution optical microscopy visualizes the close connection between membrane and the cytoskeleton in liver sinusoidal endothelial cell fenestrations. *Sci. Rep.* **5**, 16279 (2015).
42. Monkemoller, V. *et al.* Imaging fenestrations in liver sinusoidal endothelial cells by optical localization microscopy. *Phys. Chem. Chem. Phys.* **16**, 12576–12581 (2014).
43. Svistounov, D. *et al.* The Relationship between fenestrations, sieve plates and rafts in liver sinusoidal endothelial cells. *PLoS One* **7**, e46134 (2012).
44. Cogger, V. C. *et al.* Three-dimensional structured illumination microscopy of liver sinusoidal endothelial cell fenestrations. *J Struct Biol* **171**, 382–388 (2010).
45. Schwartz, T. *et al.* Direct fluorescent-dye labeling of alpha-tubulin in mammalian cells for live cell and superresolution imaging. *Mol Biol Cell* **28**, 2747–2756 (2017).
46. Bottomley, A. L., Turnbull, L., Whitchurch, C. B. & Harry, E. J. *In Methods Mol Biol* **1535**, 197–209 (2017).
47. Sorensen, K. K., Simon-Santamaria, J., McCuskey, R. S. & Smedsrod, B. Liver Sinusoidal Endothelial Cells. *Compr. Physiol.* **5**, 1751–1774 (2015).
48. Politz, O. *et al.* Stabilin-1 and -2 constitute a novel family of fasciclin-like hyaluronan receptor homologues. *Biochem J* **362**, 155–164 (2002).
49. McCourt, P. A., Smedsrod, B. H., Melkko, J. & Johansson, S. Characterization of a hyaluronan receptor on rat sinusoidal liver endothelial cells and its functional relationship to scavenger receptors. *Hepatology* **30**, 1276–1286 (1999).
50. Hansen, B. *et al.* Stabilin-1 and stabilin-2 are both directed into the early endocytic pathway in hepatic sinusoidal endothelium via interactions with clathrin/AP-2, independent of ligand binding. *Exp Cell Res* **303**, 160–173 (2005).
51. Malovic, I. *et al.* The mannose receptor on murine liver sinusoidal endothelial cells is the main denatured collagen clearance receptor. *Hepatology* **45**, 1454–1461 (2007).
52. Magnusson, S. & Berg, T. Extremely rapid endocytosis mediated by the mannose receptor of sinusoidal endothelial rat liver cells. *Biochem J* **257**, 651–656 (1989).

53. Skogh, T., Blomhoff, R., Eskild, W. & Berg, T. Hepatic uptake of circulating IgG immune complexes. *Immunology* **55**, 585–594 (1985).
54. Mousavi, S. A. *et al.* Receptor-mediated endocytosis of immune complexes in rat liver sinusoidal endothelial cells is mediated by FcγRIIb2. *Hepatology* **46**, 871–884 (2007).
55. Blomhoff, R., Eskild, W. & Berg, T. Endocytosis of formaldehyde-treated serum albumin via scavenger pathway in liver endothelial cells. *Biochem J* **218**, 81–86 (1984).
56. Smedsrod, B., Einarsson, M. & Pertoft, H. Tissue plasminogen activator is endocytosed by mannose and galactose receptors of rat liver cells. *Thromb-Haemost* **59**, 480–484 (1988).
57. Mege, J. L., Bertini, F. & McQueen, J. D. The use of formaldehyde-treated 131-I-albumin in the study of digestive vacuoles and some properties of these particles from mouse liver. *J Cell Biol* **32**, 699–707 (1967).
58. Markwell, M. A. A new solid-state reagent to iodinate proteins. I. Conditions for the efficient labeling of antiserum. *Anal Biochem* **125**, 427–432 (1982).
59. Schindelin, J. *et al.* Fiji: an open-source platform for biological-image analysis. *Nat Methods* **9**, 676–682 (2012).
60. Li, R. *et al.* Endocytosis of advanced glycation end-products in bovine choriocapillaris endothelial cells. *Microcirculation* **16**, 640–655 (2009).

Acknowledgements

We are grateful for financial support from the Research Council of Norway (grant no. 275241 to CIØ), and the European Union's Horizon 2020 research and innovation program under the Marie Skłodowska-Curie Grant Agreement No. 766181 to TH and CK (project “DeLIVER”). We acknowledge the assistance with the production of figures given by Rod Wolstenholme, Dep. of Illustration and Media, UiT. We also acknowledge Randi Olsen and Tom-Ivar Eilertsen from the Advanced Microscopy Core facility for excellent assistance with sample preparation and SEM imaging. The publication charges for this article have been funded by a grant from the publication fund of UiT-The Arctic University of Norway.

Author Contributions

V.M., H.M., W.H., G.D. and CI.Ø. performed the experiments. H.M. analyzed the SEM images. V.M. and W.H. performed and analyzed the SR-SIM images. G.D. and P.H. provided technical assistance and materials. B.K. and C.K. planned experiments, analyzed and discussed data. Furthermore, they provided the animals and facilities for LSEC isolation, and P.H. and C.I.Ø. performed cell isolation at the University of Bielefeld. GL provided scientific input and analyzed SEM data. T.H. provided imaging facilities and materials at the University of Bielefeld, scientific input, and edited the manuscript. C.I.Ø. designed the experiments, isolated the cells, acquired and analyzed data, constructed the final figures, and wrote the manuscript. All authors approved the final version of the manuscript.

Additional Information

Competing Interests: The authors declare no competing interests.

Publisher's note: Springer Nature remains neutral with regard to jurisdictional claims in published maps and institutional affiliations.



Open Access This article is licensed under a Creative Commons Attribution 4.0 International License, which permits use, sharing, adaptation, distribution and reproduction in any medium or format, as long as you give appropriate credit to the original author(s) and the source, provide a link to the Creative Commons license, and indicate if changes were made. The images or other third party material in this article are included in the article's Creative Commons license, unless indicated otherwise in a credit line to the material. If material is not included in the article's Creative Commons license and your intended use is not permitted by statutory regulation or exceeds the permitted use, you will need to obtain permission directly from the copyright holder. To view a copy of this license, visit <http://creativecommons.org/licenses/by/4.0/>.

© The Author(s) 2018

